MAGNETIC IMAGING OF 3D ARTIFICIAL SPIN-ICE STRUCTURES

By Edward Gabriel Harding

A Thesis Submitted to Cardiff University for the Degree of Doctor of Philosophy

Author: Edward Gabriel Harding

Title: Magnetic Imaging of 3D Artificial Spin-Ice Structures

Date of Submission: December 2023

Significant Contributions

The work within this thesis is a collaborative effort involving the members of Sam Ladak's research group and our collaborators. It builds upon the substantial groundwork laid by the group, contributed by: Sam Ladak, Matthew Hunt, and Andrew May, who were previously associated with Cardiff University; Michael Saccone from University of California; and Arjen van den Berg and Joseph Askey.

Training for two-photon lithography, MOKE magnetometry, and AFM/MFM measurements provided by Matthew Hunt, Andrew May, Arjen van den Berg, Joseph Askey. Training for thermal evaporation provided by Saleem Shabir, Arjen van den Berg. Oxygen Plasma Exposure training provided by Matthew Hunt.

In Section 3: Dr Michael Saccone of the University of California, Santa Cruz developed and performed all Monte-Carlo simulations, derived the mean field theory and with Arjen van den Berg, performed simulations to determine the phase diagram of 3D artificial spin-ice. Shobhna Singh wrote the code to calculate magnetic structure factors and together with Arjen van den Berg, Sean Giblin, Felix Flicker and Sam Ladak, interpreted the data. Felix Flicker carried out entropy calculations of the 3D ASI system in paramagnetic and spin-ice phases. Scanning Electron Microscopy images were collected by Arjen van den Berg.

In Section 4: The Diamond Light Source STXM experiment occurred over three days with Sam Ladak and myself remotely overseeing measurements conducted in person at the synchrotron by beamline scientist Tohru Araki (Due to COVID pandemic). The TXM experiment at ALBA took place over three days, with oversight from Peter Fischer (Berkeley), David Raftrey (Berkeley), Sam Ladak and myself. Initially, the measurements were conducted in person at the synchrotron with the assistance of Beamline Scientist Lucia Abelle. Additional support during experiments was provided by Burkhard Kaulich and Emyr MacDonald.

Following these initial measurements and training, both David Raftrey and I conducted experiments remotely. Scanning Electron Microscopy images were collected by Joseph Askey and Arjen van den Berg. Oxygen Plasma Exposure was conducted by Matthew Hunt and myself.

Abstract

This thesis is a meticulous journey into the realm of three-dimensional Artificial Spin Ices (ASI), pushing the boundaries of exploration beyond the familiar territories of two dimensions. Employing methodologies like two-photon lithography and thermal evaporation, it navigates the intricate landscape of diamond-bond lattice geometries, unveiling emergent behaviours such as monopole propagation.

Section 3 meticulously charts the ASI structure's three-dimensional phase diagram, comparing predictive Monte Carlo simulations with experimental observations. The diversity of predicted phases, from double-charged monopole crystals to conventional spin ice, is scrutinized through magnetic force microscopy (MFM), revealing new vertex types and providing data for comparisons with simulations.

Discrepancies between anticipated and observed ground states are attributed to an effective chemical potential (μ^*) and limitations in the deterministic demagnetisation protocol. Ferromagnetic dominance on the upper surface layer and a higher μ^* for monopole formation impede the anticipated double-charged crystal, except in localized disorder regions. Recommendations for modifying the topography of the surface layer are proposed to realize this state.

Delving deeper into the system, x-ray magnetic circular dichroism (XMCD) is suggested to probe layers with a 1-unit cell thickness, expanding comprehension. Future plans involve transforming the 3D ASI into a thermally dynamic system, challenging for measurement techniques like MFM due to state perturbation and extended times.

Section 4 delves into synchrotron-based techniques, notably transmission X-ray microscopy with XMCD, affirming permalloy nanowire structures' crescent-shaped cross-section. Refinements in fabrication methods, despite revealing oxidization of the magnetic coating, offer nuanced insights into magnetic behaviours within the 3D ASI. XMCD measurements hint at weak signals, particularly in SL2, suggesting the need for further fabrication refinements and envisioning polymer-free magnetic nanowire-based 3D ASI designs for future exploration.

In a meticulous journey through ASI's three-dimensional landscapes, this thesis unearths complexities, proposes modifications, and sets the stage for deeper explorations into emergent phenomena.

Dedication

I want to express my profound gratitude to my supervisor, Sam Ladak, whose unwavering support and invaluable guidance have been instrumental throughout my entire PhD journey. I extend my heartfelt appreciation to my fellow colleagues in our research group—past and present, including Matthew Hunt, Andrew May, Arjen van den Berg, Alaa Hejazi, Joseph Askey, and Satya Vani. Your generous support, wealth of knowledge, and collaborative spirit have been critical in shaping my academic path. I'm grateful for the guidance and support of my secondary supervisor, Min Gao. His involvement in my annual supervisory meetings and adaptability to the challenges posed by COVID-19 have been invaluable. I would also like to thank Hartmut Grote in his position as my mentor.

I am also deeply thankful to the external scientists who played a pivotal role in the completion of my research. Tohru Araki, Lucia Abelle, Peter Fischer, David Raftrey, Burkhard Kaulich, Michael Saccone, Shobna Singh, Sean R. Giblin, Felix Flicker & Emyr MacDonald, Angela Sobiesierski, Michael Lewis, Saleem Shabbir, and others whose contributions have been immensely valuable. While I may inadvertently omit some names, the collective effort of many has truly made this journey possible.

To my family, your unwavering support has been a pillar of strength through all my years at university. I am profoundly grateful for your encouragement and understanding.

Finally, but most importantly, I want to acknowledge and thank my partner, Nadhia, for being a steadfast source of support during challenging times, infusing joy into my life, and providing boundless love.

Thanks to you all,

Edward

Publications

First Author:

Edward Harding, Tohru Araki, Joseph Askey, Matthew Hunt, Arjen Van Den Berg, David Raftrey, Peter Fischer, Lucia Aballe, Burkhard Kaulich, Sam Ladak, *Imaging the magnetic nanowire cross section and magnetic ordering within a suspended 3D artificial spin-ice*, *APL Mater.* 1 February 2024; 12 (2): 021116. https://doi.org/10.1063/5.0176907

Co-Author:

Michael Saccone, Arjen van den Berg, Edward Harding, Shobhna Singh, Felix Flicker, Sean Giblin, Sam Ladak, *Exploring the phases of 3D artificial spin ice: From Coulomb phase to magnetic monopole crystal, Commun Phys* **6**, 217 (2023). https://doi.org/10.1038/s42005-023-01338-2

Contents

List of Symbols and Acronyms

Symbol	Definition
a	Lattice Constant
a_0	Bohr Radius
A_{ex}	Exchange Stiffness
α	Molar Diamagnetic Susceptibility
α_D	Gilbert Damping Constant
β_{eff}	Inverted Effective Temperature
B	Magnetic Flux Density
b	Dipole Length
c	Speed of Light
C	Curie Constant
C_c	Crystal Structure Impact on Exchange Stiffness
d	Distance
$d(P,t)$	Voxel Diameter (Power, Processing Time)
d_i	Monte Carlo Disorder Term
dF_z	Lorenz Force
D	Demagnetising Factor
e	Electronic Charge
E_B	2D ASI Energy Barrier
E_{crys}	Magnetocrystalline Energy per Volume
E_{DMI}	DMI Energy Density
E_{ex}	Exchange Energy
E_f	Total Magnetic Free Energy
E_{int}	Energy of interaction Between Tip and Sample
E_{mtn}	Magnetostrictive Energy
E_{MS}	Magnetostatic Energy
E_{mc}	Magnetocrystalline Anisotropy Energy
E_{sl}	Spin Orbit Coupling Potential Energy
E_S	Single State Energy
E_T	Triplet State Energy
E_{Zee}	Zeeman Energy
$\boldsymbol{\varepsilon}$	Dielectric Tensor of a Material
ϵ	Strength of Interaction Between AFM Tip and Sample Surface
η	Initiation Process Efficiency
F	Force
f	Pulse Frequency
f_2	Imaginary Component of the Atomic Scattering Factor
g_s	Spin Spectroscopic Splitting Factor
γ	Orbital Gyromagnetic Ratio
γ_P	Gyromagnetic Ratio Term
$H, \boldsymbol{H}$	Magnetic Field
$\mathcal{H}$	Hamiltonian Operator
$\mathcal{H}_{SO}$	Spin Orbit Hamiltonian
$\mathcal{H}_{spin}$	Spin Dependent Term in Effect Hamiltonian
H_c	Coercive Field
H_d	Demagnetising Field
$\boldsymbol{H}_{sample}$	Stray Magnetic Fields of Sample

$\boldsymbol{H}_{tip}$	Stray Magnetic Fields of Tip
I	Current
I	Light Intensity
j	Effective Electron Angular Momentum
J	Total Atom Angular Momentum
J_{ex}	Exchange Integral
J_1, J_2	Nanomagnet Coupling Strength
K	Surface Current Density
K_A	Anisotropy Constant
K_{MA}	Magnetic Anisotropy Energy Density
k	Spring Constant
$\boldsymbol{k}$	Light Propagation Vector
k_b	Boltzmann Constant
l	Orbital Angular Momentum Quantum Number
l_z	Z-Component of Angular Momentum
$l(P,t)$	Voxel Length (Power, Processing Time)
L	Total Orbital Angular Momentum
L_2, L_3	L-Edge Energy Levels
λ	Wavelength
M	Magnetisation
M	Monomers
M_c	Charge Crystal Ordering Parameter
M_r	Remanence Magnetisation
M_s	Saturation Magnetisation
$\boldsymbol{M}_{sample}$	Sample Magnetisation
$\boldsymbol{M}_{tip}$	Tip Magnetisation
m_e	Electron Mass
m_e	Electron Mass
m_l	Magnetic Orbital Angular Momentum Quantum Number
m_s	Spin Magnetic Quantum Number
μ_0	Permeability of Free Space
μ_l	Magnetic Moment due to Orbital Component
μ	Magnetic Permeability
μ	Chemical Potential
$\boldsymbol{\mu}$	Magnetic Moment
μ^*	Effective Chemical Potential
μ_B	Bohr Magneton
μ_a	Atomic Photo-Absorption Cross Section
μ_s	Magnetic Moment due to Spin Component
N	Demagnetising Tensor
NA	Numerical Aperture
n	Density
n	Refractive Index
n_{oil}	Refractive Index of Immersion Oil
v	Frequency of Light
O_D	Optical Density
ω	Angular Velocity
ω	Light Optical Frequency
ω_0	Beam Waist
$\omega(z)$	Beam Waist at ‘z’

p	Magnetic Charge Density / Pole Strength
P	Laser Power
PI^*	Excited Photoinitiators
ρ	Density of Radicals
ρ	Volume Magnetic Charge Density
π	Pi Constant
Q	Charge
$Q_{x,y,z}, \boldsymbol{Q}$	Voigt Vector
r	Distance
$\hat{r}$	Distance Unit Vector
r_0	Classical Electron Radius
$R\cdot$	Radical
$RM\cdot$	Monomer Radicals
s	Spin Quantum Number
s_z	Z-Component of Electron Spin
S	Total Spin
$\widehat{\boldsymbol{S}}$	Spin Angular Momentum Operator
σ_2	Effective Two-Photon Cross Section for Radical Generation
σ_2^a	Ordinary Two-Photon Absorption Cross Section
σ	Distance at which $\epsilon = 0$
σ	Standard Deviation
t	Processing Time
T	Temperature
T_N	Neel Temperature
T_b	Blocking Temperature
T_c	Curie Temperature
T_{eff}	Effective Temperature
τ	Torque
τ	Pulse Width of Laser
τ_0	Attempt Time
τ_N	Neel Relaxation Time
u	Magnetic Coulomb Energy
V	Volume
V_{sample}	Sample Volume
V_{tip}	Tip Volume
w	Width
z_R	Rayleigh Length
Z	Element Atomic Number
ψ	Wavefunction
χ	Magnetic Susceptibility
χ_d	Diamagnetic Susceptibility
$\Delta\phi$	Phase Shift
h	Planks Constant
$\hbar$	Reduced Planck Constant
$\mathrm{Im}(\chi^{(3)})$	Imaginary Part of Third Order Susceptibility
$C[I]$	Single Charge Crystal
$C[II]$	Double Charge Crystal

Acronym	Definition
2D	2-Dimensional
3D	3-Dimensional
AC	Alternating Current
AFM	Atomic Force Microscopy
AOM	Accousto-Optic Modulator
ARCCA	Advanced Research Computing at Cardiff (Supercomputer)
ASI	Artificial Spin Ice
ATW	Asymmetric Transverse Domain Wall
CAD	Computer Aided Design
DiLL	Dip-in Laser Lithography
DLW	Direct Laser Writing
DMI	Dzyaloshinksii-Moriya interaction
EDX	Energy Dispersive X-ray (Spectroscopy)
FEBID	Focused Electron Beam Induced Deposition
GSM	Galvo Scan Mode
GWL	General Writing Language
IOLS	Inverse Opal Like Structure
IPA	Isopropyl Alcohol
LLG	Landau-Lifshitz-Gilbert Equation
MFM	Magnetic Force Microscopy
MOKE	Magneto Optical Kerr Effect
NMAG	Magnetism Simulation Package
OD	Optical Density
PSM	Piezo Scan Mode
QCM	Quartz Crystal Monitor
RF	Radio Frequency
SEM	Scanning Electron Microscopy
STL	Standard Tessellation Language
STXM	Scanning Transmission X-ray Microscopy
TPL	Two-Photon Lithography
TPP	Two-Photon Polymerisation
TW	Transverse Domain Wall
TXM	Transmission X-ray Microscopy
UV	Ultraviolet
VTK	Visual Toolkit File
XAS	X-ray Absorption Spectra
XMCD	X-ray Magnetic Circular Dichroism

List of Tables

List of Figures

Introduction

Artificial spin-ice (ASI) systems are lithographically patterned arrays of magnetic nano islands arranged into frustrated geometries and offer insights into the physics of ordering and emergence. Whilst traditionally confined to two-dimensions due to fabrication simplicity, recent strides in application of advanced lithography have enabled the realisation of 3D ASIs. These 3D systems open avenues for exploring tuneable ground states, novel domain wall topologies, monopole dynamics and innovative device concepts like magnetic racetrack memory.

Recent work has enabled the visualisation of emergent monopoles traversing upper surfaces within these 3D geometries utilizing magnetic force microscopy (MFM) measurements of the two surface layers. This thesis undertakes an in-depth exploration of the 3D ASI phase diagram through comparison with a Monte Carlo simulation of the 3D ASI. A diverse phase

diagram featuring a double-charged monopole crystal, single charged monopole crystal and conventional spin ice is predicted. The experimental 3D ASI is brought to its ground state utilising a demagnetisation protocol and the three surface layers are measured with MFM. Discrepancies between the experimental demagnetised systems and predicted states are observed. Surface induced broken symmetry leads to the formation of ferromagnetic stripes upon the surface layer, preventing the formation of the double-charged crystal. Crystallites of magnetic charge are observed across an ice background, shaped by the local distribution favouring monopole generation about the 3D vertices. Engineered surface energetics are suggested as alterations that could realise the double-charged crystal ground state, whilst deeper layer measurements may demand advanced synchrotron techniques.

Direct imaging using MFM has been instrumental in understanding the physics of 3D ASI systems but is constrained in depth and resolution, limiting observation to surface layers. This work pioneers a method to fabricate 3D ASI lattices over an aperture, employing two-photon lithography, thermal evaporation, and oxygen plasma exposure. This approach enables the probing of structural and magnetic specifics through soft x-ray microscopy, utilizing X-ray magnetic circular dichroism (XMCD) as magnetic contrast. The stability of suspended polymer-permalloy lattices under repeated soft X-ray exposure is confirmed. Analysis of x-ray absorption signals allows the reconstruction of complex magnetic nanowire cross-sections, showcasing a crescent-shaped geometry. Examination of XMCD images post-application of an in-plane field indicates surface magnetic moment reduction due to oxidation while retaining a measurable signal on sub-lattices below the surface, thereby revealing magnetic ordering.

Section 1 provides an exploration of fundamental magnetism principles essential for comprehending this thesis. It initiates with a foundational understanding of magnetic moments' origins, various magnetism types, and the dynamics of magnetic domains. The discussion progresses to delve into domain walls, frustrated systems, and the fundamental physics underpinning two-photon lithography, a crucial fabrication technique employed in this thesis.

Section 3 elucidates the detailed methodology adopted for both fabricating and characterizing the produced samples. Fabrication procedures involve a sequence of two-photon lithography, thermal evaporation, and oxygen plasma exposure. The array of

measurement techniques encompasses atomic and magnetic force microscopy, accompanied by the processing methodologies. Additionally, this chapter covers scanning electron microscopy and optical magnetometry techniques. Finally, it provides an insightful explanation of applied synchrotron techniques, particularly x-ray absorption spectra and x-ray magnetic circular dichroism.

Section 4 is devoted to the utilization of two-photon lithography for fabricating a 3D artificial spin ice structure, like previously measured samples. Monte Carlo simulations are harnessed to predict the ground state, envisioning a spectrum from a double-charge crystal to single charge crystal and spin-ice phase states. The thesis delves into demagnetisation processes applied to achieve the ground state, followed by MFM measurements. Analysis of these measurements identifies known and novel vertex types, cross-examined against micromagnetic simulated MFM contrasts and underlying spin textures. The chapter culminates in producing magnetic configurations from broad MFM datasets, scrutinizing these observed ground states against those predicted by Monte Carlo simulations, revealing a discrepancy. Discussion of this discrepancy revolves around increased surface energetics and a deterministic demagnetisation protocol inhibiting the formation of predicted states, proposing future directions including improved demagnetisation protocols and engineered surface energetics.

In Section 5, fabrication of a 3D ASI structure optimized for transmission x-ray microscopy (TXM) measurement is detailed. Innovations in fabrication methods, reducing the polymer scaffold beneath the magnetic coating, enhance x-ray transmission through the structure. Cross-sectional measurements confirm the crescent-shaped cross-section of permalloy nanowires. Statistical analysis of samples measured before and after applying a magnetic field hint at a buried weak magnetic signal within the 3D ASI. The chapter concludes with contemplating future work focusing on creating a purely metallic nanowire 3D ASI using techniques developed within this thesis.

Section 6 provides a comprehensive summary of the thesis's conclusions, drawing from the culmination of research and findings. Additionally, it outlines potential future directions that emerge from these derived conclusions.

1 Background Theory

1.1 Fundamentals of Magnetism

In this chapter, the foundational theory and essential concepts crucial for understanding the thesis are explored. Specifically, the realm of magnetism is examined, shedding light on the origins of domains and domain walls. The focus extends to the intricacies of magnetism within nanowires and curved geometries. Additionally, insights are provided into the emergence of spin ice and the advancements in artificially creating magnetic analogues of spin ice through advanced fabrication techniques like two-photon lithography. This aspect holds particular significance in the context of this thesis.

To provide a comprehensive background, relevant literature related to past research on artificial spin ice is thoroughly examined. This includes an exploration of the fabrication techniques employed and the methods used to measure these frustrated systems. This thorough examination ensures that the methodologies and results presented in this thesis find context within the broader field of study.

1.1.1 Magnetic Fields: H and B

As one learns in undergraduate physics, magnetic fields are produced by moving charges. The magnetic field intensity $\boldsymbol{H}$, represents the magnetising force or magnetic field created by an electrical current flowing through a wire and can be related to the current by the following equation [1]:

$$\boldsymbol{H} = \frac{\boldsymbol{I}}{2\pi r} \qquad (1)$$

Where $\boldsymbol{H}$ is the magnetic field intensity vector in Amperes per meter (A/m), $\boldsymbol{I}$ is the current vector in amperes (A) flowing through a wire, and r is the distance between the wire and point of measurement.

The magnetic flux density B represents the strength and direction of the magnetic field within a material or within a vacuum. The magnetic flux density is related to the magnetic field intensity by the following equation [1]:

$$B = \mu H \quad (2)$$

Where B is the magnetic flux density in units of Tesla (T), μ is the magnetic permeability of the material in Henrys per meter (H/m).

1.1.2 Magnetic Moments

The magnetic moment $\boldsymbol{\mu}$ is the fundamental building block of magnetism in solids and in general can be defined in two main ways. Firstly, one can define a magnetic moment in terms of a current carrying loop [1-3] :

$$\boldsymbol{\mu} = I\boldsymbol{A} \quad (3)$$

Where I is the magnitude of the current and $\boldsymbol{A}$ is a vector with magnitude equal to the area enclosed by the loop and direction given by the right-hand rule. An alternative means to define a magnetic moment is in terms of coupled magnetic charges as shown in **Figure 1** and can be written as [1-3]:

$$\boldsymbol{\mu} = p\boldsymbol{d} \quad (4)$$

Where $\boldsymbol{d}$ is a vector, defining the direction of the moment and p is the magnetic charge density, also known as the pole density.

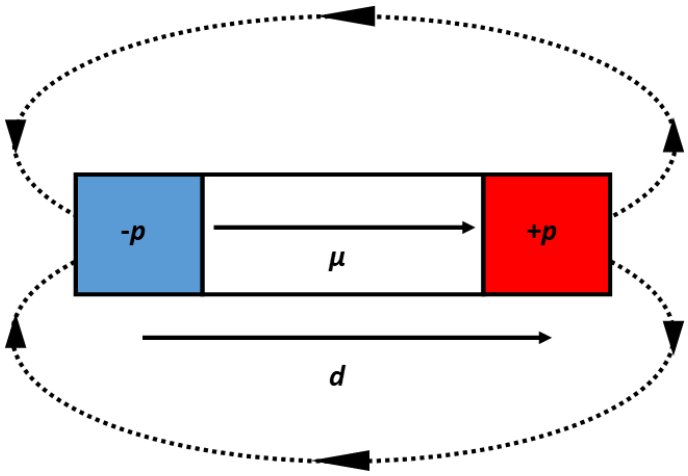

Figure 1: *A magnetic dipole with magnetic moment μ, orientation d and charges shown.*

1.1.3 Magnetisation

Quite often in condensed matter physics the magnetic moments associated with individual atoms are too small to be measured directly. It is hence convenient to define the magnetisation as the overall magnetic properties of a material. Magnetisation, denoted as M, is a crucial parameter for characterising the response of a material to an externally applied magnetic field and allows quantification of how magnetic moments within a material align themselves in response to the applied field.

Therefore the *magnetisation* M can be defined as the net magnetic moment per unit volume [1]:

$$M = \frac{1}{V}\sum_{N}\mu_i \qquad (5)$$

Where M is the magnetisation, V is the volume of the material, N is the total number of magnetic moments within the volume, and μ_i represents the magnetic moment of the ith magnetic moment.

The relationship between magnetisation, magnetic induction and an applied magnetic field is described by the magnetisation curve. This relationship can be expressed as:

$$B = \mu_0(H + M) \quad (6)$$

In this equation, μ_0 represents the permeability of free space, H is the magnetic field strength applied to the material and M is the magnetisation induced within the material.

1.1.4 Magnetic Moment in a Field

When an external magnetic field is applied to a magnetic moment, a torque τ is exerted which attempts to align the magnetic moment with the externally applied field. The torque can be calculated by using: [1-3]:

$$\tau = \mu_0(\boldsymbol{\mu} \times \boldsymbol{H}) = (\boldsymbol{\mu} \times \boldsymbol{B}) \quad (7)$$

By then integrating Equation (7) over the angle of rotation θ, and considering zero frictional force the potential energy of a magnetic moment within an applied field can be obtained [1-3]:

$$E_{Zee} = \mu_0 \mu H \int_0^{\theta} \sin\theta d\theta = -\mu_0 |\boldsymbol{\mu}||\boldsymbol{H}| \cos\theta = -\mu_0 \boldsymbol{\mu} \cdot \boldsymbol{H} = -\boldsymbol{\mu} \cdot \boldsymbol{B} \quad (8)$$

This quantity is known as the Zeeman energy and can be minimised by alignment of the magnetic moment with the external magnetic field ($\theta = 0^{\circ}$) or maximised when perpendicular to the field ($\theta = 90^{\circ}$). The energy between these two limits can be determined by [1-3]:

$$E_{Zee} = -mBcos\theta \quad (9)$$

1.1.5 Magnetostatic Field

To derive the origin of magnetostatic fields, Maxwells second equation must be considered.

$$\nabla . \mathbf{B} = 0 \qquad (10)$$

This equations states that magnetic field lines have no sources or sinks. This implies that they form closed loops. By considering that the magnetic flux density B is related to M and H by the permeability, μ, of a material, as seen in Equation (6). Combining with Maxwell's second law produces [1-3]:

$$\nabla . \boldsymbol{M} = -\nabla . \boldsymbol{H} \qquad (11)$$

This states that a non-zero diverging magnetisation, M, within a magnetised body generates a demagnetising field H_d. The H field generated within the magnetic body is known as the demagnetising field H_d, whereas the H field generated outside of the body is known as the stray field. By then using the divergence theorem:

$$\iiint_V (\nabla . \boldsymbol{M}) dV = -\oiint_S \boldsymbol{H} . d\boldsymbol{S} \qquad (12)$$

The above equation states that the divergence of the magnetisation inside a volume V corresponds to the negative flux of the magnetic field intensity H through the surface S. This indicates that the presence of magnetisation inside of a material result in a net flux of the magnetic field intensity through its surface, thereby generating a magnetic field both within the material, demagnetising field, and outside of the material, stray field.

In surface regions where the divergence of magnetisation is positive, it suggests a net accumulation of magnetic moments, akin to a magnetic source or a north magnetic pole. Conversely in regions where the divergence is negative, it implies a net depletion of magnetic moments akin to a magnetic sink or south magnetic pole. Therefore, the divergence of magnetisation within a material can lead to apparent magnetic charges or poles within the volume.

The interactions between magnets can be described through a parallel with simple electrostatics. It follows an inverse square law, describing the force between the ends of a dipole considered individually [1]:

$$\mathrm{F} = \frac{p_1 \cdot p_2}{r^2}\hat{\boldsymbol{r}} \qquad (13)$$

Here, F denotes the force, p_1 and p_2 are the pole strengths, r is the distance between the poles and $\hat{r}$ is the unit vector indicating the direction from one pole to another. Building upon this analogy, the interaction between magnetic poles can be described by [1]:

$$\boldsymbol{H_1} = \frac{p_1}{r^2}\hat{\boldsymbol{r}} \qquad (14)$$

Here a pole generates a magnetic field, where H_1 represents the magnetic field generated by a pole of strength p_1 and at a distance r from the pole and $\hat{r}$ is the unit vector. Now considering the overall case for the strength of the magnetic field produced by a magnetic dipole at any arbitrary position P at a distance r and an angle θ with respect to the axis of the dipole, shown in **Figure 2**.

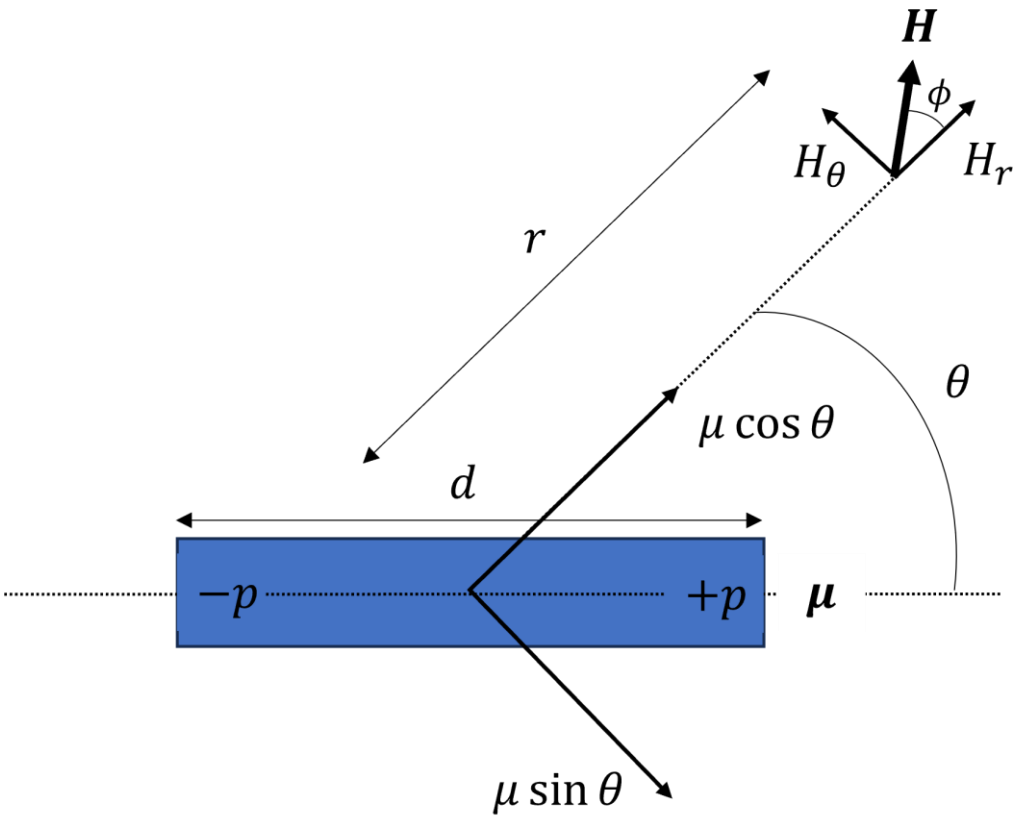

Figure 2: *Diagram showing the field strength* $\boldsymbol{H}$ *at an arbitrary position about a magnetic dipole as the sum of its constituent field strengths from poles* $-p$ *and +p. Figure adapted from [1].*

The overall magnetic moment of the dipole can be resolved into two components, radial μ_r and azimuthal μ_θ:

$$\mu_r = \mu \cos(\theta) \qquad (15)$$

$$\mu_\theta = \mu \sin(\theta)$$

Then considering the case that $r \gg d$:

$$H_r = \frac{2\mu\cos(\theta)}{r^3} \tag{16}$$

$$H_\theta = \frac{\mu\sin(\theta)}{r^3}$$

The total field strength H can be found by combining H_r and H_θ through vector addition. These two components are orthogonal to one another therefore Pythagoras' theorem can be used to calculate the magnitude of the field strength [1]:

$$|H| = \sqrt{H_r^2 + H_\theta^2} = \frac{\mu}{r^3}\sqrt{4\cos^2\theta + \sin^2\theta} = \frac{\mu}{r^3}(3\cos^2\theta + 1)^{\frac{1}{2}} \tag{17}$$

The direction of this calculated total field strength is given by the angle ϕ measured from the radial direction where [1]:

$$\tan(\phi) = \frac{H_\theta}{H_r} = \frac{\sin\theta}{2\cos\theta} = \frac{\tan\theta}{2} \tag{18}$$

This has been derived in terms of a magnetic dipole, likewise, is it possible to derive the total strength of the magnetic field at a point P produced by a current carrying loop and write the field with components parallel to μ and r as [1]:

$$H(\mu, r) = \frac{1}{4\pi}\left(3\frac{(\boldsymbol{\mu}\cdot\boldsymbol{r})\boldsymbol{r}}{r^5} - \frac{\boldsymbol{\mu}}{r^3}\right) \tag{19}$$

By combining Equation (19) with Equation (8) an equation which describes the interaction between two magnetic moments μ_i and μ_j separated by the vector $\boldsymbol{r}_{ij}$ can be generated [1]:

$$U(\boldsymbol{\mu}_i, \boldsymbol{\mu_j}, \boldsymbol{r}_{ij}) = \frac{\mu_0}{4\pi}\left[\frac{\boldsymbol{\mu}_i \cdot \boldsymbol{\mu}_j}{\boldsymbol{r}_{ij}^3} - 3\frac{(\boldsymbol{\mu}_i \cdot \boldsymbol{r}_{ij})(\boldsymbol{\mu}_j \cdot \boldsymbol{r}_{ij})}{\boldsymbol{r}_{ij}^5}\right] \quad (20)$$

Here, the first term in the enclosed brackets represents the attractive or repulsive interaction due to alignment or misalignment of the magnetic moments respectively. Whereas the secondary term accounts for the spatial dependence of the interaction.

1.1.6 Quantum Mechanical Origin of the Atomic Magnetic Moment

In quantum mechanics, the magnetic properties of atoms are rooted in two fundamental aspects: the angular momentum associated with the motions of electrons within their orbits and a unique intrinsic property known as electron spin [2-4]. This can be understood by adopting a classical view of a singular electron in orbit about a proton, akin to the Bohr model. This electrons motion generates an angular momentum due to its orbital path. In a classical perspective, this can be thought of as the electron current, defined by the electron charge e divided by the time taken to complete a single orbit [2-4].

Using the current-loop equation defined in Equation (3), the electronic magnetic moment due to the orbital component, μ_l, can be defined. By modelling this system with the area A defined by the circular loop the electron takes about the proton, with current defined by the electrons charge e as it precesses about the loop with an angular velocity ω. Using these definitions, it can be defined as [1-4]:

$$|\mu_l| = \frac{-e\omega r^2}{2} \quad (21)$$

This can be related back to the orbital angular momentum, l, of an electron with mass m_e as:

$$\mu_l = \frac{-e}{2m_e} l \qquad (22)$$

The orbital angular momentum and its associated magnetic moment are directly proportional to one another but in opposite directions. The orbital gyromagnetic ratio γ can be defined as [1-4]:

$$\gamma = \frac{-e}{2m_e} \qquad (23)$$

The orbital angular momentum magnitude of an electron is quantised due to the quantisation of the orbital motion [1-4], and this can be written as:

$$|l| = \hbar\sqrt{l(l+1)} \qquad (24)$$

$$l = 0, 1, 2, 3, \dots, n-1$$

Where l is the orbital angular momentum quantum number and is dependent upon the shape of the electron orbital, n is the principal quantum number and $\hbar$ is the reduced Planck's constant. The values of the orbital angular momentum quantum number correspond to the orbital that an electron occupies [1-4].

$l = 0$ corresponds to an s-orbital.

$l = 1$ corresponds to a p-orbital.

$l = 2$ corresponds to a d-orbital.

$l = 3$ corresponds to an f-orbital.

In the case of $l = 0$ and with only a single electron present in the s-orbital, this defines a value of $\mu_B = 9.274x10^{-24}\frac{J}{T}$. This is known as the Bohr magneton [1-4] often associated with the orbital magnetic moment and representing the magnetic moment due to the orbital motion of an electron. However, in cases where the orbital angular momentum is absent the magnetic moment is solely attributed to the intrinsic spin of the electron which is equivalent to the Bohr magneton.

When considering the projection of the angular momentum component, this can be described using a unique quantum number m_l which is called the azimuthal or spatial quantisation number. It describes the quantized values that the angular momentum L can take when projected along a specific axis, typically along the z-axis, represented by L_z, this can be expressed as [1-4]:

$$L_z = \hbar m_l \qquad (25)$$

In this equation, m_l takes on integer or half integer values ranging from $-l$ to $+l$, including zero. $\hbar$ is the reduced Planck constant. This quantisation process results in a total of $2l + 1$ possible values for L_z and therefore also for the angular momentum quantum number l. Quantisation reveals that the angle at which l aligns with a specific reference axis (where a magnetic field is applied) is also quantised. The number of allowed orientations for this precession of l is referred to as its degeneracy and is given by $2l + 1$ [1-4].

The quantised orbital magnetic moment of an electron can be expressed now as [1-4]:

$$|\mu_l| = \mu_B\sqrt{l(l+1)} \qquad (26)$$

As the spatial projections of the magnetic moment are also quantised this allows expression of the z-component of the magnetic moment as [1-4]:

$$\mu_{l,z} = -\mu_B m_l \qquad (27)$$

There is also an additional component contributing to the total magnetic moment of an electron, arising from the intrinsic angular momentum associated with the electron's spin, represented as s [1-4]. This characteristic originates from relativistic quantum mechanics. Much like Equation (22), this component can be similarly defined as:

$$\mu_s = \frac{-eg_s}{2m_e}s \qquad (28)$$

The constant of proportionality, g_s, is known as the spin spectroscopic splitting factor, and experimental measurements have shown it to be approximately $g_s \approx 2$ for purely spin angular momentum, whilst $g_l \approx 1$ for purely orbital angular momentum [1-4]. This means that the spin contribution is twice as significant towards the magnetic moment compared to the orbital angular momentum.

In a manner like the orbital angular momentum described previously, the spin angular momentum is also quantised [1-4]. This quantisation can be defined using a set of distinct quantum numbers, denoted as s. The magnitude of the spin angular momentum is given by:

$$|s| = \hbar\sqrt{s(s+1)} \quad (29)$$

Following this, and given that $g_s = 2$, along with the previously mentioned definition of the Bohr magneton, the spin magnetic moment μ_s can be written as:

$$|\mu_s| = 2\mu_B\sqrt{s(s+1)} \quad (30)$$

Assuming that the degeneracy for the spin angular momentum quantum number follows that of the orbital angular momentum quantum number and considering that the electronic spins can only occupy either "up" or "down" states, yielding a total number of 2 configurations, then it can be deduced that $2s + 1 = 2$, therefore after simplification $s = \frac{1}{2}$. Much like the spatial projection of the orbital angular momentum, the spatial projection of spin can be defined using another quantum number, m_s, where [1-4]:

$$s_z = \hbar m_s \quad (31)$$

It follows that the values of m_s are $\pm\frac{1}{2}$, corresponding to $s_z = \pm\frac{\hbar}{2}$. This quantisation leads to the definition of magnetic moment due to the electronic spin as [1-4]:

$$|\mu_s| = g_s\mu_B\sqrt{s(s+1)} \quad (32)$$

Additionally, the spatial projection along the z-direction can be defined as:

$$\mu_{s,z} = -\mu_B m_s g_s \quad (33)$$

The orbital and spin angular momentum components of an electron can couple together through the spin-orbit interaction, giving rise to an effective electron angular momentum, j, defined as the sum of these two previously discussed components [1-4]:

$$j = l + s \quad (34)$$

The potential energy associated with this spin-orbit coupling can be described semi classically as the dipole interaction between the spin and the magnetic field generated by orbital motion and is proportional to $l \cdot s$. More formally, this interaction can be defined as [1-4]:

$$E_{sl} = \frac{\mu_0 e^2 Z^4}{4\pi a_0^3 m_e} l \cdot s \quad (35)$$

Here in this equation, a_0, represents the Bohr radius, Z represents the atomic number of the element, and m_e is the electron mass. Notably, the significance of the spin orbit interaction energy increases with higher atomic numbers due to the Z^4 component. This type of interaction plays a crucial role in various magnetic properties, including the magnetocrystalline anisotropy, magnetostriction, the behaviour of hard and soft magnets as well as the anomalous and spin Hall effects [4].

Electrons associated with atoms possess magnetic moments due to their intrinsic spin and their orbital motion [1-4]. The magnetic moment of a free atom is a result of its constituent electron spins, the electron orbital angular momenta about the atomic nucleus and the change in orbital magnetic moment induced by an externally applied field.

When dealing with multi-electron atoms, calculating the total spin and orbital angular momenta can be a complex endeavour. These values are the vector sums of the contributions from individual constituent electrons. In this context the quantum numbers are used to

represent these components, specifically S for the total spin and L for the total orbital angular momentum of an atoms orbiting electrons. The total angular momentum of the atom, J, depends on both S and L [1-4]:

$$J = L + S \tag{36}$$

However, it's crucial to note that Equation (36) mainly applies for weak spin-orbit coupling in atoms with $Z < 30$. Most atoms exhibit behaviour beyond simple diamagnetism, discussed later in Section 1.2.1. While diamagnetic behaviour occurs when the net angular momentum is zero, leading to a repulsive response to an applied magnetic field, many materials demonstrate paramagnetic behaviour. In paramagnetic materials, a topic discussed in Section 1.2.2, there exist non-zero atomic magnetic moments even in the absence of an external magnetic field. These non-zero atomic moments typically cancel each other out on a macroscopic scale in the absence of an applied field, owing to disorder induced by thermal fluctuations. However, there are fascinating exceptions to this rule. Some 3d transition metals and 4d rare earth metals exhibit the unique ability to achieve collective ordering of atomic magnetic moments without the application of an external magnetic field. In these materials, a non-zero net magnetic moment may arise, leading to their classification as ferromagnetic materials. This phenomenon in ferromagnetic materials will be explored in greater detail in the subsequent sections.

1.1.7 Susceptibility and Permeability

As has been described, there exist many different classes of magnetism and as the *magnetic susceptibility* χ is defined to quantify these differences. The magnetic susceptibility is a dimensionless proportionality constant that describes the magnetisation response of a material to an applied magnetic field, $\boldsymbol{H}$. In a homogenous, linear material the susceptibility can be defined using [1-3]:

$$\boldsymbol{M} = \chi \boldsymbol{H} \qquad (37)$$

Alternatively, the magnetic flux density B is related to M and H by the permeability, μ, of a material. The permeability defines the degree to which a materials magnetic flux density B responds to a magnetic field H [1-3]:

$$B = \mu_0(H + M) = \mu_0(H + \chi_m \boldsymbol{H}) = \mu_0(1 + \chi_m)H = \mu H \qquad (38)$$

Where μ_0 is the permeability of free space. As can be seen in the final statements of the above equation, a large susceptibility results in a large permeability and the reverse is true. Therefore, the two quantities are just two different ways of describing the response of magnetic field to an external field.

By examining the magnetic susceptibility, magnetic materials can be classified into different types, including paramagnetic, diamagnetic, and ferromagnetic materials. The magnetic susceptibility helps quantify how a material will respond to an externally applied magnetic field and offers insights into its magnetic behaviour.

1.2 Magnetism Types

1.2.1 Diamagnetic Materials

Diamagnetism is a fundamental property found in all atoms, but its response is weak when compared to the more pronounced effects observed in paramagnetic and ferromagnetic materials. Diamagnetic behaviour can be primarily attributed to materials with filled electron shells, resulting in the absence of effective atomic magnetic moments. Therefore, when subjected to an externally applied magnetic field, the electrons orbits within the diamagnetic material precess in a manner that opposes the applied field resulting in a minor negative susceptibility in the range of $-10^{-5} < \chi < 0$ [1-3].

Though this classical argument provides a good estimation of the diamagnetic susceptibility, diamagnetism is quantum mechanical in origin. All materials exhibit diamagnetic behaviour

to some degree, though only those that exhibit this effect only are termed diamagnetic. The diamagnetic susceptibility, denoted as χ_d, can be expressed as:

$$\chi_d = -\mu_0 n\alpha \qquad (39)$$

Where n is the number density of atoms or molecules within the material and α is the material's molar diamagnetic susceptibility, a material specific property which quantifies the degree to which the individual atoms or molecules generate diamagnetic responses when subjected to an external magnetic field, this depends on the electron distribution within the atoms or molecules within the material.

1.2.2 Paramagnetic Materials

A paramagnetic material is characterised by having a small positive magnetic susceptibility resulting in the material tending to become magnetized in the same direction of externally applied fields [1-3]. Typical values for the susceptibility range of a paramagnet are: $10^{-5} < \chi < 10^{-3}$. Paramagnetic materials possess uncompensated electron spins and hence have a net magnetic moment upon each atom. In a paramagnetic material, non-zero atomic magnetic moment directions are distributed randomly due to thermal fluctuations and application of an increasing magnetic field yields rotation of these moments into the direction of the field and eventually yields saturation whereby all moments are aligned with the field. Typically, this effect is weak and is temperature dependent. At higher temperatures, thermal motion can disrupt alignment of magnetic moments, resulting in a reduced overall magnetisation.

The temperature dependence of the paramagnetic susceptibility can be mathematically represented by:

$$\chi = \frac{C}{T} \qquad (40)$$

Here, χ is the paramagnetic susceptibility, C is the Curie constant and T is the absolute temperature. The Curie constant is a material-specific parameter that quantifies the materials susceptibility to temperature variations. As temperature increases the susceptibility decreases due to the disruptive effect of thermal motion on magnetic alignment.

1.2.3 Ferromagnetism, Anti-Ferromagnetism, Ferrimagnetism

Further types of magnetism are dependent on the atomic scale interactions between neighbouring moments within the material. These interactions result in the material being ferromagnetic, antiferromagnetic or a ferrimagnetic.

Ferromagnetic materials exhibit a collective alignment of their individual atomic magnetic moments over long distances [1-3]. This is seen even in the absence of an external magnetic field and can result in a large macroscopic magnetisation. Ferromagnetic materials have a positive high value susceptibility typically of values $10 < \chi < 10^4$, and exhibit hysteresis, when subjected to externally applied field cycles.

When a strong external field is applied to a ferromagnet it is fully magnetised along the direction of the applied field, up to a value called the saturation magnetisation M_s. However, as temperature increases, the saturation magnetisation decreases due to the thermal fluctuations gradually overcoming the ordered arrangement of the neighbouring magnetic moments. The temperature at which this transition occurs is called the Curie temperature T_c. Above the Curie temperature, the ferromagnetic material behaves as if it was paramagnetic, displaying susceptibility to external magnetic fields. This transition is illustrated in **Figure 3**. The relative equation for the Curie temperature is:

$$\chi = \frac{C}{T - T_C} \tag{41}$$

Here, χ is the susceptibility of the material, C is the curie constant (specific to the material), T is the absolute temperature and T_c the Curie temperature. This equation highlights the critical role of the Curie temperature in governing the behaviour of ferromagnetic materials as a function of temperature.

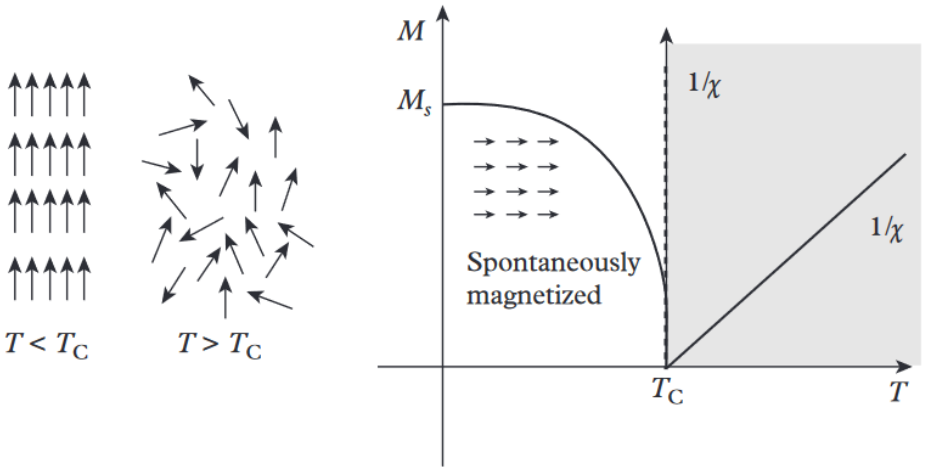

Figure 3: *Magnetisation of a ferromagnet with increasing temperature. Beyond the Curie temperature T_c it functions as a paramagnet. Figure from [1].*

In contrast, antiferromagnets are materials in which neighbouring magnetic moments may spontaneously anti-align with respect to neighbouring moments. This results in a net zero macroscopic magnetisation. This anti-alignment of neighbouring moments persists up to a certain temperature, dependent on the material, called the Neel temperature T_N above which thermal fluctuations disrupt the anti-alignment ordering and the material acts as a paramagnet, this response to temperature is shown in **Figure 4**.

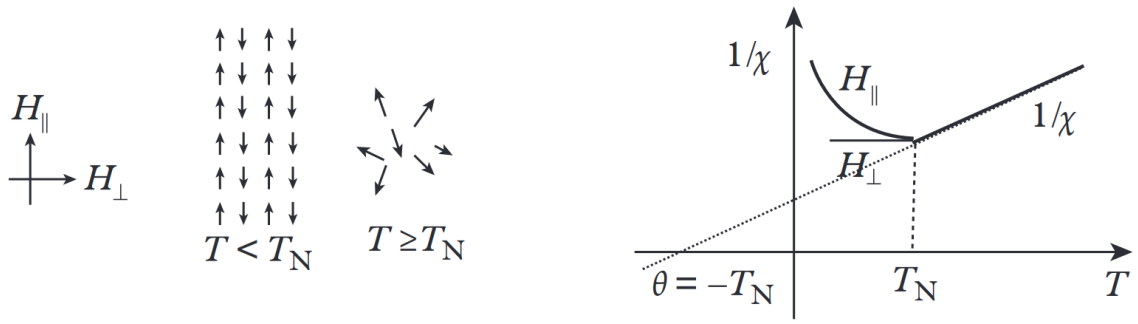

Figure 4: *An antiferromagnets response to a perpendicular or parallel aligned externally applied field under increasing temperature. The susceptibility is shown to be orientation dependent to the applied field, and the material exhibits paramagnetic ordering above the Neel temperature. Figure from [1].*

Ferrimagnets are like antiferromagnets in that their neighbouring magnetic moments may spontaneously anti-align. However, unlike anti-ferromagnets, a net macroscopic magnetisation may arise as the neighbouring moments are of different magnitudes. This is due to ferrimagnetic materials commonly consisting of multiple sublattices of different magnitude magnetic moments, all contributing to the asymmetric alignment.

Various types of magnetism in solids rely on the alignment of neighbouring magnetic moments, giving rise to collective magnetic effects. These effects stem due to the exchange interaction between adjacent magnetic moments, which will be explained shortly in Section 1.3.1.

1.3 Magnetic Energies

The ferroic order described above are dependent on the magnitude of atomic magnetic moments and the strength of interaction between neighbouring moments. In this section, the different energies that govern ferroic systems will be considered. In general, magnetic systems exhibit complex behaviours and occupy the lowest energy state available to them, minimising contributing energies where possible. The total magnetic free energy E_f is dependent on the magnitude of the: exchange, Zeeman, magnetocrystalline anisotropy, magnetostrictive and magnetostatic energies. As such the total magnetic free energy is defined as [1]:

$$E_f = E_{ex} + E_{Zee} + E_{mc} + E_{mtn} + E_{MS} \quad (42)$$

1.3.1 Exchange Energy

The exchange interaction between two adjacent magnetic moments is a purely quantum mechanical effect that arises from Pauli's exclusion principle and the Coulomb interaction [1-3]. Though in general the exchange interaction in solids, is a complex many-body problem, one can understand the physical basis by considering a hydrogen molecule consisting of two hydrogen atoms a and b, separated by a distance r_a. Each hydrogen atom has a paired electron, labelled 1 and 2, that are separated from one another by a distance r_{12}. The coordinates of the electrons can be represented by $\boldsymbol{r_1}$ and $\boldsymbol{r_2}$ respectively. This is shown in **Figure 5**.

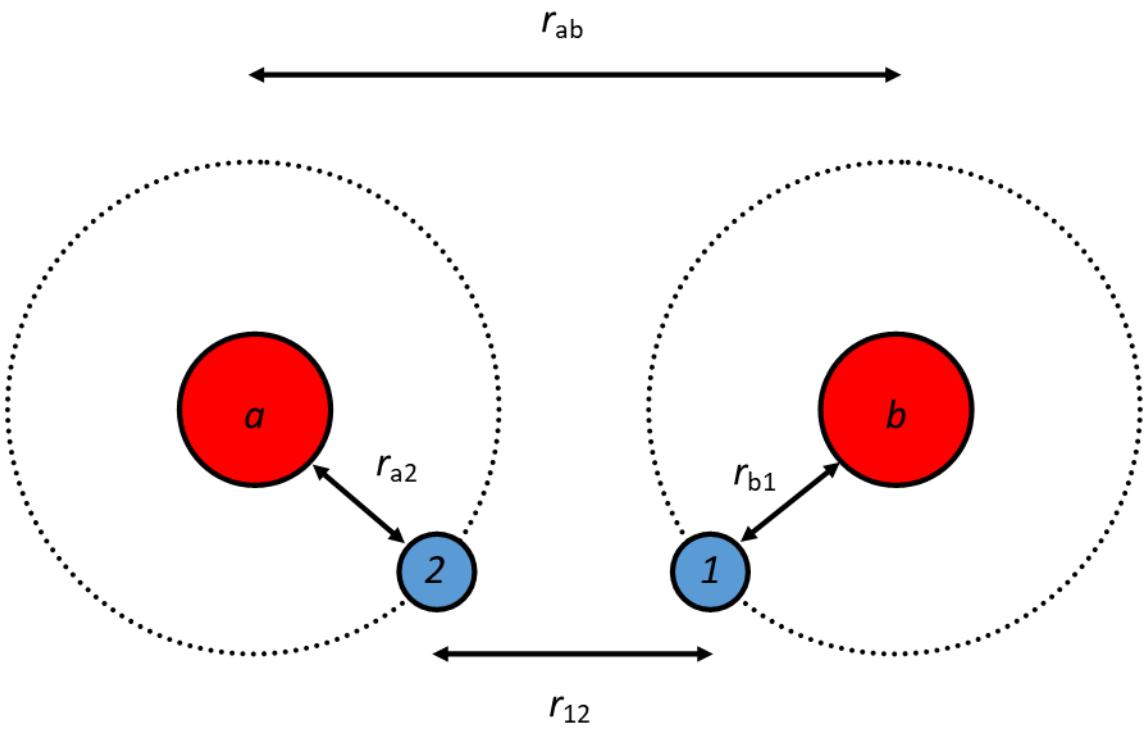

Figure 5: *Model of a hydrogen molecule H_2, consisting of two protons, a and b, with associated electrons 1 and 2. Figure from [1].*

The total wavefunction, which describes the behaviour of the two electrons together, can be made up by the product between the two electron states $\psi_a(\boldsymbol{r_1})$ and $\psi_b(\boldsymbol{r_2})$ [2]. These two electrons are indistinguishable from one another, therefore the wavefunction remains the

same regardless of whether the positions of the two are switched. The electrons observe the Pauli exclusion principle, which results in an antisymmetric wave function. The corresponding total wave functions can be written as [2]:

$$\psi_S = \frac{1}{\sqrt{2}}\left(\psi_a(\boldsymbol{r}_1)\psi_b(\boldsymbol{r_2}) + \psi_a(\boldsymbol{r}_2)\psi_b(\boldsymbol{r_1})\right)\cdot\chi_S \tag{43}$$

$$\psi_T = \frac{1}{\sqrt{2}}\left(\psi_a(\boldsymbol{r}_1)\psi_b(\boldsymbol{r_2}) - \psi_a(\boldsymbol{r}_2)\psi_b(\boldsymbol{r_1})\right)\cdot\chi_T \tag{44}$$

The symbol χ_S represents the spin part of the wave function which is crucial for characterising the spin state of a system of two indistinguishable electrons. In quantum mechanics, the behaviour of electrons is described by their spin and spatial coordinates, often considered noninteracting or separate variables. The total wavefuncti*on* ψ can be expressed as a product of the spatial wavefunction and the spin wavefunction:

$$\psi = (\psi_{spatial})(\chi_{spin}) \tag{45}$$

The Pauli exclusion principle imposes an essential constraint on the spin wavefunction. For indistinguishable electrons, it must be antisymmetric under the interchange of spin coordinates, which leads to the definition of the antisymmetric form of the spin function, describing a spin singlet state where the total spin angular momentum $S = 0$. This can be expressed as:

$$\chi_S = \frac{1}{\sqrt{2}}(\chi_{up}(1)\chi_{down}(2) - \chi_{down}(1)\chi_{up}(2) \tag{46}$$

Conversely, the symmetric form of the spin function corresponds to a spin triplet state, characterised by a total spin angular momentum $S = 1$. The symmetric spin wavefunction can therefore be written as:

$$\chi_T = \frac{1}{\sqrt{2}}(\chi_{up}(1)\chi_{down}(2) - \chi_{down}(1)\chi_{up}(2) \quad (47)$$

The selection between singlet and triplet wavefunctions is determined by the requirement for antisymmetry in the total wavefunction.

The energies of these singlet E_S and triplet state E_T can be obtained by calculating the expectation of the Hamiltonian operator as shown below [2]:

$$E_S = \int \psi_S^* \mathcal{H} \psi_S \mathrm{d}V_1 \mathrm{d}V_2 \quad (48)$$

$$E_T = \int \psi_T^* \mathcal{H} \psi_T \mathrm{d}V_1 \mathrm{d}V_2 \quad (49)$$

From this the exchange energy E_{ex} can be calculated by subtracting the triplet energy E_T from the singlet energy E_S:

$$E_{ex} = E_S - E_T \quad (50)$$

This exchange energy quantifies the effect of the exchange interaction on the system.

By then considering the normalised spin parts of the singlet and triplet wave functions and ensuring that the total spin magnitude squared, $\boldsymbol{S}^2$, remains consistent for the rules of angular momentum it can be shown that [2]:

$$\boldsymbol{S^2} = (\boldsymbol{S}_1 + \boldsymbol{S_2})^2 = S_1^2 + S_2^2 + 2(\boldsymbol{S}_1 \cdot \boldsymbol{S}_2) \quad (51)$$

Using this, $\boldsymbol{S_1} \cdot \boldsymbol{S_2}$ can be calculated in terms of the total spin [2]:

$$\boldsymbol{S}_1 \cdot \boldsymbol{S}_2 = \frac{1}{2} S_{total}(S_{total}+1) - \frac{1}{2} S_1(S_1+1) - \frac{1}{2} S_2(S_2+1) \qquad (52)$$

And as $\boldsymbol{S_1}$ and $\boldsymbol{S_2}$ are equal to ½ , and depending on whether the total spin is in a singlet state $S_{total} = 0$ or a triplet state $S_{total} = 1$ leads to different values for $\boldsymbol{S_1} \cdot \boldsymbol{S_2}$ shown by [2]:

$$\boldsymbol{S}_1 \cdot \boldsymbol{S}_2 = -\frac{3}{4} \qquad for\ S_{total} = 0\ (singlet\ state) \qquad (53)$$

$$\boldsymbol{S}_1 \cdot \boldsymbol{S}_2 = +\frac{1}{4} \qquad for\ S_{total} = 1\ (triplet\ state)$$

The effective Hamiltonian can then be expressed as [2]:

$$H = \frac{1}{4}(E_S + 3E_T) - (E_S - E_T)\boldsymbol{S}_1 \cdot \boldsymbol{S}_2 \qquad (54)$$

Where the first term of this equation is a constant and is included in other energy contributions, whereas the second term is spin dependent and holds a crucial role in ferroic ordering of materials.

By then defining the exchange constant J as the difference between the two energies of the singlet E_S and triplet E_T states divided by two, the spin dependent term in the effective Hamiltonian can then be expressed as [2]:

$$\mathcal{H}_{spin} = -2J\boldsymbol{S}_1 \cdot \boldsymbol{S}_2 \qquad (55)$$

Therefore, depending on the sign of the exchange constant it can be determined which state is energetically favourable. If J is negative, then $E_S < E_T$, which indicates that the singlet state with total spin of 0 is favourable, this is the case for antiferromagnetic materials. However, if J is positive then $E_S > E_T$ meaning that the triplet state with a total spin of 1 is energetically favourable, this is the case for ferromagnetic materials.

This example shown has been for two electrons however in a magnetic material many more electrons must be considered. To solve the Schrödinger equation of this many body problem assumptions must be made, including that the exchange interaction applies only between neighbouring atoms. This results in the Heisenberg model of exchange, which can be written as [2]:

$$E_{ex} = -2\sum_{ij} J_{ij}\, \boldsymbol{S_i} \cdot \boldsymbol{S_j} \qquad (56)$$

With J_{ij} being the exchange constant between spin i and spin j and is determined by the interatomic distance and radius of their orbits. A diagram of this is shown in Figure 5, where r_{ab} is the distance between the core of the atoms, r_{12} is the distance between the electrons and the distances between each electron and their respective nuclei is given by r_{a2} and r_{b1} respectively.

The exchange integral was calculated by Bethe and Slater and this was shown to be [1]:

$$J_{12} = \iint \psi_a^*(r_1)\psi_b^*(r_2)\left[\frac{1}{r_{ab}} - \frac{1}{r_{a2}} - \frac{1}{r_{b1}} - \frac{1}{r_{12}}\right]\psi_a(r_1)\psi_b(r_2) \qquad (57)$$

Here, ψ_a and ψ_b represent the wavefunctions of atoms “a” and “b” respectively. Bethe and Slater demonstrated that ferromagnetic behaviour is observed when J_{12} is greater than zero which typically occurs for small distances of both r_{12} and r_{ab} and for larger distances of r_{a2} and r_{b1}, this is shown in **Figure 6**.

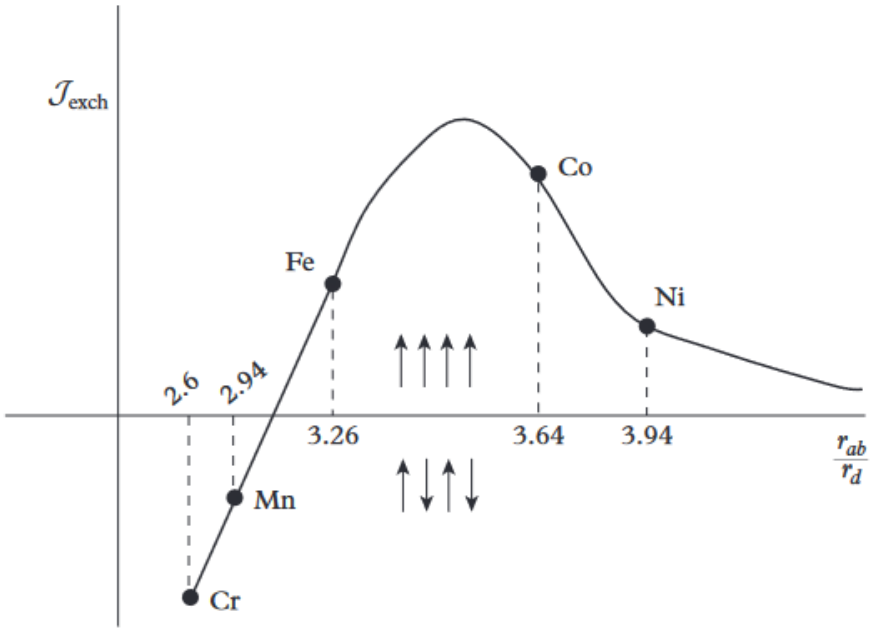

Figure 6: *The Bethe-Slater curve describing the relationship between the exchange constant and the ratio of interatomic distance r_{ab} and the radius of unfilled inner electron shell r_d. When $J_{exch} > 0$ ferromagnetic ordering is expected and when $J_{exch} < 0$, antiferromagnetic ordering is expected. Figure from [1].*

By assuming that the exchange interaction occurs primarily between atoms that are nearest neighbours and with equal exchange constants $J_{12} = J$, and also with uniform spins $|S_1| = S$, then the total exchange energy E_{ex} can be defined as [1]:

$$E_{ex} = -2JS^2 \sum_{nn} \cos(\theta_{12}) \qquad (58)$$

Where the angle between nearest neighbour spins is shown by θ_{12} and the sum is over all nearest neighbours. This can be approximated for small angles to be:

$$E_{ex} = -2JS^2 \sum_{nn} \theta_{12}^2 \qquad (59)$$

The equation above suggests that the exchange energy between two nearest neighbour spins is proportional to the square of the angle between them. In order to account for crystalline structure of magnetic materials, the direction of the nearest neighbouring magnetic moments μ_i, with direction cosines $(\alpha_{i1}, \alpha_{i2}, \alpha_{i3})$, and μ_j, with direction cosines $(\alpha_{j1}, \alpha_{j2}, \alpha_{j3})$, and considering the angular deviation between the two is small $\left(\left|\theta_{ij}\right| \approx \left|\mu_j - \mu_i\right| = \left(\boldsymbol{r_{ij}} \cdot \nabla\right)\mu\right)$, the exchange energy density can be written as [1]:

$$E_{ex_{density}} = A_{ex}[(\nabla\alpha_1)^2 + (\nabla\alpha_2)^2 + (\nabla\alpha_3)^2] \qquad (60)$$

Where A_{ex} is the exchange stiffness, a material specific parameter that quantifies the materials resistance to changes in spin orientations, and is given by [1]:

$$A_{ex} = \frac{J_{ex}S^2C_c}{a} \qquad (61)$$

where J_{ex} is the exchange integral, S is the magnitude of the spin vector associated with magnetic moments in the material, a is the lattice constant of the material and reflects the distance between neighbouring atoms and C_c is a constant specific to the crystal structure of the material. A greater exchange stiffness indicates a stronger exchange interaction and greater stability of the magnetic order in the material.

1.3.2 Magnetostatic Energy

The magnetostatic energy of a material is the potential energy associated with the stray field of a material [1-3], defined earlier in Section 1.1.5. The demagnetisation field has an energy of interaction with the magnetisation of the material, and this is known as the demagnetisation energy or magnetostatic energy, a diagram of this effect in after application and removal of an externally applied field is shown in **Figure 7**.

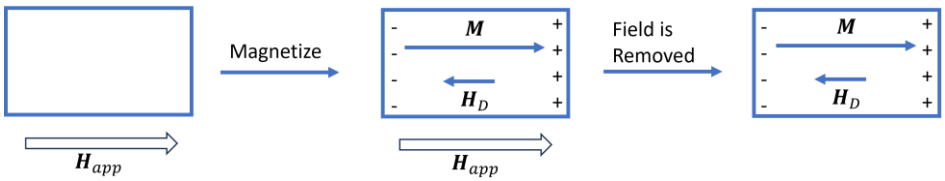

Figure 7: *Generation of a demagnetising field H_D, following the application of an external field H_{app} that magnetises a bar magnet. Figure adapted from [1].*

Since the demagnetising field is based upon the generation of magnetic surface poles, it is strongly dependent upon the geometry of the sample and the number of magnetic poles. Considering in **Figure 7** if the applied field was aligned along the short axis, rather than the long axis. The oppositely charged magnetic poles would be within a shorter range and would also be greater in number, spread out over a much larger area than is seen over the long axis. This would result in a greater demagnetisation field and a preferred alignment along the long axis direction. This preferential alignment of magnetisation along certain axis within the material, called easy axis, is an example of shape anisotropy. In general, the demagnetising field is proportional to the sample magnetisation with a strong dependence on the geometry of the sample. Therefore to account for sample geometry a demagnetising tensor N can be defined [1, 2].

$$\boldsymbol{H_d} = -N\boldsymbol{M} \qquad (62)$$

The demagnetising tensor N signifies the portion of the magnetic flux density that acts perpendicular to the surface of a magnetic material. This can be divided into three components: N_x, N_y and N_z, which collectively describes the distribution of the magnetic flux density into three-dimensional space. This demagnetising tensor can be written as as [1]:

$$N = \begin{pmatrix} N_x & 0 & 0 \\ 0 & N_y & 0 \\ 0 & 0 & N_z \end{pmatrix} \quad (63)$$

Examples of shapes that can be describes by this tensor are a sphere with $N_{x,y,z} = \frac{1}{3}$ or a flat infinitely long thin film with $N_z = 1$. In the case of a ferromagnetic ellipsoid like shape with a uniform magnetisation, N can be diagonalised and the integral to derive the magnetostatic energy E_{MS} of a sample can be produced by combining Equation (10) with Equation (11) and Equation (8) [1]:

$$E_{MS} = -\frac{1}{2}\int \mu_0 \boldsymbol{M} \cdot \boldsymbol{H}_d \mathrm{d}V = \frac{1}{2}\int \mu_0 \boldsymbol{M} N \boldsymbol{M} \mathrm{d}V = \frac{1}{2}\mu_0 V \boldsymbol{M^2} N \quad (64)$$

Where V is the volume of the sample. Considering this for a very thin plate, of infinite lateral extent with demagnetising tensor [1]:

$$N = \begin{pmatrix} 0 & 0 & 0 \\ 0 & 0 & 0 \\ 0 & 0 & 1 \end{pmatrix} \quad (65)$$

Then one can see that a component is only present along the z-direction, forcing the magnetisation to lay in the sample plane. This is an important result for thin films.

1.3.3 Magnetocrystalline Anisotropy

Ferromagnetic materials exhibit a tendency for magnetisation alignment along specific crystallographic axes. This phenomenon, known as magnetocrystalline anisotropy, originates from the interaction between electron spins and the electric field of the crystal lattice [1-3]. These couplings result in a preferred direction of the electrons orbit, which in turn influences the orientation of the electron spin. These interactions between spin, orbit, and lattice result in constraints upon the magnetisation of the sample.

Within ferromagnetic materials there exists one or many crystallographic directions denoted as the easy axis, which the magnetisation prefers to align parallel with to minimise internal energy. This contrasts with the materials hard-axis where energy is at a maximum and alignment with this axis requires substantial energy.

The magnetocrystalline energy per volume E_{crys} can be written as a power series expansion of the components of the magnetisation, using the directional cosines mentioned previously [3]:

$$E_{crys} = E_0 + \sum_i b_i \alpha_i + \sum_{ij} b_{ij} \alpha_i \alpha_j + \sum_{ijk} b_{ijk} \alpha_i \alpha_j \alpha_k + \sum_{ijkl} b_{ijkl} \alpha_i \alpha_j \alpha_k \alpha_l + \zeta(\alpha^2) \quad (66)$$

The terms $\zeta(\alpha^2)$ can be usually dismissed due to diminishing in size as order increases.

Magnetocrystalline energy is equal when magnetised in opposite directions. Its energy is dependent only upon the alignment direction of the magnetisation. This results in no odd terms of α_i occurring within the series expansion and therefore this can be reduced to [3]:

$$E_{crys} = E_0 + + \sum_{ij} b_{ij} \alpha_i \alpha_j + + \sum_{ijkl} b_{ijkl} \alpha_i \alpha_j \alpha_k \alpha_l \quad (67)$$

Given the focus on deposition of permalloy $Ni_{81}Fe_{19}$ for this thesis, characterised by a cubic crystal lattice structure, the equation can be solved. Due to the direction of the magnetisation causing no difference for the energy difference, $E(\alpha_i) = E(-\alpha_i)$, all cross terms $\alpha_i \alpha_j$ vanish. Furthermore, in cubic systems the indices (1, 2 and 3) are indistinguishable due to the cubic symmetry which means that the coefficients b_{ij} are the same for all three directions, i.e: $b_{11} = b_{22} = b_{33}$. Considering that the sum of the squares of the directional cosines must be equal to 1 (a normalisation condition that ensures that the magnetisation vector $\boldsymbol{M}$ is a unit vector with a magnitude of 1). Therefore, the second order term in Equation (67) can be simplified to [3]:

$$\sum_{ij} b_{ij}\alpha_i\alpha_j = b_{11}(\alpha_1^2 + \alpha_2^2 + \alpha_3^2) = b_{11} \tag{68}$$

Further simplification of the fourth, sixth etc. orders can be carried out and result in the following equation [3]:

$$\begin{aligned} E_{crys} = {} & E_0 + b_{11} + b_{1111}(\alpha_1^4 + \alpha_2^4 + \alpha_3^4) + 6b_{1122}(\alpha_1^2\alpha_2^2 + \alpha_1^2\alpha_3^2 + \alpha_2^2\alpha_3^2) \\ & + b_{111111}(\alpha_1^6 + \alpha_2^6 + \alpha_3^6) + 90b_{112233}\alpha_1^2\alpha_2^2\alpha_3^2 \\ & + 15b_{111122}(\alpha_1^2\alpha_2^4 + \alpha_1^4\alpha_2^2 + \alpha_1^2\alpha_3^4 + \alpha_1^4\alpha_3^2 + \alpha_2^2\alpha_3^4 + \alpha_2^4\alpha_3^2) \end{aligned} \tag{69}$$

Which in turn yields the magneto crystalline anisotropy constants, which are functions of the coefficients b that quantify the strength of magnetocrystalline anisotropy within the material [1, 3]:

$$\begin{aligned} E_{crys} = {} & K_0 + K_1(\alpha_1^2\alpha_2^2 + \alpha_1^2\alpha_3^2 + \alpha_2^2\alpha_3^2) + K_2\alpha_1^2\alpha_2^2\alpha_3^2 \\ & + K_3(\alpha_1^2\alpha_2^2 + \alpha_1^2\alpha_3^2 + \alpha_2^2\alpha_3^2) + \cdots \end{aligned} \tag{70}$$

Values of K_n tend towards zero with increasing n, therefore in practice higher order coefficients are often neglected. Furthermore, as the K_0 term is not dependent on the direction of the magnetisation it does not contribute to the directional dependence of the anisotropy energy and can be treated as a constant.

Examining the K_1 and K_2 constants of the constituent elements of permalloy (Py) [1], it is found that for Fe K_1 is greater than zero, resulting in the $[100]$-direction as the easy magnetisation axis and the $[111]$-direction is the hard axis. This is opposite to Ni, which has a K_1 value less than zero. Alloys of the two magnetic materials in the form $Ni_{81}Fe_{19}$ have been found where the implications of magnetocrystalline anisotropy vanish and K tends towards zero. This makes permalloy an attractive magnetic material as control of the spin texture is possible through shape anisotropy, that is the orientation of the magnetic moments

can be tailored through shaping of the material without influence of crystallographic axes, making it a versatile material for use in engineered magnetic systems.

The magnetocrystalline anisotropy emerges from two primary contributions. The first arises from the interaction between the orbital motion of electrons and the local crystal electric field, constituting a first-order contribution. The second contribution, a second-order effect, stems from the mutual interaction among magnetic dipoles. This energy associated with aligning a magnetic moment with the anisotropic crystal's easy axis is represented by [1-3]:

$$E_{mc} = -\frac{1}{M_S^2}\int K(\hat{n}.M)^2 dV \qquad (71)$$

Where K is the anisotropy constant (units Jm^{-3}), and $\hat{n}$ is a unit vector in the direction of the easy axis. For the case of a uniaxial material, Equation (71) can be rewritten in terms of the z-component of the magnetic moment M_z:

$$E_{mc} = -\frac{1}{M_S^2}\int K(M_z)^2 dV \qquad (72)$$

This simplifies the anisotropy energy for such uniaxial materials where magnetic moments primarily align along a single direction. To first order one can write:

$$E_{ms} = K_1 \sin^2\theta \qquad (73)$$

Where K_1 is the first-order anisotropy constant and θ is the angle between the direction of the magnetic moment and the easy axis of the material. The anisotropy energy is minimised when the magnetic moment aligns perfectly along the easy axis ($\theta = 0$), resulting in a stable magnetic state. As θ deviates from zero, the energy increases representing the energy cost associated with misalignment.

1.3.4 Dzyaloshinksii-Moriya Interaction

The Dzyaloshinksii-Moriya interaction (DMI) is consequence of the interplay between two fundamental interactions found within magnetic materials: the spin-orbit interaction and the super exchange interaction [5].

The spin-orbit interaction is a fundamental interaction in magnetic materials that arises from the coupling between an electron's orbital motion $\boldsymbol{L}$ and its intrinsic spin $\boldsymbol{S}$ within an atom. This interaction plays a significant role within the behaviour of magnetic moments in materials and can be mathematically described by:

$$\mathcal{H}_{SO} = \xi(\boldsymbol{L} \cdot \boldsymbol{S}) \qquad (74)$$

Here, $\mathcal{H}_{SO}$ represents the spin-orbit interaction Hamiltonian, ξ is the spin-orbit coupling constant, $\boldsymbol{L}$ is the orbital angular momentum operator and $\boldsymbol{S}$ is the electron spin operator. The dot product between $\boldsymbol{L}$ and $\boldsymbol{S}$ quantifies the coupling between the two angular momenta. The interaction between the electrons orbital motion and its spin can lead to a variety of effects, including the splitting of energy levels (fine structure splitting) and the generation of an effective magnetic fields that acts upon the electron's spin.

In the context of the DMI, the spin-orbit interaction is essential as it introduces an anisotropy that, in material lacking inversion symmetry, can lead to the DMI. When the crystal structure or the material itself lacks inversion symmetry, it allows for the emergence of DMI terms in the exchange interactions between neighbouring spins.

The super-exchange interaction is a crucial mechanism for mediating magnetic interactions between two next-nearest neighbour magnetic ions through an intermediary non-magnetic ion. It's especially important in understanding the magnetic behaviour of materials with localised magnetic moments. The Hamiltonian for super-exchange interactions can be described as:

$$H_{SE} = -J \sum_{ij} (\boldsymbol{S}_i \cdot \boldsymbol{S}_j) \tag{75}$$

Here, H_{SE} represents the super-exchange interaction Hamiltonian, J is the super-exchange coupling constant and the sum is taken over all pairs of neighbouring magnetic ions i and j. The dot product term describes the interaction between the spins of magnetic ions i and j. In this context, the super-exchange interaction governs how the spins of neighbouring magnetic ions interact with one another, leading to either ferromagnetic or antiferromagnetic coupling. Overall, this interaction is essential for determining the overall magnetic behaviour of a material.

The DMI energy, $E_{pair_{DMI}}$, found between a pair of electrons with spins $\boldsymbol{S}_i$ and $\boldsymbol{S}_j$ can be expressed as [6]:

$$E_{pair_{DMI}} = \boldsymbol{d}_{ij} \cdot (\boldsymbol{S}_i \times \boldsymbol{S}_j) \tag{76}$$

And therefore it follows that the DMI energy density, E_{DMI} for an entire structure by [6]:

$$E_{DMI} = \sum_{ij} \boldsymbol{d}_{ij} \cdot (\boldsymbol{S}_i \times \boldsymbol{S}_j) \tag{77}$$

Where the modulus of the DMI vector $\boldsymbol{d}_{ij}$ measures the strength of the interaction and is typically of the order of several milli-electron volts. This interaction introduces an antisymmetric component into the exchange energy, leading to a canting of the neighbouring spins. As a result, neighbouring spins no longer align perfectly parallel with one another but instead exhibit a certain angular displacement with respect to one another. This canting effect introduced is crucial in breaking the symmetry of antiferromagnetic materials, where adjacent spins would naturally align antiparallel. If the spins possess inversion symmetry, meaning that they cannot be interchanged without an alteration to the systems energy, then the DMI energy becomes zero. Consequently, DMI primarily arises in bulk materials where

the unit cells lack inversion symmetry or at interfaces where symmetry is disrupted, hence its presence in curved geometries.

In curved geometries an effective DMI emerges from competition between the exchange energy and the demagnetisation energy. This results in an induced canting of neighbouring spins, seen even within the same magnetic domain. Assuming shape anisotropy in a curved structure without this DMI effect and considering only the magnetostatic energy, the spins within the structure would naturally align along the curve's arc to minimise the formation of stray magnetic fields. However, the exchange energy is minimised when neighbouring spins are aligned in parallel, therefore these two opposing energy terms result in spins tilting out of the plane at regions of high curvature. This is a unique effect seen within curved structures and not observed within planar nanowires.

A key assumption for this scenario here is that shape anisotropy typically directs spins to align parallel with the curved structures long axis. This assumption simplifies analysis but is not an absolute rule, surface roughness or defects can introduce deviations to this assumption. Adding to this complexity is the presence of an extra contribution to the exchange energy due to the effective anisotropy E_A, acting as a geometrical potential that can vary greatly dependent on the systems geometry. This adds a further degree of intricacy to the understanding of magnetic interactions.

Therefore, this modification to the exchange energy contributions within a curved structure can be expressed through the following equation:

$$E_{ex} = E_{ex_0} + E_{DMI} + E_A \qquad (78)$$

Where E_{ex} is the total exchange energy, E_{ex_0} is the standard exchange energy contribution discussed previously in Section 1.3.1, E_{DMI} is the energy contribution attributed to the DMI, and E_A is the effective anisotropy associated energy.

1.4 Domains

Domains in ferromagnetic materials are regions where the orientation of magnetic moments transition from one direction to another and are formed to reduce the demagnetisation field of a material, thus reducing magnetostatic energy, E_{ms}. In a single domain state, where all magnetic moments align uniformly, the demagnetizing field can be significant, leading to energy costs associated with maintaining this state. As a result, it becomes energetically favourable to divide the material into smaller domains, where the magnetisation direction varies from one domain to another, thus reducing stray fields outside of material and achieving flux closure therefore reducing the magnetostatic energy of the system. The formation of multiple domains with opposing magnetisation directions results in an increase in the exchange energy E_{ex} of the system.

As stated previously, the exchange energy arises from the quantum mechanical exchange interaction between neighbouring magnetic moments within a magnetic material. This interaction tends to align adjacent moments with one another, reducing the energy of the system. When all moments within a ferromagnetic material align uniformly in one direction, called a single domain state, E_{ex} is minimised. However due to other factors, commonly shape anisotropy, it becomes energetically favourable to create domain walls and reduce the magnetostatic energy despite an increase in exchange energy.

Shape anisotropy plays a crucial role in the formation of domain walls. It arises because of the material's geometry and the distribution of magnetic moments within the material. When moments are uniformly aligned, the material develops a high pole density at its surface, leading to a significant magnetostatic energy contribution. This energy contribution is associated with the distribution of magnetic charges and the creation of a demagnetisation field H_d within the material. To minimise this energy contribution, magnetic moments need to be arranged in a way that reduces stray magnetic fields outside of the material.

1.4.1 Domain Walls

Domain walls in ferromagnetic materials are regions where the orientation of magnetic moments transition from one direction to another [1-3]. They form to reduce the

contributions between different energies discussed previously. Within this thesis the primary focus is on the magnetic material Permalloy which by design has an absence of magnetocrystalline anisotropy, this simplifies the energy considerations.

The interplay between the competing energy terms of magnetostatic energy (E_{ms}) and exchange energy (E_{ex}) creates a delicate balance within the material. On one hand, there's a drive to reduce stray fields and minimize E_{ms}, while on the other hand, there's a tendency to align magnetic moments to minimize E_{ex}. This balance results in a state where the material seeks to simultaneously reduce stray fields and align moments. When magnetocrystalline anisotropy is minimised, as is the case for Permalloy, the driving factor for domain wall formation becomes shape anisotropy. The geometry of the material becomes crucial in the formation and characteristics of domain walls within the material.

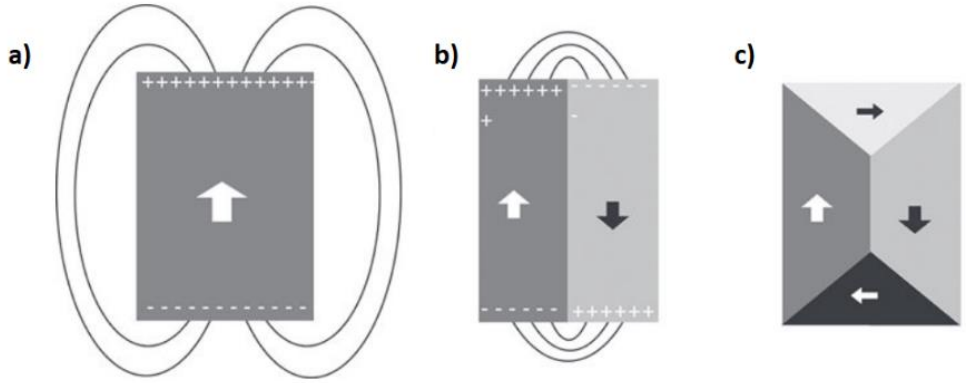

Figure 8: *Schematic diagrams of domain walls formed to reduce the contribution of magnetostatic energy. Introduction of* $180°$ *walls reduces the magnetostatic energy but increases domain wall energy contribution* ***(a-b)****. When the material's uniaxial anisotropy is weak, the inclusion of* $90°$ *walls serves to nullify the magnetostatic energy contribution but leads to an increase in the anisotropic energy contribution* ***(c)****. Such domains are designated closure domains. Figure from [1].*

Figure 8 shows a schematic diagram of domain walls formed with a range of contributing E_{ms} and E_{ex}. In **Figure 8a**, no domains have formed and all the magnetic moments within the material have been aligned, this would result in the exchange energy being at its minimum for this structure, but also its magnetostatic energy at its maximum. This is a single domain

state, where a ferromagnetic material becomes a single magnetic domain without the presence of any domain walls. **Figure 8b** shows the subdivision of this structure into two domains acting parallel to one another but anti-aligned, this will reduce the contributions from stray fields outside the material, reducing the magnetostatic energy but with increasing exchange energy due to opposing moment directions from adjacent walls. **Figure 8c** shows a scenario where closure domains have formed within the material, resulting in a net zero magnetisation. Achieving flux closure minimises magnetostatic energy contributions but increases anisotropy energy in uniaxial materials and increases elastic energy contributions due to strain from adjacent 90˚ domains. Achieving flux closure also results in an overall increase in exchange energy compared to the single domain state.

The characteristics of the transitions between domain walls depend on the type of domain wall being considered however all domain walls exhibit a gradual rotation of ***M*** rather than the abrupt changes shown in **Figure 8** [1]. This transition region, consisting of numerous individual spins, serves to minimise the deviation between adjacent magnetic moments thus reducing exchange energy costs. Depending on the wall type, this transition region can be of a thickness that extends over several atomic lattice constants. Two common wall types to be discussed are Bloch walls and Neel walls. Bloch walls and Neel walls exhibit distinct characteristics in their behaviour and distribution of magnetic poles. Bloch walls, which are prevalent in materials with uniaxial anisotropy, create poles at sample boundaries but do not possess internal poles. In contrast, Neel walls, commonly found in materials with low magnetocrystalline anisotropy, have internal poles but do not generate surface poles. **Figure 9a** shows a diagram for a thin rectangular nanowire with perpendicular magnetic anisotropy and two domains separated by a domain wall. The domain wall type will depend on the dimensions of the nanowire.

Bloch domain walls are characterised by an out-of-plane rotation of magnetisation, occurring perpendicular to the materials surface, see **Figure 9b** [1]. Bloch domain walls tend to be thicker than Neel walls, extending over several atomic lattice constants, and introduce magnetic poles at their boundaries (though not internally) resulting in a distinct magnetisation pattern and change in the magnetic field.

Neel domain walls are characterised by an in-plane rotation of magnetisation within the wall, see **Figure 9c** [1]. Neel walls exhibit a smooth and gradual transition of magnetisation from one domain to another, this minimises deviations between adjacent magnetic moments and furthermore does not produce magnetic poles at the surface but does introduce internal poles, unlike Bloch domain walls. Neel domain wall thickness commonly extends over a few atomic lattice constants.

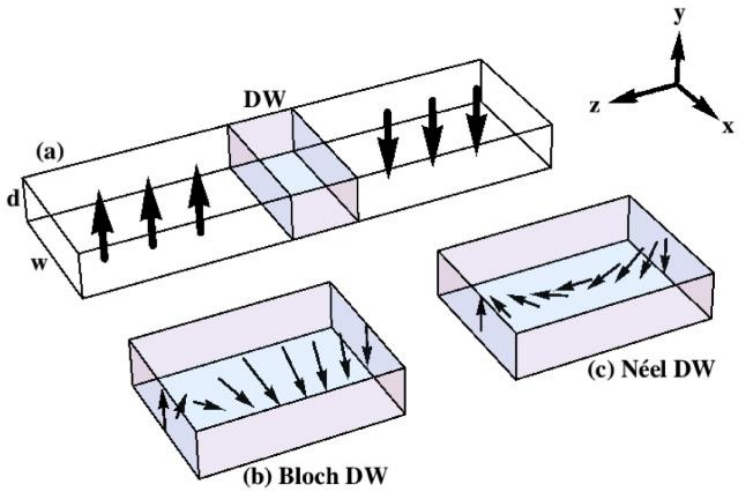

Figure 9: (a) *A diagram showing a thin rectangular nanowire with perpendicular magnetic anisotropy. Nanowire width w, thickness d. Magnetisation direction for two domains separated by a domain wall is shown by black arrows. The dimensions of the nanowire determine whether the wall is a Bloch wall* ***(b)****, or a Néel wall* ***(c)****. Figure from [7].*

These two wall types are commonly found in a range of magnetic materials. Neel walls are generally favoured within thin films where they can efficiently balance energy considerations due to their in-plane rotation. Neel walls do not produce magnetic charges due to their rotation which if present within a thin film would result in large magnetostatic energy contributions. In contrast Bloch walls are favoured within thicker bulk ferromagnetic materials where the out-of-plane rotation helps to optimise the magnetic domain structure. Magnetic charges formed by Bloch walls are separated by a greater distance in bulk materials resulting in a minimised contribution from magnetostatic energy.

The single domain limit for domain walls, mentioned earlier, occurs when the entire material is uniformly magnetised in one direction and there are no transitions between different

magnetisation directions. This can be expressed mathematically using the Weiss magnetisation function:

$$M = M_s \tanh\left(\frac{H}{H_c}\right) \quad (79)$$

In the single domain limit, the magnetisation M approaches the saturation magnetisation M_s as the applied magnetic field H becomes much greater than the coercive field H_c, the strength of field required to reverse the magnetisation of a material. This is desirable in applications where a uniform magnetisation state is desired for simplicity, however achieving this limit requires the application of high magnetic fields or specialised magnetic materials with low coercive field, such as Permalloy.

1.4.2 Nanowire Domain Walls

The domain wall types found in nanostructured nanowires or planar strips are different to those found in thin film or bulk materials due to their distinct geometries. A phase diagram showing the range of wall types is shown in **Figure 10**.

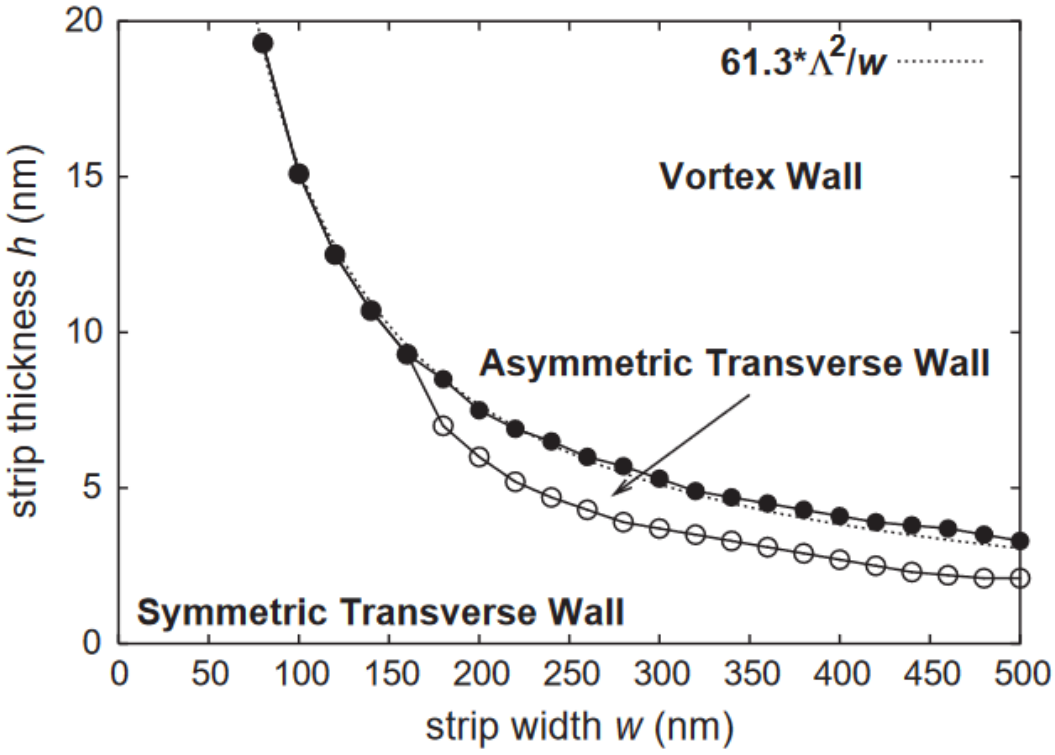

Figure 10: *A phase diagram showing the domain wall structure within permalloy strips of thickness h and width w. Figure from [8].*

A symmetric transverse domain wall (TDW), shown in **Figure 11**, are typically observed within thin and narrow nanowires, where exchange energy is minimised through near parallel alignment of adjacent moments [8]. These walls appear as gradual canting transitions between the magnetisation directions of opposing domains within the nanowire, however this results in magnetic charges forming at the boundaries resulting in a magnetostatic energy cost. It's worth noting that TDWs also exhibit chirality, indicating a handedness or directionality in their structure or rotation. Transverse domain walls are dominated by the magnetostatic energy ($\sim 93\%$), followed by the exchange energy ($\sim 7\%$).

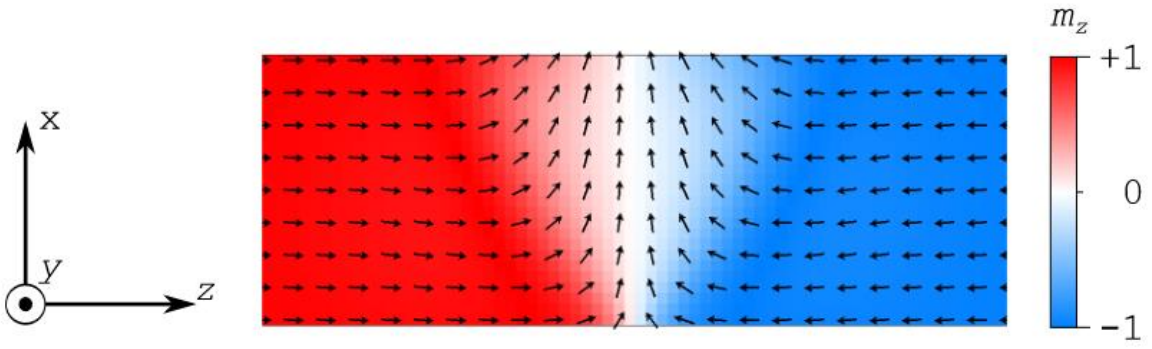

Figure 11: *Micromagnetic simulation of a symmetric transverse domain wall. Figure from [9].*

The asymmetric transverse domain wall (ATDW), shown in **Figure 12**, are a variation of the symmetric transverse wall and are typically observed in materials where the flux line within the central region of the domain wall follows an asymmetric path [8]. The exact magnetostatic energy characteristics of ATWs depend on the specifics of this asymmetric path. Like TWs, the exchange energy contribution is minimised due to the gradual canting of magnetic moments within the wall, however the unique path of the flux line can produce distinct features in their exchange energy properties.

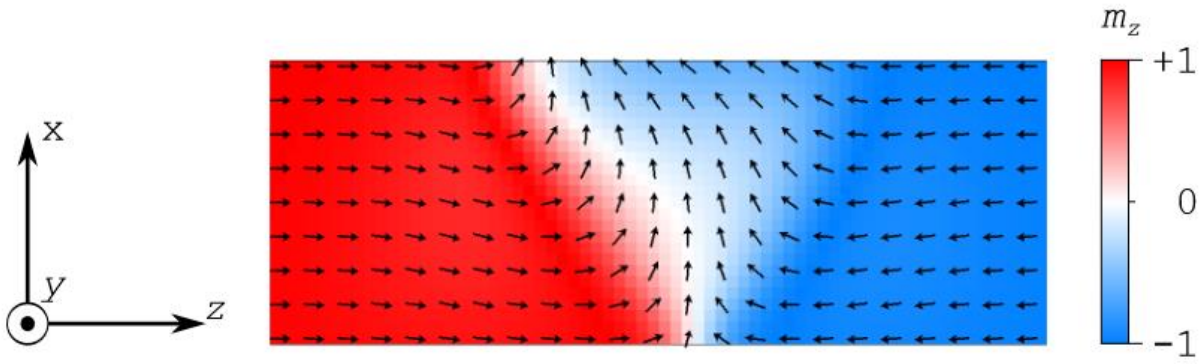

Figure 12: *Micromagnetic simulation of an asymmetric transverse domain wall. Figure from [9].*

Vortex domain walls are the preferred domain wall type in larger dimension nanostructured nanowires where magnetostatic energy minimisation becomes crucial. These walls appear as a swirling vortex pattern with magnetic moments canting towards the walls central core, this is shown in **Figure 13**. This configuration of magnetic moments nearly achieves flux closure, significantly reducing the magnetostatic energy cost, however this no longer minimises the

exchange energy [8]. This is due to the increasing gradient of magnetic moments closer to the vortex core resulting in greater exchange energy cost. Furthermore, due to the directional dependence of the magnetic moments found at the vortex core, this type of domain wall exhibits a greater number of degrees of freedom than TDW and ATDW domains. This is due to the directional dependence of the vortex core and the direction of rotation, called the Chirality, of the vortex domain wall itself. Vortex domain wall energy is primarily magnetostatic in nature $(\sim 78\%)$, with a larger exchange energy contribution $(\sim 22\%)$ compared to transverse domain walls.

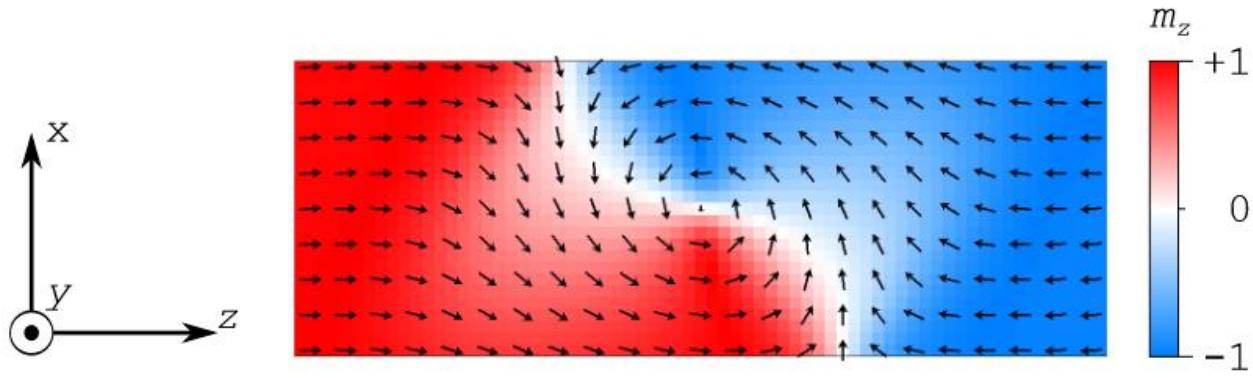

Figure 13: *Micromagnetic simulation of a vortex domain wall. Figure from [9].*

The domain wall dynamics within nanostrips and nanowires is of growing interest in the production of devices like racetrack memory or high-density magnetic storage. Domain walls can be influenced by application of an external magnetic field or introduction of a spin polarised current. The primary focus of this thesis revolves around the applications of external fields, directing attention primarily to this aspect.

Initially, when an external magnetic field is applied, the velocity of a domain wall exhibits a linear relationship with the field strength. This is referred to as the steady motion state. However, at a critical field value called the Walker field, which is dependent on the samples shape, demagnetising field H_d, and its associated demagnetising factor components, the average domain wall velocity decreases. This effect is called the Walker breakdown [1]. This decrease in velocity occurs due to the domain walls chirality oscillating between two values due to the formation of anti-vortex cores at the nanostrip boundaries. When the applied field

exceeds the Walker field, the domain wall motion enters a regime known as precessional propagation which ultimately limits the average domain wall velocity.

Walker breakdown of the domain wall velocity is a limiting factor in domain wall motion that remains a challenge to overcome. Various approaches, including changes to a sample's geometry, through its shape or curvature, have been explored to develop geometries that do not exhibit this limiting factor. Introduction of curvature to commonly planar nanowire systems introduce new additional energy terms that lead to novel exchange-driven behaviours.

1.4.3 Magnetic Reversal

Magnetic reversal is a fundamental process within magnetic materials and can be achieved by subjecting the material to an externally applied magnetic field. Reversals can be assisted by increasing the temperature of the material causing thermal fluctuations and random flips in simple single domain systems. This reversal can cause the materials magnetisation to switch from its initial orientation (+x) to its opposite direction (-x). This process of switching is dependent on the materials properties and the size of the magnetic body.

Two dominant mechanisms govern the magnetisation reversal: coherent rotation and domain wall propagation [1-3]. Coherent rotation dominates in small magnetic bodies that cannot accommodate multiple domains. In this case, the entire magnetic system can be described by a single magnetisation vector. During coherent rotation, the individual magnetic moments within remain aligned with each other, but the overall macroscopic magnetisation vector rotates.

Domain wall propagation becomes more prevalent in larger magnetic structures that support multiple domain walls. During this process, domains with a magnetisation aligned with the externally applied field expand in volume whilst those with anti-aligned magnetisation decrease in volume. This change reduces the total Zeeman energy. As the anti-aligned magnetic moments within a domain wall align with the externally applied field, some switch to the opposite side of the domain wall, causing propagation of the domain wall. Domain wall propagation can occur via the movement of existing domain walls or by the nucleation of new

ones, formed at the edges of the structure at specific threshold values of the applied magnetic field.

In the context of magnetisation reversal, domain wall pinning is another important phenomenon. This occurs when a domain wall encounters a structural defect within the material, such as a grain boundary, inclusion, precipitate, or other irregularities [2]. These defects significantly alter the energy at the location of the domain wall, either increasing or decreasing it, and effectively "pin" the domain wall in place. Releasing the pinned domain wall requires the application of an external magnetic field, which can cause a rapid change in the sizes of neighbouring magnetic domains.

During the magnetic reversal, the propagation of domain walls can result in the emission of electromagnetic signals known as Barkhausen noise. This noise is the result of the abrupt and discrete changes in magnetisation as domain walls move within the material [1-3]. The Barkhausen noise is a valuable diagnostic tool for studying the magnetic properties of materials and is widely used in non-destructive testing and magnetic characterisation, providing insight into the dynamics of magnetic domain walls and behaviour of magnetic materials during the magnetisation reversal process.

1.4.4 Hysteresis Loops

Magnetic hysteresis is a process that occurs in ferromagnetic materials when an external magnetic field is applied causing the magnetic moments contained within to align with the field resulting in magnetisation [1-3]. When the external field is removed, the alignment remains, and the material remains magnetised. This sustained magnetisation occurs due to the inability of the material to access more energetically favourable states because of the complex energy landscape generated. The material will remain magnetised until it is subjected to a sufficiently high temperature, or the application of a magnetic field in the opposite direction to the magnetisation.

Considering a magnetic material in a demagnetised state where there is no magnetic field ($\boldsymbol{B} = 0$) and no external magnetic field ($\boldsymbol{H} = 0$). When an external magnetic field is gradually applied, domains within the material that align with the field will expand in volume through

domain wall motion and those anti-aligned will naturally decrease. Domain wall motion is an energetically preferred process compared with coherent rotation. As the applied field increases in strength, domain wall motion reaches a critical point where it can no longer increase magnetisation in the field's direction. At this stage, domains at angles to the field direction will begin to rotate to minimise potential energy. This process is energetically more costly than domain wall propagation. Once both processes are complete, the material reaches a state of magnetic saturation, denoted as M_S.

However, when the external magnetic field is decreased, the materials magnetisation will begin to decrease. This decrease in magnetisation can be attributed to the demagnetising field now unopposed by an externally applied field. When the external field strength is completely removed, the ferromagnet will still exhibit a non-zero magnetisation value, referred to as remanence M_r. To reduce the magnetisation of the material to zero, an externally applied field in the opposite direction, known as the coercive field H_C, must be applied. Further application of a negative external field will result in the magnetisation to grow in the negative direction until it saturates. This cycle of changing the field direction and observing the changes in magnetisation creates what is known as a hysteresis loop, this is shown in **Figure 14**.

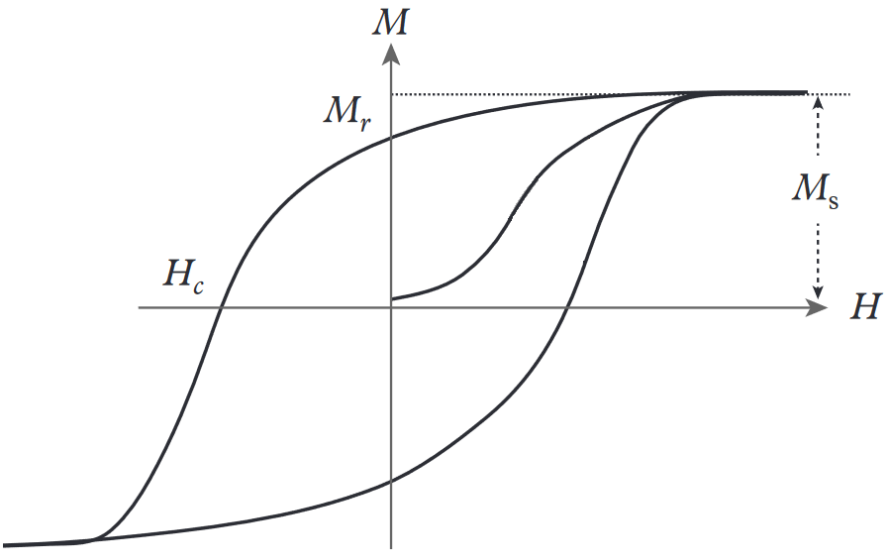

Figure 14: *A hysteresis loop showing the magnetisation response M to an applied magnetic field H. The magnetisation saturation M_s, remanence M_r and coercive field H_c are shown. Figure from [1].*

The area enclosed by this loop represents the hysteresis loss, which is the energy lost as heat during the reversal of magnetisation [1]. This energy loss has significant implications for the efficiency of magnetic materials in applications such as transformers or magnetic storage devices. Understanding and minimising the hysteresis loss is crucial for optimisation of the performance of these materials in practical applications.

1.5 Frustrated systems

1.5.1 Water Ice

Frustration occurs when the geometric configuration of a system prevents the system from minimising all its interaction energies. This phenomenon was discovered in frozen water ice [10] , and was used to explain discrepancies in the calculation of water entropy at zero temperature. Frustration arises due to the arrangement of oxygen and hydrogen in a frozen water tetrahedron, as shown in **Figure 15** . A central oxygen ion is surrounded by a total of four hydrogen ions, whereas the hydrogen ions are located between two oxygen ions. There are two minimum energy positions for the hydrogen ions to occupy, a far or a near position. The resultant minimum energy configuration is called the “two-in, two-out” Ice Rule. For a water ice tetrahedron there exist 6 degenerate ground states all of which follow this configuration, providing the tetrahedron with the lowest energy states to lie in. Considering the availability of configurations in a water ice sample at zero temperature. Of the 16 total configurations possible, only the Ice-rule configurations are energetically favourable. This yields a macroscopically degenerate ground state and as a result a residual entropy at zero temperature.

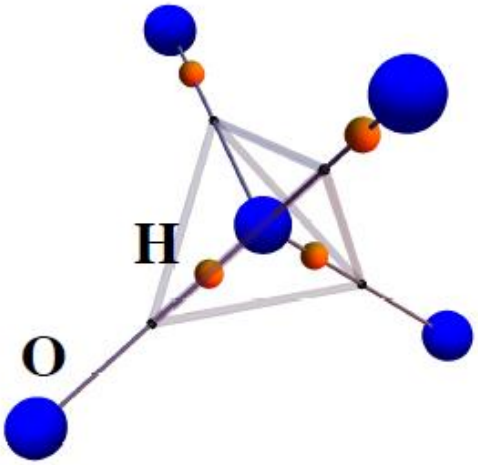

Figure 15: *The Ice rule as seen in water ice. The centrally located oxygen ion (blue) is surrounded by four hydrogen ions (red). The lowest energy configuration is seen when two hydrogen ions lie close to the oxygen, and two further away. Oxygen ions are arranged on the vertices of a diamond lattice. Figure from [11].*

1.5.2 Pyrochlore Spin Ices

Another material which exhibited similar frustration to that found in water ice are the rare earth pyrochlore oxides, such as $Dy_2Ti_2O_7$ and $Ho_2Sn_2O_7$, [12] . Frustration occurs within these materials due to the interactions between the spins of the rare earth sites. Strong crystalline anisotropy within these materials forces the spins to be directed towards or away from the centre of the tetrahedral structure, along their local $[111]$ direction, this configuration is shown in **Figure 16**. It was found that these pyrochlore materials exhibit ground state configurations analogous to the ice rule configurations seen in water ice and also exhibit the finite entropy at zero temperature [12].

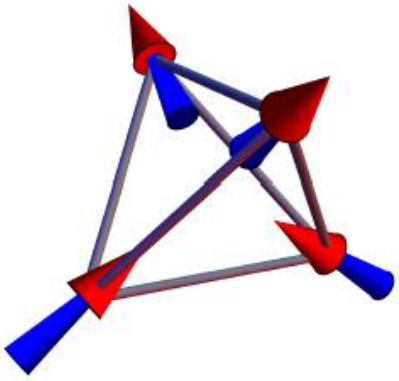

Figure 16: *The arrangement seen in water ice can be directly mapped onto the tetrahedral points of a pyrochlore spin ice material, with the rare earth ions acting as macro spins that can be directed into or out of the tetrahedra, thus capturing the frustration present in water ice. Figure from [11].*

1.5.3 Artificial Spin Ice

The discovery of pyrochlore spin ices revealed the possibility of mimicking a frustrated water ice system with magnetic analogues. Using nano-structuring fabrication techniques, magnetic analogues of spin ice can be built with the only limitation being the imagination of the designer. Such artificially designed spin ice systems are designated Artificial Spin Ice's (ASI). Due to the magnetic nature of the system, both macroscopic and microscopic techniques can study the configuration of the system greatly enhancing the understanding of the microstates and their interactions.

The first artificial spin ice systems created use the macrospins of nanomagnets to represent the rare earth spins from pyrochlore spin ice [13, 14]. The shape and size of these nanomagnets is engineered during fabrication to be of a size where a single domain dominates, producing a clear macrospin. By using a material with low magnetocrystalline anisotropy, such as Permalloy, the magnetic properties of the nanomagnets are dominated by shape anisotropy, providing an Ising-like easy axis.

In a square artificial spin ice, the nanomagnets are arranged in a lattice where four nanomagnets meet at each vertex, resulting in a coordination number of four. This structure resembles that of spin ice, however all macrospins lie within a single plane due to shape

anisotropy. This arrangement allows the macrospins to point either into, or out of the vertex creating a square lattice. In square ASIs constrained in two dimensions, unlike bulk spin ice where Type 1 and Type 2 configurations often share equal energies, there's a discrepancy in energy costs for various vertex types. This contrasts notably with bulk spin ice where the ice rules tend to enforce equivalent energies for Type 1 and Type 2 configurations, while revealing differing energy states for Type 3 and Type 4 configurations.

Within this square lattice, each vertex is categorised into one of four vertex types: Type 1, Type 2, Type 3 and Type 4. These arrangements are shown in **Figure 17**. These vertex types are associated with varying energy levels, with Type 1 being the ground state while Type 4 is the highest energy state. A square ASI lattice comprises of a total of 16 possible vertex configurations distributed among these four vertex types.

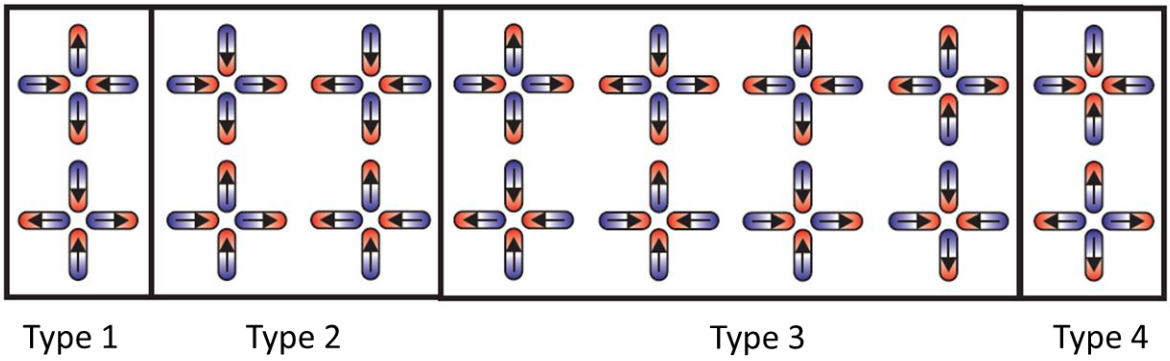

Figure 17: *The sixteen possible configurations for a square artificial spin ice. Configurations are separated by type and increase in energy with increasing type number. Figure from [15].*

In a square ASI lattice Type 1 vertices represent the ground state configuration. These adhere to the Ice Rule configuration, resulting in Type 1 vertices possessing no magnetic moment. Type 2 vertices also satisfy the ice rule configuration however they do possess net magnetic moments. The difference between Type 2 and Type 1 vertices lies in the alignment of spins that constitute them. Type 1 vertices have a lower energy state due to the energetically favourable alignment of spins with their nearest neighbours, typically in a head-to-tail or tail-to-head arrangement. In contrast, Type 2 vertices exhibit less favourable alignments, such as head-to-head or tail-to-tail. These alignments result in a magnetic moment and an energy cost not seen in bulk spin-ice.

Type 3 vertices follow a ‘three-in, one out’ or ‘three-out, one-in’ configuration and as such possess an overall magnetic moment. Type 4 vertices possess either a ‘all-in’ or ‘all-out’ configuration and as such also possess an overall magnetic moment. Type 4 vertices are significantly less common than other vertex types.

In spin ice materials, such as natural pyrochlores, the ice rules governing spin configurations are typically energetically equivalent, allowing for multiple configurations that satisfy these rules to coexist at equilibrium due to the lattice's frustration. However, in 2D artificial spin ice systems, deviations from this energy equivalence among configurations adhering to the ice rules can be observed. Specifically, in the context of Type 1 and Type 2 vertices, this energy discrepancy between ice rule-compliant configurations can lead to distinct energetic preferences and affect the dynamics and stability of these vertices in artificial spin ice nanostructures.

The advantage to research of ASI systems is the wide range of lattice geometries that can be fabricated, dependent only on the imagination of the designer. This allows manipulation of a range of properties of the system created such as: the array geometry, shape anisotropy or inter-element interactions. This has been made possible through the development of nanofabrication techniques. Through the manipulation of these properties a range of topological structures with unique properties have been created and investigated.

Another geometry commonly studied is the Kagome or honeycomb ice lattice [14]. In this geometry the macrospin islands are arranged along the edges of a hexagonal tiling pattern, the resultant lattice approximating a honeycomb configuration. The resultant vertices produced by this setup have three discrete islands meeting at each vertex, each macrospin of equal strength, this is shown in **Figure 18**. This lattice has a total of $2^3 = 8$ total configurations, with two vertex types available and a coordination of three. Kagome Type 1 follows a ‘two-in, one out’ or ‘two-out, one-in’ configuration, and Kagome Type 2 vertices are either ‘all-in’ or ‘all-out’.

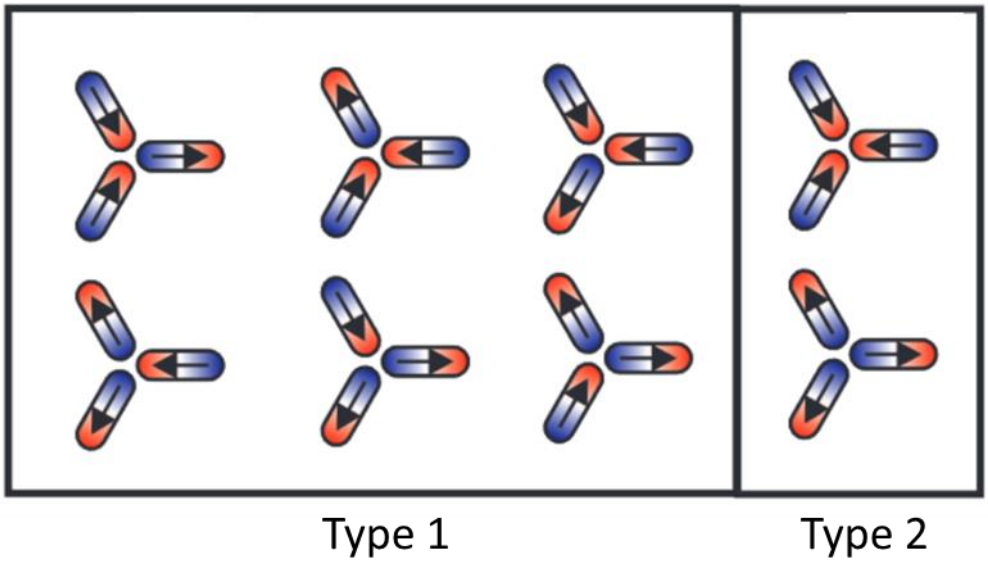

Figure 18: *The eight vertex configurations possible in a Kagome spin ice array. Figure from [15].*

Further geometries have been fabricated and studied each with unique distinctive traits [15]. Each has contributed in its own way to the understanding of artificially frustrated systems. Examples include: a square lattice geometry with reduced vertex coordination number, magnetic nano islands with perpendicular anisotropy directing magnetisation out of plane, and lattices with mixed vertex coordination number. Each of these distinctive lattice arrangements have no known analogues in nature and so the frustration and properties they possess can only be studied through the field of artificial spin ice.

1.5.4 Thermalization of Magnetisation in Artificial Spin Ice Systems

Research exploring the dynamic response of magnetisation in ASI encompasses two primary categories: thermal dynamics, governed by temperature, and athermal dynamics, induced by external magnetic fields at constant temperature [15]. The focus of these studies has been to access to ground state of ASI. Athermal dynamics assume the fixed state of the array under inspection, enabling the acquisition of a stable image. Any alterations in the array result from the application of an external field. If the energy barrier E_B between the bistable states of an island is surpass the thermal energy at the arrays ambient temperature T:

$$E_B \gg k_b T \quad (80)$$

Where k_b is the Boltzmann constant. Operating athermally and lacking ergodicity, this system's states may diverge from thermally equilibrated conditions. Despite this deviation, characterising athermal states involves employing an effective thermodynamics framework, initially intended for granular matter, which utilises AC demagnetisation to lower the energy state of the system.

This AC demagnetisation is used to lower the energy state of the system where adherence to the ice rules can be evaluated [13, 16, 17]. The sample is subjected to a decreasing AC magnetic field while rapidly spinning the sample at about $20\ Hz$. The purpose of this process is to subject the sample to the field from all in-plane directions within the array, aiming to minimize the array's magnetisation as much as feasible, ideally approaching zero.

As shown previously, see Section 1.5.3, there are 6 square ice states with zero magnetisation: two Type 1 vertices and four Type 2 vertices. Achieving ground state access through this process was found not to be possible with most vertices becoming Type 1 & 2, but with still a significant number of Type 3 and Type 4. The demagnetisation process was improved by finer field steps, the use of a linear demagnetisation protocol, and slower sweep rates allowing 60% of the lattice to be Type 1, but true ground state access still found to be unachievable.

The level of ground state fealty is constrained by a factor known as “quenched disorder” [18]. Quenched disorder refers to inherent, uniform, or unchangeable irregularities or imperfections within the lattice structure of the spin ice material. These introduce invariability within the system and prevent the entire lattice from transitioning to the ground state. The quenched disorder of a system determines the extent to which the sample can adhere to the ice rules during and after the demagnetisation process.

In summary, these field-driven protocols have shown limitations in generating fully thermalised states. This might be attributed to allowing only downward energy steps rather than the bidirectional steps observed in a genuine annealing process. Nevertheless, the states resulting from demagnetisation can still be characterised using effective thermodynamics.

The effective temperature of the macro-spin system is derived through a microscopic examination of the artificial spin ice, a departure from the macroscopic measurements required for the real temperature. The effective temperature of the system can be derived as follows [19]: the energy of a vertex of Type i is denoted by E_i, and its multiplicity (the number of equivalent configurations) by v_i. An energy scale is defined such that $E_1 = 0$ and $E_3 = 1$. This derivation doesn't account for any interactions or connections between adjacent vertices, including the basic premise that each macro-spin must behave as a dipole [19].

In this effective thermodynamics' framework, v_2, which ideally equals 4, is instead assumed to be 5. This introduces an additional Type 2 vertex functioning as a background state occupied by all macro-spins. As the macro-spins align with the rotating field, they transition among the four distinct Type 2 configurations. With the reduction in the applied field, all macro-spins in the array traverse the switching field distribution. Consequently, each vertex shifts from the background state, transitioning into one of the four 2D ASI vertex types.

The effective temperature can be found with the following equation:

$$T_{eff} = \frac{1}{\beta_{eff}} \tag{81}$$

First the fractional population n_i of each vertex type is measured, satisfying the condition $\sum_i n_i = 1$. This can be defined by a Boltzmann factor as [20]:

$$n_i = \frac{q_i \exp\left(-\beta_{eff} E_i\right)}{Z_p} \tag{82}$$

where Z_p is the partition function. The effective temperature is determined by the ratio between any two fractional populations. Yet, for consistency with the definition of zero energy, it's preferable to compare the populations of other vertex types to the fractional population of Type 1 vertices, denoted as n_1 *[20]*:

$$\beta_{eff} = E_i^{-1} \ln \left[\left(\frac{q_i}{2} \right) \left(\frac{n_1}{n_i} \right) \right] \quad (83)$$

In this equation, β_{eff} is the effective inverse temperature and characterises the thermal behaviour of the macrospin system within artificial spin ice and plays a role in assessing how the system deviates from true thermodynamic equilibrium. The variable q_i in the equation accounts for the degeneracy or multiplicity of each vertex type i.

The investigation revealed that in samples treated with AC demagnetisation, arrays with stronger couplings tended to exhibit lower effective temperatures compared to those with weaker couplings. When dealing with a system that's genuinely thermally equilibrated, both the real and effective temperatures align. Any deviation between these temperatures indicates the degree to which the system operates athermally.

Despite efforts to enhance the AC demagnetisation process, achieving true thermalisation remains a primary objective. This pursuit is crucial as it would enable the study of the authentic thermodynamics of the system, and extensive ground state ordering would facilitate the examination of excitations above it. An innovative method was discovered by [21], presenting a one-shot thermalisation process during the sample fabrication. The energy barrier to reverse the magnetisation in a magnetic nanoisland is equal to [21]:

$$E_B = K_A A d \quad (84)$$

where K_A is an anisotropy constant defined by the island shape and where A is the area and d the thickness of the nanoisland. In these soft systems the anisotropy constant can be written as [21]:

$$K_A(d,T) = \frac{\mu_0 N M^2(T)}{2} \quad (85)$$

Here, the demagnetising tensor N will be dependent on the thickness d as it affects the elements aspect ratio.

As the island is fabricated, its small volume results in a smaller E_B, which according to Equation (80), will result in free thermal fluctuation. As the island thickness d increases this increases E_B until it surpasses the thermal energy of the system $k_b T$ and it arrests. At this point, the system operates athermally and diverges from thermal equilibrated conditions [21]. Therefore, it showcases a thermal state at the specific temperature and island thickness when this arrest occurred. Samples produced using this approach exhibited extensive ground state order, characterized by sizable domains separated by domain walls and containing isolated excitations [21]. Excitations were distributed according to Boltzmann factors. Comparing a sample produced thusly and those prepared by field demagnetisation showed that truly thermalized states can be distinguished from these based on their statistical properties.

A disadvantage to this process is its limitation to occur during fabrication. Furthermore, once the sample has experienced an externally applied magnetic field and as a result is changed by it, the thermalised state produced and the ground state is lost [19]. To resolve this, an anneal of the sample can be undertaken by heating it above either the blocking temperature T_b of the macro-spins or the Curie temperature T_c of the micro-spins, and then cooling the sample back to room temperature. The blocking temperature T_b, which is the temperature below which the macrospins effectively lock into their magnetic orientations, is defined later.

This process allows imaging of the state that had originally been prepared. This was found to be difficult to do with pure metal samples as the temperatures required destroyed the fabrications.

To resolve this the samples undergo strategic doping such that the Curie temperature drops below room temperature. By doing this, samples can be heated and cooled through T_c to

recover the thermalised state [22]. Once this process was perfected, samples were produced that obtained perfect ground state order. This allows the study of deliberately introduced topological defects which can influence the energetics of the system.

The mean transition time taken for the magnetisation of a ferromagnetic single domain nanoparticle to be flipped when subjected to a temperature T can be calculated by the Neel-Arrhenius equation [1]:

$$\tau_N = \tau_0 \exp\left(\frac{K_{MA}V}{k_B T}\right) \qquad (86)$$

Where τ_N is the Neel relaxation time, K_{MA} is the magnetic anisotropy energy density, V is the volume of the nanoparticle, k_B is the Boltzmann constant. τ_0 is a material dependent characteristic length of time, also called the attempt time, and is usually of the order 10^{-9} and 10^{-10} seconds.

The blocking temperature, mentioned earlier can be obtained by setting defining the time window of a measurement τ_{meas} and using in the equation [1]:

$$T_B = \frac{KV}{k_B \ln\left(\frac{\tau_{meas}}{\tau_0}\right)} \qquad (87)$$

1.5.5 Magnetic Charges in Artificial Spin Ice

A phenomenon exclusively studied within the field of ASI's is the newly discovered magnetic analogue to electric charge currents. This phenomenon has been dubbed magnetricity, [23]. This paper proposes that excitations of vertices above the ground state, which violate the ice rules, are in fact magnetic monopoles with the necessary long-distance properties. To explain the emergence of these monopoles within spin ice a modified representation of the Hamiltonian is introduced, inspired by a model for water ice. Within this model, magnetic

moments are replaced by dumbbells consisting of equal and opposite magnetic charges ($\pm q$) at the ends of diamond bonds. The energy of such a configuration can be described by a magnetic coulomb law, like the electric coulomb law for electric charges. Overall, this representation provides a more intuitive understanding of how defects in spin ice can give rise to monopoles.

Considering a Type 1 vertex within a ground-state square ASI array, with no net magnetic moment or magnetic charge. When a single spin contained within the vertex is flipped, in violation of the ice rule, it results in the formation of a net positive and negative magnetic charge in the two vertices connected to the spin. This is called a monopole-antimonopole pair creation event. By following this initial flip with further spin flips adjacent to the original, the monopole-antimonopole pair can be separated from one another. The chain of flipped spins that is required to achieve this is called a Dirac string and acts as a flux tube connecting the magnetic flux between the two magnetic monopoles as required by Maxwell's equations. Once created and separated by a chain of flipped spins, the two oppositely charged monopoles are identifiable within the lattice, however the chain of spins flipped to separate them is undeterminable. In a 2-dimensional system the string-like excitation that connects the two monopoles is accompanied by an extra energy cost equal to the product of the string length and an effective string tension parameter. For a sufficiently long string, this string energy is dominant. In a 3-dimensional system, where a magnetic coulomb phase is realised, the string tension drops to zero and the monopole energies can be calculated through the magnetic equivalent of coulombs law. The concept of magnetricity was born upon this phenomenon, defining a concept whereby mobile magnetic charges can be created, stored, controlled within an ASI by an externally applied magnetic field.

The presence of monopoles within spin ice leads to important implications regarding its behaviour. By applying a magnetic field along a specific crystallographic direction will result in a tuneable lattice gas of magnetic monopoles. The resultant phase diagram of such a system will exhibit a first-order phase transition and a critical point, analogous to the liquid gas transition in water.

Movement of monopoles throughout a connected 2D ASI lattice were studied previously [24]. In wire ASI arrays monopoles are formed through the creation and interaction of domain walls

at the junctions between wires [23, 25]. Each magnetic nanowire can be described as a magnetic dipole containing a positive charge at one end and a negative charge located at the other end. When the magnetisation direction of a nanowire connected to two vertices is reversed it results in the formation of two magnetic charges. These oppositely charged monopoles can then be directed through the application of an external magnetic field and can be directly imaged by magnetic force microscopy [24]. These monopoles can travel throughout the network of nanowires as domain walls, with the ability to reverse direction of magnetisation of nanowires they travel through. Such monopoles cannot move freely throughout the network. Monopoles are constrained to enter nanowires with an allowed direction of magnetisation and after travel through the wire the direction of magnetisation of the wire is switched. Chiral and topological properties of the composite domain walls are expected to dominate these interactions.

1.6 Two Photon Lithography

With the fundamentals of magnetism, frustration and artificial spin ices introduced, attention is directed towards outlining the fundamental physics underlying two-photon lithography, the technique employed in this thesis for fabricating 3D nanostructures.

Lithographic techniques are fundamental in microfabrication, enabling the creation of intricate patterns on substrates to produce semiconductor devices, microelectrochemical systems (MEMS), and other nanostructures [26-28]. The main lithographic techniques include optical lithography, electron beam lithography, and various forms of direct laser writing such as two-photon lithography, which is used in this thesis.

Optical lithography (also called just photolithography) is the most established and widely used lithography technique, primarily due to a high throughput and cost efficiency for mass production. It employs light to transfer a geometric pattern from a photomask to a light sensitive chemical photoresist on the substrate [26, 27]. Variations of the technique exist with the simplest achieving resolution of $2 - 3\ \mu m$, however methods such as projection printing have shown to be capable of achieving $< 40\ nm$ resolution with an associated increase in expense and reduction in throughput as a consequence of the technique [26, 27].

Electron Beam Lithography (EBL) offers much higher resolution than optical lithography, reaching 5 – 20 nm scales due to the shorter wavelength of electrons or sometimes ions used [26, 27]. EBL does not require a photomask, making it highly flexible for prototyping and research. However, it is significantly slower and more expensive than optical lithography, primarily due to the serial writing process and the need for sophisticated equipment and vacuum conditions. This makes EBL less suitable for high volume manufacturing but ideal for applications requiring ultrafine patterns.

Focused Electron Beam Induced Deposition (FEBID) is a direct write nanofabrication technique that utilizes a focused electron beam to induce the deposition of material from a precursor gas. This process allows the creation of intricate 3D nanostructures with a high spatial resolution typically about 10-20 nm, though finer resolution is achievable [28, 29]. FEBID is used for creating complex 3D nanostructures, repairing photomasks, and fabricating nanoscale components for research in nanotechnology, electronics, and material science. It can deposit a wide range of materials including metals, insulators, and superconductors, however a limitation of FEBID is the purity of the deposited metal [28]. The process results in deposits with impurities from the precursor gas which can affect the materials properties. Furthermore, it is relatively slow and expensive compared to other lithographic techniques limiting use in high-volume manufacturing.

Two-photon lithography (TPL) is a powerful manufacturing technique that combines the chemical processes of photolithography with the 3D structure direct-writing technique from FEBID, [30-32]. Confinement of polymerisation to the focal point of a laser allows fabrication of 3D structures with resolutions of typically 200 nm though advancements in technique has resulted in sub-100 nm structures. Unlike FEBID however, TPL does not generate issues with purity contamination of fabricated structures. Advantages for TPL lie in the ability to create 3D microstructures with high precision and flexibility without need of a vacuum, however like FEBID and EBL it is a slower process compared to optical lithography, making it less suitable for large scale production.

1.6.1 Fundamentals of TPL

The basic principles of operation of TPL are as follows. A femtosecond infrared $(780\ nm)$ laser is focused to a diffraction-limited spot within a photoresist. The photoresist is generally comprised of monomers, which react directly to the light, and photosensitizers, which absorb light and transfer energy to monomers. The laser light provided to this photoresist causes photopolymerisation of the monomers through a two-photon absorption process [33].

Photo polymerisation is the process by which molecules in a liquid state use energy provided by a light source to convert to solid macromolecule through a polymerisation reaction. The liquid material that undergoes this reaction is comprised of monomers and oligomers, also called prepolymers.

Polymerisation is the process where monomers chemically bond together to form long polymer chains. This reaction is initiated by the light source, generating reactive species that start a chain reaction. The frequency of these reactions is gauged by comparing the number of polymerised monomer units of the photons necessary for polymerisation, termed the quantum yield of the reaction. In photo polymerisation this chain reaction results in a high quantum yield often in the region of several thousands, as one initiated chain reaction can add many monomer units.

Further components are required to increase the efficiency of this process. Most photoresists use photoinitiators and photosensitizers. Photoinitiator molecules (PI) are added to form species of radicals following the absorption of photons whereas photosensitizer molecules are added to absorb and transfer energy to a photoinitiator. Radicals ($R\cdot$) produced by excited photoinitiators (PI^*), following absorption of two photons (hv), react with monomers (M), producing monomer radicals ($RM\cdot$) which combine with further monomers in a chain reaction halted only by the encounter of two monomer radicals [33]. Monomers are smaller molecules comprised of multiple reactants and form the bulk of solidified resin following polymerisation. Furthermore, the percentage of monomers contained within a photoresist resin controls the viscosity of the liquid resin. This is important for fabrication of nanostructures as structures produced early in the fabrication process remain relatively stable in a highly viscous liquid.

The polymerisation process therefore is comprised of multiple steps: photoinitiation releasing radicals, chain propagation forming monomer chains and finally termination. A good photoinitiator is dependent on its ability to produce radicals or cations after exposure to light and the ability of these produced radicals/cations to react with monomers.

This three-step chemical process can be described through the following chemical equations [33]:

Photoinitiation: $$PI + hv \rightarrow PI^* \rightarrow R\cdot + R\cdot \quad (88)$$

Chain propagation: $$R\cdot + M \rightarrow RM\cdot \quad (89)$$

$$RM\cdot + M \rightarrow RMM\cdot \ldots \rightarrow RM_n\cdot \quad (90)$$

Termination: $$RM_n\cdot + RM_m\cdot \rightarrow RM_{n+m}R \quad (91)$$

Two-photon lithography acquires its name from the phenomenon that drives the polymerisation process, two photon absorption. In this process two photons of identical (or near identical) frequency ($2hv$) are absorbed by a photoinitiator in a simultaneous excitation step, or in a stepwise excitation with an intermediate energy level [33]. This causes excitation of the photoinitiator and the release of a radical/cation which initiates the polymerisation process, described in Equation (88). Stepwise TPA is akin to two sequential single photon absorptions with an actual intermediate energy level providing a resting point before absorption of a second photon to reach the required excited energy level. Unlike simultaneous TPA, stepwise TPA does not require the light incident to be coherent. For TPL micro-nanofabrication using a femtosecond laser, simultaneous TPA is the more relevant regime.

Simultaneous TPA, hereafter called TPA, is a quantum mechanical three body process. In this process a photoinitiator electron is excited to a required energy level through the simultaneous absorption of two photons in a single excitation ‘event’. It is best described

through the scenario of a single photon absorbed by a molecule pumping the energy level of the electron to a 'virtual' state with a short duration lifetime. A second photon absorbed before the decay of the virtual state pumps the electron energy level to its required excited state. As the lifetime of the virtual state is of the order of femtoseconds, as required by Heisenberg's Uncertainty Principle, this process is described as simultaneous.

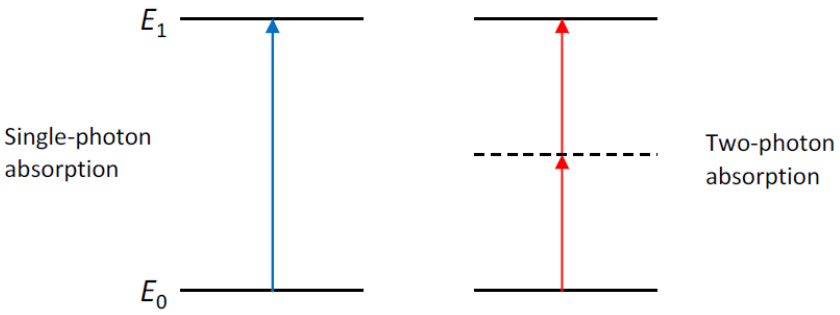

Figure 19: *The energy level diagram illustrates single-photon absorption and degenerate two-photon absorption. A dotted line indicates the virtual state involved in the process. Figure from [34].*

TPA can be classed as degenerate when the two photons absorbed are of equal frequency, and non-degenerate when the two photons are of different frequencies. TPP generally uses the degenerate process. In comparison, in Single Photon Lithography (SPL) a single photon excites a photoinitiators electron to its excited energy state using UV light wavelengths. Following excitation, the electron will relax to its original state releasing a photon of light of less energy than the excitation photon. In TPL, two photons with double the wavelength perform the same excitation through simultaneous absorption, however only one photon is released when the electron relaxes to a stable state [33]. This released photon will have a wavelength akin to the photon released by the SPL relaxation process. A comparative energy level diagram showing this step is shown in **Figure 19**.

In the realm of optical processes, TPA stands out as a third-order nonlinear phenomenon. At low light intensities, its impact is notably weaker than linear absorption by several orders of magnitude. However, as opposed to linear absorption, TPA's influence intensifies exponentially, squared to the light intensity, this can be expressed as [33]:

$$\frac{d\mathrm{W}}{d\mathrm{t}} = \frac{8\pi^2\omega}{n^2c^2} I^2 \mathrm{Im}\left(\chi^{(3)}\right) \quad (92)$$

Where ω is the light optical frequency, n is the refractive index, c is the speed of light in a vacuum, I is the light intensity and $Im\left(\chi^{(3)}\right)$ is the imaginary part of the third order susceptibility. Importantly, this equation illustrates that the absorption rate, described by $\frac{dW}{dt}$, is directly proportional to the intensity squared.

1.6.2 Mechanics and Control in TPL

TPL has significant advantages when compared with SPL. The wavelengths of the two photons required to excite the electron are double the wavelength of the single photon used in SPL. This requires the light used to be in the near-infrared regime, where polymers used by TPL have a near zero linear absorption. The laser therefore can penetrate deep into the material. Furthermore, the short time window of the order of 10^{-15} seconds, for absorption of two photons by the photoinitiator requires a high photon intensity to ensure successful excitation. This is only possible at the objective focal point of the laser; a region termed the 'voxel' which is of an ellipsoidal shape and due to the tightly confined shape provides high spatial resolution of fabricated structures. Control of this voxel allows direct writing of a structure within the polymer resin. Movement of the voxel is achieved using piezo tilting mirrors and movement of the writing stage by galvanometer motors.

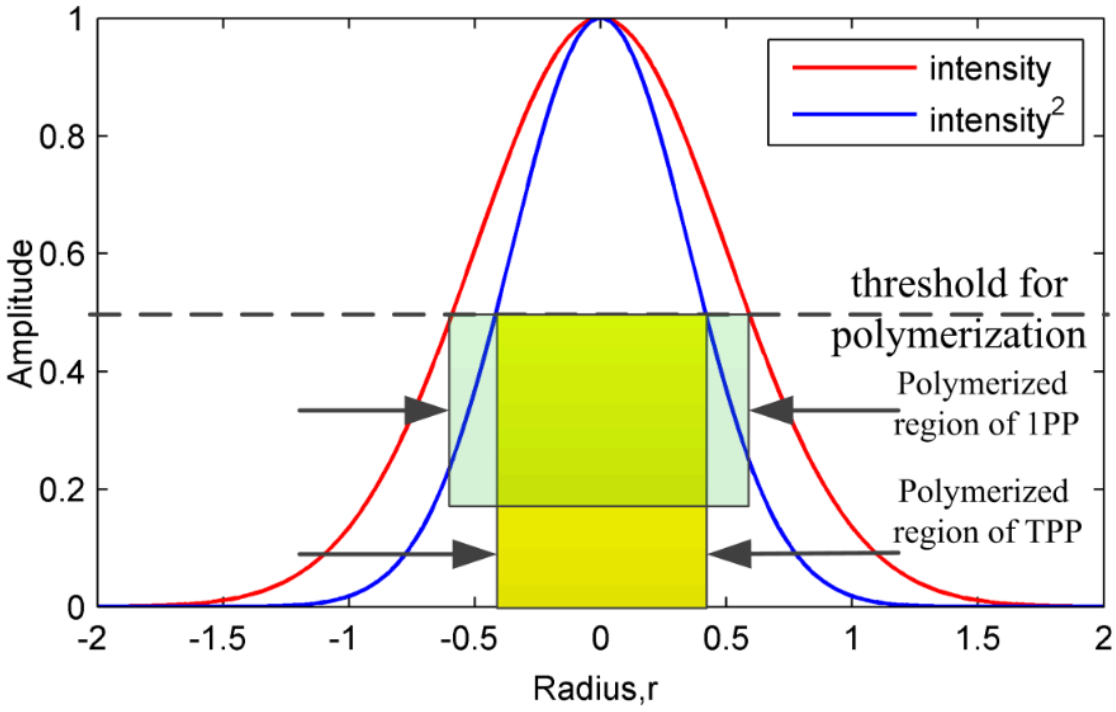

Figure 20: *Graph illustrating the intensity distribution within the laser focus of a Gaussian beam. The red line represents the intensity, while the blue line displays the squared intensity. The photopolymerisation process occurs within the region where the intensity reaches the threshold value required for polymerisation .Figure from [33].*

By plotting the light intensity's for both SPL and TPL, see **Figure 20**, for a laser focus of a gaussian beam with intensity [33]:

$$I(r) = I_0 \exp\left(-\frac{2r^2}{\omega_0^2}\right) \tag{93}$$

Where the beam waist $\omega_0 = 1$ and the light intensity at the focus is $I_0 = 1$. It's evident that TPP exhibits a narrower polymerisation area in comparison to SPL, leading to a more concentrated polymerisation region within a smaller voxel. Consequently, this enhances the resolution of the fabricated structures. Examining the impact of process parameters on TPL resolution involves considering the density of radicals, ρ, initiated by a femtosecond laser pulse with a photon flux intensity I, and the primary initiator particle density, ρ_0, as expressed in the following equations [33]:

$$\frac{\partial \rho}{\partial t} = (\rho_0 - \rho)\sigma_2 I^2 \quad (94)$$

$$\rho = \rho_0\left(1 - e^{-\sigma_2 I^2 t}\right) \quad (95)$$

Where the initial rate equation, Equation (94), can be solved with solution Equation (95), if the initial density of radical's present equals zero. And where σ_2 is the effective two-photon cross section for the generation of radicals and can be expressed in terms of the ordinary two-photon absorption cross section σ_2^a and the initiation process efficiency η *[33]*:

$$\sigma_2 = \sigma_2^a \eta \quad (96)$$

Considering a gaussian laser beam with a laser distribution of photon flux intensity $I(r, z)$, at distances r across the cross section and of z in the propagation direction from the centre. This can be expressed as [33]:

$$I(r, z) = I_0 \left(\frac{\omega_0^2}{\omega(z)^2}\right) e^{\frac{-2r^2}{\omega(z)^2}} \quad (97)$$

Where I_0 is the photon flux intensity found at the beam centre ($r = 0, z = 0$), and $\omega(z)$ is the beam radius found in the plane at distance z. In a TPP system an oil-immersion objective lens is used and for this the beam waist parameters ω_0 and $\omega(z)$ can be expressed by [33]:

$$\omega_0 = \frac{\lambda}{\pi NA}\sqrt{n_{oil}^2 - NA^2} \quad (98)$$

$$\omega(z) = \omega_0\sqrt{1 + \left(\frac{\lambda z}{\pi\omega_0^2}\right)^2} \quad (99)$$

Where λ is the wavelength of the laser beam, and n_{oil} is the refractive index of immersion oil used.

The average photon flux intensity found at the focus plane I_{focus} is given by [33]:

$$I_{focus} = \frac{P}{\pi\omega_0^2\tau f h v} \quad (100)$$

Where P is the averaged power of the laser, τ is the pulse width of the laser, f is the pulse frequency and h and v are Planck's constant and the frequency of light respectively. Now I_0 can be written in terms of I_{focus} through the following equation [33]:

$$I_0 = \frac{2e^2}{e^2 - 1} I_{focus} \approx 2.3 I_{focus} \quad (101)$$

By combining assumptions and equations above an estimation for the voxel diameter can be produced. If the density of radicals $\rho(r, z)$ required to begin the photon-polymerisation process must reach the threshold value of ρ_{th} and the photon flux intensity at the focal plane reaches its maximum when.

$$I(r,z) = I(r,0) = I_0 \exp\left(-\frac{2r^2}{\omega_0^2}\right) \quad (102)$$

Then by neglecting the loss of radicals between laser pulses the voxel diameter $d(P,t)$ can be expressed as [33]:

$$d(P,t) = \omega_0 \left(\ln \frac{\sigma_2 I_0^2 n\tau}{C}\right)^{\frac{1}{2}} \quad (103)$$

Where $n = ft$ is the number of pulses, t is the total processing time and C is defined by [33]:

$$C = \ln\left[\frac{\rho_0}{\rho_0 - \rho_{th}}\right] \quad (104)$$

Furthermore the length of the voxel $l(P,t)$ can be expressed by the following equation [33]:

$$l(P,t) = 2z_R \left[\left(\frac{\sigma_2 I_0^2 n\tau}{C}\right)^{\frac{1}{2}} - 1\right]^{\frac{1}{2}} \quad (105)$$

Where z_R is the Rayleigh length, the distance along the optical axis from the focus point of a collimated Gaussian laser beam where the beam diameter increases by the factor of the square root of 2 compared to its minimum diameter at the focus point, and is defined by [33]:

$$z_R = \frac{\pi\omega_0^2}{\lambda} \quad (106)$$

A visual examination of the response of the voxel diameter and voxel length calculated using Equation (103) and Equation (105) can be seen in **Figure 21**. An ellipsoidal shape is apparent

due to the clear larger voxel length than voxel diameter. Increased fabrication resolution is achieved by a minimised voxel size, and this is achieved a decrease in applied power, reduced exposure time and using a lower numerical aperture.

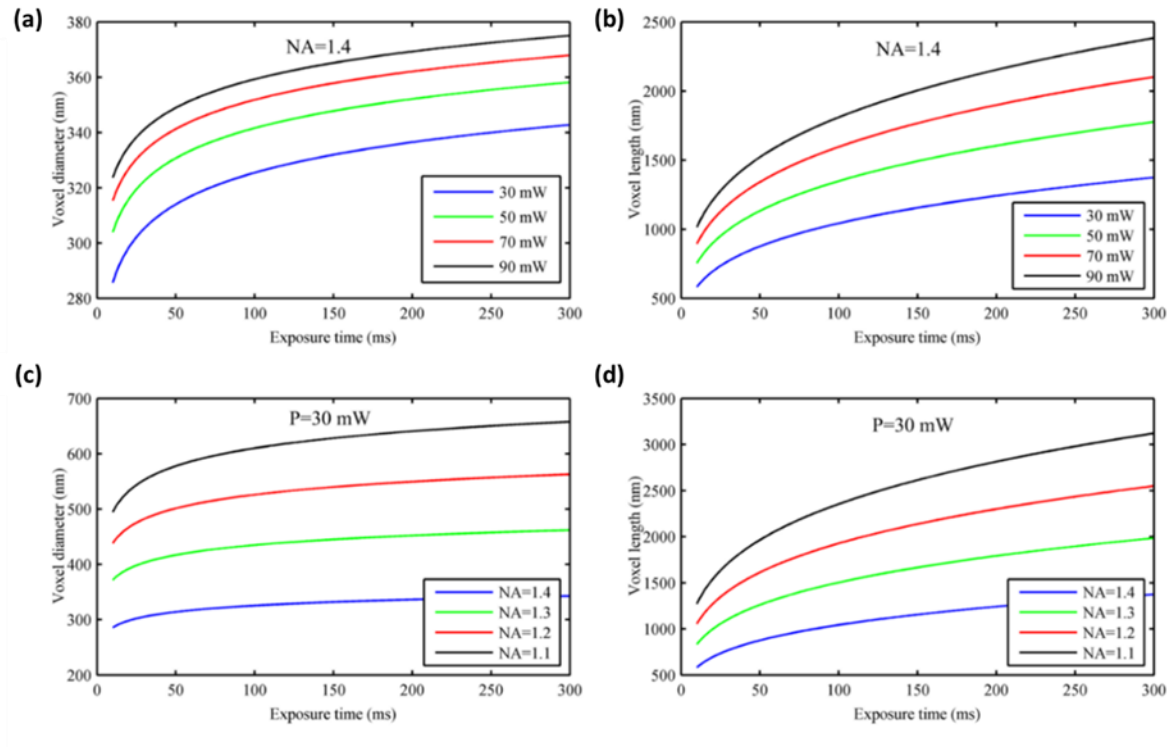

Figure 21: *Voxel diameter and voxel length compared for a range of applied laser powers* ***(a-b)****, voxel diameter and length for a range of numerical apertures* ***(c-d)****. Figure from [33].*

2 Three-Dimensional Artificial Spin Ice

The two-dimensional square artificial spin ice (ASI) doesn't perfectly mirror its naturally occurring bulk counterpart. This discrepancy can be attributed to variations in the interaction energy among nearest neighbour spins. To recover the degeneracy of bulk spin ice, the system must evolve beyond two dimensions. This chapter reviews the efforts to fabricate, measure, and characterize multi-dimensional artificial spin ice systems, with a particular focus on the previous work accomplished by the Cardiff research group. Additionally, the chapter will outline the specific goals of this thesis, highlighting how it aims to advance the understanding and development of 3D artificial spin ice.

2.1 Review of 3D Artificial Spin Ice

The interaction energies of all nearest neighbours can be equivalated by layering the ASI system in a 2.5D system [35-37]. By separating a square ASI into sublattices separated by a defined height the interaction energy between all nearest neighbours can be made equivalent and a magnetic coulomb phase can be realised.

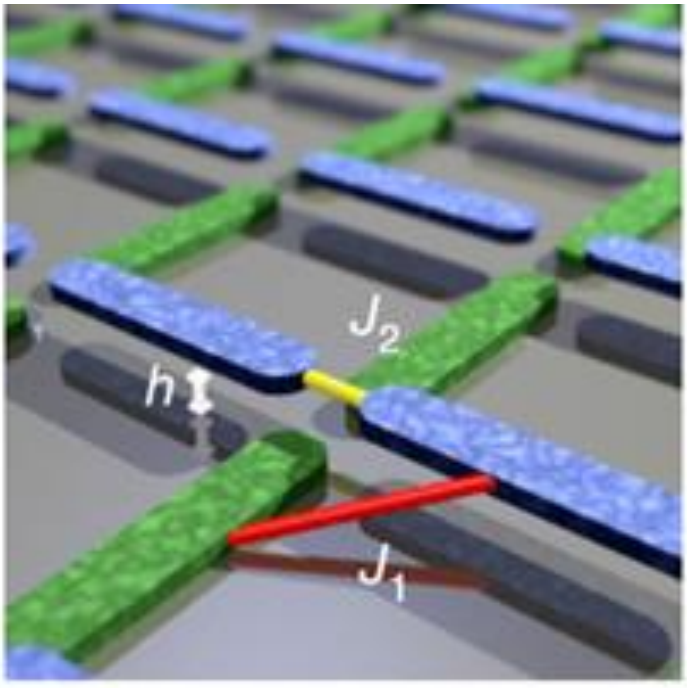

Figure 22: *A diagram of the fabricated 2.5D square ice array, the blue nano islands are shifted by height h above the green nano islands. Figure from [37].*

To achieve this, a square ASI was fabricated with two sublattices that were vertically shifted in height h, see **Figure 22**. By varying this height, the coupling strength between two perpendicular nanomagnets J_1 can be varied whilst maintaining the coupling strength between colinear nanomagnets J_2. Through variations of the height offset h it becomes possible to tune the ratio of $\frac{J_1}{J_2}$. Three arrangements are made possible: $J_1 < J_2$, $J_1 = J_2$, $J_1 > J_2$. The effects of each of these arrangements are shown in **Figure 23**. When $h = 0$ the system is a standard artificial square ice system and can be described by $J_1 > J_2$, see **Figure 23a**. When h is continually increased then J_1 will decrease in strength until the perpendicular oriented nanomagnets are magnetically decoupled $J_1 < J_2$, see **Figure 23b**. When h is set equal to a critical height offset h_c then the two coupling coefficients are made equal $J_1 = J_2$, see **Figure 23c**. This results in an equivalent interaction strength between all nanomagnets within each vertex therefore recovering the true degeneracy of the ice rule and leading to equivalent population densities of Type 1 and Type 2 vertices within the system.

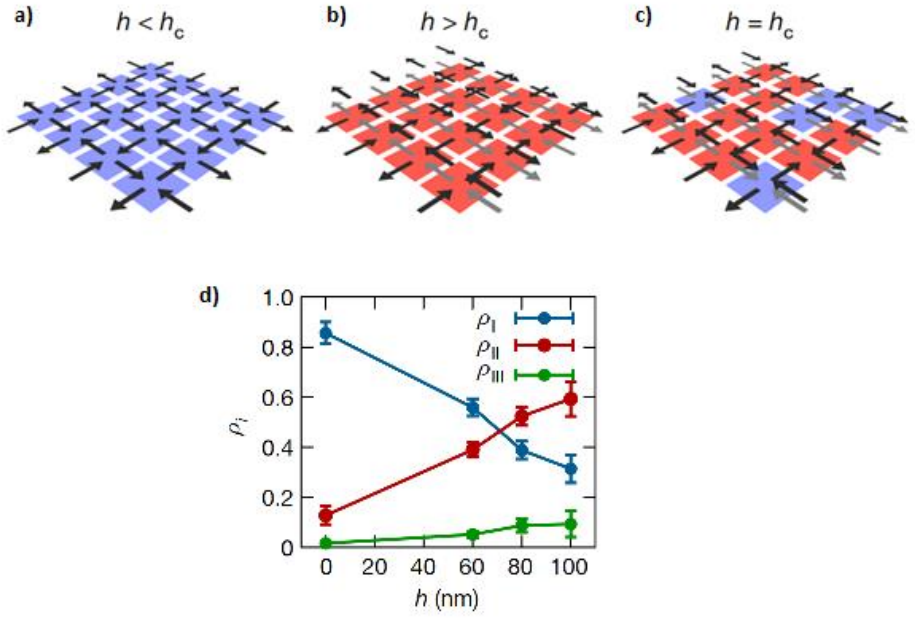

Figure 23: *Ground states of the models associated with ratio of coupling strengths:* $J_1 > J_2$ ***(a)****,* $J_1 < J_2$ ***(b)*** *and* $J_1 = J_2$ ***(c)****. Blue and red squares correspond to Type-1 and Type-2 vertices respectively. Black arrows indicate the local spin direction and grey arrows represent the projection of the spin directions of the shifted sublattice on the* $h = 0$ *plane.* ***(d)*** *Vertex type-*i *population densities as a function of the height offset* h*. Points represent the mean and error bars the standard deviation calculated from collected datasets. Figure from [37].*

Magnetic force microscopy (MFM) was performed on these 2.5D systems following a demagnetisation process. Fourier transforms were applied to this data to show the magnetic structure factor and it was seen that pinch points occur in lattices close to the critical height offset h_c. These observed pinch points indicate a coulomb phase and that the square ice has the characteristics of a dipolar algebraic spin liquid.

In [38], further attempts to engineer 2D artificial spin ice to equivalate the interaction strength was attempted. In this work two-dimensional artificial spin ice arrays with varied horizontal and vertical lattice spacings were created. By varying these lattice spacings the nearest neighbour interactions were again modified to achieve a state where the system is degenerate as seen in natural spin ice. The string tension was also noted to vanish allowing monopoles free movement throughout the lattice.

Layered and offset systems explored by [37, 38] realise a magnetic coulomb phase with their engineered topologies and equivalate the interaction energy between nearest neighbours thus recovering the ice rule. They fall short of representing the authentic physics of bulk systems since the magnetic islands aren't arranged in a configuration that mimics the spin orientations along the $[111]$ direction observed in bulk spin ice. To achieve this physical geometry fabrication techniques must be developed to realise a 3D artificial spin ice.

In [39], a method of fabricating and characterising three-dimension magnetic nanowires using focused electron beam induced deposition (FEBID) is explored. FEBID is a nanolithography technique that allows the local chemical-vapor deposition of materials using a focused electron beam that unlike traditional lithography methods do not require resists or templates making it uniquely situated for the creation of complex 3D nanostructures. Using this methodology FEBID is employed to grow 3D cobalt nanowires with high aspect ratios proving the fabrications strength in creating intricate 3D nanostructures. Characterisation of these nanowires was achieved through application of spatially resolved Magneto Optical Kerr Effect (MOKE) a technique that enabled measurement of the magnetic moment of the nanowires. It was found that the magnetisation reversal of the 3D nanowires primarily occurred through nucleation and propagation of domain walls. Furthermore, measurement through MOKE provided confirmation of the 3D magnetic functionality of these nanowires suggesting further

full bulk lattices comprising of FEBID nanowire structures can be created and measurement of a 3D artificial spin ice can occur.

This work [40] focuses on the fabrication and magnetic configuration study of a 3D tripod nanostructure, a foundational element of 3D artificial systems. Within the work, a nanostructure comprising of a tripod surrounded by a 2D magnetic film is fabricated through a combination of two-photon lithography, pyrolysis and a $GdCo$ coating. Soft x-ray magnetic laminography was used to map the 3D magnetic arrangement of the structure revealing a low-energy two-in-one-out spin ice state, akin to the kagome ice's 2D vertex. It is stated that this states degeneracy could be influenced by the surrounding 2D thin film, potentially enabling controlled charge injection. The findings illustrate the potential for complex 3D artificial spin ice system generated from arrangement of constituent tripod building blocks. This may pave the way for investigation of unique ASI behaviours, such as charge propagation and domain wall configurations.

A complementary perspective on investigating 3D ASI structures is achieved in [41]. Within this study, a 3D structure of electrodeposited cobalt is produced that closely resembles an inverse opal-like structure (IOLS), drawing its name from a resemblance to the structure of an opal gemstone but in an inverted form. An ice rule model tailored to this novel structure is developed that describes how magnetic moments are distributed within the lattice, ensuring that the net magnetic flux within each tetrahedron or cube comprising the structure equates to zero. Furthermore, the remagnetisation process of the structure after application of an applied magnetic field is explored and identification of critical magnetic fields that produce distinct magnetisation states is discovered. Overall, the paper discovers a magnetic component perpendicular to the applied magnetic field, a phenomenon that is predicted by the ice rule model and discover that the orientation of the magnetic field to the lattice exerts a great influence on this perpendicular magnetisation component.

A fully 3D ASI frustrated nanowire lattice was achieved in previous work by the Cardiff research group [42]. It was created and thoroughly investigated through a combination of two

photon lithography with line-of-sight deposition, advanced microscopy and finite element simulations.

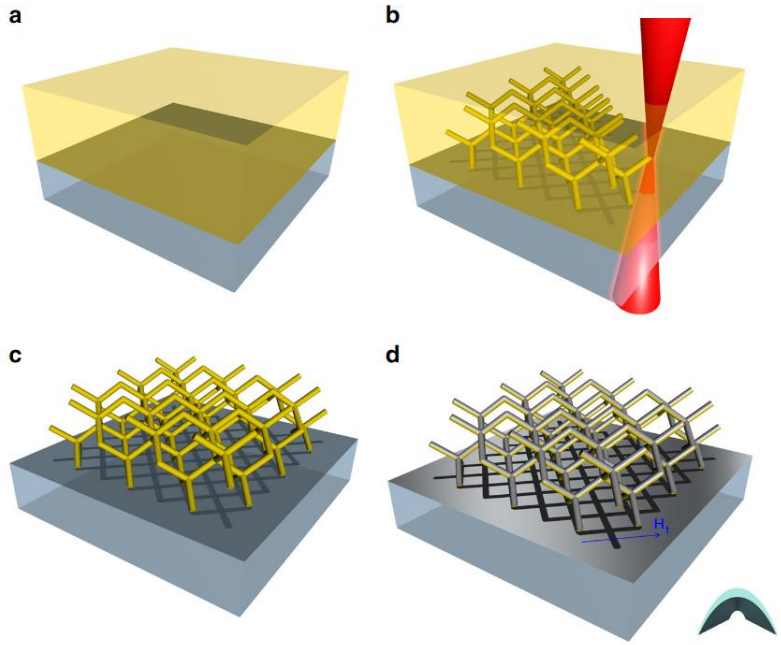

Figure 24: (a) *The substrate is coated with negative-tone photoresist.* ***(b)*** *A diamond-bond geometry lattice is written within the resist by two-photon lithography.* ***(c)*** *Development of the resist removes excess resist and leaves free standing 3D ASI scaffold.* ***(d)*** *Permalloy is thermally evaporated onto the upper surface yielding connected 3D ASI with crescent shaped wires, see inset. Figure from [42].*

The lattice fabrication began with the use of two-photon lithography, writing a diamond bond lattice geometry, see **Figure 24a-c**, to better approximate the arrangement of spins within bulk frustrated spin-ice, resulting in the desired equivalency in interaction strength between neighbouring nanowires. Following development of the polymer scaffold, a magnetic coating of Permalloy ($Ni_{81}Fe_{19}$) was then deposited atop using thermal evaporation, see **Figure 24d**. This structure was fabricated anchored into a glass substrate and was of dimensions $50 \times 50 \times 10\ \mu m$, see **Figure 25a**. Wires between vertices were of length approximately $1000\ nm$.

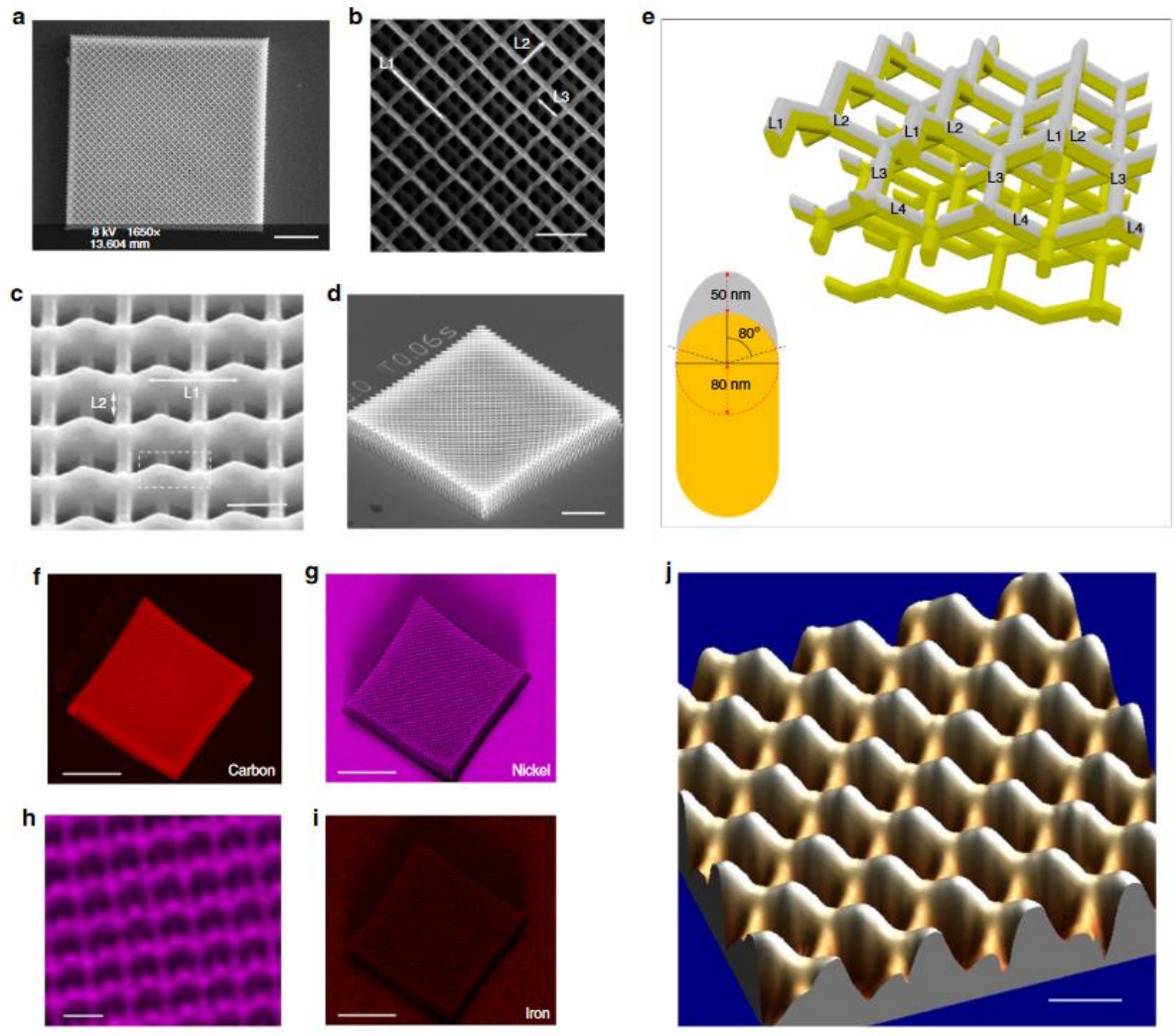

Figure 25: *Characterisation of the 3D ASI.* ***(a)*** *Top-down SEM of the 3D, scale indicates* $10\ \mu m$. ***(b)*** *Increased magnification top-down SEM showing different sub-lattice layers: SL1, SL2 and SL3. Scale indicates* $2\ \mu m$. ***(c-d)*** *Tilted SEMs of the 3D ASI. Dotted lines in* ***(c)*** *show a surface termination bipod. Scale bar in* ***(c)*** *is* $1\ \mu m$ *and in* ***(d)*** *it is* $10\ \mu m$. ***(e)*** *A schematic of the 3D ASI, the inset shows the crescent shaped cross section of nanowires. Yellow shows polymer and grey shows* $Ni_{81}Fe_{19}$. ***(f-i)*** *Energy dispersive X-ray spectroscopy images depict carbon, nickel, higher magnification of nickel, and iron, respectively. Scale indicators for carbon, nickel, and iron are* $20\ \mu m$, *while for higher magnification nickel, it's* $1\ \mu m$. ***(j)*** *3D Atomic force microscopy of the 3D ASI. Scale indicates* $1\ \mu m$. *Figure from [42].*

The 3D ASI is well-characterized, with continuous magnetic nanowires conforming to the 3D polymer template, consistent composition, and minor variations in roughness and geometry across sub-lattice layers. Nanowires are found to be single domain with high shape

anisotropy, with magnetic switching behaviour primarily driven by domain wall motion. Magnetic force microscopy utilised to measure the system found noticeable contrast patterns, validated by reverse tip measurements, providing a means for identification of vertex types upon the two upper surface layers and switching was observed through application of a saturating fields. Micromagnetic simulations show that all nanowires remain in a single domain state, approximating Ising spin behaviour, like bulk spin-ice.

Table 1: *Vertex energies calculated using micromagnetic simulations. Table from supplementary information of [42].*

Vertex Type	Energy Density (J/m)
Type I	8342
Type I	8342
Type II	7745
Type II	7746
Type III	10447
Type III	11683
Type III	11276
Type III	9907

Micromagnetic simulations were used to calculate the vertex energies of the system and notably the energies of Type 1 and Type 2 vertices agree closely this is shown in **Table 1** . By virtue of its 3D structure mimicking the bulk spin ice, this 3D ASI provides a better approximation of those systems and paves the way for detailed experiments exploring ground state ordering and monopole transport.

In conclusion, this work demonstrates the fabrication and thorough characterisation of a 3D ASI, revealing its single-domain nature and magnetic switching behaviour. The study also suggests that the system may serve as a candidate for insights into magnetic charge propagation.

Expanding upon the findings from the earlier exploration of the 3D frustrated nanowire lattice, this paper by the Cardiff research group [43], delves into a related but distinct research area. Specifically, it investigates the nucleation of magnetic monopoles and their propagation within the same lattice design. The design of the 3D ASI, as elaborated in the preceding section, remains consistent for the research detailed here. The same lattice structure is employed to investigate the propagation and generation of magnetic monopoles within this established framework.

Initial experiments using optical magnetometry conducted on the lattice identified a saturating field strength required for each sub-lattice, $30\ mT$. Subsequent MFM imaging of the lattice confirmed this after application of a saturating field whereby the contrast showed that every SL1-SL2 vertex was identical across the section of lattice measured. A methodology for interpreting contrast was identified when the MFM tip was magnetised in a specified configuration. This methodology was then used to measure a saturated lattice and apply vertex arrows across the measured section confirming the saturated state. The results of this study are shown in ***Figure 26*** with contrast clearly showing the expected saturated state after application of the fields along the SL1 and SL2 sublattice directions.

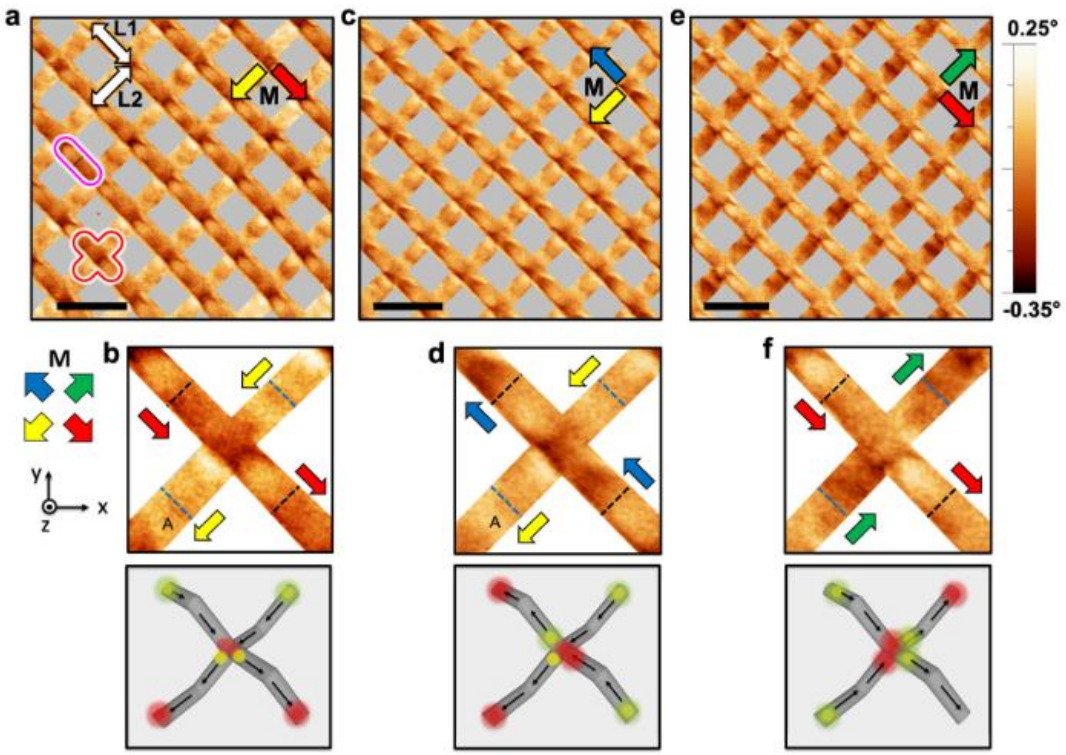

***Figure 26**: Magnetic Force Microscopy images of the saturated states of a 3D ASI. **(a)** MFM image taken at remanence post application of a saturating field applied along unit vectors:* $(1, -1, 0)$ *and* $(-1, -1, 0)$*. A coordination two, surface terminating bipod, is highlighted in pink, whilst a coordination four vertex at the intersection of sublattices SL1 and SL2 is shown in orange. Scale bar in each image represents* $2\ \mu m$*. **(b)** A magnified image of the highlighted SL1-SL2 junction shown in **(a)**, with dashed lines representing the individual islands and a diagram of the magnetisation configuration shown below. **(c)** MFM contrast shown after further application of a field along unit vector* $(-1,1,0)$ *with associated magnified contrast and diagram shown in **(d)**. **(e)** MFM contrast after application of saturating field along vectors* $(1, -1, 0)$ *and* $(1, 1, 0)$*, **(f)** shows the magnified example of contrast and diagram representation for **(e)**. Figure from [43].*

The work then explored the nucleation and propagation of monopole defects as a function of applied magnetic field along principal directions. For a given sub-lattice direction, a saturating field was first applied and an MFM image obtained to confirm a saturated state. Next, a field of approximately $9\ mT$ was applied in the reverse direction resulting in nucleation of monopole states. These were identified and vector maps of the magnetic configuration produced showing a plethora of excited states across both datasets.

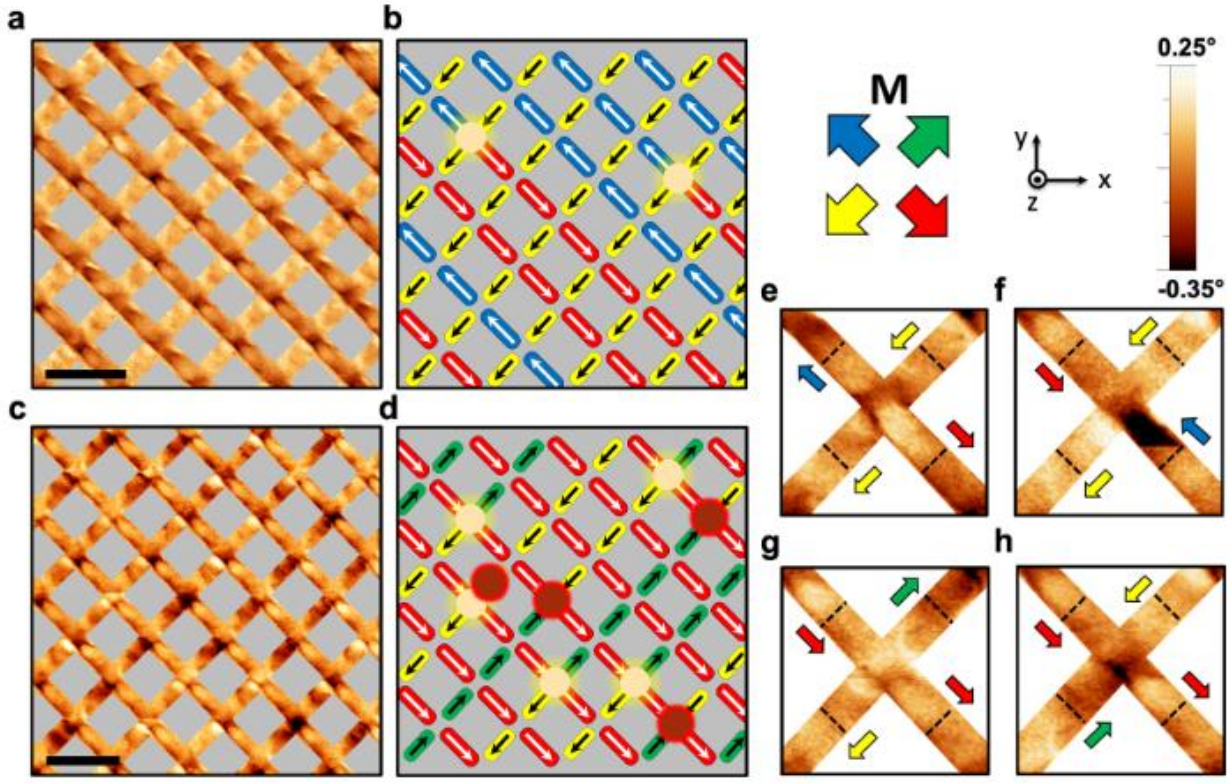

Figure 27: *MFM images of monopole-excitations. (**a**) A MFM image taken at remanence post application of a saturating field along* $(1, -1, 0)$ *and subsequent* $9.5\ mT$ *field along unit vector* $(-1, 1, 0)$. ***b)*** *Vector map showing the magnetic configuration shown by MFM contrast including monopole-excitations marked with bright yellow* $(Q = -2q)$ *and red* $(Q = +2q)$. *Each island in **(b)** represents a single bipod, coloured with the magnetisation shown by the key. **(c)** MFM image taken at remanence following a saturating field along unit vector* $(-1, -1, 0)$ *and subsequent* $8.0\ mT$ *field applied along* $(1,1,0)$. *The scale bars upon **(a)** and **(c)** represents* $2\ \mu m$. ***d)*** *Associated vector map illustrating the magnetic configuration, and presence of monopole-excitations. **(e-h)** show magnified examples of the MFM contrast associated with the SL1-SL2 junctions where* $Q = \pm 2q$. *Figure from [43].*

In later work [43], the transition between two saturated states was observed by capturing images at $0.25\ mT$ intervals. This entailed direct tracking of the reversal sequences for the SL1 and SL2 sub-lattices. Upon the upper surface layer SL1, the first switching instances are seen after applying an $8.5\ mT$ field and two monopoles are created by this switching at the intersection of SL1 and SL2, each with a charge of $-2q$. Further increments in the field prompted additional wire switching, generating two more negative monopoles at the SL1-SL2 junction before SL1 saturates within the sampled area.

This process was repeated along the SL2 wire layer with switching beginning at a lower $6.75\ mT$ field. Monopoles appear in pairs of $\pm 2q$, with additional field increments creating more monopoles, some of which move along the SL2 nanowires or exit the measured area.

The paper then notes the distinctions of emergence of monopoles on SL1 and SL2 sub-lattices. An external field component along SL1 prompts a few isolated magnetic charges within a narrow field window ($8.0 - 10.5\ mT$). These "uncorrelated magnetic charges" appear to exist without identifiable anti-monopole partners in the measured region, resulting in a local charge while maintaining an overall lattice neutrality. Notably bipod structures exhibit a lack of magnetic charge. On the contrary, SL2 switching produces a greater number of correlated pairs, producing nearly equal positive and negative magnetic charges. This process sustains a net charge close to zero across a wider field range ($6.5 - 10.75\ mT$), starting at a lower field strength ($6.5\ mT$) compared to SL1's behavior.

Micromagnetic simulations were utilized to gain early understanding into the dissimilar switching mechanisms of SL1 and SL2. These simulations highlighted a substantial disparity in the energy needed to form a magnetic charge on bipod vertices, a key result. To test for consistency, energies obtained from these micro-magnetic simulations were integrated into Monte Carlo simulations. These Monte Carlo simulations factored in surface energetic influences (α) and fabrication-related disorder (d_i), aligning with observed experimental behavior.

Simulations with enhanced surface energetics ($\alpha = 6.4$) for specific field directions demonstrated closer alignment with experimental data, notably in the scarcity of charges on surface coordination two vertices. The simulations provided valuable insights into the behaviour of magnetic charges within the 3D ASI system, offering valuable qualitative agreement with experimental findings.

The 3D ASI has two main possible means to demagnetise, as it through zero field in a hysteresis loop. Firstly, local demagnetisation on each vertex leads to the formation of monopole-antimonopole pairs, effectively neutralizing the magnetisation on the relevant sub-lattice. In addition, demagnetisation can take place via the formation of alternating

magnetisation stripes on a particular sub-lattice, exhibiting magnetic charges solely at the ends of these stripes.

The paper then defined the monopole effective chemical potential (μ^*), which quantifies the extent to which a monopole pair remains correlated after nucleation:

$$\mu^* = \frac{\mu}{u} \tag{107}$$

Where μ is the chemical potential and u is the magnetic coulomb energy given by:

$$u = \frac{\mu_0 Q^2}{4\pi a} \tag{108}$$

When a single spin-flip occurs on a coordination four vertex, the calculation yields μ^* as 1.03. The distribution of magnetic charges, especially on coordination two vertices, is impacted by surface energetics and consequently, the effective chemical potential for creating a monopole on an SL1 coordination two vertex rises to $\mu^* = 1.22$, resulting in a greater proportion of uncorrelated monopoles.

In summary, the fabrication process of the 3D ASI system revealed distinct demagnetisation behaviours along different axes, driven by variations in the effective chemical potential and energy landscapes during the dynamics of monopoles. This research serves as a catalyst for further exploration of artificial spin-ice systems, particularly in understanding the ground states in 3D geometries and exploring potential applications. Leveraging comprehensive magnetic imaging techniques promises significant strides in characterizing both bulk and surface properties of these systems.

2.2 Thesis Goals and Objectives

The work done in this thesis aims to advance the understanding and development of 3D ASI's building upon the previous work conducted by the Cardiff research group. The main focuses of this thesis lie in measuring bulk demagnetised systems and employing novel measurement

techniques (X-ray microscopy) to explore and characterise the behaviours in these 3D ASI structures. Using state-of-the-art fabrication and measurement techniques, the boundaries of what can be measured and understood in these 3D ASI systems will be advanced.

Specifically, this thesis goals encompass several key areas. First, development and refinement of methodologies using two-photon lithography and thermal evaporation to fabricate high-quality 3D ASI structures. This includes fabrication of structures previously produced by the Cardiff research group for extensive measurement using surface level techniques like MFM, but also development of new structures suspended over an aperture for measurement with x-ray microscopy.

Secondly, after fabrication of a bulk structure, this thesis will utilise demagnetisation routines to reach the ground state of the 3D ASI system and the measured ground state will then be compared with predictions from Monte Carlo simulations. Experimental measurements of the system will be achieved by improved MFM techniques which will be used to explore and document the magnetic phase diagram of the 3D ASI structures, identifying and analysing new vertex types and comparing these findings with micromagnetic simulations.

Furthermore, this thesis will aim to measure the suspended structures using synchrotron microscopy and identify magnetic contrast using the x-ray magnetic circular dichroism (XMCD) technique. Fabrication methods will be refined based on the results of initial studies to improve measurement accuracy and reliability.

In advancing the field, this thesis aims to provide a greater understanding of the magnetic configurations within the 3D ASI systems through extensive MFM and synchrotron measurements. By doing so, the capabilities of two-photon lithography in producing complex 3D nanostructures will be demonstrated. Furthermore, emergent behaviours in 3D ASI systems will be enhanced by the improved magnetic characterisation techniques. This will contribute to the wider field of research and set the stage for future research avenues and innovations in 3D nanomagnetic materials.

3 Experimental Techniques

This chapter details the methods used to create and characterise the magnetic nanostructures studied in this project. With respect to fabrication and processing, three techniques were used: two-photon lithography (TPL), thermal evaporation and oxygen plasma exposure. The main methods for measuring the structures were atomic and magnetic force microscopy, scanning electron microscopy, optical magnetometry and soft x-ray microscopy.

The chapter begins by detailing the two-photon lithography methodology, followed by an exploration of thermal evaporation and oxygen plasma exposure, mirroring the fabrication and processing workflow. Subsequent sections delve into the suite of measurement techniques crucial to this project, such as atomic/magnetic force microscopy, scanning electron microscopy, optical magnetometry, and x-ray microscopy. Finally, the micromagnetic simulations will be detailed.

3.1 Fabrication Techniques

3.1.1 Two Photon Lithography

Traditional lithographic methods have been employed for many years, typically generating 2D devices with features spanning micrometre scales using standard UV lithography. In industrial applications, extreme UV lithography achieves nano-scale precision [44]. The most common method combines the use of a custom engineered photomask, a photoresist with single-photon lithography (SPL, discussed in Section 1.6.1) as the mechanism used for polymerisation or depolymerisation of the resist. The photoresist is first coated across the substrate to be patterned, the mask overlaid atop, and then the sample is exposed to a UV light source. The mask is commonly made from a mixture of a UV opaque material, i.e. – silver halide, chromium, etc., and a transparent material such as quartz crystal. This prevents resist exposure to the UV light over desired regions and following development of the resist through a post processing chemical development procedure the desired pattern of solid resist is produced. Whether a positive-tone or negative-tone resist is used determines which portions of the resist are solidified, see **Figure 28**.

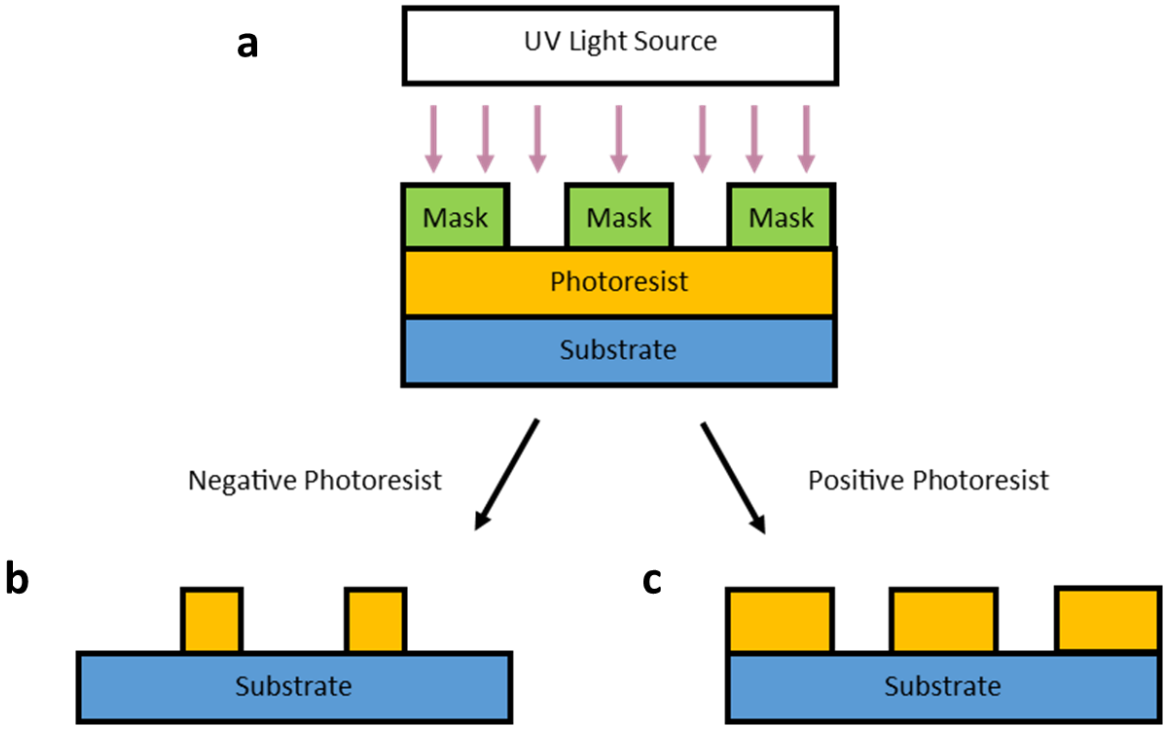

Figure 28: *Diagram of standard lithography techniques comparing positive and negative photoresist.* ***(a)*** *A photoresist coated substrate is exposed to a UV light source through a mask or pattern, initiating a chemical change in the exposed areas of the photoresist. The substrate undergoes a development process which removes exposed or unexposed parts of the photoresist depending on whether* ***(b)*** *negative or* ***(c)*** *positive resist is used.*

When a positive-tone resist is used it is commonly spin-coated onto the substrate and then heated through a soft bake process to produce a hardened uniform coating. When exposed to the UV source the regions of resist exposed become soluble to the development process and are washed away. When a negative-tone resist is used the exposed regions are solidified in a polymerisation process that is insoluble to the development process. This polymerisation process is discussed in Section 1.6.1. Unexposed regions of the negative-tone resist are washed away during the development process. Overall, photolithography is an excellent technique for the fabrication of 2D patterned structures, with custom masks allowing a range of designs that can be made repeatedly and combined with deposition techniques to produce simple 2D structures.

Standard photolithography's limitation stems from the isotropic blanket nature of the UV source, which uniformly exposes uncovered regions following a line-of-sight principle. While

this enables variability along the z-axis for structures, achieving intricate 3D shapes across multiple axes proves challenging within this method. [44, 45].

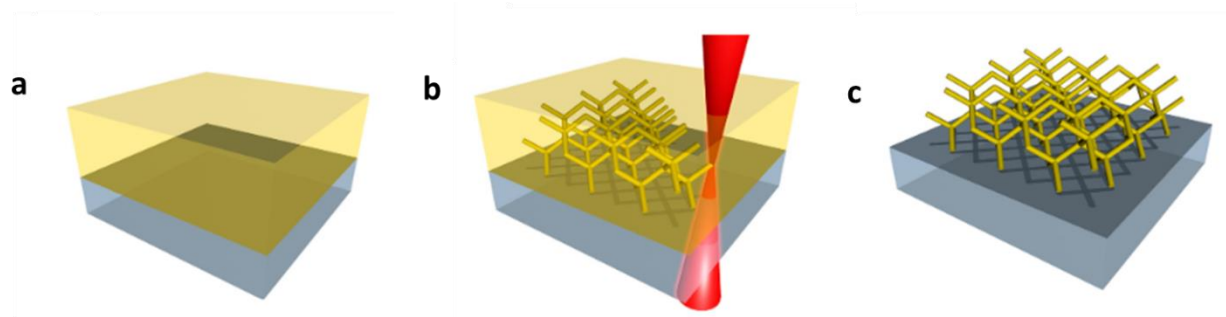

***Figure 29**: TPL writing process. **(a)** Negative-tone resist droplet atop opaque silicon substrate. **(b)** Laser writes out described structure. **(c)** Subsequent development washes away unused resist leaving desired structures [42].*

Two-Photon Lithography (TPL) is a technique employing a femtosecond laser that generates a high flux of photons densely concentrated within a tightly shaped voxel. This technique, distinct from OPA, operates via two-photon polymerisation (TPP), a process triggered by the localized absorption of two photons simultaneously, inducing polymerisation within the voxel region. By confining the polymerisation or depolymerisation process within a tightly controlled voxel, the necessity for a photomask is eliminated. The precise manipulation of this voxel in all three dimensions facilitates the fabrication of complex 3D geometries. See Figure 29 for a visual representation of the TPL writing process.

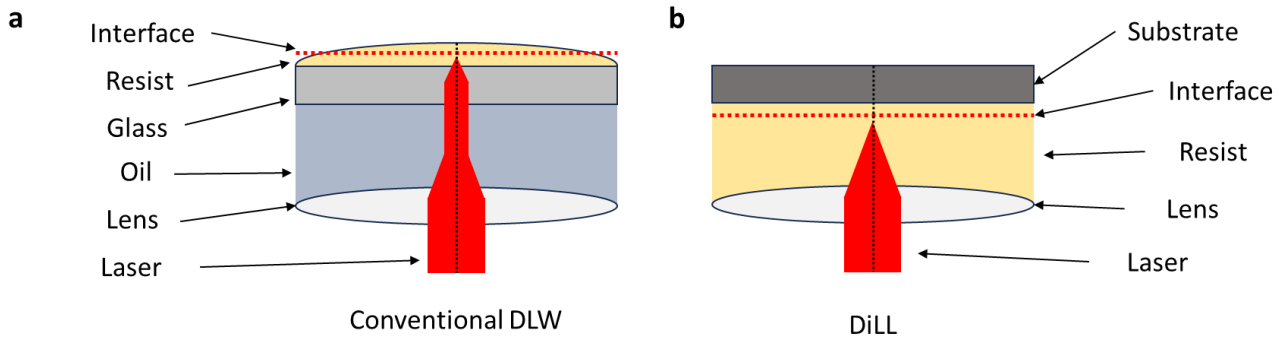

***Figure 30**: Illustration of TPL configurations. **(a)** In conventional DLW the laser passes through an index matched oil and then the glass to focus onto the glass substrate surface within the resist. **(b)** In DiLL the laser focuses through an index matched resist onto the substrate surface.*

The primary focus of this project has been crafting polymer scaffolds across an aperture on a silicon substrate using dip in laser lithography (DiLL). An alternate TPL configuration used in this thesis is conventional direct laser writing (DLW). Comparison of the printing setups for DiLL and DLW is depicted in Figure 30.

In the conventional TPL employed by most of the research group [34, 42, 43, 46, 47], specifically using the DLW configuration, the laser beam is directed through the glass substrate into the photoresist. This setup necessitates the use of immersion oil between the microscope objective and the substrate to achieve an optimal focus at the substrate/resist interface. However, as the laser delves deeper into the resist to create taller structures, the focus quality diminishes due to spherical aberrations. The maximum attainable height of the structure is limited by both the working distance of the microscope objective and the thickness of the substrate.

In the DiLL configuration the microscope objective is directly immersed into the photoresist, see Figure 30. This arrangement ensures minimal and consistent spherical aberrations across the entire printing range. Unlike other configurations, there are no interfaces that impose limitations on the height of the structures. The maximum achievable height is solely restricted by the capabilities of the sample holder and can potentially exceed 2 millimetres [48]. This configuration is employed specifically for printing on opaque substrates, such as the apertures featured in this thesis.

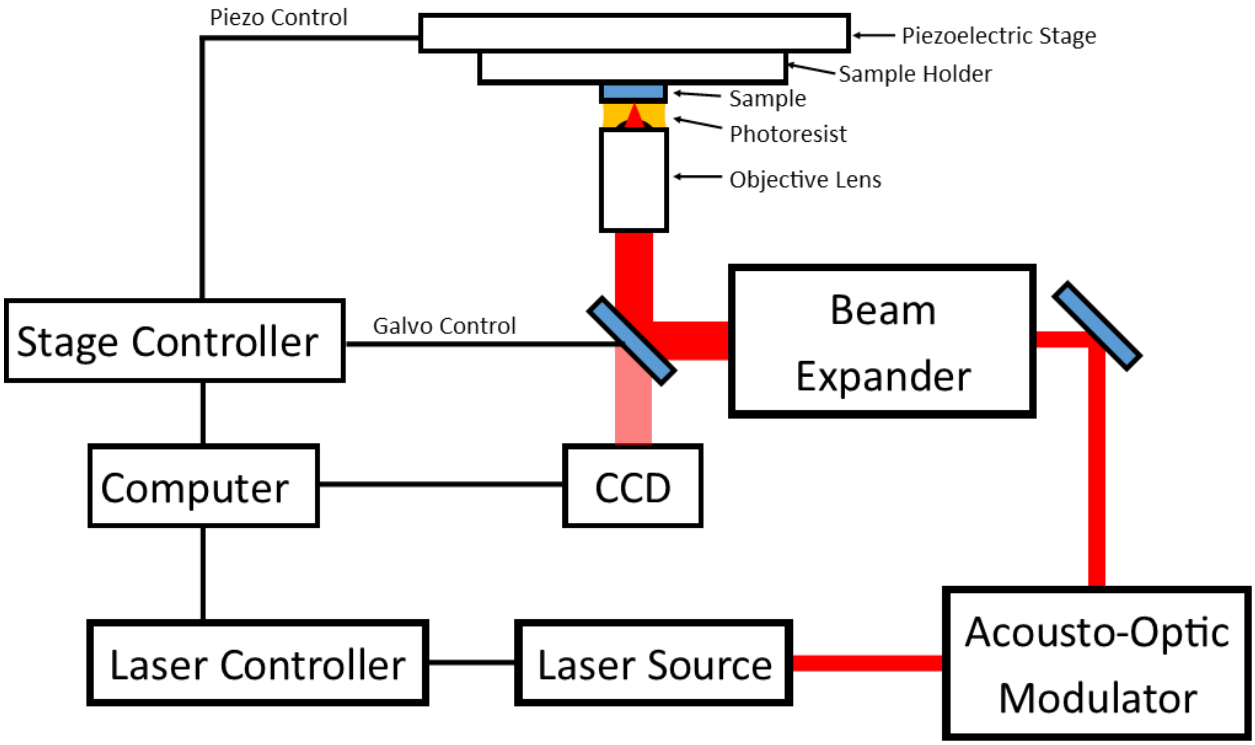

Figure 31: *Nanoscribe Photonic Professional GT Schematic displaying the path of laser beam and control units for stage and laser.*

In this section the configuration of the Nanoscribe Photonic Professional GT device used throughout this thesis will be explained along with the path the laser takes to ultimately write a structure on the substrate surface, see **Figure 31**. The Nanoscribe Photonic Professional GT is equipped with a pulsed femto-second fibre laser source with a central wavelength of $780\ nm$ [48]. The laser power commonly ranges from $50 - 150\ mW$ with a pulse length between $100\ fs - 200\ fs$. The laser has a repetition rate of $80\ Mhz$ and can reach a peak power of $25\ kW$. The generated laser is first passed through an acousto-optic modulator (AOM) which modulates the power of the laser beam. The laser then passes through a beam expander and is focused through an inverted microscope equipped with a high numerical aperture objective lens $(NA = 1.4)$. The focused beam, now directed into the resist, has a beam waist of $113\ nm$, calculated using Equation (99), resulting in a spot diameter of approximately $226\ nm$ at the focus.

Before fabrication can occur, a geometry is designed. This is frequently done within the software DeScribe, which is offered alongside the Nanoscribe TPL system [48]. DeScribe is the

General Writing Language (GWL) editor developed by Nanoscribe specifically for laser lithography usage. It contains an inbuilt debugger and pre-visualization of the structure.

Regarding stage parameters, there are two options available for the scanning mode used by the Nanoscribe. These are the Galvo Scan Mode (GSM) and Piezo Scan Mode (PSM).

In GSM, the stage remains fixed, and the beam is scanned across the substrate using mirrors on the beam optical path rapidly moving the voxel across a 2D plane whilst z-axis movement is fixed. For each of these planes, DeScribe computes the intersection contours of the structure with the plane and fills each obtained contour with a line hatch [48]. During writing, the laser voxel will provide a polymerisation dose along these line hatches and so to yield a solid structure. The slicing thickness and line hatch distances must be carefully selected by the user. Typically, when the slicing and hatching distances are decreased, a higher-quality structure is achieved. This is because increasing the number of line hatches enhances the fidelity of the original CAD design. Moreover, by fine-tuning fabrication settings to lower the polymerisation dose applied, you can create structures with finer resolution compared to PSM.

After a layer is complete, the stage shifts along the z-axis and the next layer is written, resulting in a stack of completed layers that produce a 3D structure. This scanning process is rapid with a voxel scan speed of tens of cm/s commonly being used. The maximum galvo scan region is a disc of approximately $200\ \mu m$ in diameter with a height of $300\ \mu m$ [48]. Structures produced using the galvo scan mode are restricted however to this layer-by-layer approach and cannot be scanned along the z-direction. For most structure designs this is a non-issue however when scanning in all three dimensions is required the PSM can be used.

In contrast to galvo systems, PSM operates using a fixed beam and a mobile stage. Here, the laser concentrates on a single point, and the piezoelectric-controlled stage moves around this laser voxel, continuously creating polymerized material. This method naturally increases the polymerisation dose but guarantees the formation of connected structures. Scan speeds for this mode are drastically reduced compared to Galvo scan mode with speeds of $20 - 300\ \mu m s^{-1}$ commonly being used. The maximum piezo scan region is a cuboid of dimensions $300\ \mu m\ x\ 300\ \mu m\ x\ 300\ \mu m$ and the Nanoscribe manual describes the piezo scan mode as

being able to produce high resolution structures with a 10 nm positioning accuracy in comparison to galvo scan mode structures. Throughout this project both piezo and galvo scan modes were used dependent on the requirements of the produced geometry.

The following section will explain the process of conventional DLW, the most commonly used methodology used with the Nanoscribe TPL. Then an explanation of the methodology used with DiLL will be provided.

For DLW the substrates used are $22\,mm \times 22\,mm$ glass coverslips (Fisher Scientific, thickness $0.16\,mm - 0.19\,mm$). These slides undergo a standard cleaning procedure: initial washing with water to remove larger debris followed by wiping with an acetone-soaked laboratory cloth to minimize any remaining debris. These are then cleaned by submersion in acetone and subjected to an ultrasonic bath for fifteen minutes. After this slides are then submerged in isopropyl alcohol (IPA), then placed into the ultrasonic bath for a further fifteen minutes. They are then dried using compressed air and loaded into the Nanoscribe slide holder.

Once the slides are securely positioned, a droplet of immersion oil (Zeiss Immersol 518F) is placed on the central region of each glass slide. It's important to avoid air bubbles during this process; any bubbles observed are agitated using a plastic spatula from the immersion oil bottle until none remain. Similarly, on the reverse side of the glass slides, a droplet of photoresist (Nanoscribe's IP-L 780 photoresist [48]) is carefully deposited in the same region as the oil using a pipette, ensuring the absence of air bubbles by thorough inspection and removal.

The sample holder is then loaded into the Nanoscribe system, and the lens surface is carefully brought into contact with the oil on a single slide. An automated procedure that locates the upper interface between the glass slide and the resist is then used. Focusing through the oil minimizes and maintains consistent spherical aberrations throughout the entire printing process. Specifically designed index-matched photoresists compatible with DLW for Nanoscribe hardware are utilised.

Through adapting the GWL code for fabrication, the laser power, scan speed and stage velocity are specified. These parameters must be optimised to produce an accurate reproduction of the geometric design, and this can be done with a dose array. A dose array is where a series of repeated structures are written onto a substrate surface with a range of laser and sometimes stage parameters used for each structure. This is regularly done when creating a geometry for a first time, since optimal parameters for one design may not translate to those required by another. By varying the laser power and scan speed used throughout the dose array the ideal parameters for the design can be found by inspection using subsequent optical microscopy and scanning electron microscopy.

The process starts by loading the GWL code for writing into the Nanoscribe software and initiating the job. Through coding, the number of samples to be written can be specified, enabling an automated procedure. The objective lens retracts, moves to a new sample, aligns itself, finds the interface, and proceeds with the fabrication without requiring user interaction.

Once all the samples are fabricated, the objective lens retracts, and the samples are taken out from the Nanoscribe. Carefully removing them from the Nanoscribe sample holder, they are then immersed in a developer solution of propylene glycol mether acetate (PGMEA-$C_6H_{12}O_3$). The development of IP-L 780 is 20 minutes [48]. Keeping structures in the developer for a longer time is possible without changing the structure properties significantly. Typically, throughout this thesis samples were left in developer for 12 hours.

After the photoresist development, the samples are submerged in IPA to remove excess photoresist and developer. Subsequently, they are meticulously dried using a compressed nitrogen air gun and stored individually in sample boxes within a desiccator.

What follows is the sample fabrication for DiLL onto a silicon substrate using a negative-tone photoresist (IP-DIP) followed by an explanation of procedures for sample fabrication for conventional DLW onto a glass coverslip.

The initial step involves cleaning circular glass coverslips ($30\ mm$ in diameter, with a thickness ranging from $0.13 - 0.18\ mm$). These coverslips are cleaned in a similar manner to DLW. Simultaneously, silicon substrates slated for writing undergo a similar cleaning process.

To prepare a sample for DiLL, first a circular slide and silicon substrate are removed from IPA and thoroughly dried using a compressed air gun. The silicon substrate then adhered to the slide using GE varnish, a semi-permanent general-purpose adhesive which maintains properties down to cryogenic temperatures.

For DiLL, only one sample can be loaded at a time in the DiLL specific sample holder. This is a limiting factor in the speed of production of samples fabricated using DiLL. After secured in the holder, a droplet of IP-DIP photoresist is placed onto the silicon substrate surface using the provided IP-DIP bottle plastic spatula to agitate any bubbles that may be observed. Throughout this project, Silson TEM aperture silicon chips were utilised ($5\ mm\ \times\ 5\ mm$, $200\ \mu m$ thick, $50\ \times\ 50\ \mu m$ aperture). When applying resist to the aperture chips, care must be taken to remove any trapped air from the aperture region by agitation using spatula and examination with a magnifying glass. If a bubble is released into the aperture after loading the sample, the sample must be unloaded, and bubble removed before fabrication over the aperture can take place.

Once prepared the sample holder can be loaded appropriately into the TPL system and the objective lens brought into contact and focus within the resist, see ***Figure 30***. The previously loaded GWL file directs the movement of the stage to locate the writing position using either the provided stage controllers or inputting specific codes. Precise positioning of the written structure holds significant importance, especially when covering the corners of apertures. To ensure accuracy, reference structures are initially written on the substrate surface away from the aperture. These serve to delineate the region within the camera view where the system will generate the structure. This delineated area is then aligned precisely over the aperture corner before executing the writing of the intended structure.

Following writing of structures, the lens is lowered away from the sample and extracted. The tape securing the sample in place is removed and the glass-substrate sample is submerged in a petri dish containing propylene glycol mether acetate (PGMEA) for a minimum of twenty

minutes. Throughout this project, samples were left in this PGMEA solution overnight (16 hours) as this was found to guarantee development of all samples.

After this, the PGMEA was pipetted out of the petri dish and replaced with an equal amount of IPA. Whilst in IPA, samples were mechanically stabilized by an additional ultraviolet (UV) exposure [49]. The IPA is replaced three times, being careful not to reduce the amount of liquid in the dish to a height lower than the substrate uppermost surface. Care is also taken to withdraw and replace the liquids away from the samples within the petri dish to avoid disturbing the structures. Replacing the PGMEA with IPA in this manner minimizes damage to written structures from surface tension and stiction effects when removing from the dish of developer to a dish of IPA [49]. The purpose of submergence in IPA is two-fold, first the PGMEA leaves behind a residue that is diluted by the IPA, second the IPA loosens the GEVarnish adhering the substrate to the slide such that it can be moved off the slide using tweezers.

Samples are commonly deposited with magnetic material after production, this requires them to be mounted on square slides that are accepted by the evaporator holder hence the removal from circular slides. After removal from the circular slide the silicon substrate are left in IPA for a further ten minutes before removal and dried with a compressed air gun. They are then kept secure within clean sample boxes within a desiccator until required for further fabrication processes or examination.

3.1.2 Thermal Evaporation

Following completion of the TPL writing process a deposition technique is required to coat the structures with a magnetic material to produce the magnetic nanostructures. Several options are available but for this project thermal evaporation is used due to simplicity. It has been used for decades and can repeatedly deposit ultra-high purity magnetic films comparable to previous work. The main evaporator used in this project is situated in a separate lab class 1000 clean room, a schematic of the evaporator setup used is shown in **Figure 32**.

Prior to evaporation onto the samples, they must first be mounted, if required, onto cleaned square glass coverslips ($22\ mm\ \times\ 22\ mm\ \times\ 0.2\ mm$). For silicon substrate samples this is achieved by removal from the circular coverslips during the development procedures outlined in Section 3.1.1, followed by subsequent re-adhesion to a cleaned square glass coverslip with GEVarnish.

For permalloy ($Ni_{81}Fe_{19}$), the most deposited material for this project, a Tungsten evaporation boat with an alumina coating is used. If a tri-layer is to be deposited, then other metals can be loaded onto the carousel-like setup within the evaporator with appropriately chosen boats.

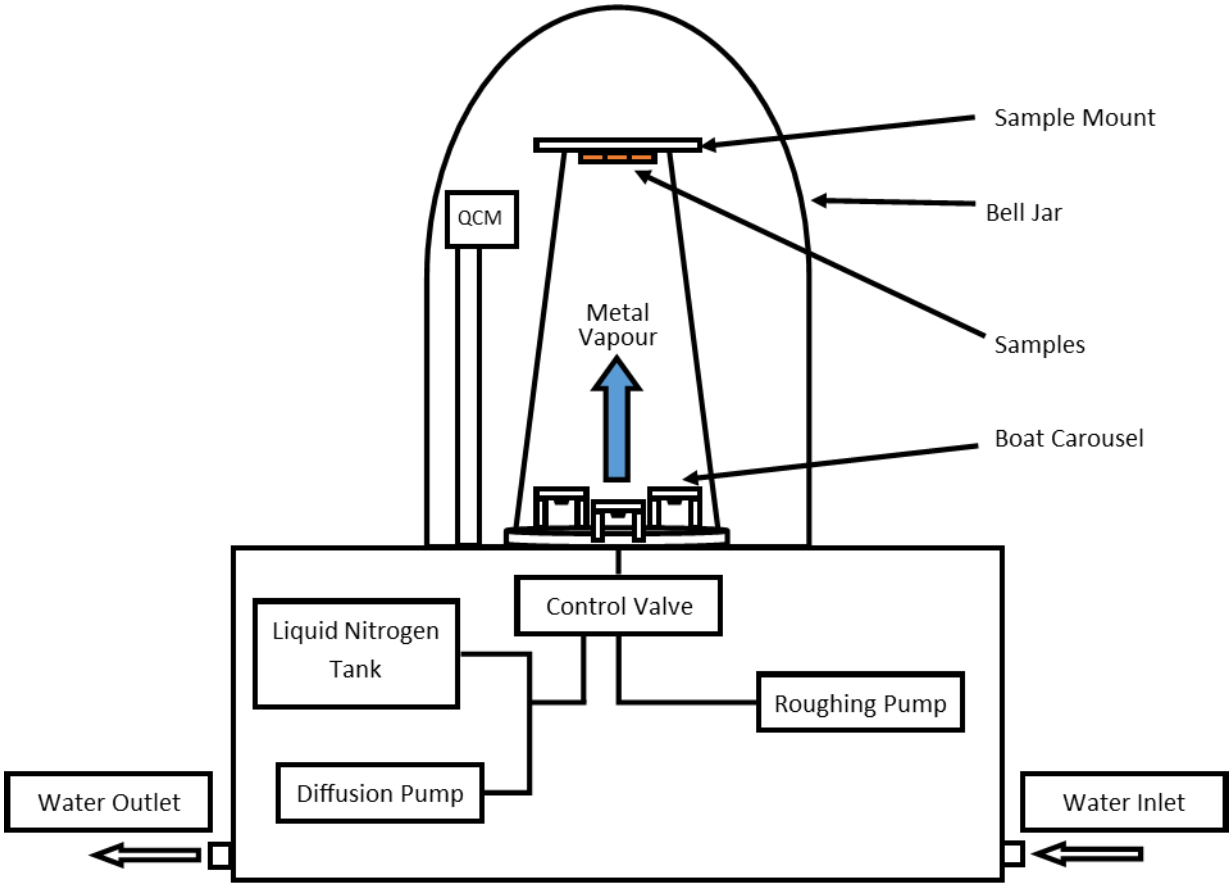

Figure 32: *Schematic of principle components of a thermal evaporator used in this project. A carousel of evaporator boats held by electrodes contains the metal to be deposited directly below the sample mount. The quartz crystal monitor (QCM) is placed such that it can detect evaporated material without blocking flow. All is contained within a glass bell jar which contains the vacuum created by a series of pumps and a nitrogen tank located below. Water cooling is constant during operation.*

Samples are mounted positioned directly above the boat atop a metallic platform with space available for evaporated metal to reach the samples. The distance between the sample and boat is approximately $28.5\ cm$. The setup is brought to vacuum within a bell jar to a pressure 1×10^{-7} mBarr before evaporation begins.

Boats are increased in temperature slowly to reduce boat fracturing and after the metal has melted and begun evaporation the shutter is opened and line of sight deposition of the metal onto the samples begins. This process is normally isotropic across all samples within a given position and the rate of deposition is measured throughout evaporation by a quartz crystal monitor (QCM).

A tri-layer evaporation was commonly used throughout this project to cap the permalloy magnetic material within a protective layer of aluminium. An example of common thicknesses of this are $Al\ (3\ nm)/Py\ (40\ nm)/Al\ (3\ nm)$,. This was achieved by loading both aluminium and permalloy into respective boats within the evaporator before pumping down to appropriate vacuum pressure. Aluminium was deposited first, using the shutter to deposit a specific thickness, before rotating the carousel such that the permalloy boat was connected to the active electrode. All permalloy within the boat is then evaporated and then the carousel is switched back to the aluminium boat for a final capping layer. Care is taken increasing the current for the aluminium boat as these tend to crack and require replacement often. This is due to aluminium tendency to alloy with refractory metals causing cracks in the boat.

When evaporating an alloy, such as permalloy, all the metal contained within the boat must be evaporated. This is due to the constituent elements (nickel and iron) having different melting points. If a remnant is left in the boat, the remaining material may not have the same nickel-to-iron ratio as the original permalloy, leading to a non-stoichiometric composition. Consequently, the deposition would also not have the exact proportion of nickel and iron as intended. To deposit a required thickness for an alloy a calibrated weight vs thickness is used. For this project it is known from previous studies [42] that using 0.06 grams of permalloy generally results in a deposited thickness of 40-50 nm. This is not the case for a pure element to be evaporated, such as aluminium. For pure elements, specific thickness to be deposited can be controlled by opening and closing the shutter once the required thickness has been deposited.

3.1.3 Oxygen Plasma Exposure

Oxygen plasma exposure serves as a crucial process in material science and microfabrication, altering the surfaces of various materials. Its applications range from fabricating microelectronic devices to modifying biomedical materials and enhancing adhesion in polymers [50]. This process relies on energetic oxygen species (ions, radicals, and excited particles) generated within the plasma, interacting with material surfaces.

In this thesis, oxygen plasma exposure is employed to interact with the polymer scaffold underlying the deposited metal layer. The primary purpose of this process is to remove the polymer, thereby decreasing the overall thickness of the wires. This reduction in thickness is essential for enhancing the transmission of x-rays during x-ray microscopy. By effectively thinning the polymer layer, the x-ray penetration improves, leading to better imaging quality and more accurate measurements.

The generation of oxygen plasma involves subjecting a mixture of oxygen and an inert gas, like argon, to high-power radio waves ($50\ kHz$). This ionizes the gas, forming a plasma consisting of oxygen ions, electrons, and neutral species. These energetic oxygen species then engage with the material surface, initiating chemical reactions and physical changes such as etching, cleaning, and surface activation. These alterations modify the surface's chemical and physical properties, enhancing its reactivity and making it more amenable to further chemical modification.

In the context of this thesis, oxygen plasma interacts with the cross-linked monomers within the negative tone photoresist used to create the 3D scaffolds in the ASI design. The plasma ions break apart the cross-linked monomers in an energetic reaction combusting the resist. The resulting radical species from this reaction combine with O_2 molecules, forming water and CO_2, which are removed from the sample chamber [50].

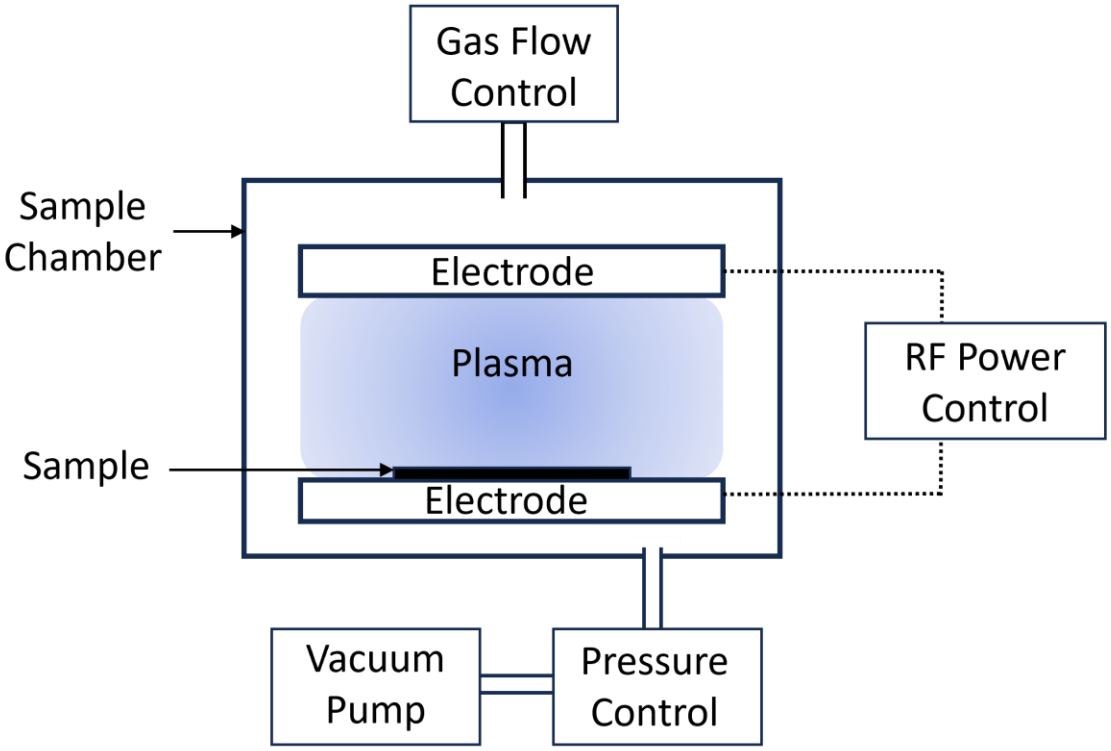

Figure 33: *Schematic of the setup for oxygen plasma exposure. A sample chamber containing two electrodes with a sample stage between the two can be brought to a low pressure by a vacuum pump and a plasma formed through gas flow and an RF power source.*

The conditions of the plasma exposure, such as the power, pressure, and duration of the exposure, can be controlled to optimize the surface modification for a specific application. For example, increasing the power or decreasing the pressure can increase the energy of the oxygen species, leading to more aggressive etching.

The equipment used during fabrication of samples is an Inseto, Venus Series. A schematic diagram of the setup for oxygen plasma exposure is shown in **Figure 33**. A sample chamber containing two electrodes controlled by an external RF power control is brought to low pressure by a connected vacuum pump. Samples are placed between the two electrodes on a stage about which the plasma forms. Gas flow rate, RF power and timings of exposure are controlled through a computer with bespoke programmed software. The applied settings were a fixed radio-frequency power of $60\ W$ at an oxygen flow rate of $30\ SCCM$. Using these standardised settings samples were subjected to varied amount of time within the pressurised chamber to achieve varied levels of carbonisation of the polymer scaffold.

Samples produced on silicon via dip-in writing methodology were commonly adhered to a glass slide during this exposure using GE Varnish as the adhesive. After the oxygen plasma exposure, the GE Varnish cures and hardens due to the heat. However, in preparation for submission to synchrotrons, the sample required detaching the substrate from the glass slide mount. This presents challenges and multiple methods were attempted, initially using acetone and IPA to soften the GE Varnish bonds. Subsequently a scalpel was employed to separate the substrate from the glass slide mount.

During this procedure, it was observed that the IPA and acetone caused the GE varnish to flow beneath the sample and up through the aperture, resulting in damage to the lattices. In later attempts, a more cautious approach was taken, involving the careful use of a scalpel to gradually detach the samples from the glass slides. This method was executed slowly to prevent both breakage of the glass slide beneath the GE Varnish and the introduction of GE varnish chips into the aperture region of the sample.

3.2 Measurement Techniques

3.2.1 Atomic Force Microscopy

Atomic Force Microscopy (AFM) is a powerful method for analysing samples at a nanometre scale. In this thesis, the hardware utilized is Bruker's Dimension Icon, positioned on an air-cushioned table, offering high precision in measurements.

The AFM process begins with selecting a suitable probe. Throughout this study, the “Nano-sensors Super Sharp-Magnetic Force Microscopy - Reflex Coating probe” (SSS-MFMR) was predominantly used [51]. Specifically designed for high-resolution magnetic force imaging this probe, under ideal conditions, offers resolution down to $20\,mm$. Its thin hard magnetic coating provides it with a low magnetic moment $(0.25 \times 10^{-13}\,emu)$, making it highly sensitive for detecting magnetic forces in Magnetic Force Microscopy (MFM). This versatile tip can also perform AFM measurements concurrently with MFM.

AFM relies on understanding the interaction between the AFM tip and the sample surface. This can be conceptualised using the Lennard-Jones potential $V(r)$, a model in molecular

physics that elucidates the energy dynamics between neutral atoms or molecules. It can be expressed as:

$$V(r) = 4\epsilon \left[\left(\frac{\sigma}{r}\right)^{12} - \left(\frac{\sigma}{r}\right)^{6} \right] \quad (109)$$

Where $V(r)$ represents the potential energy between the AFM tip and the sample surface at a given distance r, ϵ signifies the depth of the potential energy well, indicating the strength of interaction, σ denotes the distance at which the potential energy is equal to zero.

AFM modes of operation: contact, non-contact and tapping, rely on principles encompassed within the Lennard-Jones potential, where distinct operational regimes govern the interaction between the AFM tip and the sample surface.

In contact mode, the AFM tip remains in constant physical contact with the sample surface during scanning. The tip-sample interaction, akin to the repulsive regime of the Lennard-Jones potential, maintains a constant force between the probe and the sample. This mode is suitable for harder sample materials, preventing sample damage while detecting surface topography through cantilever deflection and laser beam reflection.

Conversely, non-contact mode operates within the attractive regime of the Lennard-Jones potential. The AFM tip is held at a distance above the sample surface, minimising direct contact. Weak van der Waals forces induce variations in amplitude, frequency and phase of the oscillating cantilever, enabling measurement of softer materials' topography. However, due to the weak forces there's a resolution trade-off in non-contact mode AFM.

Tapping mode utilises aspects of both attractive and repulsive regimes. The tip oscillates at its resonant frequency, periodically contacting the surface during the peak of oscillation. This intermittent contact minimises sample damage whilst preserving resolution, adjusting tip-sample distance based on the feedback loop's detection of surface interaction.

Throughout this thesis tapping mode is primarily used and optimising AFM parameters is crucial for efficiently capturing high-quality images of the sample surface while minimizing

sample damage. However, a common challenge in this optimisation is tip strike, occurring when the cantilever forcefully contacts the surface, potentially damaging both the sample and the probe. This is evident in the produced image as a bright line along the fast-scan axis and can render the tip unusable. Tip strike is less frequent in 2D samples but can occur with steep z-direction changes. In contrast, it's more common in 3D samples with varied topography, like the samples measured in this thesis. Another issue arises when measuring tall features; as the probe scans along the fast-scan axis, it slants upwards when encountering a tall feature. This motion can distort and blur the measured feature, resulting in an inaccurate representation of the surface topography. Despite these challenges, AFM finds extensive use across diverse fields and often complements secondary techniques like electric force microscopy and magnetic force microscopy.

3.2.2 Magnetic Force Microscopy

Magnetic Force Microscopy (MFM) is a technique utilized alongside AFM, enabling simultaneous collection of magnetic configuration and surface topography data of a sample. Operating within scanning probe microscopy, MFM employs a magnetic tip to map a sample's magnetic properties. This technique measures the interaction between the magnetic probe tip and the sample, generating a detectable force used to create an image reflecting the sample's magnetic characteristics.

The of magnitude of the force upon the tip can be written as:

$$\boldsymbol{F} = \mu_0(\boldsymbol{\mu} \,.\, \nabla)\boldsymbol{H} \qquad (110)$$

Here $\boldsymbol{F}$ is the force, μ_0 is the magnetic permeability of free space, $\boldsymbol{\mu}$ is the magnetic moment of the tip and $\boldsymbol{H}$ is the magnetic stray field above the sample surface. The energy of interaction between the tip and the sample can be described by [1]:

$$E_{int} = -\int_{V_{tip}} \mu_0 \boldsymbol{M}_{tip} \cdot \boldsymbol{H}_{sample} dV = -\int_{V_{tip}} \mu_0 \boldsymbol{M}_{sample} \cdot \boldsymbol{H}_{tip} dV \quad (111)$$

Where E_{int} is the energy of interaction, $\boldsymbol{M}_{tip}$ and $\boldsymbol{M}_{sample}$ are the tip and sample magnetisations respectively, $\boldsymbol{H}_{tip}$ and $\boldsymbol{H}_{sample}$ are the stray magnetic fields of the tip and sample respectively. The tip and sample volumes are described by V_{tip} and V_{sample}.

Magnetic Force Microscopy begins with the selection and preparation of an appropriate probe tip for the sample to be measured. For measurement of samples throughout this thesis a Nano-sensors Super Sharp-Magnetic Force Microscopy - Reflex Coating probe is used. This probe is chosen as the magnetic moment of the probe is great enough that $\boldsymbol{M}_{tip}$ is not reversed by $\boldsymbol{H}_{sample}$ and the moment is low enough that $\boldsymbol{H}_{tip}$ does not influence $\boldsymbol{M}_{sample}$ This probe is prepared for MFM by bringing into close contact with a permanent magnet of high field strength ($\sim 80\ mT$) such that the probe is magnetised parallel or anti-parallel with the tip axis. This direction of magnetisation is recorded.

During MFM imaging, the interaction between the sample and the probe tip causes the cantilever to deflect. The direction of deflection depends on whether the probe was magnetized parallel or anti-parallel with the tip axis. This interaction alters the spring constant of the cantilever, described by [1]:

$$k - k_0 = \frac{\delta F}{\delta z} \approx \Delta\phi \quad (112)$$

Where k represents the changed spring constant, k_0 denotes the initial spring constant at rest, and $\frac{\delta F}{\delta z}$ represents the force gradient experienced by the probe. The phase shift ($\Delta\phi$) detected in MFM is proportional to the change in spring constant ($k - k_0$) as expressed in Equation (112). The force gradient experienced by the probe is associated with the magnetic field (H_z) as the probe interacts with the sample, as described by Equation (110), therefore combining these relationships [52]:

$$\Delta\phi = \frac{\delta F}{\delta z} \propto \frac{\delta^2 H_z}{\delta z^2} \quad (113)$$

Hence the phase shift detected by MFM is proportional to the second derivative of the vertical component of the magnetic field (H_z) with respect to the vertical distance from the sample (z). This change in phase is detected and utilised to generate an image depicting the magnetic properties of the sample.

Avoiding close contact with the sample during the MFM pass is crucial to prevent non-magnetic interactions that might produce artefacts in the image. Thus, maintaining a constant lift height (approximately $80 - 100\ nm$) above the sample is essential. However, before commencing MFM measurements, accurate sample topography measurements via AFM are necessary to sustain this consistent lift height throughout the process. While increasing the lift height can reduce the chances of tip-strike (common in 3D samples), it decreases MFM resolution [53]. Striking a balance between these considerations is vital for optimal results.

The process of conducting an MFM scan involves multiple steps. After preparing the probe, mounting it, adjusting the laser, and tuning it onto the piezotube, the tip is engaged using an automated process, like the earlier-described AFM setup. Initially, the MFM settings are inactive, and the tip scans in tapping mode, akin to AFM. The settings are optimized for superior resolution and image quality, ensuring that the trace and retrace scans match before enabling the MFM system. During the MFM measurement, the probe scans within a specified area, performing two passes (trace and retrace) along each line. After completing the initial line scan of the sample's topography, the probe is raised to a predetermined lift height and rescanned over the same line (trace and retrace) to gather data on the sample's magnetic configuration. Subsequently, the probe shifts along the slow-scan axis to begin scanning a new line.

The user can adjust various settings during the scan, to enhance the resolution and quality of the resultant image. Specific to MFM, common parameters altered during this process include the MFM drive amplitude and the scan lift height. The MFM drive amplitude, resembling the AFM drive amplitude mentioned earlier, is typically set below the AFM drive amplitude. This

adjustment aims to minimize tip strike while ensuring high signal-to-noise MFM images. Moreover, the lift scan height is often maintained between $80 - 100\,nm$. This range is selected to ensure insignificant non-magnetic interactions and limit tip strike, all while maintaining lateral resolution. Adjusting these parameters enables users to strike a balance between minimizing unwanted effects and achieving optimal image quality.

3.2.3 MFM Electromagnet

Throughout this thesis, both AFM and MFM are utilized to measure systems in their initial as-deposited state and after the application of a magnetic field. Additionally, measurements were taken following successive applications of an in-plane magnetic field in the same direction. However, the AFM/MFM system lacks the capability to apply this field directly. To address this limitation, a custom electromagnet is employed for field application.

This electromagnet, depicted in **Figure 34**, comprises four coils and poles connected to a power supply. The power supply allows manual adjustment of current values up to a maximum safe current of $\sim 3\,A$, enabling the application of magnetic fields up to $40\,mT$. The sample is positioned on a specially designed 3D printed stage, maintaining a consistent height between the poles and the entire setup can be positioned on the AFM/MFM sample stage. This allows seamless measurement of the sample, followed by withdrawal of the tip and application of a magnetic field to the sample. Following this the field can be removed, the probe relowered and sample measurement proceeds. This setup allows repetitive measurements of the same sample area in a timely manner.

The electromagnet's configuration, shown in **Figure 34**, enables field application along user-designated positive and negative directions of one axis between the labelled poles A and C or between D and B, depending upon connection. Coils are connected to the power supply in parallel to enable this field application. This setup ensures controlled and directed magnetic field applications for comprehensive sample characterization.

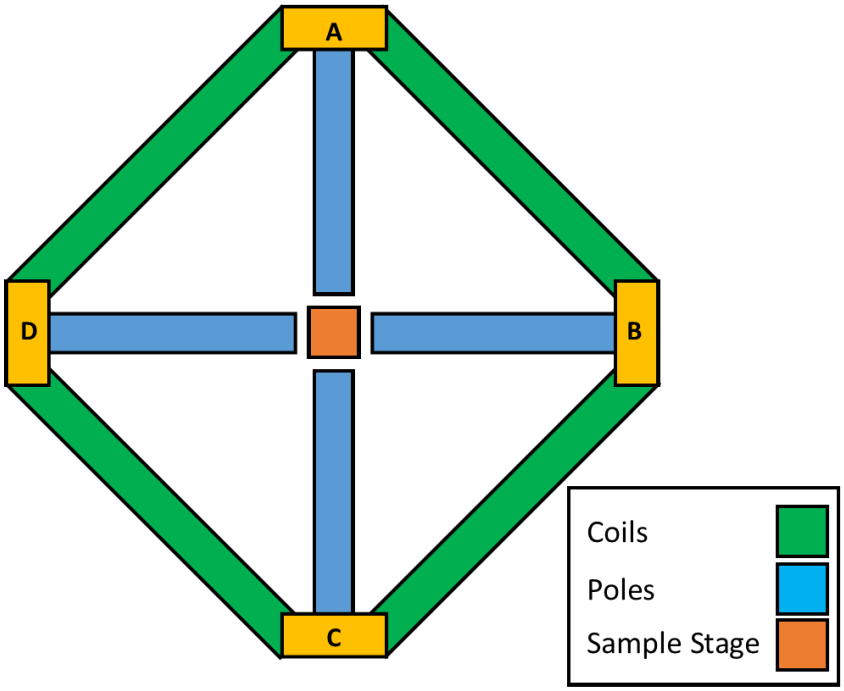

***Figure 34**: Diagram of the electromagnet setup.*

The calibration of the electromagnet is conducted before any field application. To achieve this, a hall probe is suspended from a precision holder, positioning it between the poles at the same height as the sample would experience when placed on the 3D printed stage. The calibration process involves varying the current and recording the measured field values across the expected range of field values for the experiment. This meticulous calibration procedure ensures accurate and predictable field application for subsequent experiments.

3.2.4 AFM/MFM Processing

After capturing AFM and/or MFM images, processing of the data is often necessary before examination, utilizing software packages like WSxM 4.0 and Gwyddion. These datasets frequently contain artifacts, such as tip strike lines and uneven height variations, which can complicate data interpretation.

The typical data processing steps are as follows:

Removal of Tip Strike Lines: This involves manual or automated selection of identified tip strike lines, followed by applying a filter that substitutes the selected line's data with an average obtained from the adjacent lines above and below it.

Automatic Flattening: To address inherent image tilt in AFM/MFM images, an automatic flattening process is performed. This process calculates a background height of the image, which represents the average surface height. A mathematical algorithm is applied to determine this plane, which is then subtracted from the image data, thereby normalizing the overall height variation and achieving a uniform surface level.

Colour Range Alteration: The final step involves altering the colour range utilised for visualisation of the data. This process modifies how data values are translated into colours. It does not analyse or modify data but influences how the values appear, enhancing contrast, highlighting small variations and improving the overall clarity and interpretability of the data.

The subsequent data processing, facilitated by a Python program detailed in the appendices (Section 8.1), delves into managing the intricate topographical influence within the 3D systems that significantly affects the MFM data. This systematic process navigates through crucial steps aimed at mitigating the topography's impact on the MFM data.

Initially, the mean and standard deviation of the MFM dataset are computed. Outliers, primarily induced by topographical variations, are identified, and clipped using a threshold set at three standard deviations from the mean. This threshold is chosen to balance the removal of artifacts while retaining genuine magnetic signals.

Following this, a meticulous process of line-by-line subtraction of the AFM image from the MFM data is undertaken. This involves leveraging curve fitting techniques to extract and eliminate the AFM signature from the MFM data. A linear fit is first applied to address the primary topographical features, removing the bulk of the AFM-related influence. However, this may not be sufficient to fully eliminate all topographical effects.

To further mitigate residual topographical effects, parabolic fitting is applied. This step is crucial as it handles more complex variations in the topography that a linear fit alone cannot address. The combination of linear and parabolic fits ensures a more thorough removal of topographical artifacts, resulting in a cleaner MFM signal.

Lastly, normalisation of the resulting image is performed. This involves clipping values that fall beyond a user-defined threshold, again set at three standard deviations from the mean. This step effectively diminishes the influence of any remaining outliers, ensuring that the final MFM data is as free from topographical artifacts as possible.

The thresholds set at three standard deviations from the mean are empirically chosen to strike a balance between preserving genuine magnetic features and suppressing topographical artifacts. This empirical balance is essential to ensure that the final processed MFM data accurately reflects the underlying magnetic phenomena without being skewed by topographical variations.

By systematically applying these processing steps, the program ensures that the MFM data is accurately interpreted, providing reliable insights into the magnetic properties of the 3D systems under study.

The validation process of this methodology involved imaging the identical region using tips with opposing magnetisations. By subtracting these two MFM measurements, the topographical data was effectively eliminated. The resulting summation of these two MFM measurements led to the cancellation of magnetic features, generating data that solely represented the surface's topography, akin to the AFM image.

Throughout this thesis, the described processing method plays a pivotal role in augmenting MFM contrast. However, to ensure the reliability of the enhanced images, comparisons with the original MFM images were consistently conducted. These comparisons were instrumental in identifying any potential artifacts that might have been introduced by the processing steps. By juxtaposing the processed images with their original counterparts, this approach aimed to meticulously validate the authenticity of the enhanced MFM contrast while remaining vigilant in detecting and addressing any artifacts that could arise from the processing methodology.

3.2.5 Scanning Electron Microscopy

Scanning Electron Microscopy (SEM) is pivotal in characterizing physical features of micro- and nano-scale samples. While optical microscopy can observe samples of similar dimensions, its limitations arise when dealing with nano-sized features due to the comparable size of these features to the wavelength of visible light. Hence, SEM becomes essential for detailed analysis.

The SEM hardware used in this thesis comprises the Hitatchi SU8230 and a Zeiss Sigma HD. To analyse samples, they are secured onto an SEM holder, typically held in place by a small clip or adhesive, taking into consideration the sample's electrical conductivity. This SEM holder is then placed onto a stage within the SEM input chamber, which is subsequently evacuated to a vacuum pressure of less than $< 1 \times 10^{-4}\ \mathrm{mB}$ prior to imaging.

The stage hosting the sample is adjustable in all cardinal directions and can be tilted up to a 45-degree angle, allowing for versatile observation angles. Electrons are generated using a field emission gun, creating a strong electric field that extracts electrons from their atoms. These emitted electrons are then accelerated by a positively charged anode plate through a condenser lens, controlling the electron beam's size and quantity. The resolution of the resulting image is determined by the beam's size.

The electron beams trajectory is further managed by apertures along its path, offering additional control. A scanning coil, generating a magnetic field, rasters the beam along the x- and y-planes, deflecting it as needed. Finally, a last objective lens concentrates and focuses this primary beam into a small spot size onto the sample for imaging. A diagram detailing the beams path to the sample and a typical setup of an SEM is shown in **Figure 35**.

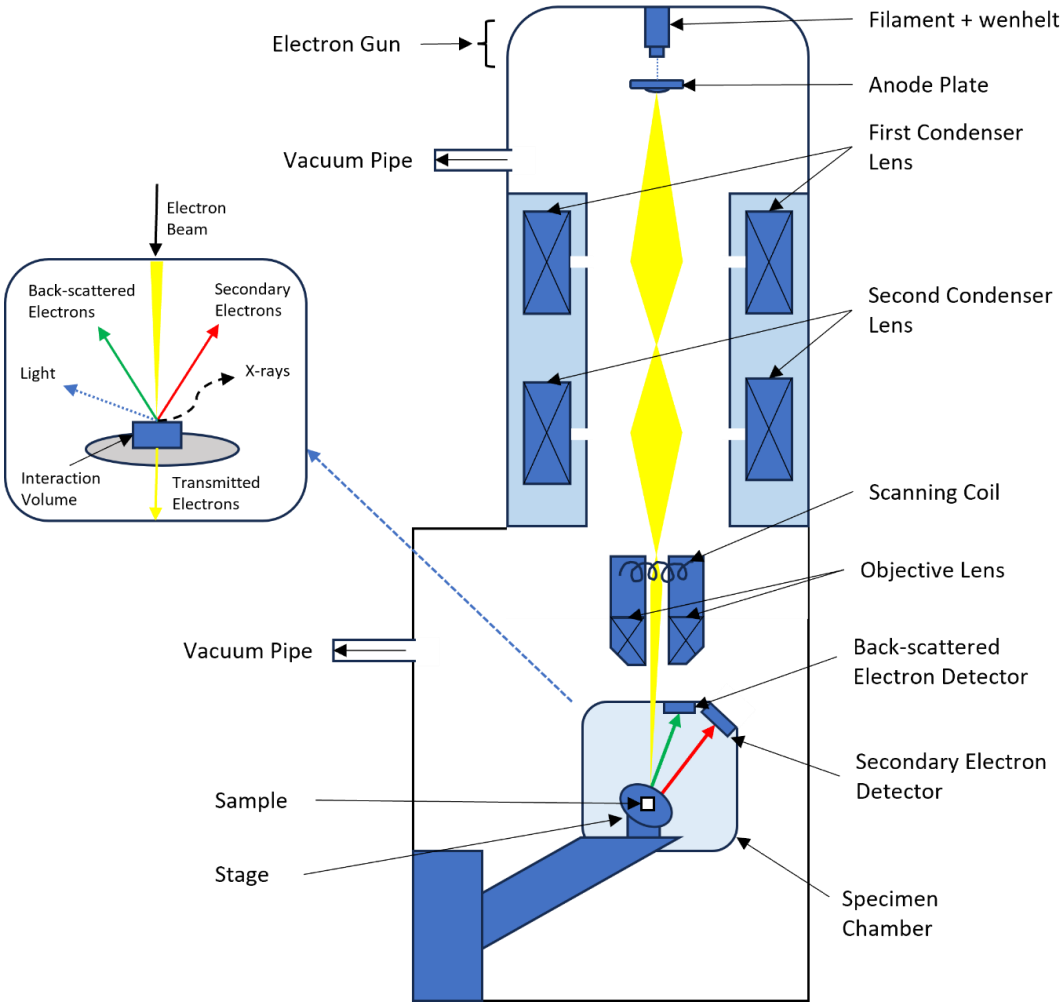

Figure 35: *Diagram of the Scanning Electron Microscopy setup. Adapted from [54].*

In SEM imaging, two types of electrons play a crucial role in generating the final image of the sample: backscattered electrons and secondary electrons. Backscattered electrons are those reflected off the sample due to elastic interactions with the primary beam. On the other hand, secondary electrons are emitted from the sample when the primary electrons undergo inelastic scattering with the sample's electrons. Typically, it's the secondary electrons that are detected within the measurement chamber and then translated into an image by a computer.

One critical aspect in SEM imaging revolves around the grounding of the sample during measurements. Failure to ground a sample can lead to the accumulation of charge, resulting in a blurring effect during image processing. To prevent this, samples intended for SEM analysis should be fabricated to be conductive, this is primarily done by deposition of metal, commonly magnetic permalloy. Furthermore, the methods used to mount these samples

must also ensure conductivity. Charging issues, especially concerning the polymer scaffold - the primary material for samples in this thesis, can potentially cause damage to the sample being examined.

3.2.6 Optical Magnetometry

Optical magnetometry is a technique that uses light to measure the magnetisation of a sample. It is based on the interaction between the magnetisation and the polarization state of light. By analysing the polarization of light, optical magnetometry can provide sensitive and non-invasive magnetic field measurements of a variety of magnetic nanostructures across a broad range of fields [55].

Optical magnetometry has several advantages over traditional magnetic field measurement techniques, such as its high sensitivity, non-invasive nature, and ability to measure magnetic fields in real-time. However, optical magnetometry also has several limitations, such as its limited spatial resolution, dependence on light intensity, and the need for sophisticated optical setups.

The setup for optical magnetometry used in this thesis consists of several key components shown in **Figure 36**. A computer-controlled laser ($\lambda = 637\ nm$) serves as the primary source, emitting a user-defined power beam. Before polarization, the beam undergoes widening via a beam expander to a diameter of $1\ cm$. Expansion of the beam is crucial as it enables the subsequent focusing of the beam to a suitably small spot. By widening the beam, it allows greater control and precision in focusing ensuring the beam can be concentrated onto the sample.

Linear S-polarization follows using a Glan-Taylor polariser, this polarisation direction enhances sensitivity to surface magnetisation. A spot size of approximately $\approx 20\ \mu m^2$ is achieved by focusing through an achromatic doublet ($f = 10\ cm$). By combining two lenses in an achromatic doublet chromatic aberration is minimised, ensuring different colours of light converge at the same focal point. This setup is fine-tuned with visual inspection aided by a camera observing the sample's positioning.

The sample itself is mounted using vacuum grease onto a non-magnetic aluminium rod, which is connected to a computer-controlled motorized stage. This arrangement allows multi-directional movement and rotation of the sample for experimentation purposes. An electromagnet is present at the sample position, allowing a field of up to $0.3\ T$ to be applied. During measurements, these coils are situated approximately $1 - 2\ mm$ from either side of the sample, ensuring that light reflected off the sample is directed away from the coils.

Once the laser beam reflects off the sample, it passes through a series of focusing lenses and mirrors, ultimately reaching a secondary Glan-Taylor polarizer known as the analyser. This analyser, positioned within a $< 3°$ rotation difference from the initial polarizer, further filters the beam based on its polarization. However, this part of the setup, after the beam reflects off the sample, requires manual adjustment by the user for each measured sample.

The samples mounted on the rod might not be perfectly flush, causing variations in the beam's path after it reflects off each sample. Additionally, any movement or rotation of the sample can further affect the beam's trajectory. These variations post-reflection or after sample adjustments can potentially influence the quality and consistency of the measured data, emphasizing the need for careful adjustment to maintain accuracy in the optical path of the beam for every sample measurement.

The beam, having passed through the analyser, is then refocussed and reflected into an amplified Si photodetector. Additionally, the light rejected by the analyser is collected and directed towards a secondary photodetector for measurement of intensity of rejected beam. This supplementary data collection helps improve the overall quality and precision of the gathered results for comprehensive analysis and interpretation.

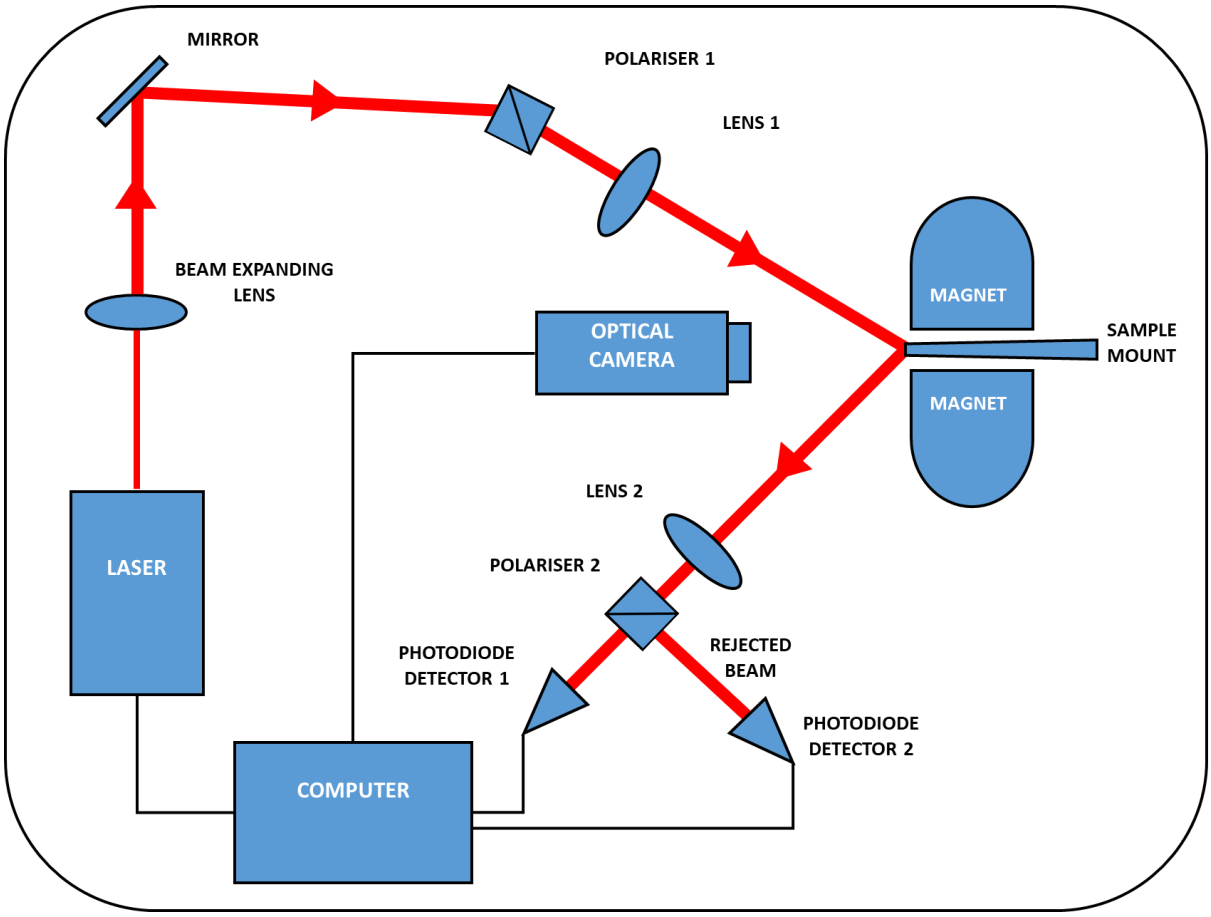

Figure 36: *A diagram showing the components and arrangement of a MOKE setup.*

The Magneto Optical Kerr Effect (MOKE) is a pivotal technique in probing sample magnetisation, relying on the interactions between polarized light and magnetic properties. When a linearly polarized optical beam reflects off the sample, the MOKE manifests as a rotation within the beam's polarization plane, arising from the interaction between the light and the sample material. This phenomenon is the reflection equivalent of the Faraday effect, which involves the rotation of light's polarization plane in transmission through a sample. The angle of rotation is directly proportional to the magnetisation of the sample and the length of the light's path.

In this setup, the initial polarizer and the analyser, when positioned perpendicular to each other, result in the photodiode detecting no signal unless this rotation occurs. Therefore, the signal measured by the photodiode quantifies the extent of this rotation, providing insights into the local magnetisation of the sample interacting with the laser.

However, achieving a distinct signal becomes challenging when both polarizers are perpendicular, leading to lower signal-to-noise quality. To address this, the analyser is first rotated to minimize the detected laser amplitude (indicating perpendicular alignment to the initial polarizer) and then fine-tuned by a slight margin termed the analyser angle.

Previous studies [56] utilizing the same MOKE setup and measurement of samples detailed in this thesis delved into the signal-to-noise ratio (SNR) concerning data collected by the photodiode, specifically examining the impact of the analyser angle. When assessing thin magnetic films, the detected signal notably amplifies, resulting in photodetector oversaturation. Consequently, an analyser angle of 1° emerged as the optimal setting in such scenarios. This adjustment ensures accurate measurements by mitigating detector saturation caused by the increased signal intensity. Conversely, investigations revealed that an analyser angle of 2° optimizes the signal-to-noise ratio (SNR), specifically benefiting the evaluation of magnetic nanostructures akin to those studied in this thesis. This setting proved particularly suitable for examining magnetic nanostructures, enhancing the precision and quality of measurements under these conditions [55].

The physics of this phenomena can be described by the interactions of light with matter in terms of the complex dielectric tensor of the material. In an isotropic material, this tensor $\boldsymbol{\varepsilon}$ is given by [1]:

$$\boldsymbol{\varepsilon} = \varepsilon \begin{pmatrix} 1 & -iQ_z & iQ_y \\ iQ_z & 1 & -iQ_x \\ -iQ_y & iQ_x & 1 \end{pmatrix} \quad (114)$$

Where Q is the Voigt vector, described by:

$$\mathbf{Q} = Q_x\hat{\imath} + Q_y\hat{\jmath} + Q_z\hat{k} \quad (115)$$

Such that Q is parallel to the magnetisation $\boldsymbol{M}$ and Q is a materials constant that describes the magneto optic rotation of the plane of polarisation of the light [1]. When considering

linearly polarised light interacting with this material, the dielectric tensor unfolds two circularly polarised modes with specific dielectric constants which portray how the material affects the light, showcasing differing behaviours during propagation within the material. These constants are given by [1]:

$$\varepsilon^{+} = \varepsilon(1 + \mathbf{Q} \cdot \mathbf{k}) \qquad (116)$$

$$\varepsilon^{-} = \varepsilon(1 - \mathbf{Q} \cdot \mathbf{k})$$

Where $\boldsymbol{k}$ is the direction of the propagation of light. This interaction causes these circularly polarised modes to exhibit different paths within the material. Once these modes recombine, after reflection or transmission, they generate elliptically polarised light. This polarisation manifests as a rotation of the primary axis of light polarisation, illustrating how the material affects and alters the characteristics of light passing through it.

Within the realm of magnetic materials, comprehending the Faraday and Kerr effects delves into the interplay of spin-orbit interactions, as previously explored in Section 1.1.6. Spin-orbit interactions play a pivotal role in determining magnetocrystalline anisotropy, tightly linking the Kerr effect and perpendicular magnetic anisotropy.

In discussions regarding light polarization, reference is made to the electric field E. When indicating linear polarisation along a specific direction (e.g., the y-axis), it signifies that E oscillates along that given direction. However, the concept of linearly polarized light can be conceived of as a coherent blend of equal components of right- (σ^{+}) and left- (σ^{-}) hand circularly polarized light. Here, circular polarization refers to E rotating in a plane perpendicular to the propagation direction.

When these polarizations interact with a material, (σ^{+}) and (σ^{-}) induce charges within the material to rotate clockwise and counterclockwise, respectively. Consequently, their orbital angular momentum changes but in opposite directions for the (σ^{+}) and (σ^{-}) components [1].

In a ferromagnetic material, the majority of spins in domains spontaneously align along the magnetisation direction. This spin-orbit coupling results in small energy contributions of equal magnitude but opposite signs for left- and right-handed circularly polarized light. Consequently, these polarizations propagate differently within the material, emerging with distinct amplitudes and phases. Left- and right-handed circular polarizations exhibit different refractive indices within the material, described by complex values like $\tilde{n} = n + ik$.

The real part of this interaction introduces a phase shift ($\Delta n = n^{+} - n^{-}$), known as magnetic circular birefringence [1], while the imaginary part causes a discrepancy in the reflected (Kerr) or transmitted (Faraday) amplitudes ($\Delta k = k^{+} - k^{-}$). Upon exiting the material, the combination of (σ^{+}) and (σ^{-}) yields elliptically polarized light. This emergent light exhibits a rotation of the main polarization axis by an angle θ_F or θ_K, and an ellipticity, ε_{F} or ε_{K} for the Faraday and Kerr effects, respectively.

The rotation observed θ_K, plotted against the applied magnetic field to the sample, serves as a measurement of the sample's magnetisation [1]. This involves sweeping a magnetic field applied to the sample, allowing it to reach both positive and negative saturation states, resulting in a hysteresis loop representation.

To record the magnetic field during sample measurement, a gaussmeter is positioned within the electromagnet. Enhancing the signal-to-noise ratio (SNR) and minimizing the influence of random noise involves sweeping the magnetic field between saturation points multiple times. Averaging the detected signal across each cycle enables the construction of a hysteresis loop, providing a clearer depiction of the sample's magnetic properties.

MOKE measurements are conducted in three distinct geometries, delineated by the orientations of the magnetisation concerning the plane of incidence and reflects light. Each geometry enables the measurement of different facets of the magnetisation vector.

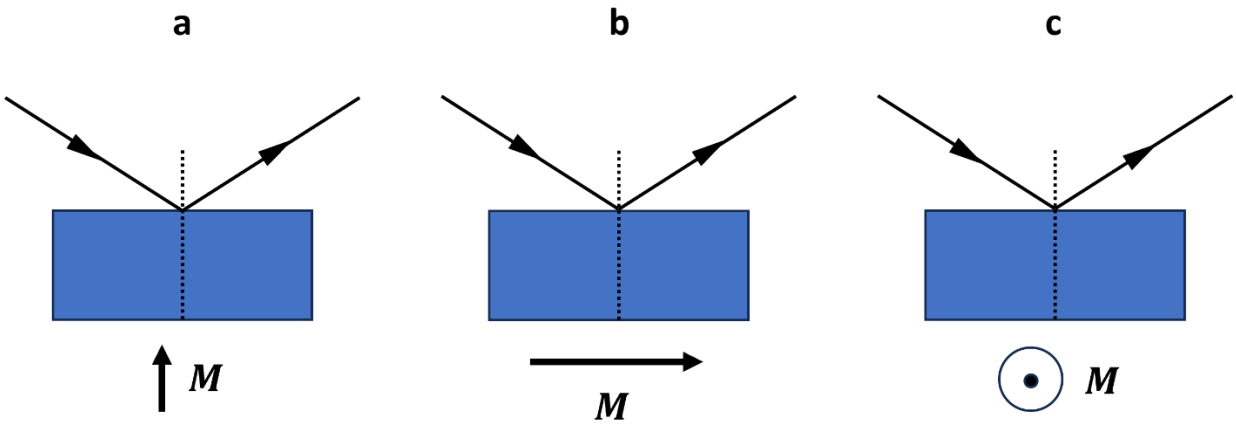

Figure 37: (a) *The polar Kerr effect,* ***(b)*** *the longitudinal Kerr effect,* ***(c)*** *The transverse Kerr effect.*

In polar MOKE, shown in **Figure 37a**, the magnetisation is perpendicular to the sample plane. In this configuration, the highest signal intensity is found for normal incidence. If oblique incidence is employed, the MOKE technique becomes sensitive to the in-plane component of the magnetisation. For longitudinal MOKE, **Figure 37b**, the focus lies on the in-plane component of magnetisation that resides within the plane of light propagation. Contrastingly, transverse MOKE, **Figure 37c,** is designed to measure the in-plane magnetisation component that stands perpendicular to the plane of light propagation. These geometries allow for selective measurement of specific aspects of the sample's magnetisation. During work in this thesis, longitudinal MOKE is primarily used.

3.2.7 Soft X-Ray Microscopy

In the past decade, the application of synchrotron radiation as a measurement tool has significantly expanded. Synchrotron radiation is emitted by electrons as they circulate within a high-energy accelerator and pass through an undulator, causing transverse oscillations that result in the emission of intense and coherent light. Over recent years, advancements in synchrotron techniques have led to this emitted light becoming exceptionally bright, featuring a narrow bandwidth and high intensity.

This highly intense light, primarily in the form of X-ray photons generated through this process, has found widespread use in analysing the electronic and geometric structures of

various samples. Synchrotron radiation's role in exciting soft X-ray emission spectra significantly enhances the capabilities of spectroscopic methods. By employing monochromatized soft X-ray photons, this approach offers a greater degree of energy selectivity compared to electron-based methods.

In the soft X-ray range, spanning from $50\,eV$ to $1200\,eV$, a wide array of X-ray edges is accessible. These include the K-edges (such as C, N, O, F) and the initial transition metal L-edges ($Ti, Cr, Mn, Fe, Co, Ni, Cu, Zn$), among others [57]. This expansive energy range grants access to a diverse set of atomic and electronic structures, enabling detailed analysis and comprehension of various materials' properties and behaviours.

In X-ray absorption spectroscopy (XAS) a broad energy range of x-rays (tuned to pass over an element specific edge) is passed through the sample causing non-resonant or resonant excitation [58]. Non-resonant excitation occurs when the x-ray energy surpasses a samples constituent elements binding energy. This results in the ejection of an electron through the photoelectric effect. Whereas, resonant excitation occurs when the x-ray energy matches the electron binding energy of the specific element, resulting in the electron's transition from a core shell to a valence shell. When this energy precisely aligns with the binding energy it leads to a phenomenon called resonance formation wherein a highly efficient and rapid excitation of the electron occurs. Upon relaxation, a valence electron may return to the core shell, emitting a photon during this process. This emitted photon may in turn be absorbed by another electron leading to the emission of a secondary electron called the auger electron. XAS measurements can gather data from a variety of sources during this process: the emitted x-ray fluorescence photons, auger electrons or transmitted x-rays may be detected and analysed. In this thesis, XAS are produced from the transmitted photon intensity.

The measurements obtained from the detection methods are then plotted against the energy of incident x-rays and this plot is known as the XAS spectra. This spectrum displays characteristic peaks and features corresponding to the binding energies of the elements present within the measured sample. By analysing the intensity and position of these peaks, element identification can occur and the chemical environment or valence state within the sample may be understood. Therefore, the significance of this soft X-ray wavelength range

lies in its ability to precisely probe distinct atomic transitions, enabling the creation of detailed and element-specific images crucial for various scientific investigations and analytical studies.

The L_2 and L_3 edges are characteristic absorption features observed in X-ray absorption spectroscopy and refer to specific energy levels corresponding to the excitation of electrons in $2p$ orbitals to unoccupied states in $3d$ orbitals [57]. The energy difference between the L_2 and L_3 edges is due to the fine structure splitting within the energy levels of the atom. They provide critical information about the electronic structure and bonding characteristics of transition metals [59]. Analysing these edges offers insights into the elemental composition, oxidation states, and chemical environments of the transition metal atoms within the material being studied. These features are fundamental in understanding and characterizing the properties and behaviours of materials in various scientific investigations.

The capacity for polarization in X-ray light significantly enhances soft X-ray spectroscopic techniques, allowing for more nuanced exploration of chemical information [60]. This capability to manipulate polarized X-ray light enriches and refines the investigative capabilities of spectroscopic methods utilized across diverse scientific inquiries. One such method used in this thesis is x-ray magnetic circular dichroism (XMCD) which utilises distinct absorption coefficients for left and right-circularly polarized X-rays when engaging with magnetic substances. The dissimilarity emerges from the interplay between the X-ray's helicity (spin angular momentum) and the magnetic moments of the materials constituent elements.

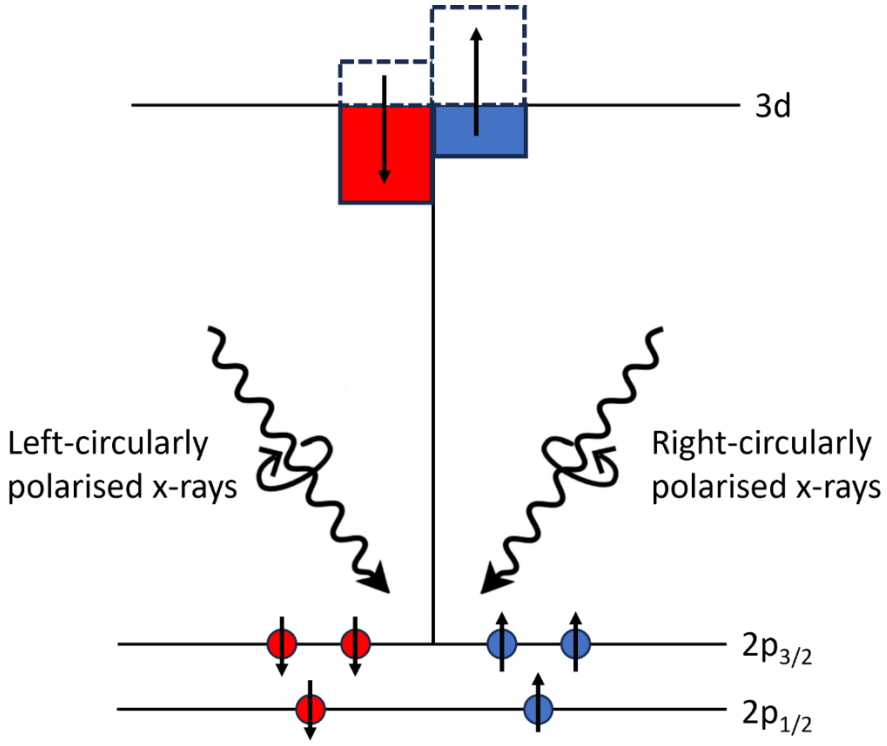

Figure 38: *Oppositely circularly polarized X-rays selectively excite electrons with either up or down spin orientations, determined by their alignment relative to the direction of X-ray propagation. Adapted from [61].*

Circularly polarized x-rays, much like non-polarized x-rays, trigger transitions within the electronic structure of the sample. However, due to their polarization, specific selection rules ($\nabla m = \pm 1$) for the orbital component lead to different transition probabilities for left- and right-circularly polarized light into the polarized valence band [62]. Here, the light indirectly influences the electron's spin through the spin-orbit interaction, without directly interacting with it. The strength of this interaction significantly impacts dichroism (the difference in light absorption based on its polarization). While in the visible and near-infrared light range, this interaction's effect on transitions is minimal compared to higher-energy radiation like x-rays. In XMCD, the core-level spin-orbit interaction is notably larger, often reaching tens of eV [62]. This results in the formation of distinct $j = l \pm s$ levels, see **Figure 38**.

Measuring at the L_3 and L_2 photon edges in with XMCD holds critical importance in determining the magnetic characteristics within the material, primarily due to the specific energy levels associated with these transitions. At the L_3 edge, the transition occurs from the $2p_{\frac{3}{2}}$ to the $3d_{\frac{5}{2}}$ level, while the L_2 edge corresponds to the transition from the $2p_{\frac{1}{2}}$ to the $3d_{\frac{3}{2}}$

level within the electron shells of the atoms comprising the material [62]. These energy levels, sensitive to changes in atomic magnetic moments, are pivotal for XMCD investigations owing to their pronounced effect on X-ray absorption based on the material's magnetic state.

When conducting XAS or XMCD measurements, one crucial consideration is the transmission of X-rays through the sample. To ensure effective transmission without substantial interaction with a substrate, samples are often positioned on a transmission electron microscopy grid or aperture.

A commonly employed method involves using a silicon-nitride membrane ($\sim 100\ nm$) across the aperture, serving as a platform for placing the sample to be measured. It's essential to ensure both the sample and the underlying substrate are sufficiently thin to allow a significant portion of X-rays to pass through and be detected after interaction.

The transmission of x-rays through a material follows the exponential attenuation law, described by the Beer-Lambert law. This law quantifies how the intensity of an x-ray beam changes as it passes through a material [60, 63]:

$$I = I_0 \exp(-n\mu_a d) \qquad (117)$$

Where I is the intensity of x-rays after transmission, I_0 is the initial x-ray intensity, d is the thickness of the sample and μ_a is the atomic photo-absorption cross section of the material at a specific x-ray energy and is defined as [63]:

$$\mu_a = 2r_0\lambda f_2 \qquad (118)$$

Where r_0 is the classical electron radius, λ is the wavelength, and f_2 is the imaginary component of the atomic scattering factor.

X-ray microscopy is a powerful tool for studying the internal structure of materials with high spatial resolution. Two types of x-ray microscopy that are commonly used are Transmission

X-ray Microscopy and Scanning Transmission X-ray Microscopy. Both techniques use the measured transmission of synchrotron produced x-rays through a sample to produce high-resolution images of the sample and study the chemical and structural properties of the sample at the nanoscale.

Transmission X-ray Microscopy (TXM) operates via a simultaneous, holistic imaging approach, capturing the entirety of the sample at once. Employing a focused X-ray beam, TXM detects transmitted X-rays across the entire sample surface, enabling rapid acquisition of high-resolution three-dimensional representations of nanoscale material structures, see **Figure 39a**. However, despite its comprehensive imaging capability, TXM encounters challenges linked to radiation-induced sample damage, particularly noteworthy in sensitive samples, thereby imposing limitations on prolonged X-ray exposure.

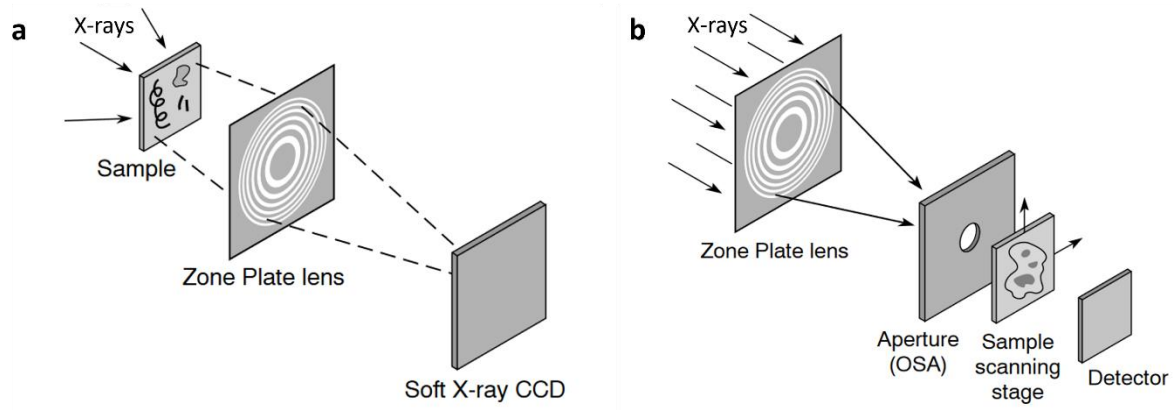

Figure 39: (a) *Schematic diagram of a TXM microscope.* ***(b)*** *Schematic diagram of a STXM microscope, Figure from [64].*

In contrast, Scanning Transmission X-ray Microscopy (STXM) follows a sequential and meticulous imaging strategy. Utilizing a focused X-ray beam, STXM systematically scans and measures transmitted X-ray intensities at discrete locations across the sample while modulating X-ray energy, see **Figure 39b**. Through this point-by-point scanning methodology, STXM gradually compiles a detailed image, acquiring valuable information regarding the internal structure and chemical composition of the sample. Despite its advantage in delivering detailed chemical analyses and superior spatial resolution, STXM's serial scanning process inherently demands more time, resulting in a comparatively slower imaging speed when compared to TXM.

The process by which STXM or TXM is used in this thesis to obtain chemical and magnetic information from the fabricated samples is now described. Samples are fabricated such that they are exposed over an aperture such that x-rays can be transmitted through the sample and collected by a detector. Samples have been fabricated such that the thickness of the material through which the x-rays must transmit is minimised. Samples sent to the synchrotron are characterised with Scanning Electron Microscopy, Optical Microscopy and Optical Magnetometry prior to the experiment and samples are prioritised based on the quality of the nanostructures examined.

Priority samples are loaded into the synchrotron and brought to vacuum conditions. Initial images are taken of the sample with an x-ray energy range over the L_2 and L_3 edge of the magnetic materials the sample is comprised of (Nickel and Iron). These initial images are used to identify where the structures are within the aperture, as well as determining whether the structures are stable after exposure to the x-ray beam.

For TXM, the sample specific energy range for the L_3 and L_2 edges of the magnetic material are identified by generating an Xray Absorption Spectra (XAS). To obtain an x-ray absorption spectrum, the sample is first exposed to a range of x-ray energies that cover the relevant absorption edges of the element of interest. These absorption edges correspond to energies at which the x-rays are absorbed by the inner-shell electrons of the element's atoms, causing them to be excited to higher energy levels or ejected from the atom altogether. The transmitted x-rays are measured by a detector and the intensity of the x-rays at each energy is plotted as a function of energy. Through examination of the produced graph the L_3 and L_2 edges can be identified by strong peaks where x-rays are absorbed by the material. From this the L_3 and L_2 edges are identified and noted for this sample. Further information can be obtained from this absorption vs. photon energy graph. Oxidisation of the material can be identified by shoulder peaks that may be present close to the L_3 and L_2 absorption edges. Comparison of these shoulder peaks with available literature allows identification of the element which corresponds to the peak.

In Scanning Transmission X-ray Microscopy (STXM), this same process involves scanning a designated region of the lattice through a series of energy scans. These scans encompass various energy ranges, starting approximately $30\ eV$ below the L_3 edge. Initially, coarse

energy steps of $2\ eV$ are employed, gradually approaching within 5eV of the L_3 edge. Finer steps, approximately $0.2\ eV$, are then taken within this $5\ eV$ range around the L_3 edge. Post the L_3 edge, rougher steps resume until reaching around $5\ eV$ from the L_2 edge, followed by finer steps nearing the L_2 edge. Again, after surpassing the L_2 edge, coarser steps are taken until the x-ray energy reaches approximately $30\ eV$ beyond the L_2 edge. This entire scanning process is duplicated for both left- and right-circularly polarized light to collect STXM data.

To extract X-ray Magnetic Circular Dichroism (XMCD) from the acquired data obtained via STXM or TXM, a standardized approach is followed. Initially, Optical Density (OD) images are derived from the captured images using:

$$O_D = \ln\left(\frac{I_0}{I}\right) \qquad (119)$$

Where O_D is the optical density, I_0 is the incident photon intensity, located from sample free regions of interest, and I is the transmitted intensity. This transformation helps normalize the X-ray absorption by the sample, rendering the data comparable across scans and polarizations.

Subsequently, the difference in absorption between left- and right-circularly polarized X-rays is computed. This difference, calculated using:

$$XMCD = \frac{L - R}{L + R} \qquad (120)$$

where L and R denote the intensities of left-circularly and right-circularly polarized lights respectively, reveals vital insights into the magnetic properties of the sample. This information includes details about its magnetic moment and orientation concerning the X-ray beam.

The experimental setup at the ALBA TXM beamline was such that the more convenient measuring protocol was fixing the x-ray beam polarization (to circular left) and acquiring

images at absorption edges with opposite dichroic contribution in order to extract the magnetic contrast [65, 66]. Approximately 300 images were captured at both $Fe\ L_3$ and $Fe\ L_2$ photon energies. These images were aligned and normalized against a flat field image. Normalisation against a flat field image, capturing only background and imaging setup variations, ensured removal of non-sample-related x-ray intensity fluctuations. This process enabled accurate analysis focused on genuine sample features. Normalised images were converted to optical density before an XMCD signal was calculated using:

$$XMCD = L_{3,Fe} - 2 \cdot L_{2,Fe} \qquad (121)$$

Where $L_{3,Fe}$ is the O_D image at the $Fe\ L_3$ photon energy and $L_{2,Fe}$ is the O_D at the $Fe\ L_2$ photon energy.

3.3 Simulation Techniques

In this thesis a software package NMAG is used. NMAG a Finite Element simulation package specialised in simulating magnetic materials. NMAG computations rely on CPU processing and require substantial memory allocation, therefore the Advanced Research Computing at Cardiff (ARCCA) supercomputer is used.

Running an NMAG simulation requires uploading a mesh file defining the geometry, a python script describing the simulation parameters and protocols and a SLURM file outlining the technical job specifications.

NMAG employs the Landau-Lifshitz-Gilbert (LLG) equation to model ferromagnetic behaviour [3, 67]:

$$\frac{d\boldsymbol{m}}{dt} = -|\gamma_P|\boldsymbol{m} \times \boldsymbol{H_{eff}} + \left(\frac{\alpha_D}{M_S}\right)\left(\boldsymbol{m} \times \frac{d\boldsymbol{m}}{dt}\right) \quad (122)$$

This equation encapsulates the time-dependant response $\frac{d\boldsymbol{m}}{dt}$ of a magnetic moment $\boldsymbol{m}$ to an effective magnetic field H_{eff} [1, 3]. Here, the effective field encompasses various components [67]:

$$\boldsymbol{H_{eff}} = \boldsymbol{H_{ext}} + \boldsymbol{H_{anis}} + \boldsymbol{H_{exch}} + \boldsymbol{H_{demag}} + other \quad (123)$$

Equation (122) involves the gyromagnetic ratio term (γ_P) and the Gilbert damping constant (α_D). For time-independent simulations α_D is fixed at a value of 1 to expedite simulation runtimes.

The LLG equation, a crucial model describing magnetisation evolution within materials under external influences, comprises two main components. The precessional motion component captures the rotational behaviour of magnetic moments when subjected to an effective magnetic field H_{eff} [3]. This component involves a cross-product between the magnetic moment and the effective magnetic field, depicting the tendency of moments to align or rotate in response to the field.

The equation also incorporates a damping term signifying energy dissipation within the system, affecting the rate at which magnetic moments align with the effective field [3]. In simulations of $Ni_{81}Fe_{19}$, consistent parameters such as $M_S = 8.6 \times 10^5\,\mathrm{Am}^{-1}$, $A = 1.3 \times 10^{-13}\,Jm^{-1}$, and zero magnetocrystalline anisotropy are used. Thermal effects are neglected $T = 0\,K$.

Simulated geometries in NMAG were characterized by mesh spacing between $3\,nm$ and $5\,nm$, with finer spacing in thinner regions, all kept below the exchange length of $Ni_{81}Fe_{19}$, approximately $5.3\,nm$. The exchange length, $\sqrt{\frac{2A}{\mu_0 M_S^2}}$, denotes the distance over which the

magnetisation remains uniform. Maintaining cell sizes below this characteristic length ensures an accurate representation of the spatial gradient of magnetisation.

While there exists a notable difference in the coercive field H_C between modelled results at $0\ K$ and experimental measurements at room temperature, there's confidence in the fidelity of the spin texture agreement [67]. Both simulations and their experimental counterparts exhibit a strong alignment in the spin texture, showcasing coherence and consistency in the magnetic behaviour of the material. This convergence in spin texture despite the discrepancy in coercive field underscores the robustness and accuracy of the simulated magnetisation dynamics in capturing the essential features of the material's magnetic properties.

Following the simulation, data is processed to generate VTK files for 3D visualization using software packages like Paraview, and text files containing applied field values and system energy density components. Additional analysis is achieved using external tools such as Python or graphing software like Origin.

4 Charge Crystal

4.1 Introduction

Artificial spin-ices have been a focal point in studying frustration and emergent behaviour, primarily in two-dimensional (2D) geometries. Recent strides, see Section 2 [34, 42, 43], have extended this exploration into three-dimensional (3D) configurations, offering a direct observation of emergent monopoles propagating across the surface.

This chapter seeks to investigate the three-dimensional artificial spin-ice phase diagram within a diamond-bond lattice geometry, proceeding from prior work that harnessed two-photon lithography and thermal evaporation to craft these systems.

Within the bulk spin ice community there has been controversy over whether such systems can reach a definitive ground state. Whilst the Hamiltonian in ASIs is fundamentally different, since only dipolar energies are dominant, the extent to which this system can realise a ground state and how this depends upon key lattice parameters is of fundamental interest.

For the frozen 3D ASI systems studied here, the focus lies in the application of a demagnetisation routine like previous studies [68] and comparing the results with Monte-Carlo as well as micromagnetic simulations. Previous measurement of the upper two surface layers via MFM unveiled the formation and propagation of monopoles across the lattice with identification of some vertex types within the systems measured [43]. However, to capture the ground state accurately, techniques evolved to enable confident analysis of contrast observed on lower wires within the lattice and to identify vertex types beyond those previously observed.

Monte-Carlo simulations upon 3D ASI systems predict a rich phase diagram encompassing a double-charged monopole crystal, a single-charged monopole crystal, and conventional spin ice. This exploration aims to bridge the gap between these predictions and experimental observations.

4.2 Monte Carlo Simulations

The exploration of intricate behaviours displayed by magnetic monopoles within spin-ice materials is extensively investigated in this section through Monte Carlo simulations. These simulations aim to unravel the diverse phases predicted and observed in previous studies [43], setting the stage for comparison with the experimental data presented later in this thesis.

Dr Michael Saccone of the University of California, Santa Cruz developed and performed all Monte-Carlo simulations. His work is presented here to set the context for experimental studies carried out by Edward Harding.

Building upon previous works, a framework [43] that conceptualizes spins in bulk spin-ice as dimers with equal and opposite charges, subsequent investigations have revealed intriguing properties of magnetic monopoles within these bulk spin-ice systems [23, 69].

These magnetic monopole excitations emerge as local deviations from the ice-like background, obeying interactions governed by Coulomb's law. Previous experimental studies have provided supporting evidence [70, 71] showcasing the transport of magnetic charge within bulk spin-ice materials.

Understanding the ground state of spin-ice materials hinges upon the understanding of magnetic charge. A crucial parameter in this understanding lies in the ratio between the chemical potential (the energy required to create a pair of monopoles) and the magnetic Coulomb energy associated with a nucleated pair, see Section 2 with Equations *(107)* and *(108)*. As this effective chemical potential approaches a specific threshold—half the Madelung constant (M/2 = 0.819 for a diamond lattice)—a phase transition to a charge crystal is envisaged, characterized by a structured arrangement of alternating charges across the entire system [72].

In contrast, canonical spin-ice materials exhibit an effective chemical potential of $\mu^* = 1.42$, indicating a state where monopoles freely propagate. This results in the emergence of a disordered spin-ice phase. The distinction in these states, governed by the interplay between

chemical potential and magnetic Coulomb energy, underscores the diverse behaviours and phases exhibited within spin-ice materials.

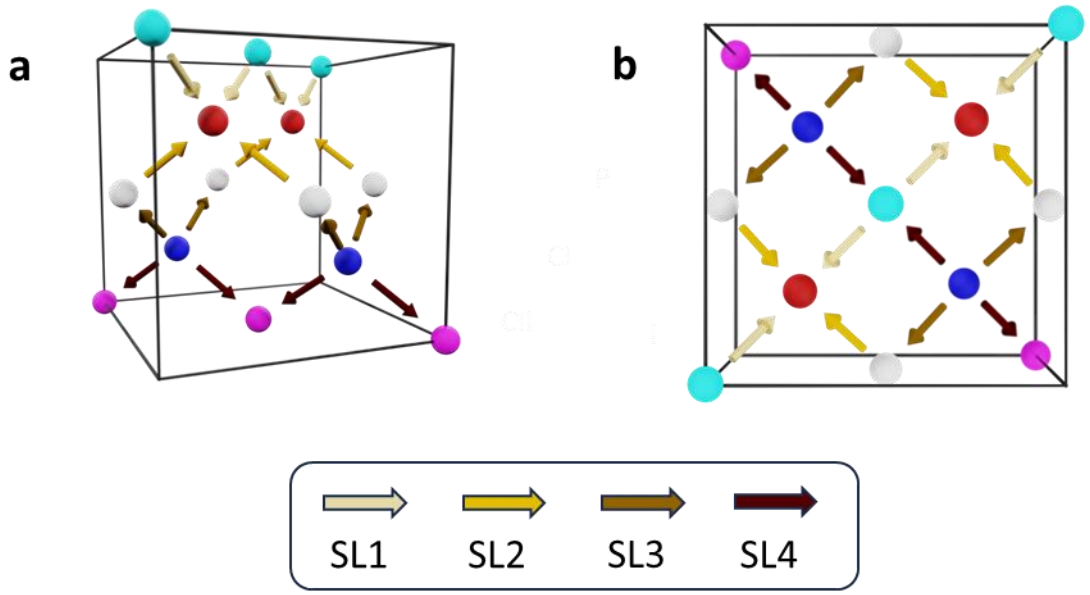

Figure 40: Example arrangement for unit cell of simulated geometry. (a) *Side-view depicting layered unit cell geometry.* ***(b)*** *Top-down perspective showcasing the unit cell layout. Magnetic charges illustrated as spheres and dipoles as arrows, colour-coded to represent sublattice layers.*

A detailed mapping of ordering in idealized 3D ASI systems within a diamond-bond lattice geometry is initially performed using finite temperature MC simulations. The MC simulations involved the arrangement of compass needle dipoles on a diamond-bond lattice, sized at 15 x 15-unit cells laterally and a single unit cell in thickness, an example of unit cell geometry is shown in **Figure 40**. This lattice geometry was segmented into sub-lattices, identified as SL1 – SL4, the arrangement of which are shown in **Figure 40a**. The upper surface ended in coordination-two vertices (SL1), succeeded by two layers of coordination-four vertices (SL2, SL3), and finally terminating in coordination-two vertices at the lower lattice surface (SL4). This geometry mimics the experimental 3D ASI system described and measured previously, see Section 2.

The interaction energy between two artificial nanomagnets within the 3D ASI geometry is accounted for through the compass needle model, which considers the finite size of these nanomagnets.

The approximated energy of interaction between two individual point charges situated at the ends of two nanomagnets denoted i and j is defined as:

$$E_{ij} = \alpha_{ij} \frac{\mu_0 \mu^2}{4\pi L^2} \left[\frac{1}{|\boldsymbol{r}_{ai} - \boldsymbol{r}_{aj}|} - \frac{1}{|\boldsymbol{r}_{ai} - \boldsymbol{r}_{bj}|} - \frac{1}{|\boldsymbol{r}_{bi} - \boldsymbol{r}_{aj}|} + \frac{1}{|\boldsymbol{r}_{bi} - \boldsymbol{r}_{bj}|} \right] \quad (124)$$

Where E_{ij} represents the energy of interaction, μ the nanomagnet magnetic moment, L the the length of the nanowire, and α_{ij} a surface energy factor which has been normalised by the strongest interactions E_{max}. The variable μ_0 represents the permeability of free space, r_{ai} and r_{bi} are the positions of the magnetic charges with the subscript showing their associations with positive or negative charges and specific nanowires. This approximated energy formulation accounts for the interaction between nanomagnets through Coulombic attraction and repulsion.

The nanomagnets' length significantly influences energy scales, emphasizing nearest neighbour interactions, but defining this "length" and charge distribution relies heavily on the nanomagnet's geometry and domain wall arrangement.

The energy expression was used to conduct a Metropolis method Monte Carlo analysis. This analysis focused on evaluating a charge crystal order parameter, denoted as M_c, assessing similarity to observed patterns in charge-ordered systems, where M_c is expressed as:

$$M_c = \left| \sum_i \Delta_i \, Q_i \right| \quad (125)$$

Here, Δ_i is a template of +1's, -1's and 0's representing a ground state. Each Δ_i value indicates the expected charge at a specific lattice site i in the ground state. Q_i represents the charge at

lattice site i. The sum calculates the total deviation of the simulated charge distribution from the ground state configuration. Taking the absolute value ensures both positive and negative deviations contribute equally to the order parameter. Higher values of M_c indicate a greater degree of charge order, whilst lower values suggest a more disordered charge distribution.

Employing the Metropolis method enabled the systematic exploration of the configuration space, allowing for an extensive investigation into the system's configurations and behaviours at diverse conditions or temperatures. This algorithm was applied to ascertain the system's ground state across a wide temperature range by varying the dipole length (b) while maintaining a fixed lattice spacing $(a = 1)$.

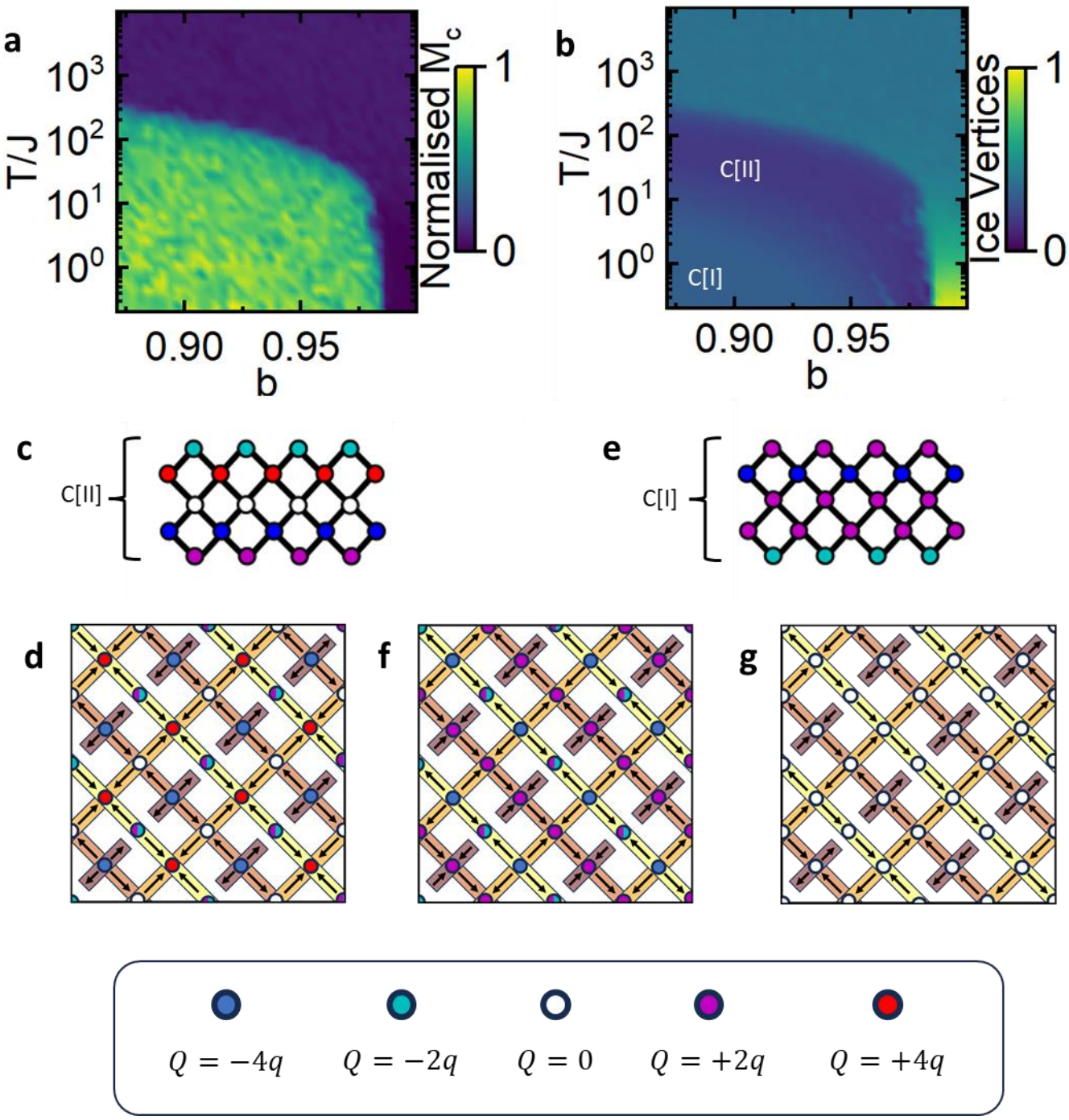

Figure 41: (a) *Phase diagram showcasing the charge crystal order parameter* (M_c) *of 3D ASI, exhibiting its dependence on temperature,* T*, and reduced dipole length,* b*.* ***(b)*** *Phase diagram demonstrating the variation in ice-rule vertices concerning temperature,* T*, and reduced dipole length,* b*. Three primary phases are distinguishable: a double charge crystal (*$C[II]$*) depicted in* ***(c)*** *and a single charge crystal (*$C[I]$*) shown in* ***(d)****. Additionally, a third phase, an ice-phase, emerges at high* b *values and low temperatures. Vertex diagrams of the three phases are shown in* ***(e)*** $C[II]$*,* ***(f)*** $C[I]$ *and* ***(g)*** *ice-phase.*

The phase diagram, derived through this method, illustrates the variability of ice-rule vertices and the previously defined order parameter when varying dipole length and temperature, as presented in **Figure 41a** and **Figure 41b**. Three distinct phases are discernible from **Figure 41a**: a double charge monopole crystal denoted as $\mathrm{C[II]}$ (visualized in **Figure 41c** and **Figure 41d**), a single charge monopole crystal identified as $\mathrm{C[I]}$ (depicted in **Figure 41e** and **Figure 41f**), and an Ice phase (depicted in **Figure 41g)** observed at low temperatures and high dipole length values ($\mathrm{b} > 0.99$).

At low temperatures, a high b lattice prompts strong localized Coulomb interactions at vertices, forcing charge neutrality and leading to the creation of a spin ice ground state, depicted in **Figure 41g**. In this ground state, ice vertices are abundant at a frequency that closely aligns with the inherent probabilities of various vertex configurations, ensuring a thorough and unbiased exploration of the accessible states. The surface SL1 layer is seen to form ferromagnetic strings, which has been previously predicted [73].

When b is reduced, it results in a decrease in the chemical potential resulting in a transition at low temperatures towards a double charge crystal $\mathrm{C[II]}$, depicted in **Figure 41c** and **Figure 41e**. This novel state is defined by $\pm 2\mathrm{q}$ charges located at the coordination-two vertices on layers SL1 and SL4, and $\pm 4\mathrm{q}$ charges located at the SL1/SL2 and SL3/SL4 coordination-four vertices. A neutral layer of Type 1 vertices is found at the SL2/SL3 coordination-four vertices. Overall, the order parameter for this $\mathrm{C[II]}$ state is found to be greater than 0.8, see yellow region of **Figure 41a**.

4.3 Vertex Type Identification Methods

To comprehensively understand the ground state of a 3D ASI using MFM in experiments, it is crucial to interpret the magnetic contrast observed among different vertex types within the data. Previous studies [43] have recognized the existence of Type 2 and Type 3 vertices, defined in Section 1.5.3 , specifically within the surface layers of SL1 and SL2 during field driven studies, however Type 1 and Type 4 vertices have not been identified nor their MFM contrast understood. It is also obvious that merely assessing the upper two surface layers is insufficient to fully comprehend the system's ground state. Therefore, advancements have

been made in MFM techniques and analytical methods to probe deeper into the SL3 sub-lattice layer and determine the vertex types observed.

This section focuses on exploring these procedures and techniques with the ultimate objective of assessing the magnetic configuration across an extensive MFM dataset of a demagnetised 3D ASI to understand the systems ground state.

A sample (180227AA) of 3D ASI lattices was fabricated in a similar manner, using TPL and thermal evaporation of Permalloy ($Ni_{81}Fe_{19}$) to previous experiments [34, 42, 43]. The upper surface layers of SL1 to SL3 are uniformly coated with permalloy, forming a connected wire network. However, SL4 exhibits a shadowed region at its junction with SL5 due the overlying SL1 layer. Additionally, all polymer nanowires below SL4 are shadowed by layers above, resulting in obscured deposition in this region. The sample comprised a series of 3D ASI lattice arrays, where the power ranged from 27% to 35% of the maximum laser power, adjusted in increments of 2%. Exposure times ranged from 0.03 seconds to 0.06 seconds, incremented by 0.01 seconds. This method yielded a spectrum of lattices resembling those from prior experiments, with MFM measurements specifically focusing on samples featuring wire widths comparable to those observed previously resulting in single domain Ising-like nanowires. The dimensions of each lattice are $50\ \mu m \times 50\ \mu m \times 10\ \mu m$, see **Figure 42a**. Wire lengths remained consistent with prior literature at $863\ nm$ and wire widths were measured, to be at $199\ nm\ \pm 6\ nm$ as shown in **Figure 42b.**

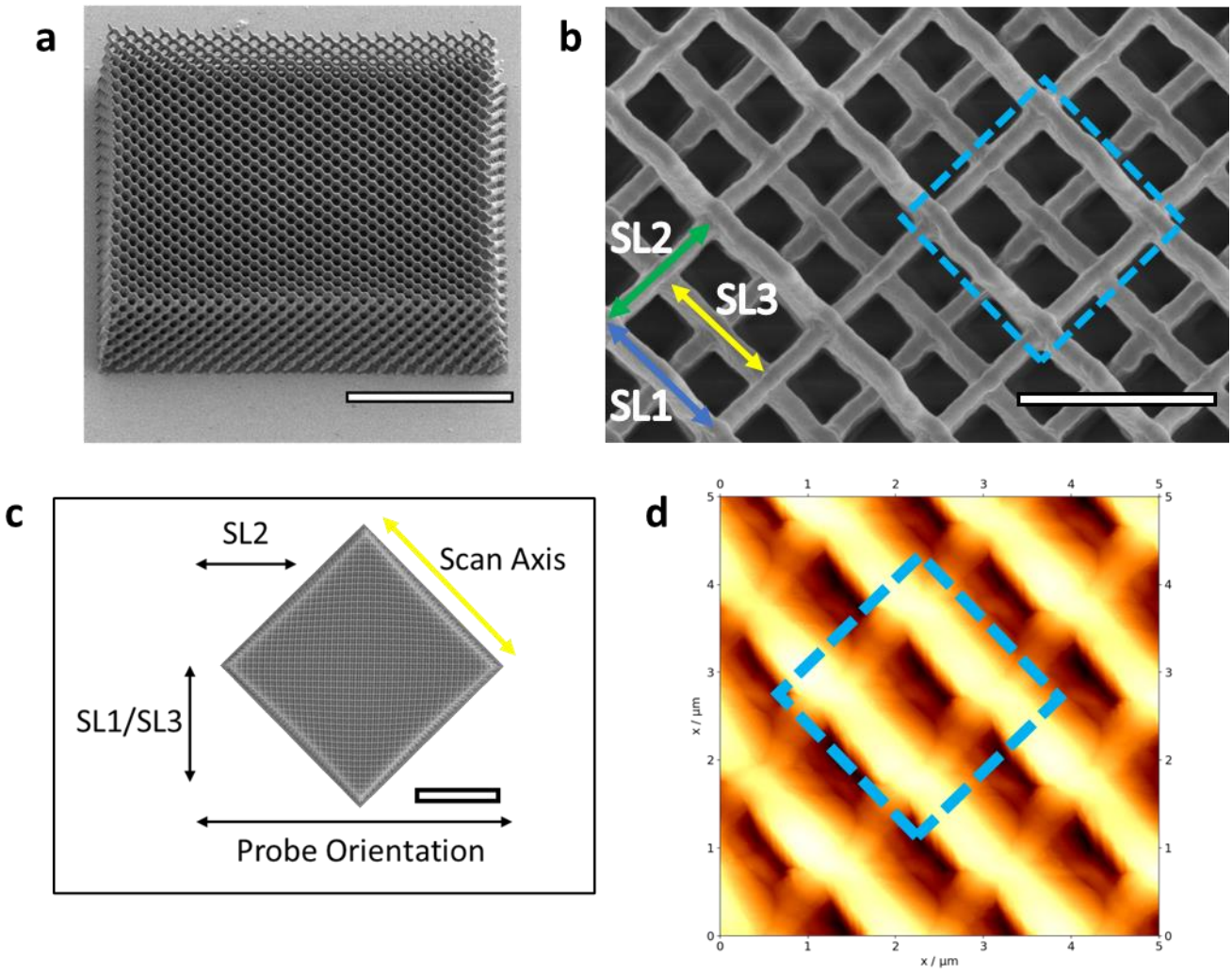

Figure 42: (a) *A SEM micrograph tilted at a 45-degree angle showing a representative 3D ASI lattice. Scale shown* $20\ \mu m$. ***(b)*** *A top-down perspective of the lattice with highlighted region of interest (ROI). Directions of SL1/SL2/SL3 sub-lattices shown. Scale shown* $2\ \mu m$. ***(c)*** *Top-down SEM with orientation of SL1/SL2/SL3 sub-lattices shown. Scan axis and probe orientation relative to sample shown. Scale shown* $20\ \mu m$. ***(d)*** *Resultant AFM image with ROI shown, SL3 layer visible.*

MFM was performed using a Bruker (Dimension Icon) scanning probe microscope utilising tapping mode, see Section 3.2.2. Ultra-low moment ($0.25 \times 10^{-13}\ emu$) probes were consistently magnetised along the tip axis utilising a $0.5\ T$ permanent magnet. MFM techniques have been optimised to increase the interaction between the MFM tip and the concealed SL3 layer. This was done by increasing the height at which the MFM tip is poised above the upper surface of the sample and concurrently increasing the drive amplitude of oscillations of the tip allowing measurements deeper into the lattice. An increase in the tip's

height above the sample allowed for a necessary safeguard against tip-strike when probing the SL2/SL3 wire layers, however this elevation typically correlates with a reduction in resolution due to the greater distance between the tip and sample surface. To compensate for this potential loss in resolution and reduce probe to sample surface distance an increase in drive amplitude is used. The combination of height adjustment and drive amplitude increment was chosen to strike a balance between accessing the SL2/SL3 wire layers, avoiding tip-strike and maintaining an optimal signal-to-noise ratio.

Samples were situated on the scanning probe microscopy stage such that the SL2 sub-lattice is parallel to the probe cantilever. A 45-degree scan angle relative to the SL1 sublattice was used during data collection, this arrangement is shown in **Figure 42c**. As a result of this arrangement during measurement broadening of the SL1 layer previously observed [42] due to the chosen axis of measurement and probe geometry was reduced, therefore gaining access to the SL3 wire layer, see **Figure 42d**.

In addition to these enhancements, a processing procedure is employed to mitigate the impact of topography on the MFM phase image. By subtracting the topological information from the MFM phase image, the methodology used in this thesis ensures that the data obtained accurately represents the magnetic characteristics of each layer, minimizing any potential confounding topological factors. This developed approach to MFM aids in exploring the complexities of the 3D ASI structure, providing a deeper and more precise understanding of how the SL3 layer's magnetism works. As a consequence of this processing step, while magnetic contrast is enhanced, the precise measurement of the phase change becomes unfeasible due to the applied processing procedure.

To verify consistency of contrast upon sample 180227AA with previous research [43], a saturating field reversal study was conducted, see **Figure 43**. A saturating field of strength $30\ mT$ was applied along the unit vectors $(1, -1, 0)$ and $(-1, -1, 0)$. Contrast visible upon the SL1 surface layer and SL2 layer shows good agreement with previous research with ferromagnetic ordering seen along both sub-layers. Lobes of strong positive contrast are seen across the upper-left of the nanowires with negative contrast in the bottom-right. Across the SL2 sub-lattice lobes of bright contrast are found in the top-right with dark contrast found in the bottom left. A field of $30\ mT$ was then applied along the unit vectors $(-1, 1, 0)$ and

$(-1, -1, 0)$. Contrast is seen to invert upon SL1 whilst SL2 contrast is visibly unchanged providing confidence in the magnetic properties of this sample and agreement with past results. To further confirm these observations of magnetic contrast, separate scans with reverse tip magnetisation were conducted and showed contrast inversion (not shown).

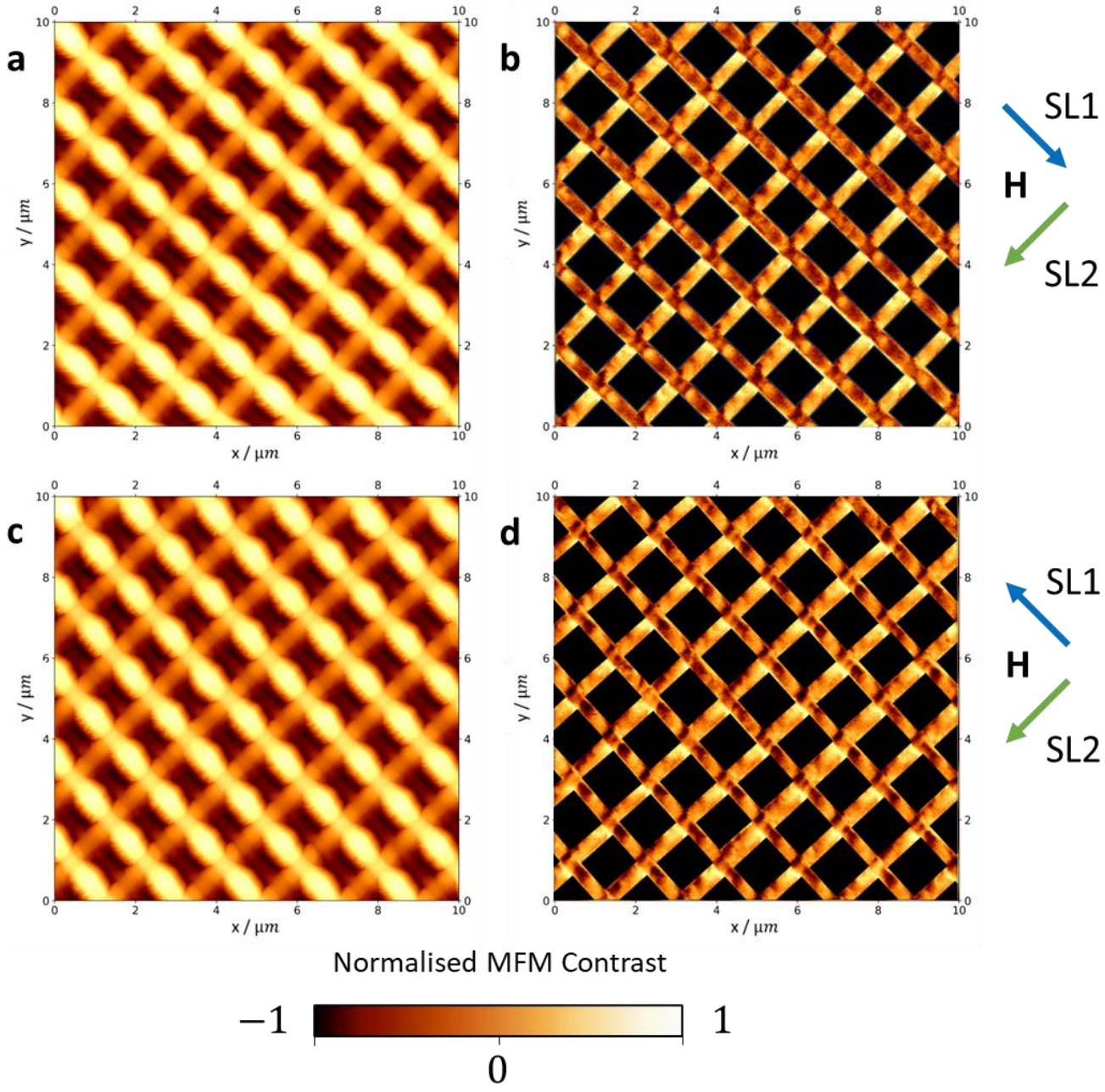

Figure 43: *Field saturation study conducted on 180227AA.* ***(a-b)*** *AFM and MFM of lattice measured post application of* $30\ mT$ *along* $(1, -1)$ *and* $(-1, -1)$. ***(c-d)*** *AFM and MFM of lattice measured post application of* $30\ mT$ *along* $(-1, 1)$ *and* $(-1, -1)$. *Field direction and sub-lattice layer arrows shown. MFM images masked for comparison with previous data.*

To prepare lattices for measurement, the lattices on sample 180227AA were subjected to a demagnetising protocol following methodology described in previous literature [68]. The sample underwent rotation at a speed of 1000 revolutions per minute, oriented with its axis perpendicular to the substrate plane, within an alternating field electromagnet. The magnetic field initiation commenced at $0\,mT$, ascending to $75\,mT$ at a rate of $2.5\,Ts^{-1}$, remaining constant for 1 second. Subsequently, the field reduced at a rate of $2.5\,Ts^{-1}$ to $-75\,mT$ and sustained this value for an additional 1-second duration. This cyclic process persisted as the field reduced, gradually diminishing in strength over a cumulative period of five days.

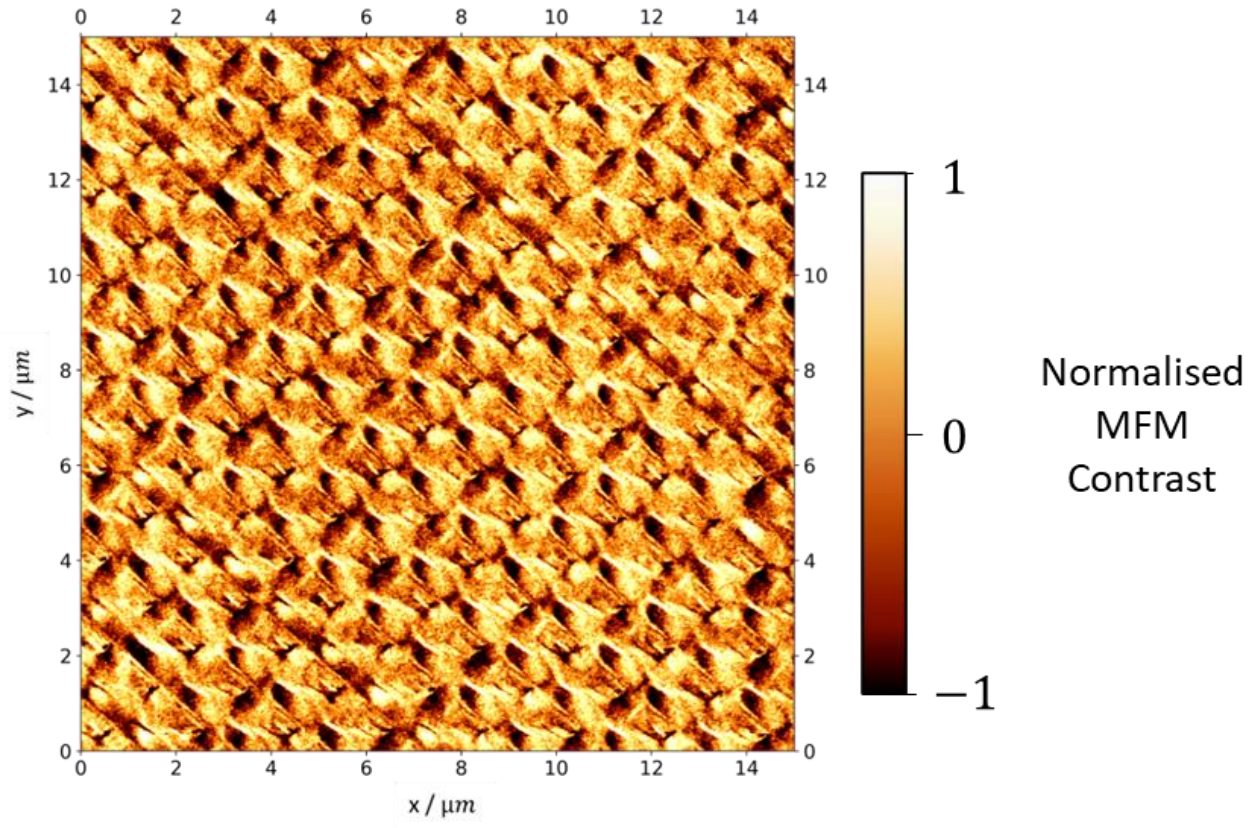

Figure 44: *A representative* $15\,\mu m \times 15\,\mu m$ *MFM image of a lattice on 180227AA after applying demagnetisation protocol.*

Several scans of size $15\,\mu m \times 15\,\mu m$ were conducted across the lattices following the demagnetising protocol revealing a rich array of vertex types. Line profile scans were used to explore the vertex types uncovered following the demagnetisation procedure. To maintain consistency with earlier work, this thesis interprets MFM contrast where high to low phase contrast signifies the orientation of magnetisation. Line profile measurements aided in

determination of overall phase change through location of peak and trough contrasts, cross-referenced with wire and vertex positions. This process involved loading the MFM image into an image processing software, ImageJ, and generating a line-profile spanning the entire length of the wire for interpretation. Line profiles were commonly set to a width of $\sim 30\ px$ to account for contrast across the entire widths of wires rather than focusing solely on the central region. Line profile graphs show a value proportional to phase on the Y-axis because of the topography processing procedure, see Section 3.2.4.

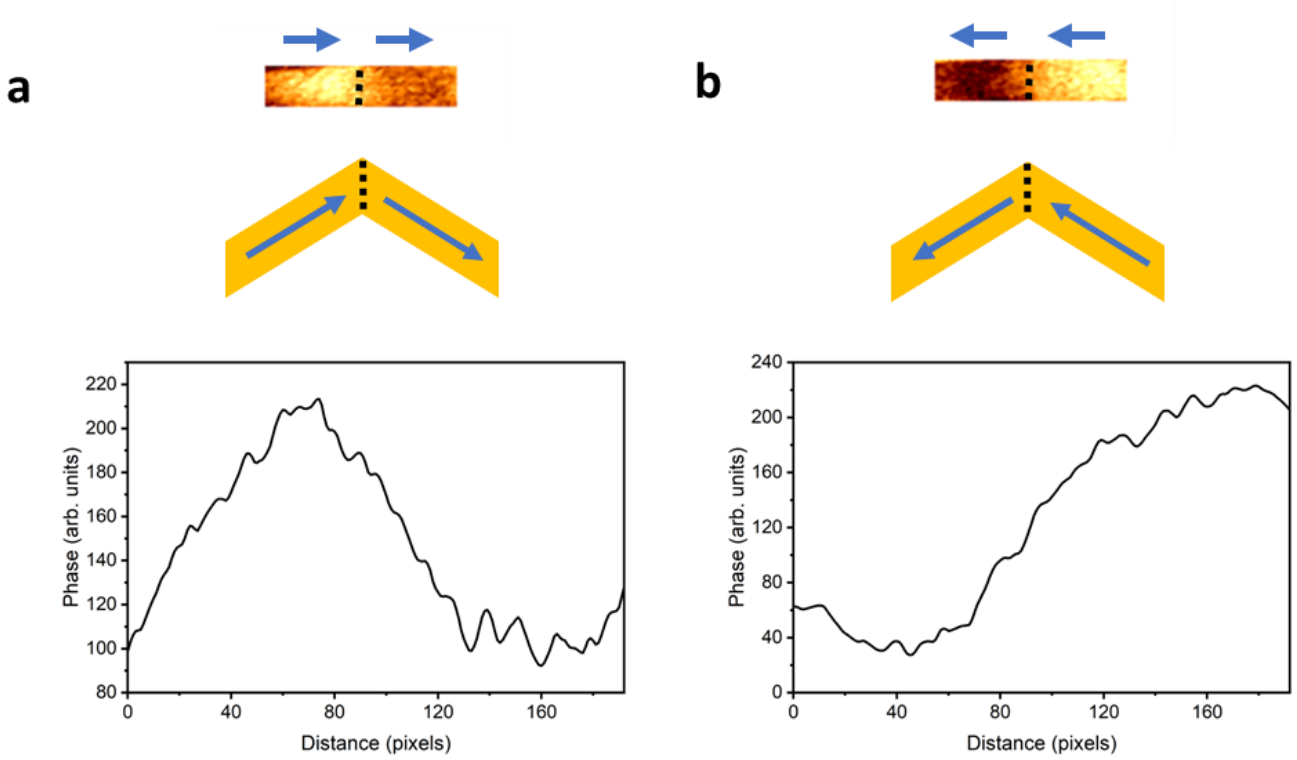

Figure 45: *SL1 vertex contrast of coordination-two vertices with opposing M_x direction. Side profile view of coordination-two vertices shown. Dotted line indicates bipod vertex. Line scans of vertices shown.*

Line scans of identified opposing M_x coordination-two vertices are shown in **Figure 45**, comparison with previous results shows good contrast agreement [42, 43]. Line scans identify the pattern of contrast change across bipod vertex. Overall contrast distinctly changes across constituent wires resulting in clear identification through visual inspection.

In this thesis finite element simulations were conducted to represent all 16 possible vertex states, previously defined in Section 1.5.3. This was done to further facilitate comparison

between simulated MFM contrast and experimentally observed vertex types. This also enabled elucidation of the simulated spin texture for each vertex type. The simulations were produced using the software NMAG using the geometry of a tetrapod defined using dimensions used using fabrication of experimental samples. Micromagnetic simulations were setup and performed by Arjen Van den Berg. All analysis upon output datasets were performed by Edward Harding.

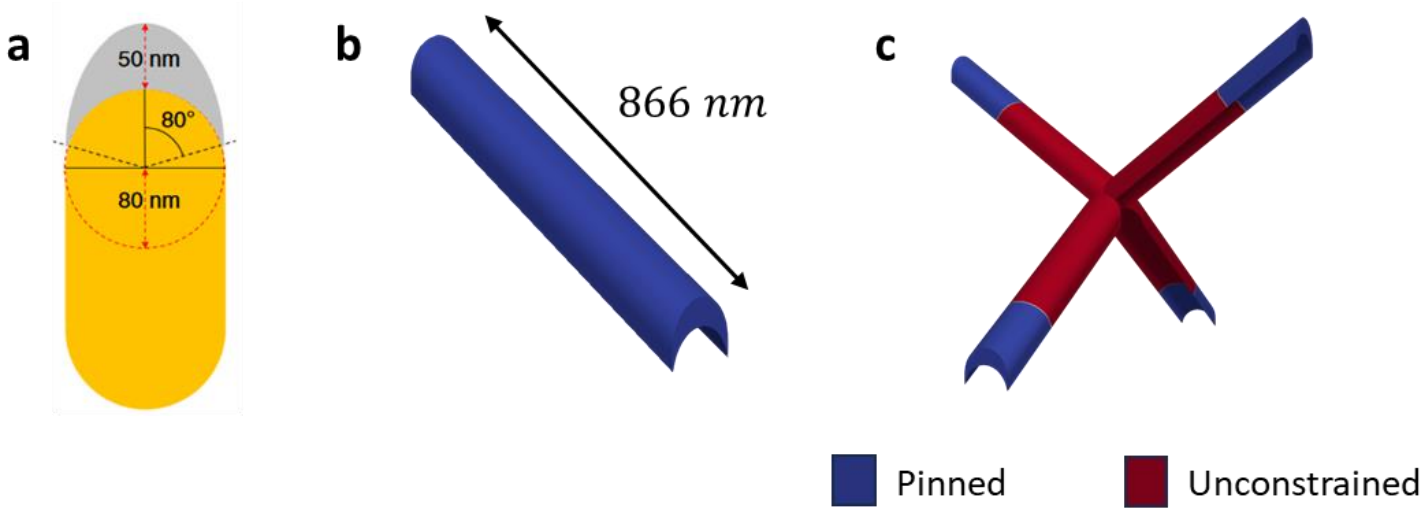

Figure 46: Geometry of simulated tetrapods. (a) *Cross-section of wire polymer and deposited* $Ni_{81}Fe_{19}$ *used for generation of nanowire geometry [2].* ***(b)*** *Single nanowire for generated tetrapod.* ***(c)*** *Pinning setup used throughout simulations. Regions in blue were pinned along long axis of individual nanowires dependent on required vertex to be simulated.*

The tetrapod mesh incorporates a defining element: the crescent-shaped cross-section of the $Ni_{81}Fe_{19}$ nanowire. Following prior research [42, 43], the mesh was designed to mirror similar dimensions, see **Figure 46a**. The wires feature a crescent-shaped profile, where the arcs subtend a $160°$ angle. To achieve this, the inner arc originates from a circle with an $80\ nm$ radius, aligning with the $160\ nm$ lateral dimension of the TPL system. The outer arc follows an ellipse with an $80\ nm$ minor radius and a $130\ nm$ major radius, resulting in a gradual thickness change of $50\ nm$ across the structure. For computational feasibility, the wire length was fixed at $866\ nm$, see **Figure 46b**. All geometries were meshed using adaptive spacing, ranging from a minimum of $3\ nm$ to a maximum of $5\ nm$. The required vertex states were achieved by arranging a range of pinning parameters prior to relaxation. The process

involved deliberate fixation of the wire ends, aligning magnetisation either inward or outward along the long axis of the individual tetrapod nanowires, toward or away from the vertex. Subsequently, the system was relaxed to achieve the desired vertex state.

To estimate the contrast obtained through MFM, an alternative method based on the divergence of magnetisation ($\nabla \cdot M$) is used. MFM contrast is known to be sensitive to the second derivative of the out-of-plane magnetic field with respect to z $\left(\frac{d^2H_z}{dz^2}\right)$. An approximation of this can be obtained simply by calculating the divergence of magnetisation according to the equation [2]:

$$\nabla \cdot \mathrm{M} \;=\; -\nabla \cdot \mathrm{H} = -\left(\frac{\partial H_x}{\partial \mathrm{x}} + \frac{\partial H_y}{\partial \mathrm{y}} + \frac{\partial H_z}{\partial \mathrm{z}}\right) \qquad (126)$$

Here, $\nabla \cdot M$ represents a volume magnetic charge density ρ, which is employed as an approximation of the simulated MFM contrast. This is due to it representing the location of magnetic poles within the material, and these act as sources for the field being imaged. Equation (126) indicates that the volume magnetic charge density is proportional to the negative derivative of the stray field H with respect to all three components. Therefore, though only a first derivative is considered this serves as an approximate indication of the MFM contrast and has been used previously in literature [42, 43]. By adopting this approximation, an insight into the MFM contrast can be obtained without explicitly calculating the stray field distribution around the nanostructure and then performing differentiation within the scanning plane.

Using these tools and training on demagnetised datasets a range of vertex types were identified and their spin textures examined and compared with MFM and simulated MFM contrast. This data is shown in full in Section 8.2, though a discussion of the key findings and results is provided in Section 4.4. These examples were then used to aid in identification of the broader demagnetised datasets through a process explained in Section 4.5.

4.4 Experimental and Simulated Vertex Types Discussion

The showcased demagnetised datasets have effectively presented examples of all vertex types, accompanied by a comprehensive explanation of the identification methodology employed, see Section 8.2. In particular, comparative SL1/SL2 monopoles have been successfully identified, demonstrating notable alignment with previously documented instances in literature. Notably, previously undiscovered Type 1 vertices have been revealed, shedding light on their magnetic contrast pattern.

Upon examining the simulated spin texture of these newfound Type 1 vertices, an intriguing observation emerged: the presence of an anti-vortex domain spin texture oriented either into or out of the plane, contingent upon the orientation of constituent wires. This has been previously discovered in micromagnetic simulations of connected 2D artificial spin ice [74]. This finding suggests a polarity differentiation among Type 1 vertices, with their configuration being directed either out of or into the plane. However, to ascertain whether each Type 1 state can exist with either polarity—essentially indicating a potential degeneracy in polarity—further simulations are imperative. These additional simulations aim to probe the possibility of each Type 1 state existing in a manner that allows for both polarities, thus revealing potential complexities within these vertex configurations. The discovery of the anti-vortex wall and its associated rise in exchange energy offers an initial explanation for the anticipated elevation in energy expenditure linked to this vertex type [42, 43]. Consequently, this circumstance positions Type 2 vertices as the most energetically favourable among the vertex types within this 3D ASI.

The distinction between two variations of Type 3 vertices has been established by scrutinizing the spin structure. Prior research [2, 3] predicted a divergence in energy cost of approximately 12%. This discrepancy is attributed here to the variance in spin texture reliant on the orientation of wires directed into or out of the vertex.

Two variations have surfaced: one exhibiting an anti-symmetric domain wall, akin to micromagnetic simulations of Type 3 vertices on a 2D connected square ASI [74]. Another variation, revealed in **Figure 108** and **Figure 110**, showcases a novel symmetric domain wall. This distinct configuration unveils point sources/sinks of magnetisation on the lower

connecting wires, resulting in visually striking bright or dark lobes in magnetic contrast, respectively.

Additionally, a novel discovery emerges in the identification of Type 4 vertices, undiscovered in earlier research, exhibiting an overall charge $Q = \pm 4q$, situated on the SL2/SL3 vertices. These vertices manifest as striking, concentrated bright or dark contrasts positioned at the vertex centre, extending outward across all constituent wires. Notably, Type 4 vertices exhibit such intense contrasts that they can be readily recognized within a broader MFM scan, clearly distinct amidst the surrounding vertices.

The examination of spin texture in both Type 4 examples sheds light on the significant energy increase linked to these vertex types. Notably, highly energetic vortex domain walls are evident in both cases. While these structures aim to diminish magnetostatic energy, they lead to a considerable elevation of exchange energy.

In prior micromagnetic observations of 2D connected square ice [74], vortex walls were present on Type 4 vertices, yet their location differs in the 3D ASI due to its unique geometry. Unlike the 2D ASI where these walls are located at the vertex centre, in the 3D ASI, they shift onto the lower wires. Instead, a distinct configuration emerges: an anti-vortex domain wall occupies the vortex centre for $Q = -4q$, or an antisymmetric domain wall in the case of $Q = +4q$. These additional elements in the spin texture contribute to heightened exchange energy costs during their formation.

The increase in both the MFM lift height and drive amplitude of the MFM cantilever has enabled deeper measurements of the SL2 and SL3 wires within the 3D structure. The increase in lift height results in a reduction in tip strike occurring whilst measuring the SL2/SL3 layers, and the increased distance between probe and wire caused by this is reduced by an increased drive amplitude. As a result, clearer contrast is now observable on the SL2/SL3 vertices, facilitating the identification of vertex types previously unrecorded in literature. Despite a lower signal-to-noise ratio compared to SL1/SL2, meticulous analysis using line profiles and simulated comparisons has ensured confident identification of these vertex types.

The decrease in signal-to-noise is linked to the greater distance between probe and wire. Using basic trigonometry based on wire lengths $(863\ nm)$ and the tetrahedral bond angle for this diamond geometry $(35.25°)$, calculations suggest that the SL2/SL3 vertex and the minimum measuring point for an SL3 wire are at least $1\ \mu m$ below the uppermost point of the 3D ASI, namely the coordination-two bipods. For further measurements of the SL3 wires, a depth of approximately $1.5\ \mu m$ is required, a depth significantly greater than typically measured in AFM/MFM experiments. To measure subsequent layers within this structure, employing novel measurement techniques like x-ray microscopy or scanning NV centre magnetometry could prove essential. Not only would this approach potentially offer faster measurements, but it also presents a non-interacting method with the 3D ASI, a crucial consideration when dealing with a thermal system.

The identification and characterization of various vertex types on both SL1/SL2 and SL2/SL3 junctions have yielded contrast patterns crucial for interpreting magnetic configurations across a broader dataset. However, a critical consideration arises regarding the MFM contrast: are all vertex types distinctly discernible enough to be uniquely identified in large-scale images? While these established patterns aid in identifying similar vertices, the challenge lies in the potential limitations posed by increased signal-to-noise ratios (particularly on the SL2/SL3 vertices) and the presence of topological artifacts. These factors may occasionally obscure or alter the appearance of vertices, prompting a need for meticulous analysis and application of lessons learned from this study for precise vertex identification within large-scale datasets.

The observed MFM contrast on the upper surface SL1 wires closely resembles the contrast observed in both connected and disconnected 2D ASI lattices [75]. In these studies, individual magnetic nanoislands exhibited a distinct bright-to-dark pattern indicative of their magnetisation orientation. However, within this 3D ASI framework, a comparable pattern emerges across two individual nanowires converging at a coordination-two bipod vertex, notably on the upper wire layers (SL1).

Conversely, a divergence is evident when examining the lower wire layers (SL2 and SL3), where the bright-to-dark contrast can manifest over a single wire, showcasing distinctive behaviour compared to the upper surface SL1 wires in this 3D ASI structure. This deviation

can be attributed to the geometry inherent in the 3D ASI. The contrast across the coordination-two bipod vertices spreads across two wires due to the greater distance over which the orientation can align. Conversely, wires residing on layers primarily consisting of coordination-four vertices showcase a reduced working distance over which the spins must align with both coordination-four vertices they are connected to, influencing the observed contrast patterns.

However, it's crucial to acknowledge that whilst simulations provide clear and distinct phases within the vertex junction, experimental observations might exhibit a different appearance. Instead, an emphasis on comprehending the collective phase characteristics within the junction of both simulated and experimental findings is vital for vertex identification. Whilst identifying bright or dark lobes of contrast in experimental findings can provide valuable insights, the focus must extend beyond these individual features. Taking a comprehensive approach enhances the accuracy of interpreting experimental data.

When considering the influence of diverse magnetic phases observed in simulations on experimental data, it becomes imperative to consider their collective impact. This entails identifying the bright and dark lobes present on adjoining SL2 wires in SL1/SL2 vertices or SL3 wires in SL2/SL3 vertices, which significantly contribute to the analysis. Additionally, accounting for the magnetic configurations of neighbouring vertices remains crucial. This comprehensive analysis not only aids in confidently applying magnetic configurations to interpret experimental findings but also holds paramount importance in extending these orientations across a broader measured lattice area.

The goal involves leveraging these experimentally measured vertex types used in conjunction with simulations, to extrapolate magnetic configurations across a significantly larger dataset. Ensuring accurate application of these configurations is vital as it enables the determination of the ground state of this 3D ASI for comparison with the single- and double-charged crystal states predicted by Monte-Carlo simulations.

This detailed approach promises a more accurate and confident translation of simulated magnetic behaviours into real-world experimental data, essential for comprehensive understanding and interpretation.

4.5 Process for Magnetic Configuration Identification of Large Demagnetisation Datasets

In this section the process through which a large, demagnetised datasets magnetic configuration is described. This process evolved after experience and training on demagnetised datasets of size $15\ x\ 15\ \mu m$. During this training process, a range of vertex types were identified including novel Type 4 vertices, variations of Type 3 vertices and Type 1 vertices which had not been previously identified. The full results of these vertex type identification, with examples shown and simulated contrast and spin textures of their respective vertex types are shown in detail in the appendix in Section 8.2. These examples produced a library of common vertex types that could be used for comparison with the larger datasets for identification of those vertices within the larger images. However, not all vertices nor wires measured were as clear as those examples shown, and a holistic method of approach to identification was required to produce the full magnetic configuration maps shown in Section 4.6. This process is now described in order:

Identify SL1 (Top Layer)

- Clear Contrast Identification: Use high-resolution images to identify both wires forming the upper surface bipods. Apply arrows onto vertex map indicating the direction of magnetisation across the entire region being examined.
- Weak Contrast Confirmation: If the contrast is weak, use line profiles to confirm the direction of contrast change (see **Figure 45**).
- Monopole Identification: Identify monopoles on the upper surface bipods by looking for areas of extreme brightness or darkness.
- Vertex Junction Monopoles: Identify monopoles at the SL1/SL2 vertex junctions, focusing on $\pm 4q$ monopoles, though Type 3 monopoles may also be visible.
- Artifact Identification: Compare the dataset of applied arrows with unprocessed MFM data and reversed tip MFM images to identify and account for any artifacts.

Identify Clear SL2 Wires (Middle Layer)

- Clear Examples: Identify 50-70% of SL2 wires through bright/dark nodes and use of bright to dark contrast pattern across individual wires. These hallmarks can be clearly seen and confirmed with line profiles where uncertain. Bright nodes connecting an SL2 wire with the Sl1/SL2 junction indicate a configuration pointed away from the junction, whereas dark nodes indicate the reverse.
- Vertex Comparison: Compare SL1/SL2 junctions with known vertex types library and with simulated MFM contrast.
- Monopole Verification: Strong bright/dark contrast at the vertex junction suggests a monopole; ensure this is consistent with surrounding arrows.
- Artifact Check: Compare with unprocessed MFM data and reversed tip images to identify artifacts.

Identify Clear SL3 Wires (Bottom Layer)

- Clear Examples: Identify significant proportions of SL3 wires through bright/dark nodes and use of bright to dark contrast pattern as previously described.
- Vertex Comparison: Compare SL2/SL3 junctions with the known vertex types library.
- Vertex Contrast: Assess overall contrast at SL2/SL3 junctions. Darker centres suggest $+2q$ or $+4q$ vertices, whilst brighter centres suggest $-2q$ or $-4q$ vertices.
- Artifact Check: Compare with unprocessed MFM and reverse tip images to identify artifacts on these wires.

Once these initial steps are complete, most wires magnetic configurations will have been placed in a consistent and confident manner. The next steps on uncertain wires require a more holistic approach, considering all connected and neighbouring wires and the potential configurations produced when a single wire is considered directed into or out of a vertex. These steps are to be carried out for a single wire before making a final decision, and then the process begins again for the placement of the next uncertain wire. At each repeat, the area considered evolves with the new configuration suggested by previous placement providing more data for evaluation of missing wire configurations. At this point in the process, remaining unidentified vertices are unlike any of the experimental or simulated examples

shown in the library as these are expected to have already been identified by the initial steps described above. This process is completed in full for uncertain wires with each successive step within this process providing an argument for its configuration and the final wire configuration is then determined from these arguments.

1. Review a patch of vertices (approximately 5 x 5 vertices in size) across all layers and choose one uncertain wire within that region as the focus for this process.
2. Visual Contrast: For uncertain wires, consider visual contrast of all neighbouring wires and vertex arrangements. Is there a visible contrast change across neighbouring wires and this wire that indicates direction?
3. Line Profile Analysis: Conduct line profiles of wire to be considered, connected wires, and neighbouring wires to confirm magnetisation directions. Does the line profile of wire to be considered show contrast change indicating direction?
4. Vertex Charge Consideration: Evaluate the contrast of vertex junctions closest to uncertain arrow. Does the contrast indicate a charged or neutral vertex and does placement of arrow on uncertain wire determine this to be so. If it makes sense to apply arrow to make charged/neutral do so and consider the overall configuration. Does the region considered make sense?
5. Dataset Vertex Comparison: Consider other previously identified vertices within the dataset which have confident arrow placement and compare whether the contrast pattern observed is like the wire under consideration. Does such a magnetic configuration make sense in for this vertex as well?
6. If still uncertain, apply the arrow according to a best approximation of line profile measurement and mark this wire as uncertain with a clear visual marker. Move on to other wires and reconsider this one again when more of the vertex map is finished. Repeat the whole process with new information of surrounding vertices.
7. Collaboration and Resolution: If a wire remains uncertain with all wires and vertices about it confident in placement, discuss this with alternate researcher. Use markers to indicate the uncertain wires and collaboratively review magnetic configurations. Resolve discrepancies through discussion and consensus.

This process was repeated in full for both large demagnetisation datasets until a final configuration for both vertex maps was produced.

4.6 Large Demagnetisation Datasets

After initially identifying vertex types within demagnetized MFM images, a comprehensive investigation was carried out on two distinct 3D ASI lattices on sample 180227AA. Lattice Number 1 (hereafter called Lattice1) was fabricated using 31% of the maximum laser power and exposed for 0.04 seconds. In contrast, Lattice Number 2 (hereafter called Lattice2) was formed using 33% of the maximum laser power with the same exposure time of 0.04 seconds. Despite the discrepancy in laser power both Lattice1 and Lattice2 maintained nanowire widths of approximately $200\ nm$ and had not been previously examined before gathering the broader dataset. This ensured minimal damage had occurred to the lattice due to AFM tip strike. The MFM imaging involved collecting tiled windows sized at $15\ \mu m \times 15\ \mu m$, resulting in four quadrants that constituted the overall $30\ \mu m \times 30\ \mu m$ MFM scan. An example of the combined MFM image collected for Lattice1 is shown in **Figure 47**

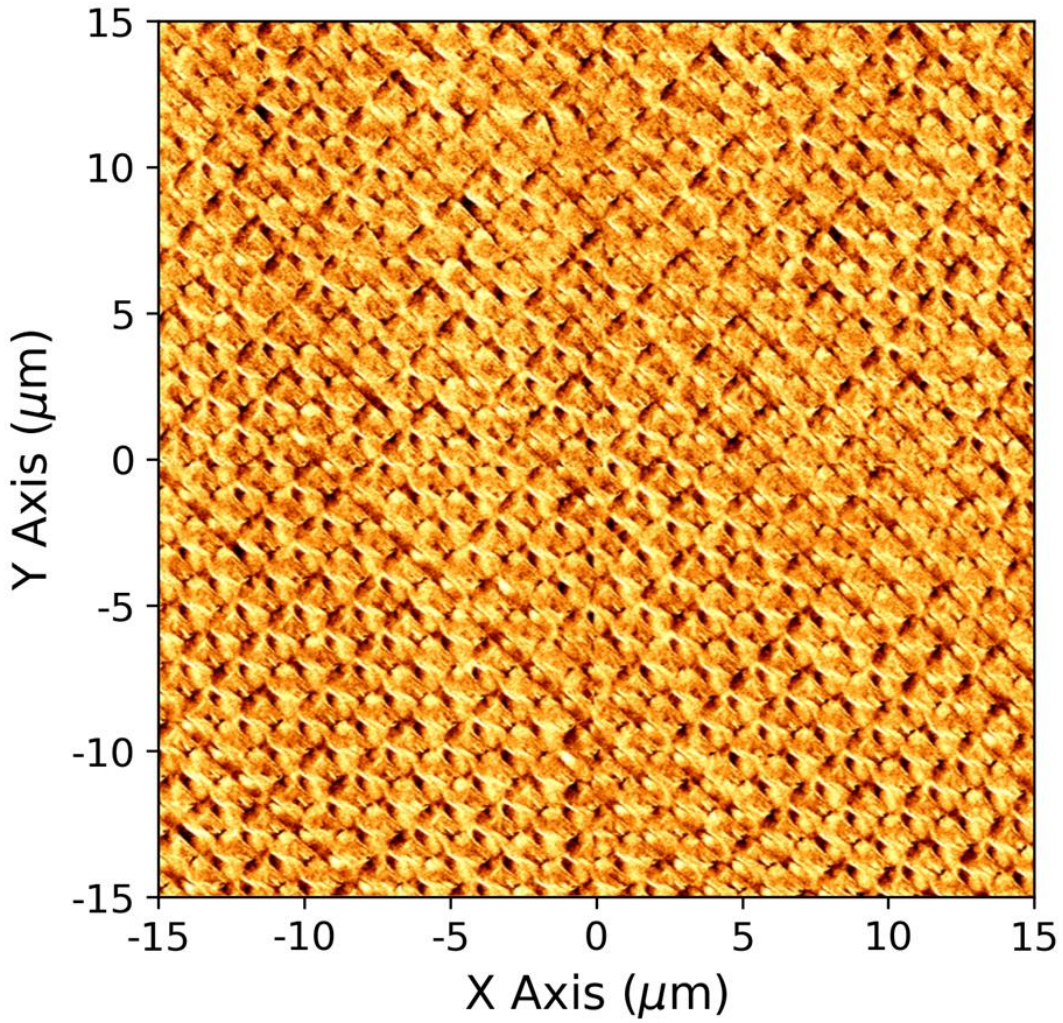

Figure 47: *An MFM image displaying a* $30\ \mu m\ \times\ 30\ \mu m$ *section of Lattice1.*

Having two independent researchers, Myself and Arjen Van Den Berg, conduct separate analysis prior to comparison of results significantly enhances the confidence in the observed MFM contrast for all Types evident in the demagnetized sample data. This approach offers a substantial advantage by allowing cross-verification and validation of results. Each independent researcher brings unique perspectives, methods, and potential interpretations of the data, reducing the likelihood of bias or oversight. This separate analysis prior to comparison was utilised on both Lattice1 and Lattice2. Any discrepancies between these analyses were thoroughly discussed and re-evaluated together using methodology described in Section 4.5 before reaching a final decision.

Using previously demonstrated vertex configuration analysis techniques, a comprehensive magnetic configuration spanning the surface layers SL1 through SL3 was generated for the

surveyed area. **Figure 48** presents a representative vertex map derived from these findings. Notably, within the measured area of Lattice1, no coordination-two monopoles were detected. This observation aligns with earlier findings indicating a higher monopole effective chemical potential and an elevated energy barrier, making the formation of such charge configurations infrequent or absent within the measured region of the demagnetized system.

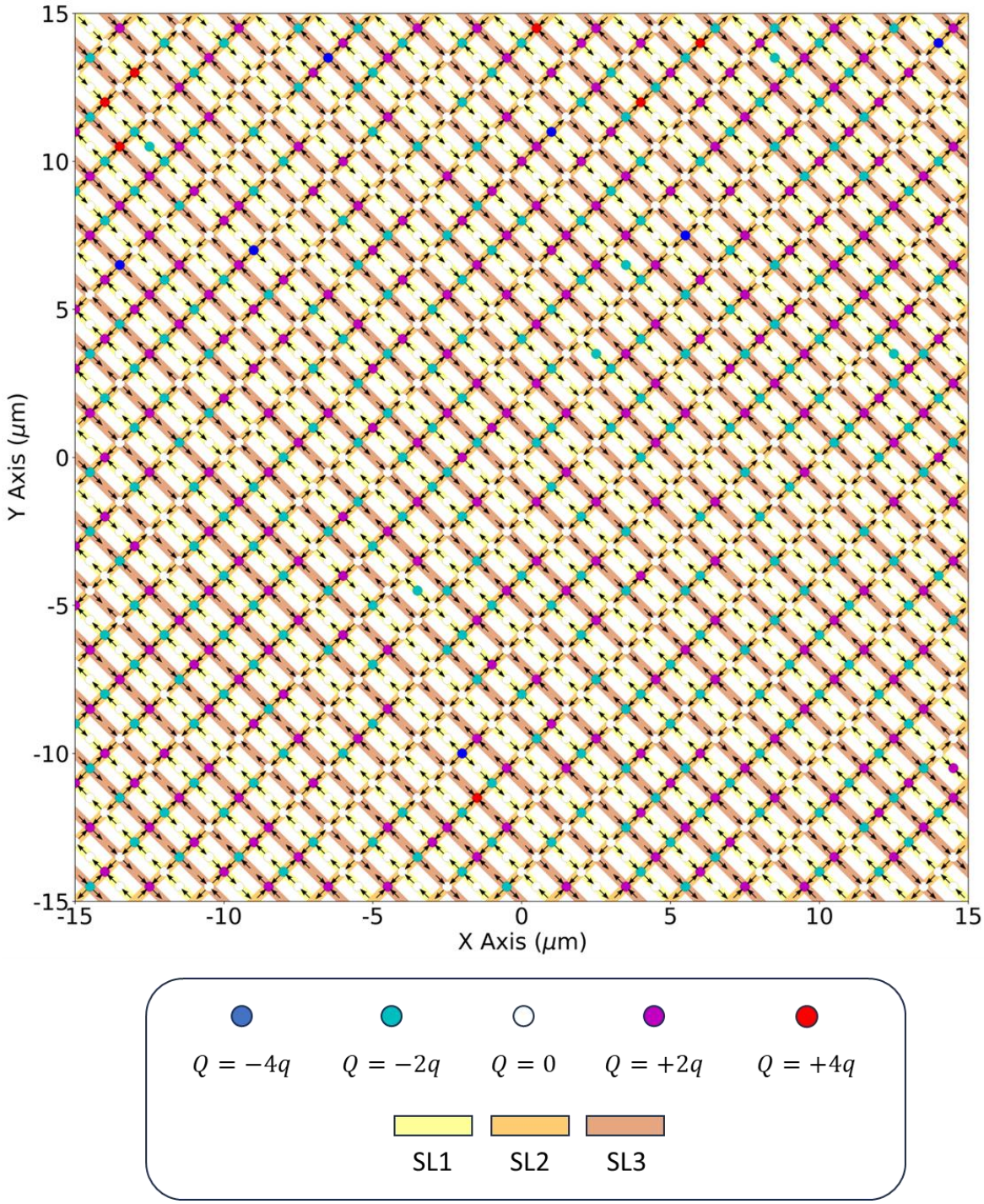

Figure 48: *Magnetic configuration vertex map produced from Lattice1 MFM. Key illustrates representative charge colour-coding along with layer colouration for easier identification purposes.*

Figure 49 displays the statistical analysis of vertex types within the measured region of Lattice1. **Figure 49a** and **Figure 49b** indicate charge neutrality within standard error, showcasing equal proportions of $\pm 2q$ and $\pm 4q$ vertex types across the measured region. The

mean charge is calculated to be $+0.025q$, with a standard error of $\pm 0.088q$ suggesting that the dataset is charge neutral. The analysis reveals Type 3 vertices comprising 62.8% of the total, followed by Type 2 vertices at 27.2%, Type 1 at 8.3%, and Type 4 at 1.6%.

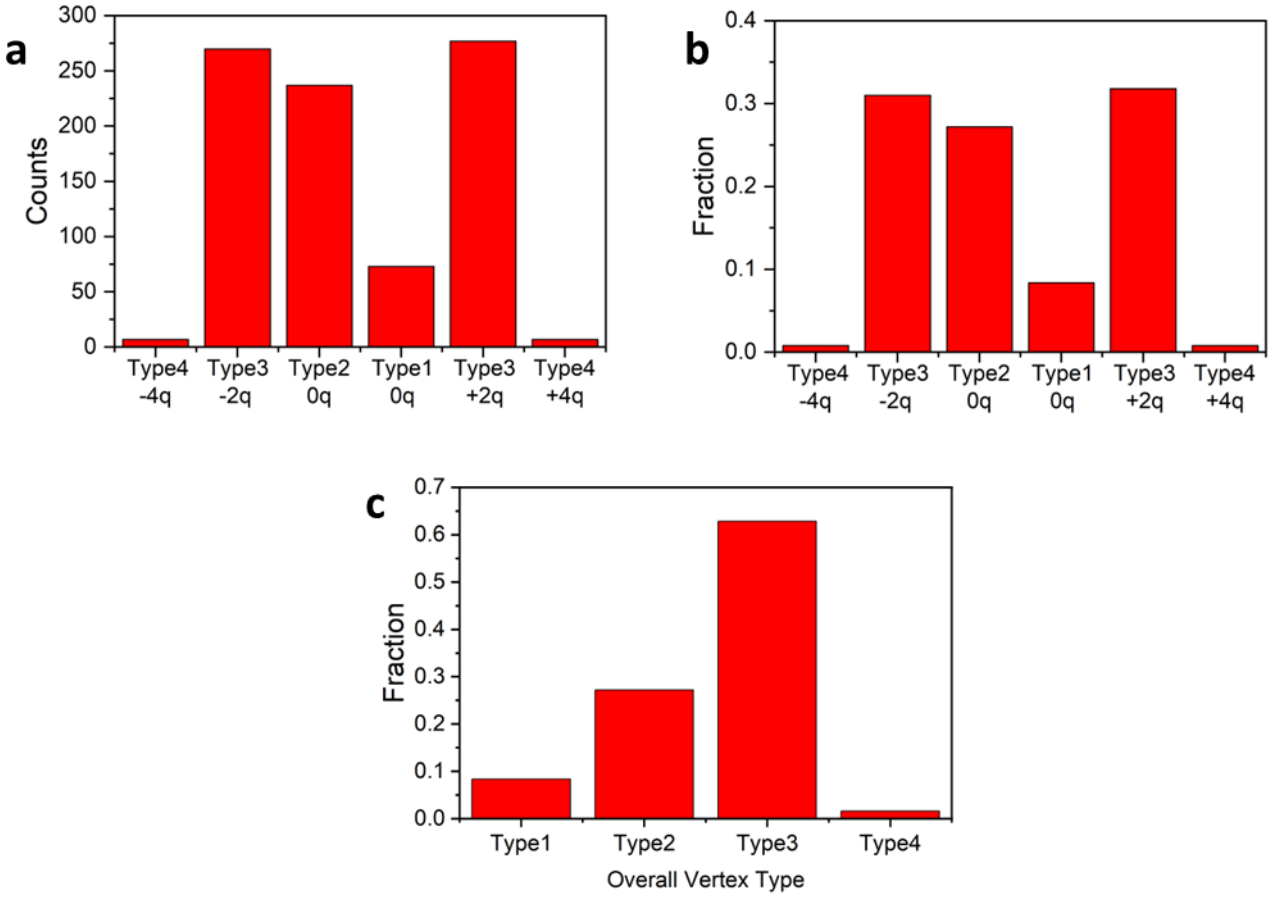

Figure 49: *Statistical analysis of vertex types present within the measured region of Lattice1, excluding coordination-2 vertices.* ***(a)*** *Illustrates the absolute count of each vertex type.* ***(b)*** *Displays the proportional fraction represented by each vertex type, separated into positive and negative charge types.* ***(c)*** *Represents the proportional fraction displayed by collated vertex types.*

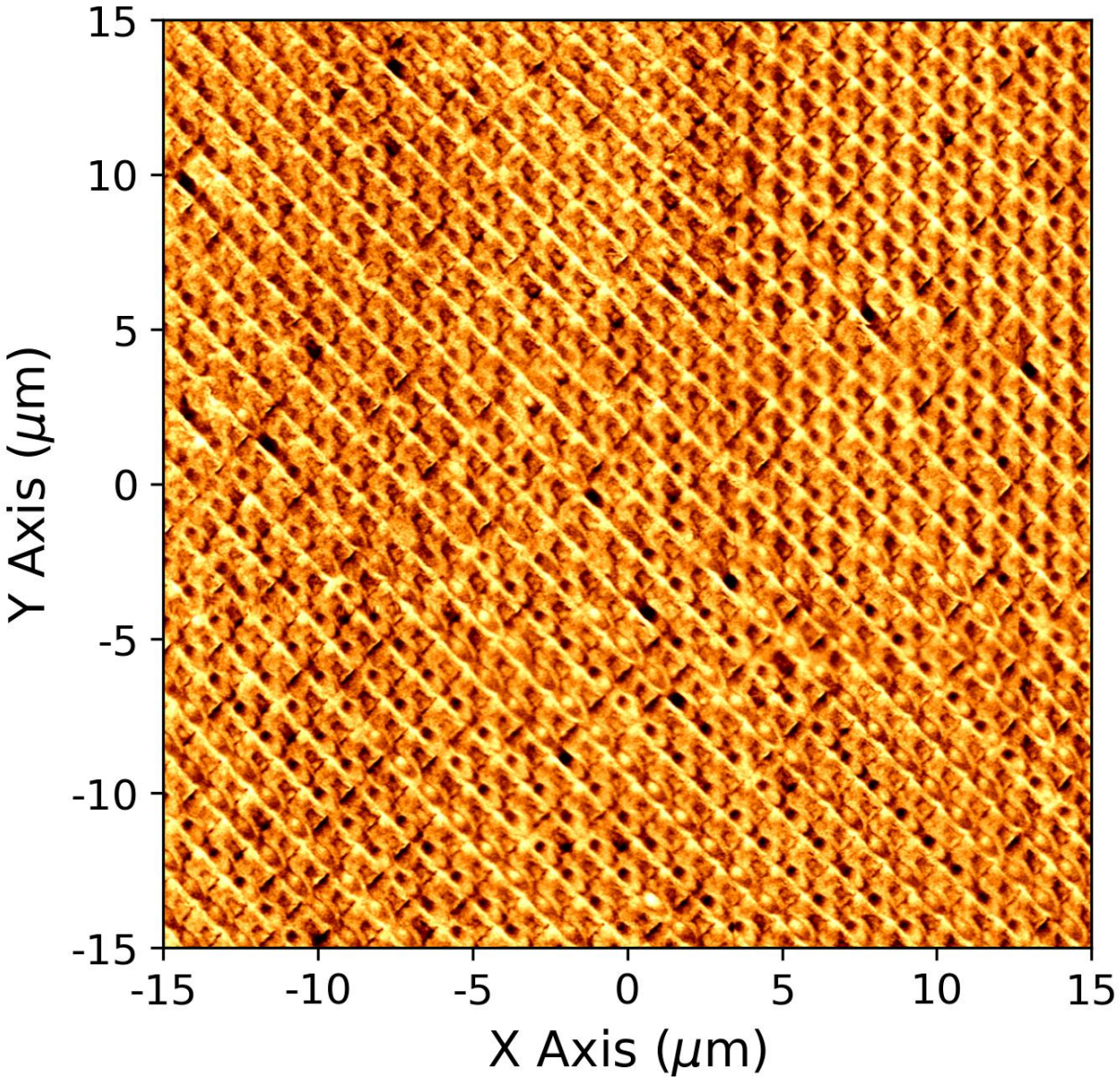

Figure 50: *An MFM image displaying a* $30\ \mu m\ \times\ 30\ \mu m$ *section of Lattice2.*

Initial analysis of the MFM of the measured region of Lattice2, see **Figure 50**, immediately identifies several rare coordination-two monopoles present within the region. Subsequent analysis of the vertex configurations across the entire region resulted in a magnetic configuration vertex map for the measured region and this is shown in **Figure 51**.

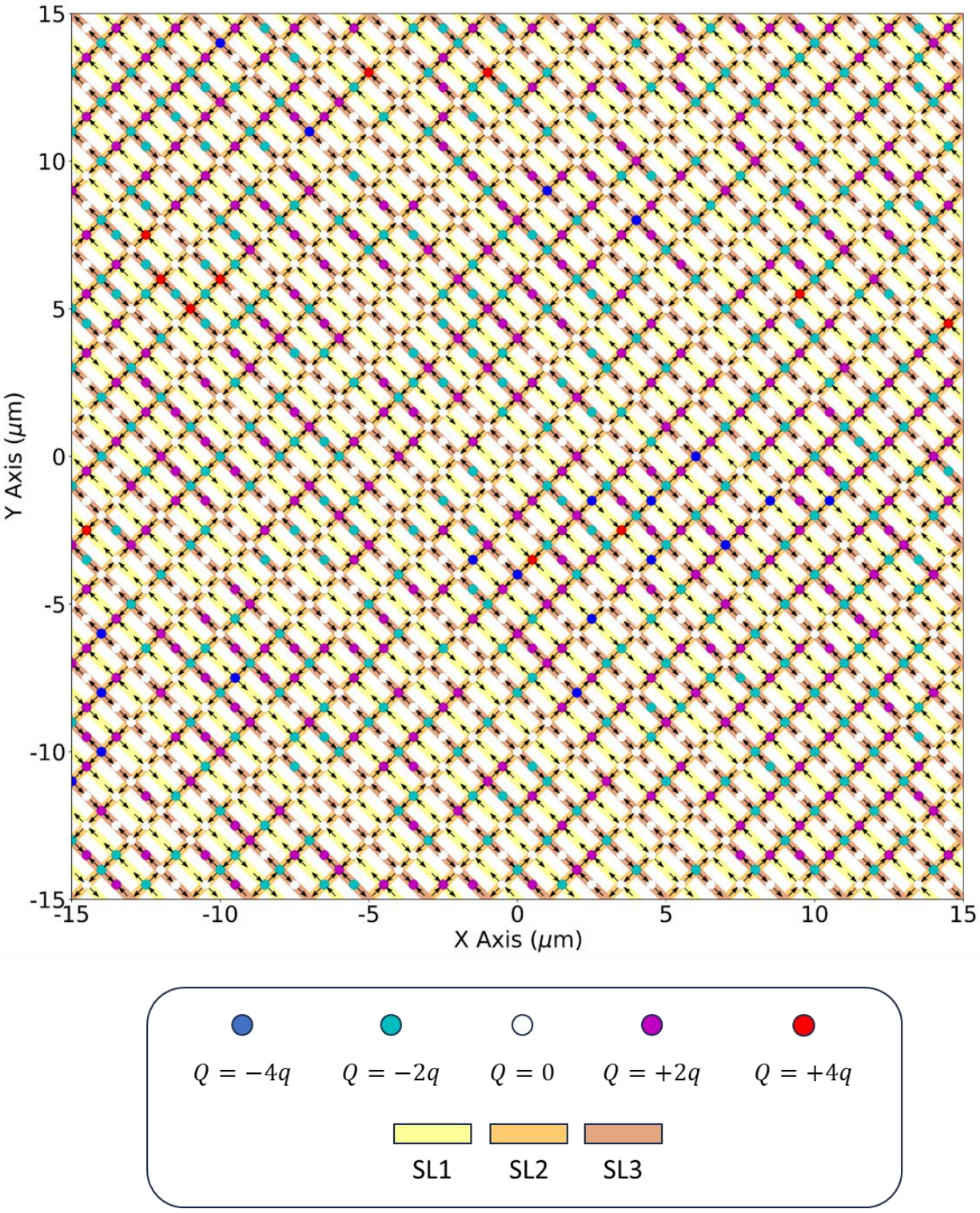

Figure 51: *Magnetic configuration vertex map produced from Lattice2 MFM. Key illustrates representative charge colour-coding along with layer colouration for easier identification purposes.*

Statistical analysis of vertex types within Lattice2 measured region, shown in **Figure 52**, identifies a similar proportion of vertex types as seen in Lattice1. Though a greater proportion

of high energy Type 4 vertices are present, charge neutrality is close to being observed across the lattice. The mean charge is calculated to be $-0.139q$, with a standard error of $\pm 0.085q$. The mean charge is slightly negative, but the standard error indicated that this deviation is within a small range, suggesting that the dataset is close to charge neutrality. The most common vertex type is Type 3 with 60.5%, Type2 with 29.5%, Type 1 with 5.7% and Type 4 with 4.2%. Overall, between both datasets it can be determined that the novel 3D geometry results in an energy landscape that results in a modified proportion of vertex types within the system compared to the expected proportion for 2D ASI geometries (Type 1 12.5%, Type 2 12.5% and Type 3 75%). The observed higher percentage of Type 2 vertices aligns with previous micro-magnetic simulations, indicating their status as the lowest energy vertex type within the 3D geometry [43].

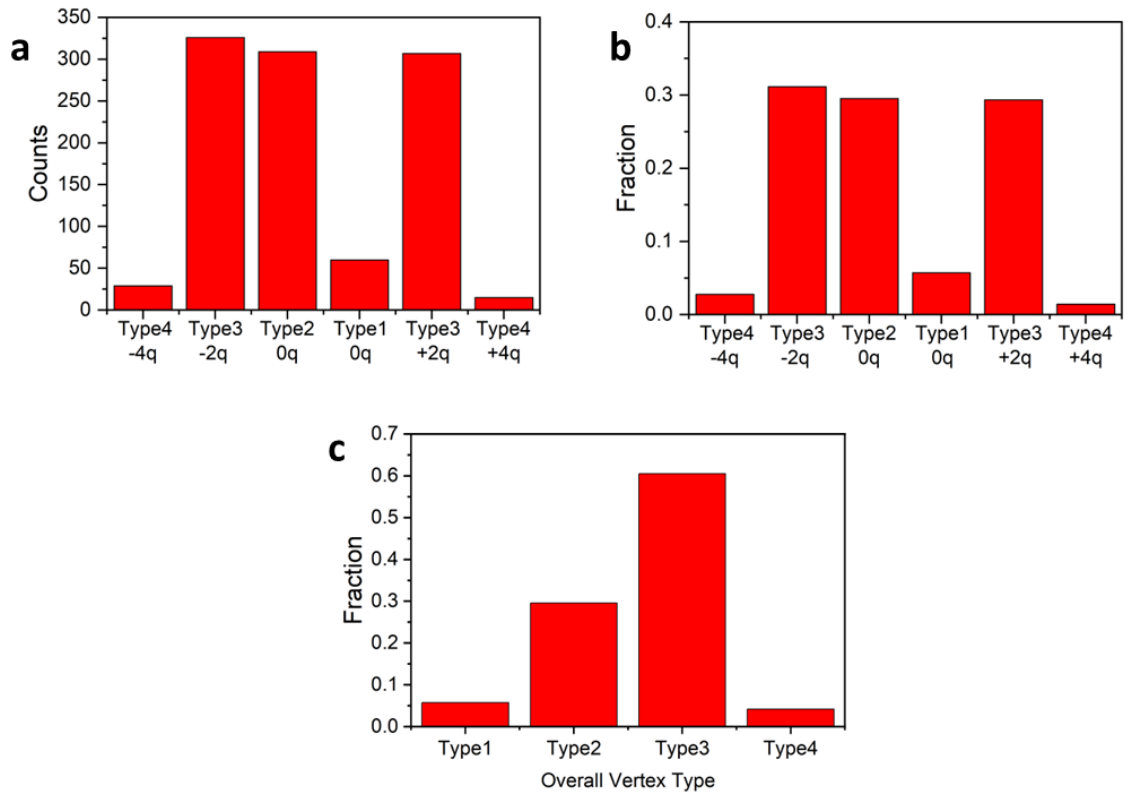

Figure 52: *Statistical analysis of vertex types present within the measured region of Lattice2, excluding coordination-2 vertices.* ***(a)*** *Illustrates the absolute count of each vertex type.* ***(b)*** *Displays the proportional fraction represented by each vertex type, separated into positive and negative charge types.* ***(c)*** *Represents the proportional fraction displayed by collated vertex types.*

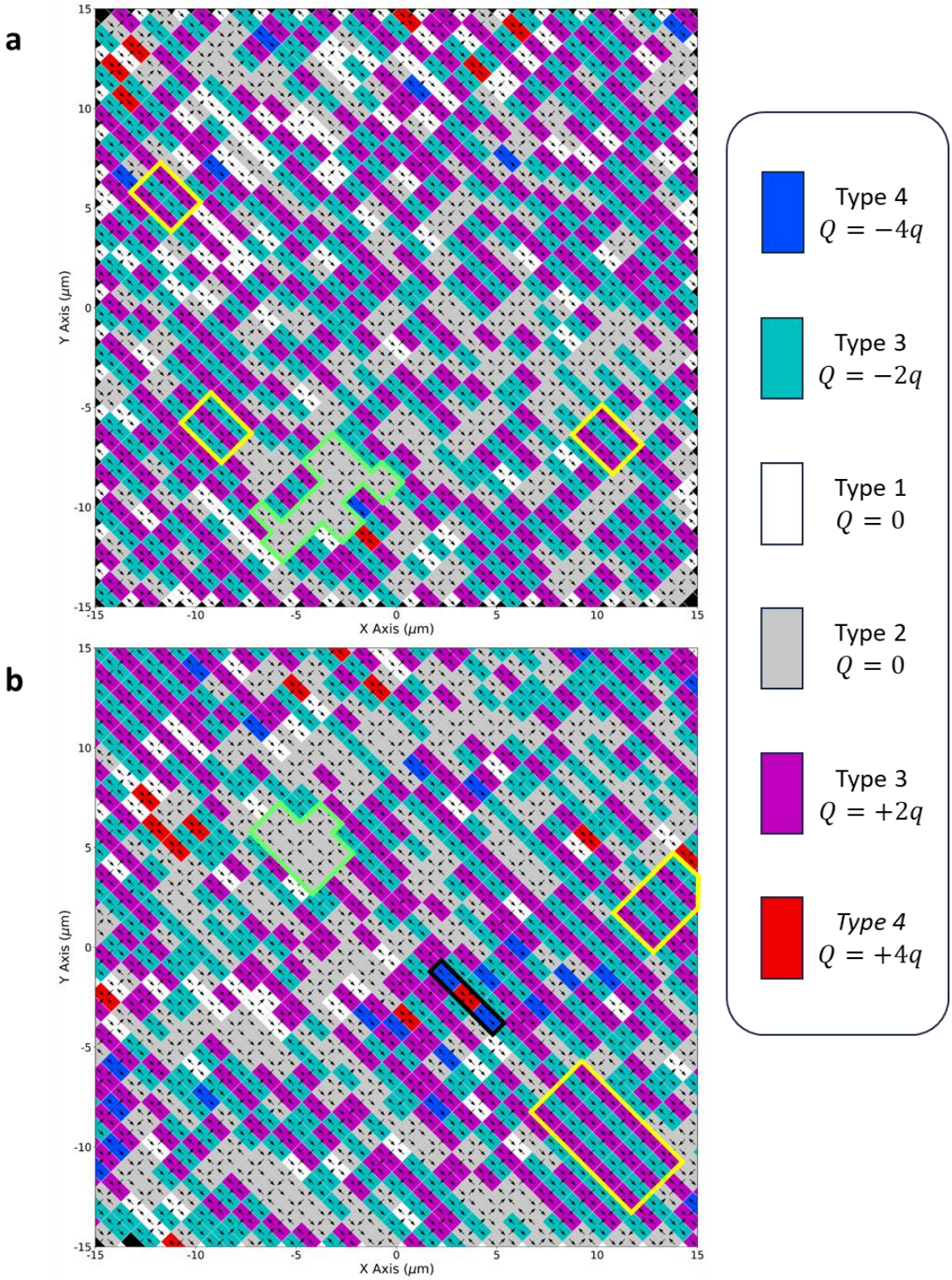

Figure 53: *Representative charge maps illustrating the measured regions of* ***(a)*** *Lattice1 and* ***(b)*** *Lattice2. Key showcases the colour assignment for each charge type, distinguishing Type 1 and Type 2 vertices* $(Q = 0)$ *separately. Coordination-two bipods have been excluded from the charge map analysis. Regions of interest in both* ***(a)*** *and* ***(b)*** *containing distinct phases have been highlighted: single charge crystallite (orange outline), examples of ice-phase with Type 2 tiling (green outline) and double charge crystallite (black outline).*

Across both datasets, extensive ice-phase backgrounds primarily composed of Type 2 vertices are prevalent. These backgrounds are more favourable due to the altered energy landscape of the 3D geometry, whereas Type 1 vertices, also frequently connected to these ice-phase regions, are comparatively less common. Superimposed on this background are alternating $Q = \pm 2q$ crystallite formations.

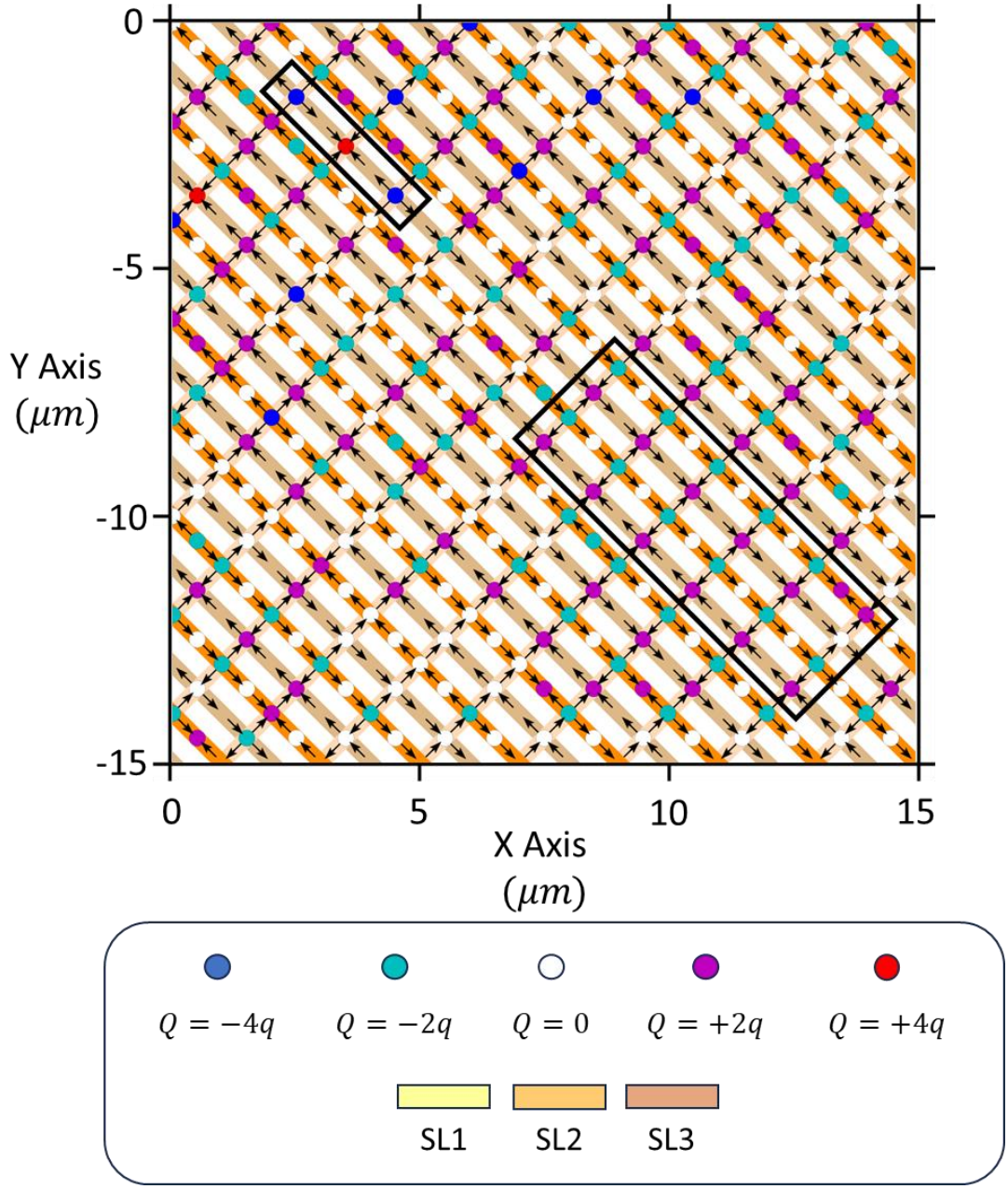

Figure 54: *Arrow map of the double crystallite region and the single charge crystallite seen. Key illustrates representative charge colour-coding along with layer colouration for easier identification purposes.*

Further examination of these datasets uncovers two additional phases. An infrequent occurrence observed solely within the Lattice2 dataset involves a double charge crystallite, encompassing two Type 4 $-4q$ monopoles enclosing a Type 4 $+4q$ monopole on the SL1/SL2 vertex. This phase is a rarity, absent across both datasets and notably absent in all previous initial measurements of demagnetized data encompassing vertex type identification. A representative vertex map, shown in **Figure 54** (taken from the bottom right quadrant of **Figure 48**), shows this double charge crystallite region, its position on the constituent layers of the lattice and the surrounding magnetic configuration.

Within regions of both Lattice1 and Lattice2, segments featuring a single charge crystallite are evident, characterized by alternating $\pm 2q$ tiling. The analysis presented in **Figure 55** of SL1, SL2, and SL3 ordering exposes that these phases emerge when SL1 and SL3 ordering exhibit ferromagnetic properties within a region, while SL2 ordering assumes an anti-ferromagnetic nature. Comparative analysis of the charge map presented in **Figure 53** with regions of antiferromagnetic ordering within the SL2 sub-lattice identify that interruptions in the ordering appear to prevent the creation of Type 4 vertices within the lattice.

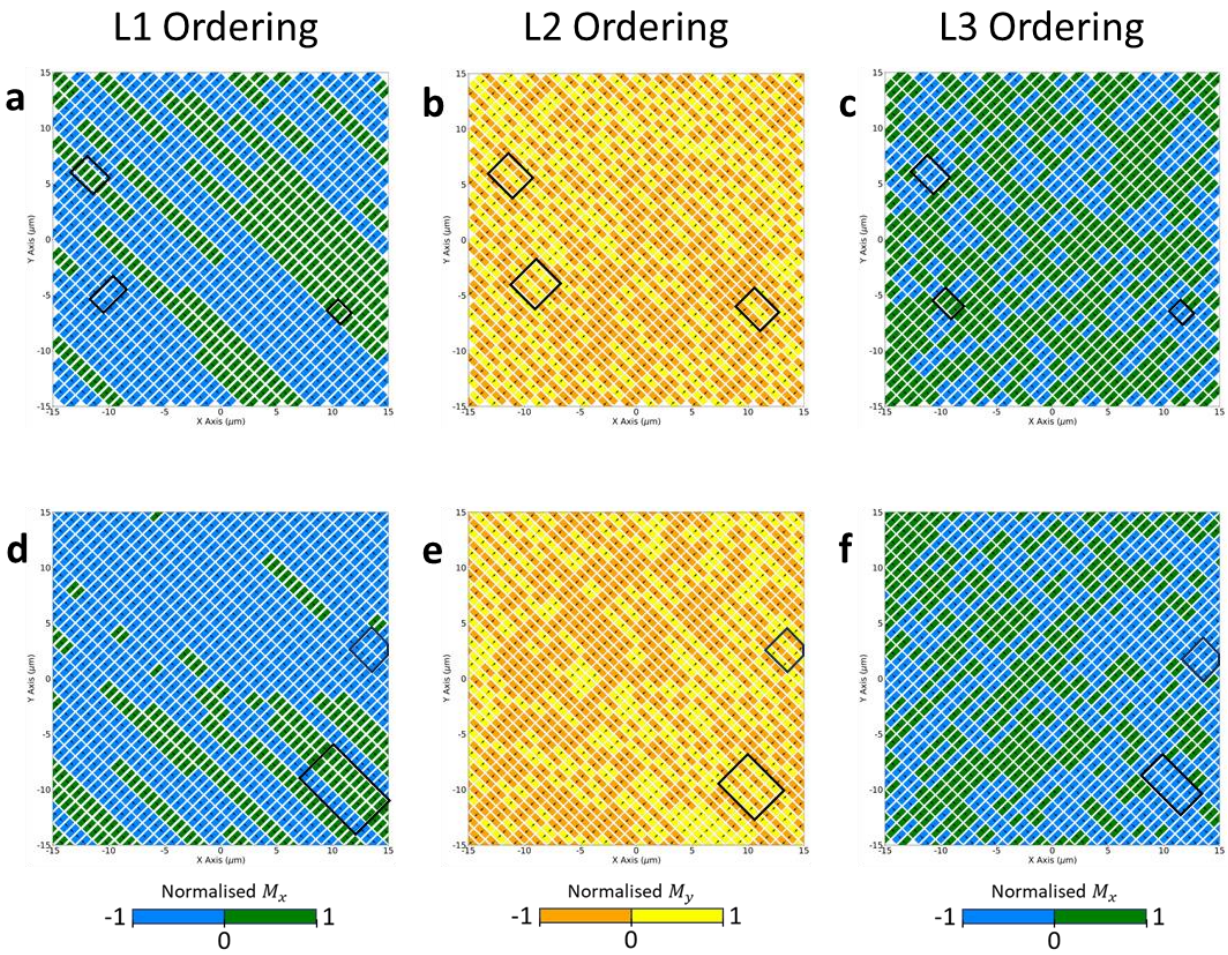

Figure 55: *Analysis of antiferro and ferromagnetic ordering present on all three sublattices for* ***(a-c)*** *Lattice1,* ***(d-f)*** *Lattice2. Regions of single charge crystallite found on* ***Figure 53*** *are highlighted with black outline.*

Upon analysing charge ordering across SL1/SL2 and SL2/SL3 vertices in both datasets, see **Figure 56**, a significant level of ordering is evident between these layers. Notably, a loss of charge neutrality is observed between SL1/SL2 and SL2/SL3 layers, resulting in an overall positive/negative charge within both layers. However, it's essential to note that overall charge

neutrality is maintained across all measured layers. It's noted that there's an inversion in the overall charge between the SL1/SL2 and SL2/SL3 layers between the two datasets.

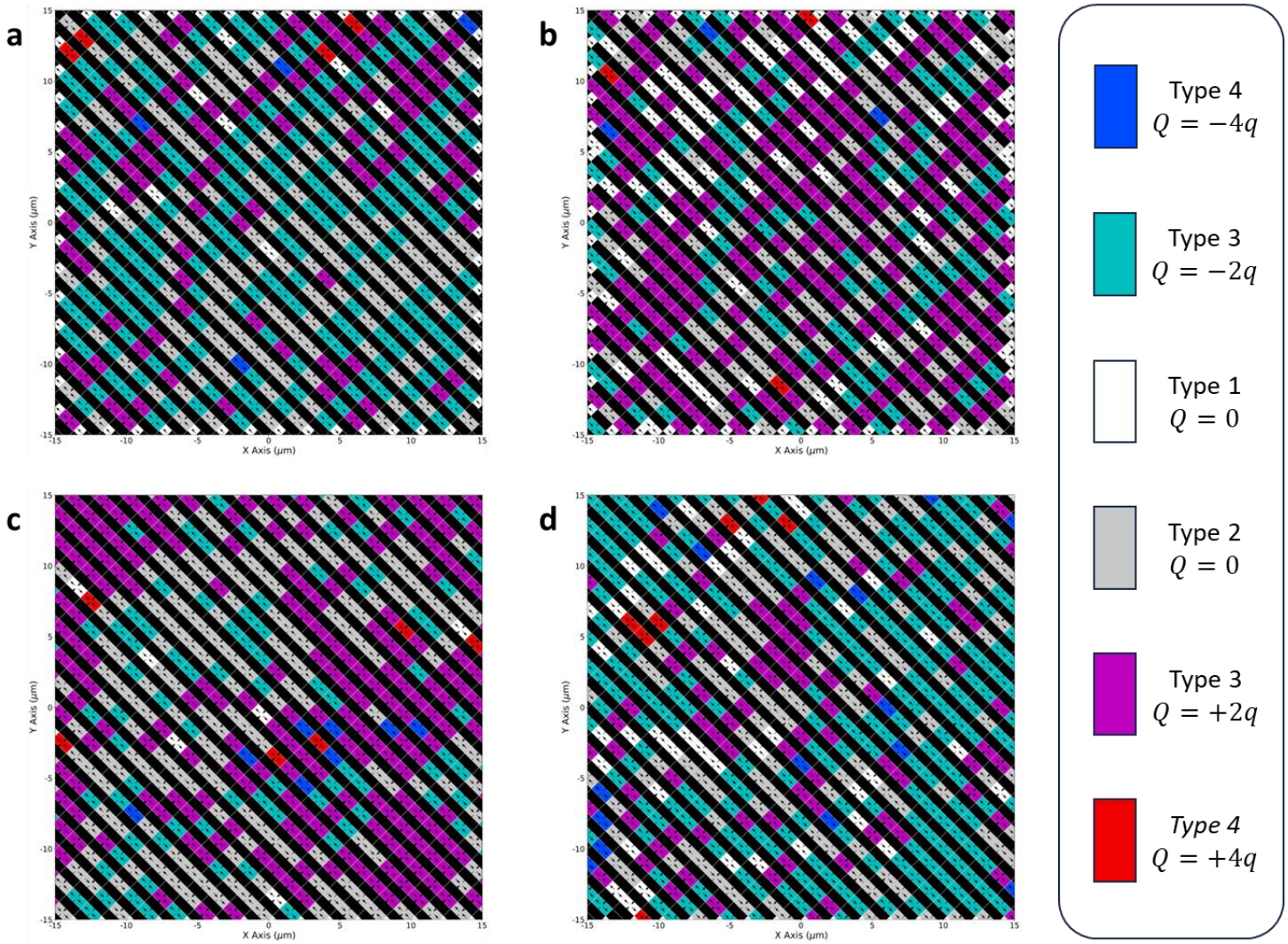

Figure 56: *Lattice1 charge maps for* ***(a)*** *SL1/SL2 and* ***(b)*** *SL2/SL3 vertices. Lattice2 charge maps for* ***(c)*** *SL1/SL2 and* ***(d)*** *SL2/SL3 vertices.*

4.7 Comparing Simulations and Data

To align the experimental findings with Monte Carlo simulations, an estimation for the ratio $\frac{b}{a}$ in the experimental lattice must be established. In the context of Monte Carlo simulations, magnetic dipoles are treated as two separated monopoles within a compass needle model [76]. The ground state of the Monte Carlo system depends on the dipole length (b) with a fixed lattice spacing (a). To compare the experimental system with the Monte Carlo simulation, an approximation for the $\frac{b}{a}$ ratio is determined. Micromagnetic simulations, known for their reliability in correlating with the identified vertices in the experimental data, were utilized for this purpose. These micromagnetic simulations, conducted by Arjen Van den Berg, were analysed by Edward Harding to derive measurements for the b/a ratio.

In this analysis, the parameter a is defined as the length between vertices, determined by the wire lengths. Parameter b is derived from a by subtracting the average domain wall width found at the wire ends. The wire lengths in both experimental and simulated datasets match prior literature at $866\ nm$. To measure domain wall widths, wires are analysed within each simulated vertex type. Using Paraview software, slices are obtained along the wire's central portion, aligned parallel to either the X or Y axis, see **Figure 57a-c**. A magnetisation plot along the primary axis direction was generated, see **Figure 57d**, starting from the vertex centre and extending along the measured wire. The domain wall width for each wire was defined as the distance along this plot where magnetisation reached 95% of the maximum measured along the wire. This process was repeated for all four wires to produce an estimation for the domain wall width.

While measuring a single component of magnetisation provides a straightforward approach to estimating the DW width, it is important to consider the potential limitations of this method, particularly in the nanowires curved geometry. The divergence of magnetization, which represents the distribution of magnetic charges within the nanowire and has been used to simulate MFM contrast, could also have been used to indicate the positions of magnetic monopoles and domain walls. In this thesis however the magnetisation was used instead for a simplified and consistent approximation across different wire segments and vertex types. It

was found that checking the divergence of magnetisation yielded values differing by $\sim 5\ nm$ when compared to values obtained from magnetisation component.

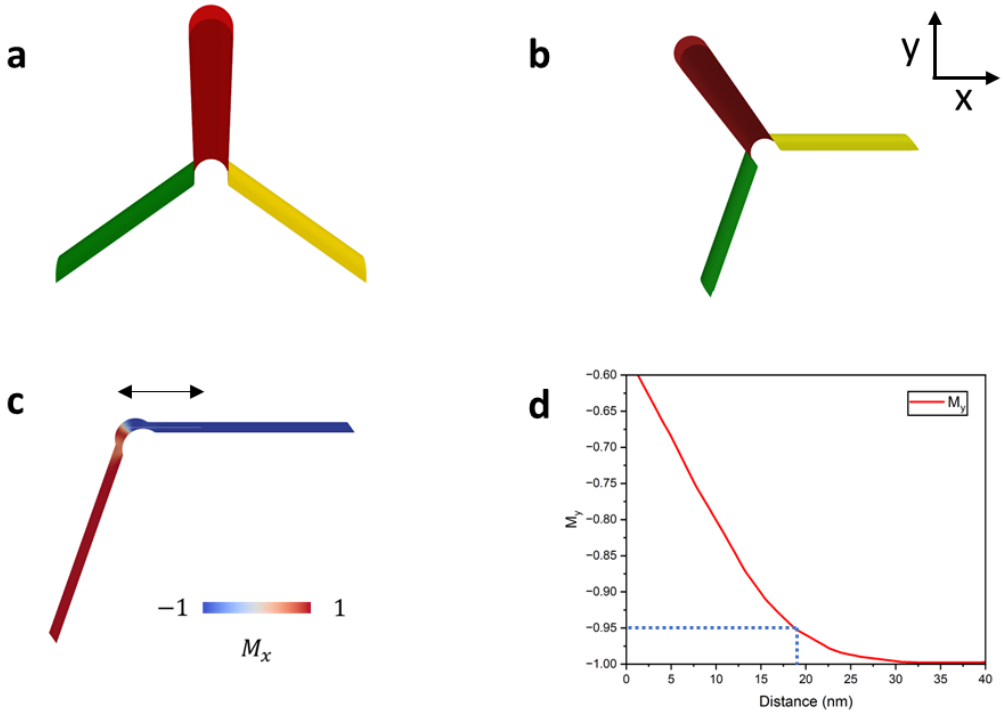

Figure 57: *Method for measuring domain wall width:* ***(a)*** *Simulated tetrapod's side view, and* ***(b)*** *transformed tetrapod with wire identification colouration.* ***(c)*** *Slice taken along the* $(1, 0, 0)$ *unit direction, displaying the identified line profile location.* ***(d)*** *Plot of normalised* M_y *vs. Distance along the measured axis, identifying the location of the minimum threshold at 95%.*

Utilizing this approach, domain wall widths were measured across all vertex types. Notably, Type 3 vertices exhibit consistent domain wall widths for both positively and negatively charged vertex types, aligning with expectations. To determine the $\frac{b}{a}$ ratio for each vertex type, an average domain wall width was calculated and used in the formula:

$$b = a - 2 \cdot (Avg.\,Domain\,Width) \qquad (127)$$

Here, b is derived from a by subtracting twice the average domain wall width, considering domain walls at each end of the wire, the results of this for each vertex type are shown in **Table 2**.

An overall analysis across Ice-rule vertices yielded an average $\frac{b}{a}$ ratio of 0.89. Initially, this ratio would suggest an experimental system in a $Q = \pm 4q$ monopole crystal ground state. However, contrary to this expectation, the observed configuration is different. Instead of the anticipated $Q = \pm 4q$ monopole crystal, the system displays a background of ice along with sets of $Q = \pm 2q$ crystallites.

Table 2: *Measured vertex type average domain wall width, corresponding 'b' and b/a calculation.*

Vertex Type	Average Domain Width (nm)	$b\ (nm)$	b/a
Type1	19.875	826.121	0.95
Type2	71.25	723.371	0.84
Type3	95.375	675.121	0.78
Type4 $(Q = -4q)$	205	455.871	0.53
Type4 $(Q = +4q)$	192	481.871	0.56

4.8 Discussion

The discrepancy between the predicted and observed states can be attributed to several factors and by considering differing behaviour on various sub-lattices. Past studies suggest that in 3D ASI systems, magnetic charges at coordination-two vertices are highly unfavourable. The energy required to create such a charge is significantly higher compared to a monopole at coordination-four vertices and the effective chemical potential is $\mu^* = 1.22$ [43]. Therefore, monopole / anti-monopole pairs are forced to nucleate over two lattices spacings.

The reduced confinement along with a deterministic field protocol, yields ferromagnetic stripes upon SL1. This is a configuration that immediately forbids the anticipated formation of a $Q = \pm 4q$ crystal, except in regions with local disorder. However, the SL2 sub-lattice has a lower effective chemical potential ($\mu^* = 1.03$) meaning monopole anti-monopole pairs are more likely to remain a bound stable pair upon nucleation. As the demagnetisation protocol evolves, the threshold field to move them apart is reduced and so the system can only reduce its energy by tiling charges upon SL2 with respect to the initial nucleated pairs yielding regions of antiferromagnetic order. Combining the ferromagnetic stripes upon SL1

and antiferromagnetic ordering upon SL2, yields charges crystallites. The type II background observed can be attributed to the fact that these are the lowest energy vertex, and their net magnetisation makes them difficult to remove when using a deterministic field protocol.

The distinction in effective chemical potentials between SL1 and SL2 directly influences the observed charge ordering. The higher effective chemical potential on SL1 prevents anti-ferromagnetic ordering and therefore restrains the formation of a Q=±4q crystal, favouring only a single charge crystal. In contrast, the lower effective chemical potential on SL2 allows for the formation of charge crystallites due to the increased stability of monopole pairs. This dual ordering on SL1 and SL2 eventually leads to the observed charge-ordered patches.

Type 3 vertices display a diverse distribution of magnetic charge and complex domain walls, resulting in an overall lower b value ($b = 0.78$). This reduction in b correlates with a decreased effective chemical potential ($\mu^* = 0.91$), therefore stabilizing monopole pairs produced by these Type 3 vertices forming on SL2. Upon nucleation of Type 3 vertices on SL2, the growth of regions of these charge crystallites is anticipated to minimize vertex-vertex Coulomb interactions, with residual ice-rule regions indicating areas yet to reach equilibrium.

The complexities in the effective chemical potentials and their implications on charge ordering across SL1 and SL2 shed light on the observed experimental configurations. Further investigation into the interplay between these sub-lattices and their chemical potential disparities could offer deeper insights into the charge ordering within the 3D ASI system.

The absence of charge ordering in 2D Square ASIs despite its theoretical potential can be attributed to the prevalent energy landscape determined by different vertex types. In a study from previous literature [77], the energies associated with Type 1, Type 2, and Type 3 vertices in a 2D disconnected square ice system were detailed. This dataset enables the determination of the effective chemical potential necessary for the creation of a monopole pair in these specific systems.

For instance, in this referenced 2D square lattice, a Type 1 vertex holds the position of the lowest energy vertex, with an associated effective chemical potential of $\mu^* \approx 2.5$, decreasing

the probability for charge ordering to occur. Conversely, Type 2 vertices possess higher energy levels, with an effective chemical potential $\mu^* \approx 0.44$.

The Monte Carlo simulations suggest that charge crystallization, observed in systems like the 3D ASI, might be feasible in a 2D square ice system under a modified geometry, wherein a Type 2 vertex with a decreased effective chemical potential assumes the lowest energy state. However, due to the prevalent energy landscape where Type 1 vertices dominate as the lowest and most probable energy configuration, charge ordering is not observed in these systems.

Interestingly, simulated alterations in 2D systems have demonstrated a reduction in Type 2 vertex energy and a consequent increase in Type 1 energy by employing connected lattices of nanowires [74]. This manipulation of geometry potentially enables a shift in the lowest energy vertex type, presenting an avenue for achieving the required conditions for charge crystallization in a 2D square ice system.

In a similar manner to the proposed modification of the 2D Square ice geometry to lower the energy of Type 2 vertices, potentially enabling charge crystallization within the 2D system, analogous adaptations could be explored within the 3D ASI design. One significant challenge in forming a double-charged monopole crystal within this structure is the high effective chemical potential required for monopole creation on a bipod.

One possible solution involves altering the geometry by introducing a defect on this bipod, thereby stabilizing the formation of a monopole within the system. This modification aims to facilitate the realization of a double-charged monopole crystal.

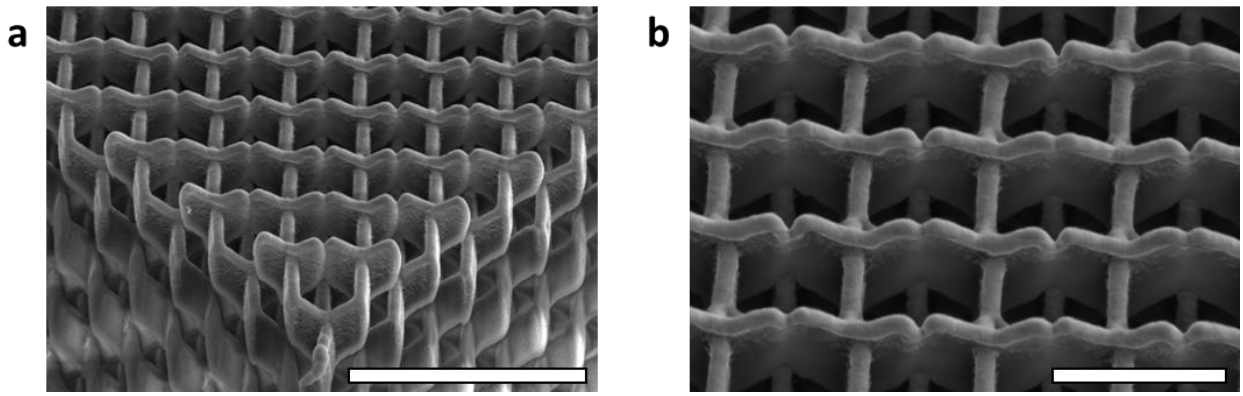

Figure 58: (a) *11000x magnification SEM image taken at a 45-degree tilt of a 3D ASI lattice with modified surface termination bipods. Scale bar shown* $5\ \mu m$. ***(b)*** *20000x magnification SEM image of lattice depicted in* ***(a)****. Scale bar shown* $2\ \mu m$.

The TPL fabrication methodology offers a means to achieve this adaptation. Initial attempts were made to implement this concept, shown in **Figure 58**, leading to an increase in observations of coordination-two monopoles during the early MFM measurements on the modified geometry. Because the defect sizes varied on the bipod, the system didn't perform as expected in achieving the targeted double-charged monopole state. This highlights the need for refining the fabrication process before effectively exploring this system.

4.9 Conclusion

This study enhances the comprehension of the phase space within simulated and experimental 3D ASI systems and expands the efficacy of tools employed to measure these systems. The investigation of demagnetized datasets in the 3D ASI has unveiled diverse vertex types, including newly discovered Type 1, Type 3 variations which are utilized to explain the difference in energy landscape predicted for this 3D ASI. Notably, Type 1 vertices exhibit polarity differentiation due to the presence of an anti-vortex domain wall, and their configuration could potentially possess a degeneracy in polarity, necessitating further simulations for comprehensive understanding. Type 3 variations arise due to the creation of a unique symmetric domain wall. This occurs when one of its wires with a different magnetic orientation is positioned among the upper wires. Conversely, an antisymmetric domain wall manifests when the odd wire out is among the lower wires.

Previously undiscovered Type 4 vertices, exhibiting a charge of Q= ±4q, and complex domain walls have been identified on SL2/SL3 vertices, previously unobservable. The intricate spin textures reveal pair of vortex domain walls and a simultaneous anti-vortex wall in the case of $Q = -4q$. Conversely, in the oppositely charged Type 4 $Q = +4q$, a vortex domain wall and an antisymmetric wall are observed. These findings shed light on the heightened energy expenditure associated with these monopoles.

The alignment between simulations and experimental findings aids in interpretation, simulated MFM contrast readily agrees with identification of lower surface wires. Though it is noted that a comprehensive approach considering collective phase characteristics is required for interpretation of the upper layer and vertex centre. Signal-to-noise challenges in deeper SL2/SL3 measurements are overcome through rigorous analysis of observed contrast with line profiles, comparison with simulated contrast and previous literature findings. These methods are applied to a broader MFM dataset for comparison of the demagnetised ground state of this system with Monte Carlo simulations.

The complexities of effective potentials across SL1 and SL2 elucidate the observed experimental configurations and their discrepancy with predicted configurations. Understanding the interplay between these sub-lattices and their chemical potential variations provides insights into charge ordering within the 3D ASI system, suggesting avenues for further investigation.

Potential refinements in the topography and geometry of 3D ASI designs, along with expanded demagnetisation protocols, might lead to the realization of the predicted double-charged crystal. Additionally, advancements in measurement techniques, such as utilizing x-ray magnetic circular dichroism through sophisticated synchrotron methodologies, may enable measurements beyond a single-unit cell in thickness, thereby advancing the comprehension of these systems.

5 Soft X-ray Measurement of Suspended 3D Artificial Spin-ice Structures

5.1 Introduction

This chapter delves into the pursuit of realizing a 3D ASI structure suspended over an aperture using TPL, thermal evaporation and oxygen plasma exposure. The primary objective is to ascertain the magnetic configuration of the suspended lattice via advanced techniques such as x-ray magnetic circular dichroism, specifically through soft x-ray transmission methods.

Historically, research on artificial spin ice systems has primarily centred on 2D configurations due to the simplicity of fabrication and measurement. Recently, innovative two-photon lithography techniques [42, 43] have enabled the creation of 3D artificial spin-ice structures, more closely mimicking the pyrochlore arrangement seen in bulk spin ice crystals. These engineered 3D systems offer fresh opportunities for exploring tuneable ground states, monopole behaviour, domain wall topologies, and their potential application in advanced devices like magnetic racetrack memory [78-80].

Prior studies on these 3D systems largely relied on MFM for probing magnetic configurations [43]. Nonetheless, MFM's limited depth and resolution posed challenges. While initial attempts managed to probe the upper two surface layers (SL1 and SL2), refinements in MFM techniques now permit probing of the third layer, SL3. Yet, this method's fundamental requirement to access surface topography to gather magnetic data poses difficulties when applied to complex 3D ASI designs. This constraint arises from the probe's lift height, typically confined to $50 - 100\ nm$.

Looking ahead, plans involve shrinking feature sizes and fabrication methods to create a truly thermal 3D ASI system, with nanowire switching times on the order of seconds. However, the act of measuring such a system using a magnetized tip in close proximity would perturb its state, rendering results inaccurate. Additionally, magnetic force microscopy necessitates a minimum measurement time of around 30 minutes to gauge a $10 \times 10\ \mu m$ section of the

3D ASI system with reasonable resolution. In a genuinely thermal system, the state would change multiple times before the dataset is complete.

Considering the challenges posed by the limitations in measurement techniques for the proposed thermal 3D ASI system, a paradigm shift towards employing transmission x-ray microscopy, coupled with XMCD, emerges as a promising avenue for robust and high-resolution characterization. This approach facilitates the exploration of deeper layers within the system while achieving sub-50 nm resolution. By leveraging XMCD, the aim is to mitigate the perturbation issues encountered with other measurement methods, enabling more precise and expedited data collection across the system's layers. This chapter delves into the utilization and optimization of transmission X-ray microscopy with XMCD to effectively capture and analyse the dynamic behaviour of the thermal 3D ASI system.

The initial research was centred on developing a 3D ASI system optimized for x-ray spectro microscopy investigation. This required a fundamental shift away from using conventional fabrication, which yielded 3D ASIs that were anchored directly onto the substrate (examples being silicon and permalloy-coated glass). Instead, the approach involved utilizing a silicon substrate that featured an aperture window. This innovative approach allowed for the creation of a suspended 3D ASI structure over the aperture, facilitating unobstructed x-ray transmission. Initial two-photon lithography attempts targeted simple structures: planar nanowires spanning the aperture and corner-suspended nanowires. However, spanning the entire aperture proved structurally unfeasible due to lattice deformation. Refined methods focused on creating structures on the corners of the aperture.

The initial 3D ASI structures spanning the corners consisted of two layers (SL1 and SL2) and were fabricated using the piezo mode of writing with TPL. The creation of these wires followed a sequence wherein they were first anchored to the substrate and then extended over the aperture, serving to provide preliminary structural reinforcement for the subsequent lattice connections. Subsequently, the development of polymer scaffold nanowires took place, and an ensuing line-of-sight deposition procedure coated the upper surface of these nanowires with Permalloy ($Ni_{81}Fe_{19}$), serving as the magnetic material. This magnetic layer was deposited in a tri-layer arrangement, wherein permalloy was sandwiched between aluminium seed and capping layers, functioning as an effective shield against oxidation.

Reducing the polymer scaffold thickness beneath the magnetic nanowires involved exposing the structure to an oxygen plasma, which carbonized the polymer scaffold, thereby reducing its thickness to enhance x-ray transmission. Scanning electron microscopy confirmed reduced polymer scaffold thickness post-plasma exposure, while magneto-optical Kerr effect measurements validated the robust magnetic signal of the $Ni_{81}Fe_{19}$ deposition.

Samples were then measured with scanning transmission x-ray microscopy at Diamond Light Source, capturing x-ray absorption spectra tuned to Nickel and Iron's L_3 and L_2 edges using both circular polarizations. This data enabled the calculation of x-ray magnetic circular dichroism, potentially yielding the magnetic configuration of the lattice. Unfortunately, no reliable magnetic contrast could be discerned from this initial dataset. However, further data analysis allowed reconstruction of the magnetic nanowires cross-section, validating prior assumptions. Overall, this study yielded insights into fabrication and provided ideas on how samples could be improved to obtain magnetic contrast.

Subsequent fabrication on a second sample set sought to reduce the polymer scaffold thickness for improved transmission and enhance the TPL write process for speed and layer count. Shifting from piezo to galvo scan mode for TPL created sharper nanowire geometries over a shorter timeframe. Increased oxygen plasma exposure significantly reduced the new samples' polymer scaffold thickness whilst the tri-layer of $Al/Py/Al$ was maintained as the magnetic coating.

Samples were evaluated at the ALBA synchrotron, employing transmission x-ray microscopy with energies tuned to the Iron L_3 and L_2 edges. Data analysis unveiled a magnetic signal embedded within the SL2 sub-lattice, with applied fields producing the anticipated magnetic configuration.

5.2 Initial Testing of Fabrication

Previously, achieving true 3D artificial spin ice fabrication involved employing two-photon lithography to create nanowires anchored onto a substrate, often glass or silicon [42, 43]. Subsequent layers were added until the structure reached approximately $10\ \mu m$ in height. Then, line-of-sight deposition applied a magnetic material to coat the surface layers. This resulted in presumed crescent-shaped nanowires, suitable for magnetic force microscopy (MFM) or magneto-optical Kerr effect (MOKE) measurements, without interference from the Permalloy film on the substrate surface. However, to enable x-ray microscopy, the structure had to be constructed over an aperture corner, presenting novel challenges for TPL techniques.

A silicon substrate, measuring $2\ mm \times 2\ mm \times 0.2\ mm$, was selected, and featured a central aperture of $50\ \mu m \times 50\ \mu m$. The detailed procedures and challenges encountered during substrate fabrication and Nanoscribe processing, including the methodology variations between dip-in and conventional direct laser writing, have been extensively discussed in Section 3.1.1.

Initial experiments focused on identifying the parameters required for polymerisation of a nanowire using the dip-in methodology of writing with the Nanoscribe using a specialist photoresist. Previous work has been focused on using conventional direct laser writing using IP-L as the photoresist and therefore before fabrication of suspended structures over the aperture, first the parameters must be explored. This was achieved by fabricating a dose array of nanowires onto a silicon substrate using the dip-in write methodology. This dose array comprised of increasing percentage power values used by the laser with a systematic varying scan speed.

As nanowires were to be written out over an aperture with minimal anchor points for support, the range of scan speeds explored with the laser were in the higher range such that produced wires were made quickly so that a secondary anchor point might be made before the structure collapses. The minimum parameters for producing a self-supporting nanowire across the aperture region was identified as a scan speed of $100\ \mu m/s$ with a power level set at 17% of the laser's maximum, as revealed by optical imagery of the produced dose arrays,

see **Figure 59**. Importantly, it should be noted that the primary focus of the investigation was on establishing feasibility rather than refining the parameters optimally suited for this objective.

During this fabrication process, the Nanoscribe employed the piezo scan mode for writing. This method involves continuously moving the laser point spread function through the photoresist, following the predefined path between coordinates outlined in the coded writing script. This approach anchored the wires to the substrate and completed the writing process of a single nanowire in one step, providing structural reinforcement upon completion.

Initial aperture-based fabrication trials focused on simple nanowire structures, approximately $50\ \mu m$ length, spanning the entire aperture. However, these structures proved weak and often collapsed during the write or subsequent development process, when the partially polymerized nanowires were immersed in a developer. Further investigation revealed that fabricating nanowires over aperture corners alleviated strain, as these nanowires received structural support from the two anchor points. This concept is depicted in **Figure 59**.

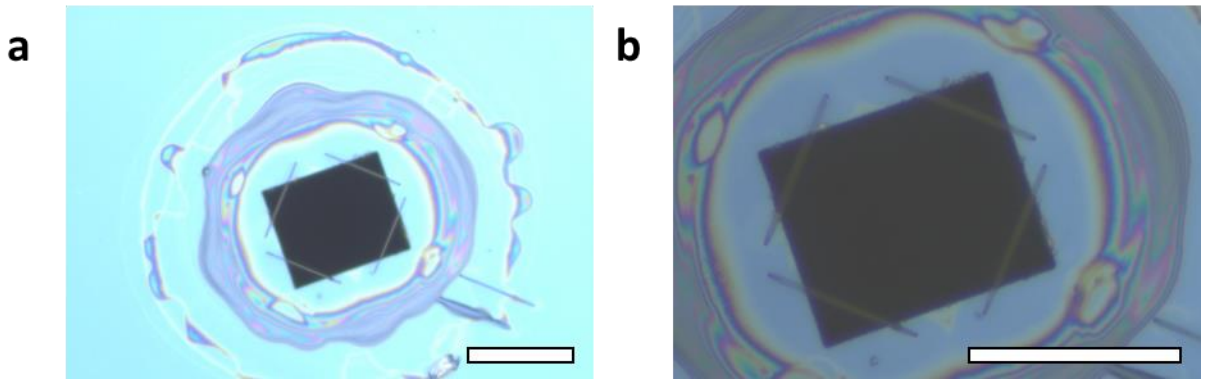

Figure 59: (a) *50x magnification and* ***(b)*** *100x magnification optical images showing initial fabrication of nanowires of length* $30\ \mu m$ *over corners of aperture, approximate aperture dimensions of* $50\ \mu m\ \times\ 50\ \mu m$*. Scale bar shown* $40\ \mu m$*.*

The wire lengths measured approximately 30 µm, and the wire widths between $\sim 300 - 400\ nm$, as inferred from the images presented in **Figure 59**. It's important to note that the width estimations drawn from the optical image may exhibit greater variability due to the limited resolution inherent in this imaging method.

Prior research has successfully produced single-domain permalloy nanowires with a width of $\sim 250\ nm$ and length of $863\ nm$ [42]. Therefore, achieving a reduction in nanowire width for 3D ASI fabrication will be necessary based on this established precedent.

Following development, the fabricated nanowires demonstrated stability, laying a robust groundwork for the creation of more intricate 3D ASI structures, particularly those centred around corner-based configurations.

5.3 Fabrication of a Suspended 3D ASI (Diamond Light Source)

In this section, the fabrication process employed to create samples intended for measurement at Diamond Light Source will be outlined. This fabrication comprised a three-step process.:

1) Polymer Scaffold Fabrication: Initially, a polymer scaffold was written over the aperture utilizing two photon lithography.
2) Magnetic Material Deposition: Following the scaffold creation, a magnetic material was deposited. This material was enclosed within a protective layer of aluminium, shielding it from oxidation.
3) Polymer Scaffold Reduction: The final step involved reducing the polymer scaffold's thickness through exposure to an oxygen plasma.

These three pivotal steps collectively formed the foundation for the subsequent investigations and measurements conducted at Diamond Light Source.

5.3.1 Simple 3D ASI fabricated using piezo-mode TPL

Fabrication concentrated on creating a 3D artificial spin ice structure, half a unit cell thick, over the aperture's corners. The 3D ASI is comprised of two sub-lattice layers designated SL1 and SL2. This was achieved while utilizing the piezo scan mode, allowing for longer exposure times and firm anchoring. Initially, wires were written from the edge of the lattice anchored into the substrate and then extended over the aperture, establishing connections with subsequently written wires, as shown in in **Figure 60a (**SL2**)** and **Figure 60b (**SL1**)**. Experiments involving scaffold structures created before the artificial spin ice lattices were unsuccessful. The scaffold supports augmented the weight of the wires extended over the aperture, leading

to the collapse of the entire structure into the aperture. Moreover, these supports introduced extra nanowires that x-rays would have to penetrate, resulting in diminished signals in those regions. Consequently, this exploratory approach was abandoned due to its lack of utility.

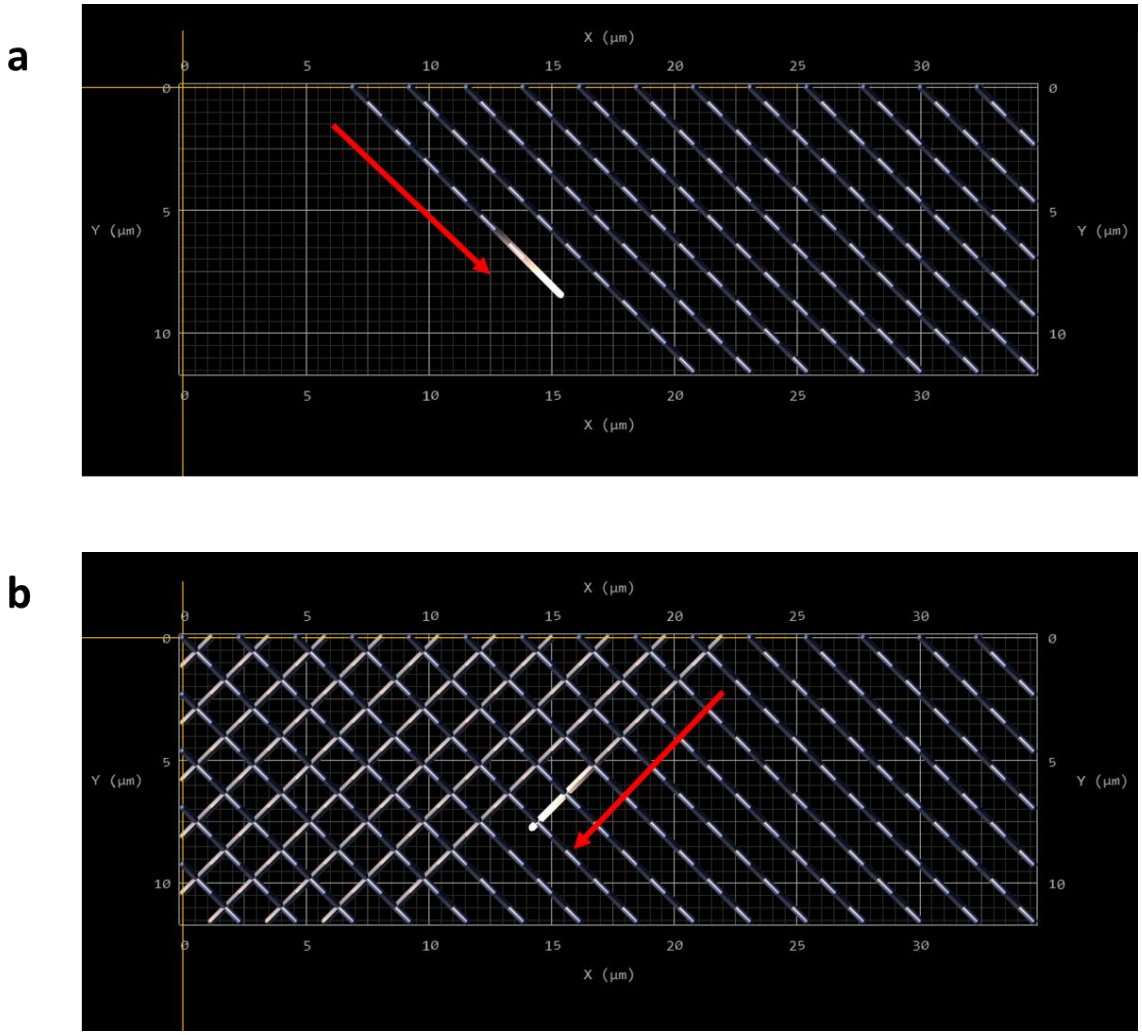

Figure 60: *Stepwise depiction via DeScribe software showcasing the fabrication process of a half unit cell thick 3D ASI lattice using piezo scan mode, laser direction of motion shown by red arrow.* ***(a)*** *Top-down view displaying continuous individual wire-by-wire writing until completion of the first layer.* ***(b)*** *Sequential rendering exhibiting the addition of the second layer of the lattice, wire by wire. Scales indicated in µm.*

Figure 61 shows the full stepwise process of the method of fabricating a 3D ASI over the corner of an aperture using piezo scan mode.

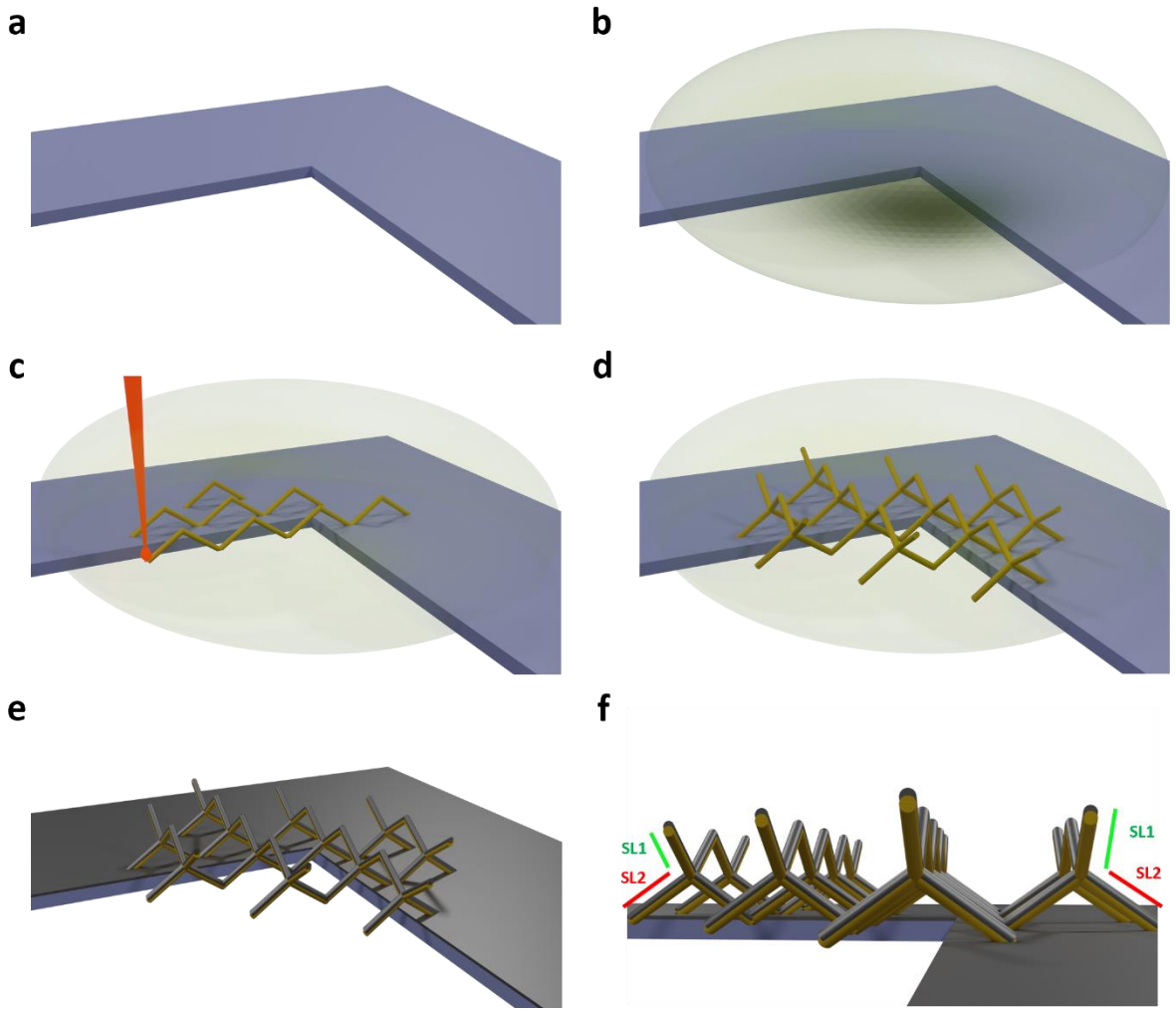

Figure 61: *Fabrication of a suspended 3D ASI.* ***(a-b)*** *A Silicon chip with* $50\ \mu m \times 50\ \mu m$ *aperture is cleaned in an ultrasonic bath with acetone and then rinsed with IPA, excess IPA is then removed with a compressed air gun. Surface of silicon chip is coated with Negative-tone resist (IP-DIP).* ***(c-d)*** *Two photon lithography is used to polymerise the resist in a pre-defined 1/2-unit cell thick diamond bond lattice over the aperture corner. Wires are written in one continuous motion extending out over aperture. Dimensions of structure are approximately* $12\ \mu m \times 35\ \mu m \times 1\ \mu m$. ***(e)*** *Development of resist and cleaning in IPA removes excess resist and reveals solid polymer scaffold structure. Permalloy* $(Ni_{81}Fe_{19})$ *is deposited onto the upper surface of lattice via thermal evaporation resulting in the suspended 3D ASI structure.* ***(f)*** *The 3D ASI is comprised of four sub-lattice layers designated SL1 through to SL2.*

The final samples featuring 3D artificial spin ice lattices encompassed a total of four lattices around each corner of the aperture. These samples provided redundancy for synchrotron measurements. The lattice dimensions were $12\ \mu m \times 35\ \mu m$, and the write directions were

determined by first anchoring the lower layer SL2 into the substrate before proceeding with subsequent wire layers. Wire lengths between adjoining vertices were set to $1\ \mu m$, selected for direct comparison with previously fabricated 3D ASI structures [42].

5.3.2 Deposition of Permalloy (Thermal Evaporation)

The samples were coated with a tri-layer of Aluminium (Al), Permalloy (Py), and Aluminium of approximate thickness $3\ nm/\ 40\ nm/\ 3\ nm$ respectively, exact thicknesses are shown in **Table 3**. The Aluminium capping layer was strategically placed to shield the magnetic material from oxidation during subsequent fabrication stages. Thermal evaporation, guided by a quartz crystal microbalance (QCM), was employed for deposition, and an additional control sample was utilized to determine the deposited thickness. The complete tri-layer was deposited in one continuous evaporation process, maintaining a vacuum throughout to minimize Permalloy exposure to oxygen. In total, two deposition cycles were carried out, yielding a total of ten 3D ASI aperture samples along with two control samples. Subsequently, optical imaging was performed to assess whether the deposition of an approximately $50\ nm$ thick metal layer had caused the structures to collapse due to weight. From this set, 5 samples were selected based on their stability assessed through optical imagery and scanning electron microscopy. These selected samples, showing intact structures without any visible deformities, constitute the final sample set for further processing before submission to Diamond Light Source.

5.3.3 Oxygen Plasma Exposure

Of this selected sample set of five, three samples underwent varying degrees of oxygen plasma exposure, as is shown in **Table 3**. This was an experimental attempt to reduce the thickness of the polymer scaffold, aiming to enhance x-ray transmission through the structure, thus improving the signal-to-noise ratio. This was performed after the permalloy deposition so that a continuous metallic wire network akin to previous work had been formed prior to any damage to the surface layer of polymer scaffold network that is required to support the formation of such a network. The aluminium capping layer is deposited to protect the permalloy from oxidation during this process.

Table 3: *Sample labels with associated oxygen plasma exposure, deposited tri-layer expected thickness (based on QCM measurements) and measured average wire thickness, standard deviation shown as error. The measurement process of wire thickness discussed in Section 5.4.2 and representative SEM images, utilised for these measurements, are provided therein. Flush plasma exposure indicates the sample was positioned flat on the sample stage during exposure, whereas lifted indicates a sample with one edge intentionally raised up to facilitate plasma flow through the aperture.*

Sample Label	Oxygen Plasma Exposure Time (minutes)	Deposited Al/Py/Al expected thickness (nm)	Estimated average wire thickness (µm)
200309E/C	0	4/48/4	n/a
200309E/A	0	4/48/4	1.07 ± 0.11
200309E/B	30 – Flush	4/48/4	1.09 ± 0.05
200310E/B	30 – Lifted	3/47.5/3	0.85 ± 0.06
200210E/A	60 – Flush	4/48/4	0.94 ± 0.13

The first sample, 200309E/B, underwent a thirty-minute exposure with the substrate positioned flat on the sample holder surface. For the second sample, 200310E/B, one edge of the square substrate was elevated to ensure that only one edge remained in contact with the sample holder. This configuration facilitated the flow of oxygen plasma through the aperture region, ensuring more comprehensive access to all areas of the polymer scaffold. The final sample, 200210EA, was laid flat but received an extended exposure time of sixty minutes. Post-plasma exposure, samples were imaged again with an optical microscope, and the lattices were observed to remain stable and intact.

Optical imaging was conducted at various stages throughout the fabrication process to monitor the presence and integrity of the lattices. A primary concern during fabrication was the potential presence of dirt or GE Varnish within the aperture, which could potentially damage the lattices. This concern was particularly pronounced after the oxygen plasma exposure step.

5.4 Characterisation of a suspended 3D ASI (Piezo Scan Mode)

5.4.1 Optical Imaging

During the fabrication process, several reference lattices were created away from the aperture, on the Silicon. This step aimed to assess the Nanoscribe's interface finder, ensuring that the written lattices were appropriately anchored to the substrate without being submerged below its surface. In some instances, multiple reference lattices were generated before proceeding to write over the aperture.

These reference lattices were later instrumental in identifying and tracking lattices across optical images, scanning electron microscopy (SEM) images, and subsequent synchrotron images for each sample slated for examination at Diamond Light Source. The labelling of lattices positioned over the aperture followed a systematic approach. The lattice nearest to a reference lattice on the substrate was denoted as "Lattice A". This can be seen clearly in **Figure 62a** and **Figure 62b**, with the bottom-left lattice being denoted as “Lattice A”. Subsequent lattices encircling the aperture were sequentially labelled as "Lattice B," "Lattice C," and "Lattice D" in a clockwise manner, starting from "Lattice A". Dark field images of this same arrangement are shown in **Figure 62c** and **Figure 62d.**

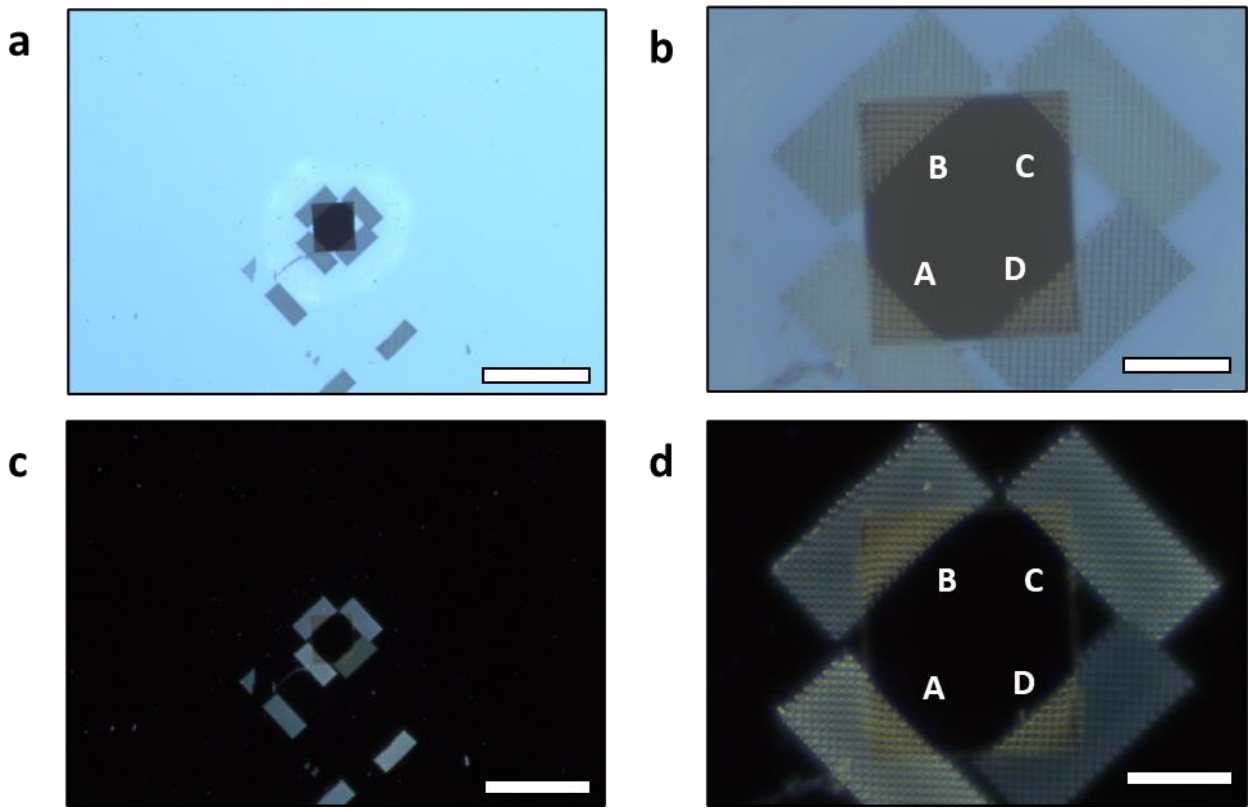

Figure 62: *Optical images of sample 200210EA for the Diamond Light Source experiment. Brightfield images shown in* ***(a)*** *and* ***(b)****, darkfield images in* ***(c)*** *and* ***(d)****. Lattices are of dimensions* $12\ \mu m \times 30\ \mu m$*. Aperture size is approximately* $50\ \mu m \times 50\ \mu m$*. Scales indicate* ***(a-c)*** $100\ \mu m$ ***(b-d)*** $10\ \mu m$*. These images serve as representatives of the entire sample set.*

5.4.2 Scanning Electron Microscopy

Scanning electron microscopy images were captured for each sample designated for evaluation at Diamond Light Source. This comprehensive imaging process involved obtaining top-down views of the lattices to precisely measure wire width, vertex-to-vertex distances, and to discern any lattice deformities. These SEM images played a crucial role in prioritizing specific lattices for subsequent synchrotron measurements. Furthermore, lattices were imaged at a 45-degree tilt angle. This unique perspective facilitated measurements of the thickness of the polymer scaffold. The analysis of these tilted images was performed using ImageJ. All SEM images were taken post-deposition of the permalloy to prevent accumulation of charge during measurements and deformation of the polymer scaffold.

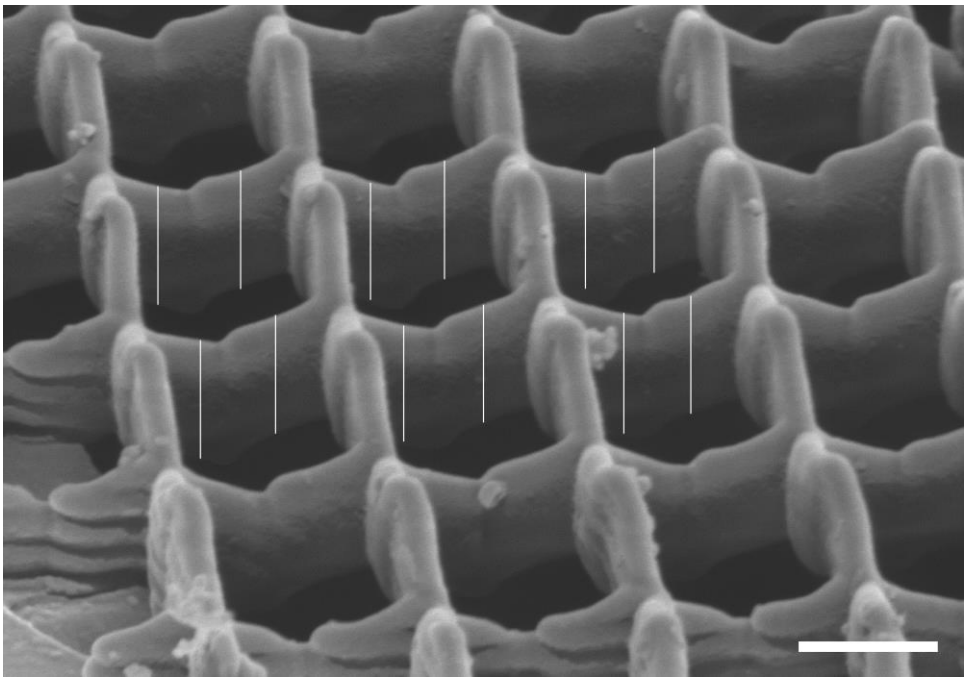

Figure 63: *SEM image of a 3D artificial spin ice, subjected to no oxygen plasma exposure, suspended over the aperture viewed from a* 45^0 *tilt. Measurements annotated show the regions of wires measured for thickness measurements. A trigonometry calculation, shown in Equation (128), was used to transform the measured values to account for tilt of image. This was repeated for each sample. Scale bar shown is* $1\ \mu m$.

For each sample, multiple measurements of the scaffolds and wires were systematically recorded, as depicted by the white line markers in **Figure 63**. Subsequently, the actual thickness d of the polymer scaffold was calculated using:

$$d = \frac{t}{\cos(\theta)} \qquad (128)$$

Where t is the measured thickness and θ is the SEM tilt angle.

These calculations yielded an average thickness at the tilt angle, and the results of these measurements are presented in **Table 3**. The error associated with each thickness value is represented by the standard deviation of the measured results.

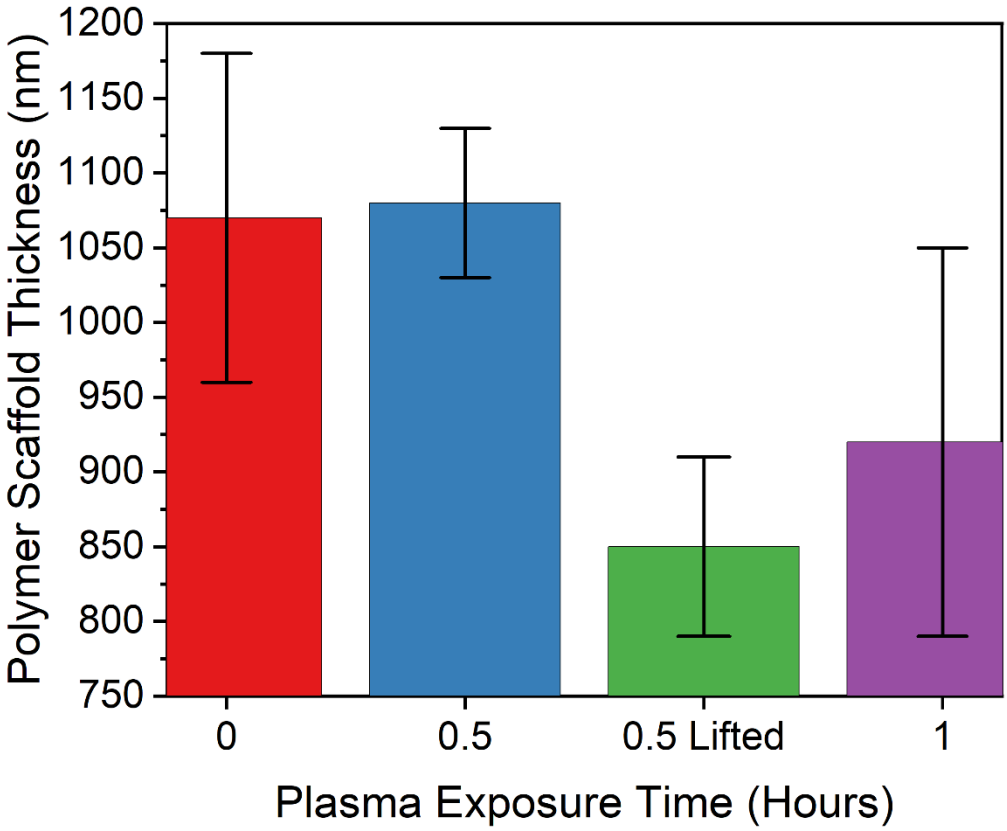

Figure 64: *Average polymer scaffold thickness measured from tilted SEM micrographs plotted against the oxygen plasma exposure time. The 0.5-hour lifted sample (200310EB) with one edge raised to increase plasma flow through aperture saw an increased level of reduction in polymer scaffold thickness compared to the 0.5-hour standard sample (200309EB). A ~10% drop in scaffold thickness for 1-hour of plasma exposure was measured. Error bars are based upon the standard deviation.*

The scaffold thickness notably decreases in the 0.5-hour lifted sample (200310EB), depicted in **Figure 64**, compared to other samples, indicating a substantial 20% reduction. However, the reasons behind this anomaly are deferred for discussion in subsequent sections of this thesis, see Section 5.6.3. Similarly, the 1-hour exposure exhibits a comparable reduction in polymer scaffold thickness, suggesting the potential for further diminishment without risking sample integrity. As a result, the practice of tilting the substrate in the oxygen plasma was disregarded. Additionally, the 1-hour sample (200210EA) demonstrates significantly higher measurement standard deviation compared to other samples. This variance is attributed to

an uneven reduction in scaffold thickness across the sample particularly between measurements taken close to the aperture edge and furthest from the aperture edge, resulting in varying measured thickness levels. Uneven reductions in the polymer thickness during plasma exposure could be attributed to various factors. Samples were deposited with permalloy prior to exposure, and stray magnetic fields on wires of the lattice shielding underlying polymer may be the cause of irregularities in exposure intensity about the scaffold. Furthermore, the permalloy coating may exhibit localised heating under plasma exposure with variations in heating across the scaffold surface leading to potential non-uniform reduction of the polymer.

The transmission T of x-rays through the polymer layer can be determined using:

$$T = \exp(-n\mu_a d) \qquad (129)$$

where d is the thickness of the layer, calculated for each sample using Equation (128), with density n, and atomic photo-absorption cross section μ_a is defined as:

$$\mu_a = 2r_0\lambda f_2 \qquad (130)$$

where r_0 is the classical electron radius, λ is the wavelength, and f_2 is the imaginary component of the atomic scattering factor. Based on the Henke tables, estimates of x-ray transmission through the average of all sample sets thickness with measurement $930 \pm 40\ nm$ suggested a transmission of 62% at the $Ni\ L_3$ photon energy and 46% at the $Fe\ L_3$ photon energy, as shown in **Figure 65**. In contrast, a $100\ nm$ thick Si_3Ni_4 membrane has a transmission of approximately 85-90% at the $Ni\ L_3$ edge photon energy and 80-85% at the $Fe\ L_3$ edge photon energy. The decreased transmission due to thickness of polymer present in the structures will add substantially to the non-magnetic background and reduce the signal-to-noise of XMCD measurements. Later samples produced for ALBA synchrotron measurements focus on decreasing the polymer thickness even further with improved writing techniques and greater exposure to oxygen plasma.

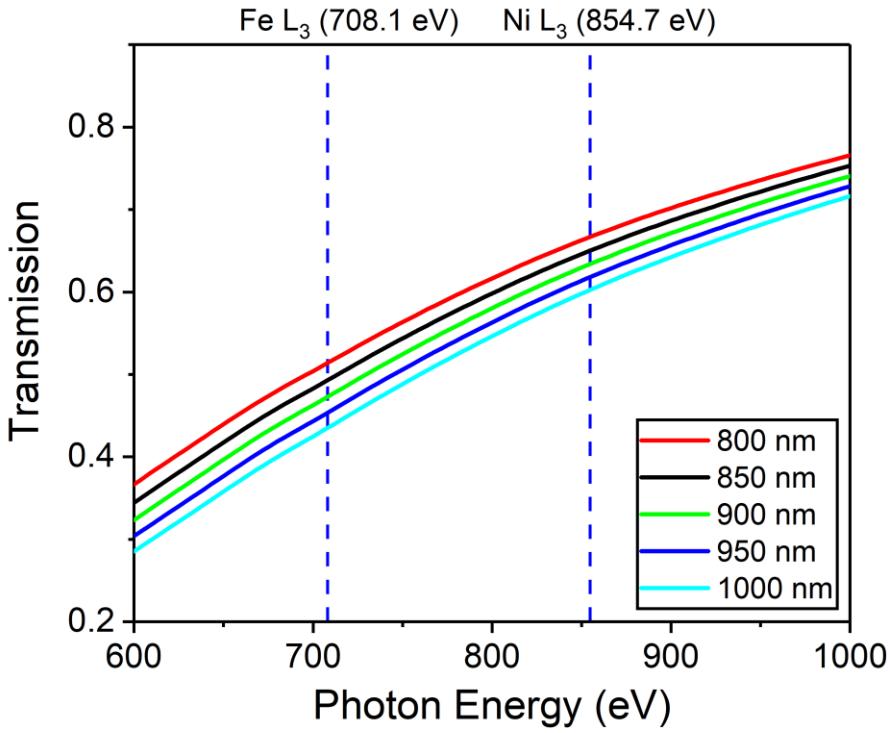

Figure 65: *Calculated transmission of x-rays through PMMA* $(C_5H_8O_2)$ *for different values of polymer thickness, as indicated in legend. The* Fe *and* Ni L_3 *edges are shown at the top of the panel. Transmission calculations were carried out using centre of x-ray optics online tool utilising Henke tables [63] with PMMA as approximate resist material.*

Figure 66a shows a top-down SEM image of reference lattices built into the substrate mentioned previously. The lattice shown in the lower-left corner of **Figure 66a** is of the dimensions used by lattices positioned over the corner of the aperture, approximately $10\ \mu m \times\ 30\ \mu m$. An increased magnification SEM image of this same lattice is shown in **Figure 66b.**

Figure 66c shows a wide area view of the entire aperture with labelled lattices. Some debris is seen about the region, with Lattice B being particularly damaged and showing debris. Using images such as this one for each sample allowed identification of prioritised lattices for measurement, dependent on the quality of lattice produced and prevalence of debris and damage to the lattice.

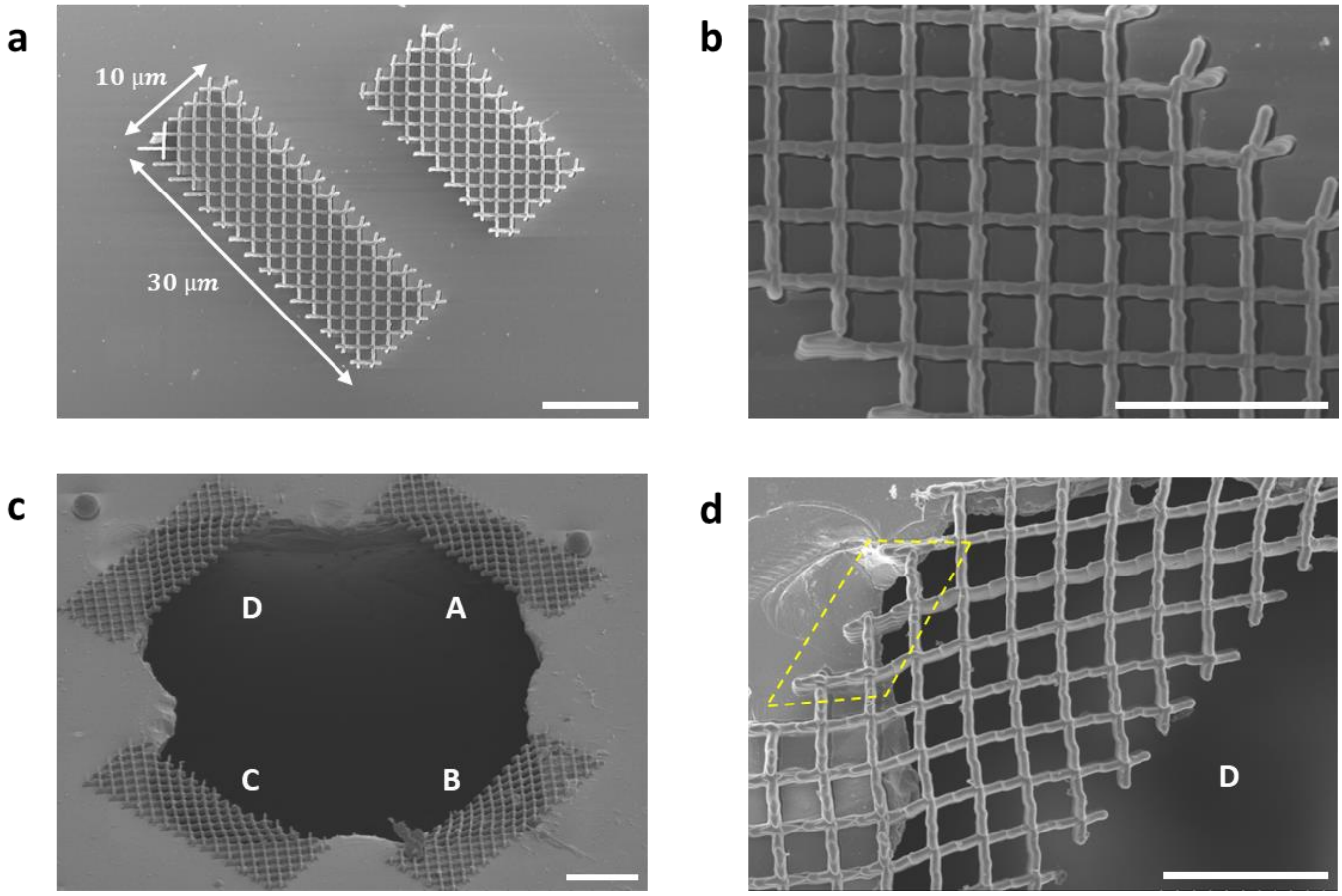

Figure 66: (a) *Scanning electron microscopy top-view image of a 3D ASI reference lattice built on the substrate besides the aperture. Top-down view at 2000x magnification, scale shown is* $10\ \mu m$. ***(b)*** *Top-down view of same lattice at 9000x magnification, scale shown is* $5\ \mu m$. ***(c)*** *Scanning electron microscopy* 45^0 *tilt view image at 1500x magnification showing fabrication of multiple lattices over corners of an aperture. Lattices are labelled according to a reference lattice not seen on the image; scale shown is* $10\ \mu m$. ***(d)*** *Top-down view of lattice D at 9000x magnification. A sagging of the lattice is clearly seen over the aperture region. Yellow ROI shows section of lattice with reflections causing increased roughness. Scale shown is* $5\ \mu m$.

Figure 66d shows a top-down magnified view of Lattice D. A notable observation, highlighted in the figure region of interest, is the increased wire roughness of wires built directly into the substrate, observed as a layering effect in the polymer wires. This enhanced roughness is attributed to reflection of the laser occurring during the fabrication process. As measurement of these wires will not occur and wires exposed over the aperture do not show this roughness this was deemed acceptable for the sample set.

Furthermore, a sagging effect of the lattice into the aperture is also clearly seen. Estimation of the total tilt into the aperture via SEM measurement comparing vertex-to-vertex distance off the aperture with vertex-to-vertex distance on lattices tilting into the aperture calculates an approximate tilt angle of $20°$ into the aperture. Approximate estimation of the area of lattice protruding over the aperture based on SEM images suggest a total of 31 vertices present over an area of approximately $70\ \mu m^2$. This provides ample area for measurement with STXM. The size of this working area is dependent on the positioning of lattices during the fabrication step, the variability of this can be seen in **Figure 67**.

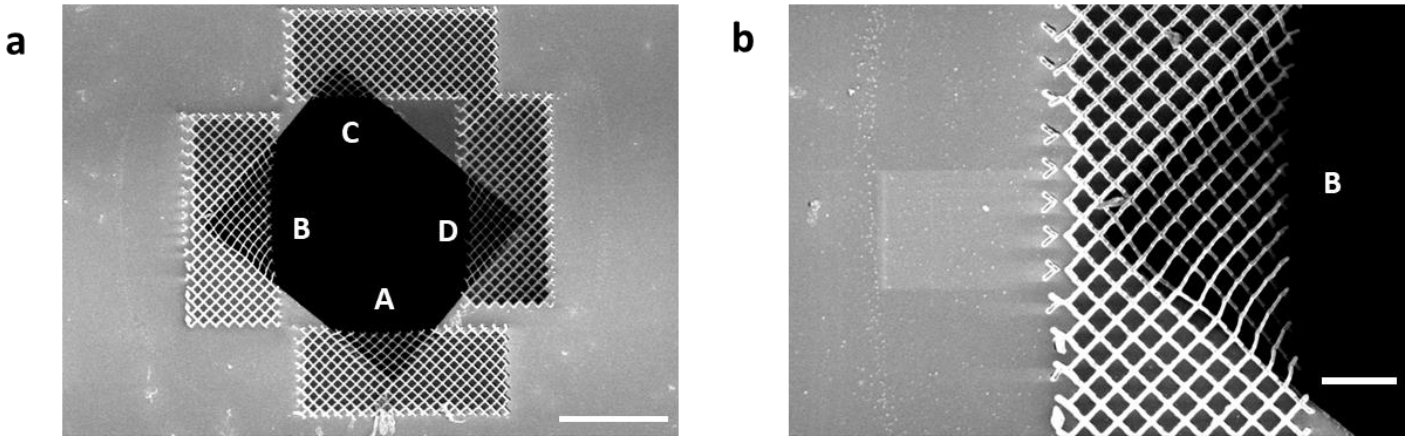

Figure 67: (a) *Scanning electron microscopy top-down view image at 1100x magnification showing lattices built over all corners of aperture. Scale shown is* $20\ \mu m$. ***(b)*** *Top-down view of lattice B from at 3010x magnification. Scale shown is* $5\ \mu m$.

Figure 67 shows top-down SEM images of an alternate sample (200210E/A) measured at Diamond. This sample was measured extensively due to the large working area and quality of lattices present. Images, such as **Figure 67b** allowed direct comparison of STXM images with SEM images by alignment of notable features, commonly the furthest vertex from the aperture edge.

5.4.3 Magneto Optical Kerr Effect measurements

Magneto Optical Kerr Effect (MOKE) measurements were conducted on the permalloy sheet film that surrounds the aperture. This was also present during exposure to the oxygen plasma.

The measurements, see **Figure 68**, for samples exposed for 0- and 30-minutes, confirm the occurrence of oxidation due to plasma exposure despite an aluminium capping layer. A study [81] on the interaction of aluminium capping layers, permalloy and oxygen plasma revealed that a $2.5\ nm$ capping layer on $40\ nm$ of permalloy sees no reduction in permalloy magnetic properties for an exposure time of 30 minutes. However, on uncapped permalloy samples substantial magnetic decay was seen in $40\ nm$ thickness samples after just 30 minutes of exposure.

The observed decrease in measured coercivity to $0.9\ mT$ implies a fraction of permalloy oxidation, resulting in the formation of antiferromagnetic NiO, ferrimagnetic $NiFe_2O_4$, and Fe_3O_4 as the primary species within the resulting oxide layer [81]. This aligns with the reduced coercivity measured [82]. This oxidation leads to an overall reduction in the material's total magnetic moment per unit volume, subsequently lowering the saturation magnetisation and, consequently, the coercivity. These formed oxides significantly alter the magnetic behaviour of the samples. The ferrimagnetic compounds, as discussed in Section 1.2.3, will contribute weakly to the overall magnetic moment. On the other hand, the contribution from antiferromagnetic NiO, is considered negligible due to the substantial $5\ T$ field strength required to significantly influence its magnetic alignment [83].

Despite the observed reduction in coercivity attributed to oxidation and the formation of oxides within the permalloy film, the measured coercivity remains consistent with values reported in the existing literature [84]. This result suggests that, despite oxidation, the magnetic properties of the permalloy film remain following exposure to an oxygen plasma. This provided confidence to proceed with measurements of these samples with STXM.

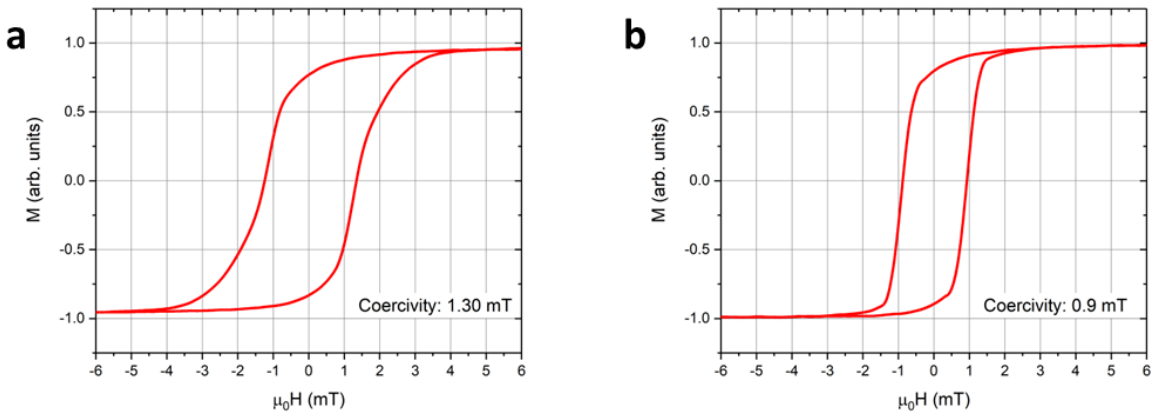

Figure 68: *Longitudinal magneto-optical Kerr effect loop of the thin-film from* ***(a)*** *200309EA (0-minutes plasma oxygen exposure sample),* ***(b)*** *200309EB (30 minutes plasma oxygen exposure).*

5.5 Diamond Experiment 1 (Samples written using piezo scan mode)

The Diamond Light Source STXM experiment occurred over three days with Sam Ladak and myself remotely overseeing measurements conducted in person at the synchrotron by beamline scientist Tohru Araki (Due to COVID pandemic). Initial images of the samples were taken prior to the experiment date and examples of these are shown in **Figure 69**. These images, used alongside submitted sample information, were used to identify lattices based on the labelling methodology discussed previously in Section 5.4.1. During experiments, images such as **Figure 69b** were used as maps of the designated lattice locations and using these maps smaller windows ($8\ \mu m\ x\ 5\ \mu m$) were selected and measured with greater resolution.

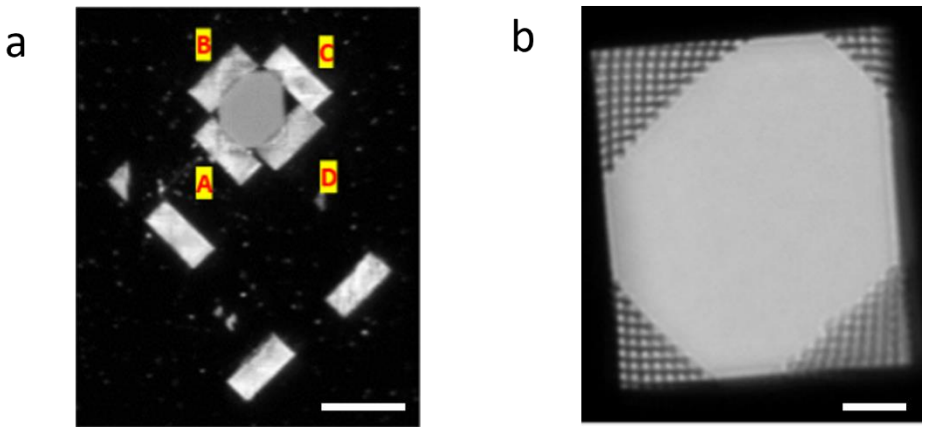

Figure 69: (a) *Widefield x-ray absorption image of substrate surface and aperture. Reference lattices on substrate surface behind aperture lattices allow identification of lattices for comparison with optical and scanning electron microscopy images. Scale bar* $50\ \mu m$. ***(b)*** *Full aperture window x-ray absorption spectra image, taken at* $850\ eV$*. Large portion of lattices visible for x-ray transmission and measurement. Scale bar* $10\ \mu m$.

5.5.1 X-ray Absorption Spectra

Initially x-ray absorption spectra (XAS) were obtained by scanning across photon energies ($845\ eV$ – $885\ eV$) allowing identification of the specific $L_{2,3}$ edge photon energies associated for each sample. Optical density (O_D) images were obtained from these by using:

$$O_D = \ln\left(\frac{I_0}{I}\right) \qquad (131)$$

Where I_0 is the background photon intensity, located from sample free regions of interest, and I is the transmitted intensity. An example XAS for Nickel is shown in **Figure 70** with the $Ni\ L_{2,3}$ photon energies shown. The peak locations identified for the $Ni\ L_{2,3}$ photon energies were identified by plotting optical density against the measured energy range. The values measured for both Ni- and Fe- were found to be within $1\ eV$ of literature values [85], the discrepancy can be attributed to slight oxidation of the deposited permalloy, resulting in the formation of $NiFe_2O_4$ and NiO which will contribute a shoulder peak with an increased energy ($2\ eV$ and $0.5\ eV$ respectively) [86, 87]. Evidence of this oxidation is seen in the slight shoulder peak at the $Ni\ L_3$ edge, and the more prominent peak seen at the L_2 edge. This

measurement of the $L_{2,3}$ edges and identification of peak values was repeated each time a different sample was measured.

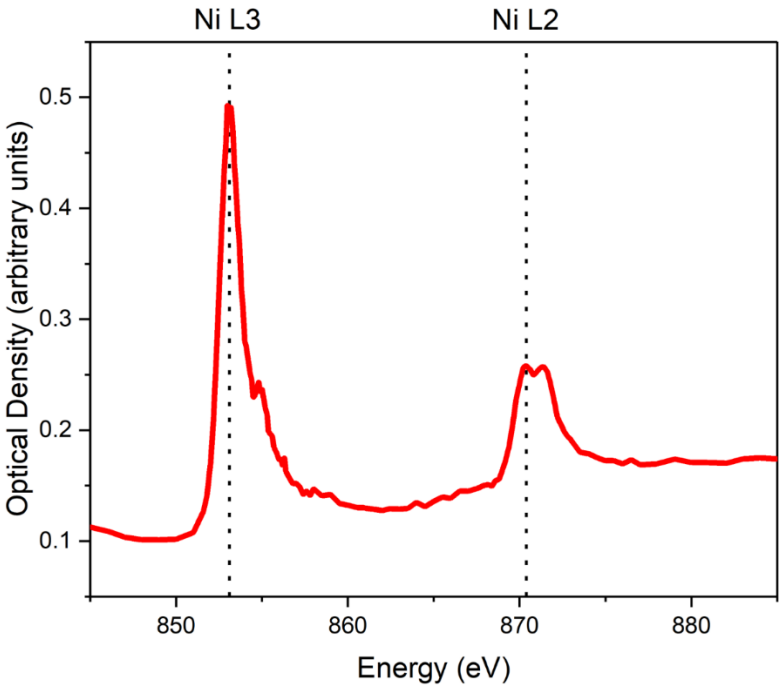

***Figure 70**: X-ray absorption spectra over the $Ni\ L_3$ $(853.1\,eV)$ and $Ni\,L_2$ $(870.4\,eV)$ absorption edges.*

During the initial experiments, it was observed that repeated measurements of the same lattice led to some deformation. Initially, the lattice exhibited a tilting motion into the aperture during the first measurements but gradually stabilized in subsequent measurements. This initial tilting of the lattice created challenges in aligning the image stacks during post-processing. Hence, only datasets acquired after the lattice had stabilized were utilized for XMCD analysis. Example XAS images captured post-stabilization at the peak $Ni - L_{2,3}$ edge photon energies are presented in **Figure 71**, showcasing well-aligned lattices with minimal distortion. This alignment underscores the reliability of datasets obtained post-stabilization for subsequent XMCD analysis, affirming their suitability for meaningful interpretation. Additionally, a discrepancy in contrast between the two photon edge energies is evident, primarily attributed to reduced absorption at the L_2 edge, as depicted in **Figure 70** by the reduced optical density. This contrast variation underscores differing absorption behaviours at distinct photon energies, contributing to the observable differences in the XAS images.

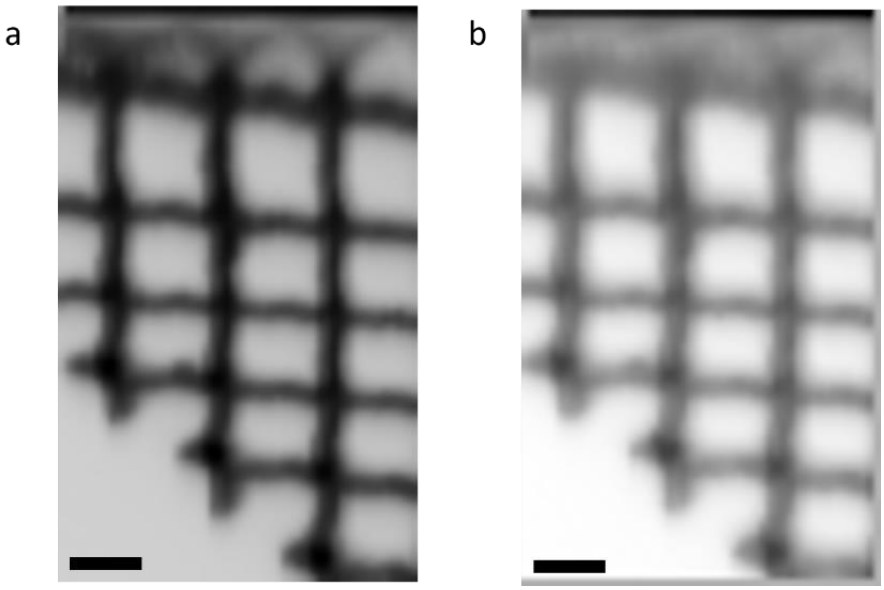

Figure 71: *X-ray absorption images at the* ***(a)*** $Ni\ L_3\ (853.1\ eV)$ *and* ***(b)*** $Ni\ L_2\ (870.4\ eV)$ *absorption edges. Image size is* $8\ \mu m\ \times\ 5\ \mu m$ *with 10 pixels per* $1\ \mu m$*. Scale bar is* $1\ \mu m$*.*

5.5.2 Cross-sectional thickness of magnetic nanowires

Iron and Nickel thickness maps were obtained by analysis of XAS images obtained and by using the aXis2000 software package [88]. The process involved subtracting the optical density image at the pre-edge absorption energy from the relevant resonance absorption peak. Pre-edge energies were identified from the XAS spectral region before the L_3 absorption edge where the x-ray absorption intensity starts to increase but hasn't reached the edge onset. Estimating the absolute thickness of the deposited material could theoretically be achieved by utilising the atomic scattering factors found in the Henke tables [63]. However due to the presence of oxidation in the magnetic material, suggested by XAS in the previous section, the ability to accurately determine the overall chemical composition and density was limited. Thus, only the relative change in thickness can be produced, which provides sufficient information to estimate the cross-sectional geometry of the wires by comparing with SEM images in Section 5.4.2 and through knowledge of the elliptical shape of the two-photon lithography voxel discussed in Section 2.

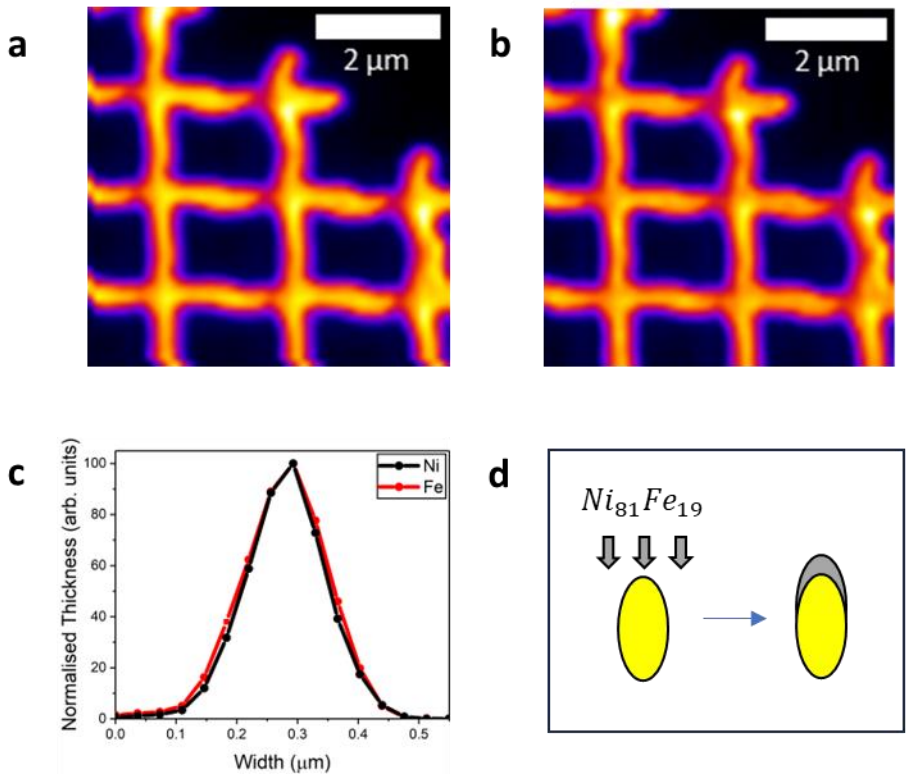

Figure 72: (a) *Ni thickness map,* ***(b)*** *Fe thickness map.* ***(c)*** *Extracted Ni and Fe cross-sectional thickness profile of wires.* ***(d)*** *Elliptical cross-section of a TPL voxel (yellow) and the crescent shaped cross-section of $Ni_{81}Fe_{19}$ (Grey) obtained when adding a graded thickness as suggested by the measured thickness maps.*

The relative change in the cross-sectional thickness is presented in **Figure 72**. Previous work hints that the wires will have a novel crescent-shaped cross-section [42]. **Figure 72a** and **Figure 72b** show the thickness maps of the Ni and Fe components of the magnetic material deposited upon the lattice respectively. These both show a uniform deposition across the lattice with a region of decreased material thickness found at the intersection of SL1 and SL2. At this location a decrease in optical density of 40% relative to the rest of the lattice is observed. This can be attributed to the tilt of the suspended lattice into the aperture, discussed in Section 5.4.2, which combined with the evaporation at normal incidence to the sample will result in a change in the deposition thickness transverse to the tilt axis.

Line profiles were extracted across the wire width that show the thickness variation of the cross section as shown in **Figure 72c**. A total of 16 measurements were taken across a range of SL1 and SL2 nanowires shown in **Figure 72a** and **Figure 72b**. Images were aligned prior to measurements to ensure the same location was measured in both. Peak of line profiles were

aligned for each dataset and an average was taken of the line profiles to produce data shown in **Figure 72c**. These profile shows a graded thickness across the wire as previously suggested by SEM imaging [42]. Considering the cross-sectional geometry of the TPL voxel, which has an elliptical geometry [34], the graded $Ni_{81}Fe_{19}$ thickness profile suggests wires of a crescent-shaped cross section, **Figure 72d**. Magnetic nanowires with a crescent shaped cross section are expected to host domain walls with perturbed spin texture, due to the curvature yielding effective anisotropy and Dzyaloshinksii-Moriya energies, discussed in Section 1.3.4 [89].

5.5.3 XMCD

Figure 73a shows a top-down SEM image of sample 200210EA with a region that was measured with STXM marked out within the dotted lines. The XMCD results for the $Ni\ L_3$ edge photon energy are shown in **Figure 73b** and L_2 edge photon energy images shown in **Figure 73c**. XMCD images were processed first by removing the dark photon count for the beamline and converting to optical density via Equation (131). Both left circularly polarised (*L*) and right circularly polarised (*R*) images were aligned, using the built in function of aXis2000 [88]. Then the normalised difference calculation, Equation (132) repeated here, was carried out between the images of opposite circular polarisation for each energy:

$$XMCD = \frac{(L - R)}{(L + R)} \qquad (132)$$

$Ni\ L_3$ edge results are shown in **Figure 73b** and peak L_2 photon energy results are shown in **Figure 73c**. Given that each wire along a given sub-lattice features an alternating $\pm\ 35.25°$ angle out of the substrate plane and considering that XMCD measurements are sensitive to the magnetisation component along the photon propagation direction (normal to the substrate), the expectation is to observe two distinct contrasts in wires.

According to theory, see Section 3.2.7, the contrast visible on L_3 XMCD images is expected to be opposite to that seen in L_2 XMCD images. When the peak $Ni\ L_3$ XMCD image in **Figure 73b** is compared with the peak $Ni\ L_2$ image in **Figure 73c**, some agreement in the expected

contrast reversal is observed. However, regions of disagreement are also noticed, particularly in areas near the tips of the wires exposed over the aperture (top-right corner of the image) and the section of wires towards the bottom of the image.

Furthermore, a significant percentage of the measured wires show little discernible contrast, especially from the centre of wires towards the left-hand edge. Therefore, statistical analysis of the two opposing XMCD images was carried out to identify whether a magnetic signal was buried within the noise apparent in the images. This was achieved by measuring an average XMCD intensity for each individual wire for both the L_3 and L_2 XMCD images and comparing these results. This is shown in **Figure 74**.

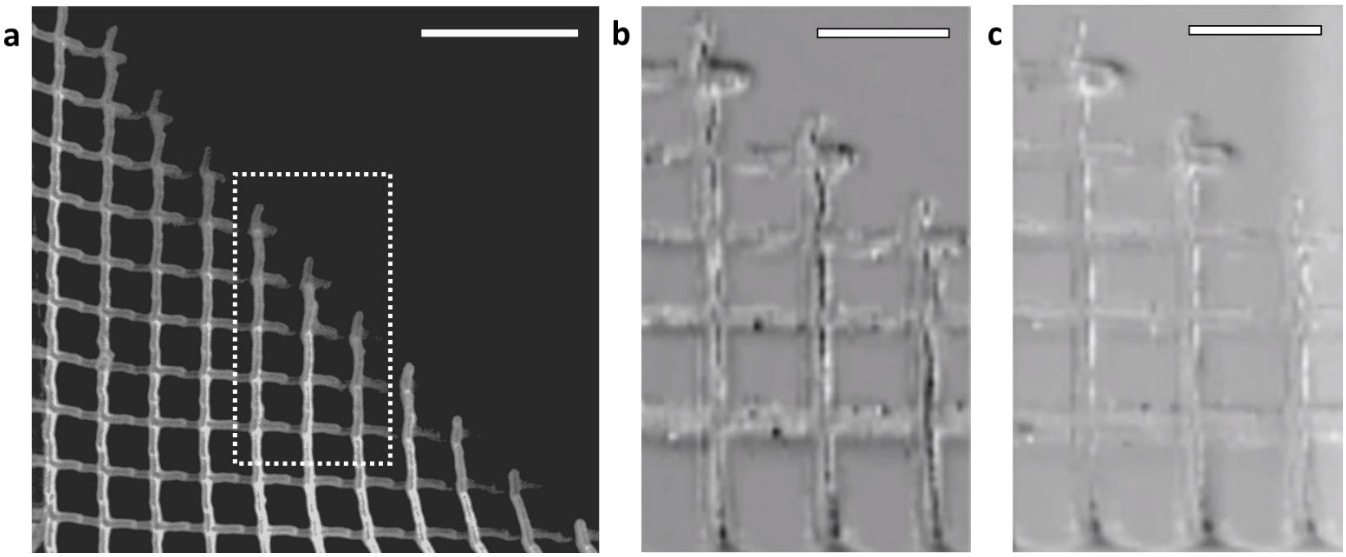

Figure 73: (a) *Scanning electron microscopy image with region measured highlighted, scale bar shown is* $5\ \mu m$*. Nickel XMCD images of* ***(b)*** L_3 *edge* $(852.9\ eV)$ *and* ***(c)*** L_2 *edge* $(871.3\ eV)$*. Scale bar in* ***(b-c)*** *is* $2\ \mu m$*.*

To produce **Figure 74** both the peak L_3 and L_2 XMCD images were normalised and then each individual wire that comprises the structure was measured for both the SL1 layer **Figure 74a** and the SL2 layer **Figure 74b**. The measurement was conducted along 'chains' of wires, wherein connected wires on a specific sub-lattice were measured sequentially to identify potential patterns of magnetisation orientation based on the obtained results. An expectation was set for a pattern of opposing XMCD intensity between the two XMCD images when comparing the $L_{2,3}$ XMCD images. However, contrary to this expectation, what is observed is

a close matching of the $L_{2,3}$ measurements, which suggests that any component of magnetic signal is weak and undetectable.

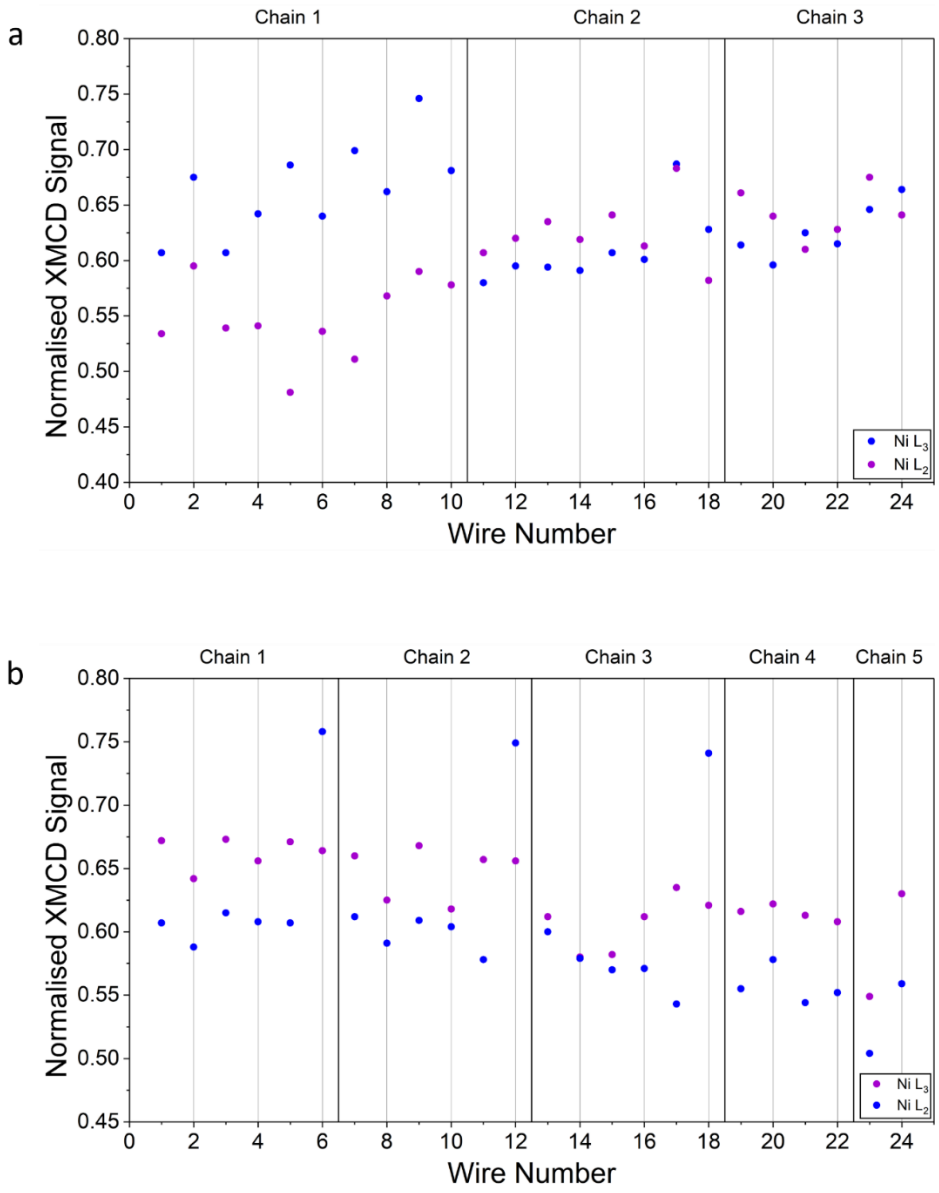

Figure 74: *Measured normalised XMCD signal for wires for* ***(a)*** *SL1 wires and* ***(b)*** *SL2 wires. For each sub-lattice the* $Ni\ L_3$ *edge (purple) and* $Ni\ L_2$ *edge (blue) XMCD signal are shown.*

The source of both the noise and the absence of a discernible magnetic signal in this experiment is reasoned to be attributable to two primary factors. First, the observed noise is likely contributed by the reduced transmission of x-rays through the polymer scaffold. Second, the presence of an oxidized component within the magnetic material is likely diminishing the strength of any detectable magnetic signal. Based on these findings, efforts

were made to initiate improvements to the fabrication process to generate a sample set for a further x-ray microscopy experiment at the ALBA synchrotron.

5.6 Fabrication of a Suspended 3D ASI (ALBA Experiment)

To tackle the challenge of reduced x-ray transmission through the polymer scaffold, a transition was made from the slower Piezo Scan Mode (PSM) of operation to the efficient Galvo Scan Mode (GSM) for the Nanoscribe. The GSM, as described in Section 3.1.1, systematically traverses all coordinates within the lowest z-plane before incrementing to the subsequent layer of coordinates. This is unlike PSM, which constructs a single wire from start to finish resulting in a greater dose causing polymerisation during wire creation, this increases the dimensions of produced polymer scaffold. The GSM concurrently generates all wires from lowest layer to the top, at a significant increase in speed of construction. By strategically overlapping the coordinates to be polymerised and optimising exposure times and percentage power supplied per coordinate, a polymer scaffold with reduced dimensions would be created.

Moreover, this methodological change was expected to yield a robust overall structure. The initial lowest layer of coordinates would be generated without an overall connection to the substrate to provide support. This would result in deformation of this lowest layer of nanowires produced by these coordinates as diffusion-based motion of the polymerised coordinates within photoresist would naturally occur. However, due to the rapid write speeds provided by GSM, any such deformation was anticipated to be negligible at best or confined to the lowest layer at worst.

Consequently, it was decided to increase the number of layers of the system by two, creating a full unit cell of the 3D ASI. While the lowest layer (SL4) would be the least measurable due to layers above it as well as the predicted deformation during the write process those layers above it (SL3 - SL1) would benefit from increased structural integrity due to the supporting layers below. It was predicted that this would reduce tilt into the aperture thereby maintaining a consistent projection for all wires in each sub-lattice during measurement. Maintaining a uniform projection will ensure a consistent strength of the XMCD signal for reliable and comparable measurements across the sub-lattice for statistical analysis.

Additionally, a decision was made to pursue a more significant reduction in the polymer scaffold by subjecting samples produced using the aforementioned method to an extended oxygen plasma exposure. Previous iterations of this process had effectively decreased scaffold thickness by $10\% - 20\%$, as observed in **Table 3**. It was believed that further refinement could be accomplished by investigating extended exposure times to achieve an even thinner scaffold. To prevent additional oxidation of the magnetic material during this process, it was deemed necessary to employ a thicker aluminium capping layer.

These comprehensive modifications to the fabrication process, as well as detailed specifics for the samples, will be discussed in the following sections of this thesis.

5.6.1 Galvo Scan Mode TPL

The exploratory use of GSM two-photon lithography was initiated through preliminary tests. These tests involved the creation of a dose array using the IPL-780 negative tone photoresist in DIP-in mode, applied on a silicon substrate. While in the PSM, the primary parameters for optimization are scan speed and the percentage of laser power, in GSM, the focus was shifted to the exposure time for each coordinate and the percentage of laser power. To determine the ideal settings for this new approach, lattices with varying parameters were generated and examined through optical microscopy and scanning electron microscopes (SEMs). The optimal settings were identified by achieving a fully formed lattice that was written with the fastest writing speed, combined with the thinnest wires. With these settings, progress was made to fabricate a 3D ASI suspended over the corner of an aperture.

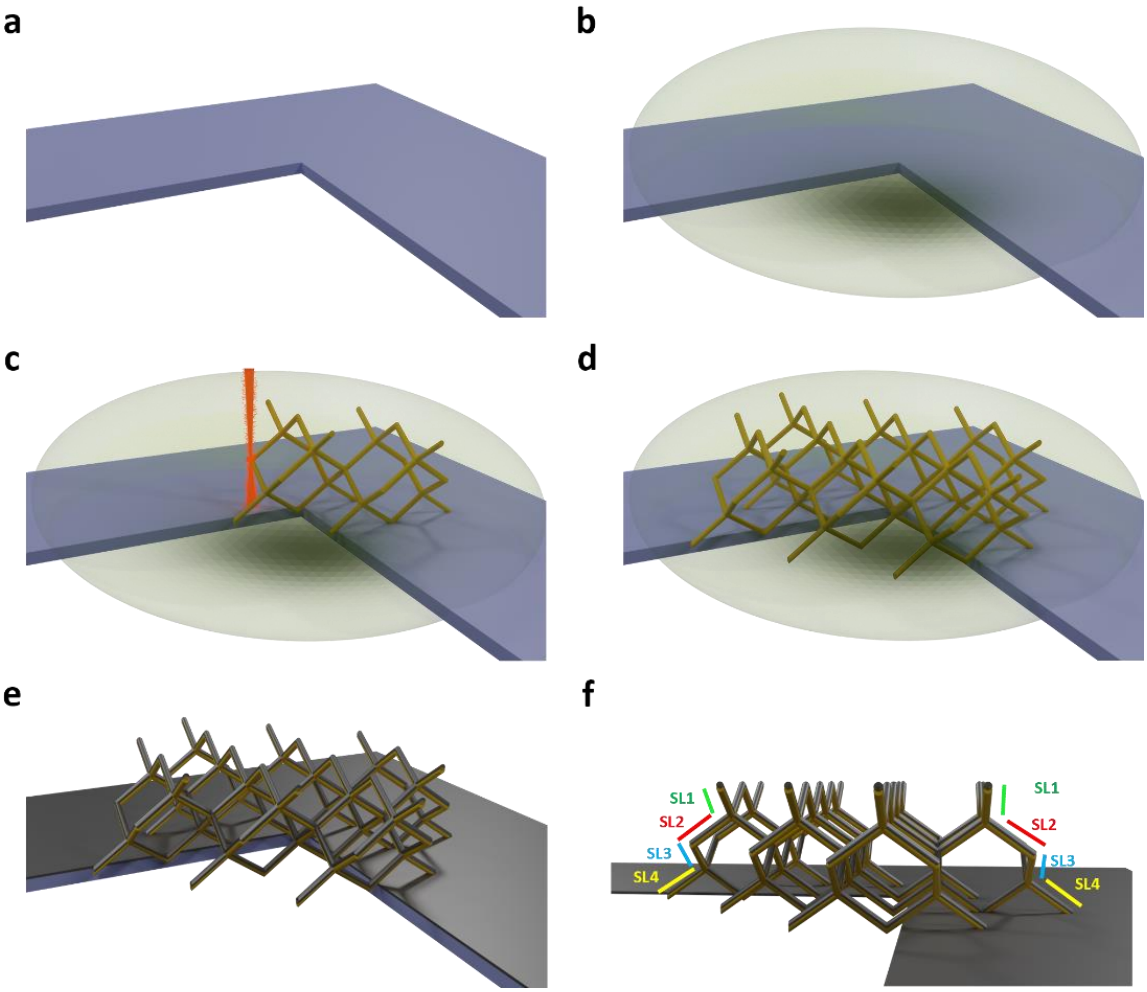

Figure 75: Sequence of suspended 3D ASI fabrication. ***(a-b)*** *A Silicon chip with* $50\ \mu m \times\ 50\ \mu m$ *aperture is cleaned in an ultrasonic bath with acetone and then rinsed with IPA, excess IPA is then removed with a compressed air gun. Surface of silicon chip is coated with Negative-tone resist (IP-DIP).* ***(c-d)*** *Two Photon Lithography is used to polymerise the resist in a pre-defined 1-unit cell thick diamond bond lattice over the aperture corner. Dimensions of structure is* $12\ \mu m \times\ 30\ \mu m \times\ 2\ \mu m$. ***(e)*** *Development of resist and cleaning in IPA removes excess resist and reveals solid polymer scaffold structure. Permalloy* $(Ni_{81}Fe_{19})$ *is deposited onto the upper surface of lattice via thermal evaporation resulting in the suspended 3D ASI structure.* ***(f)*** *The 3D ASI is comprised of four sub-lattice layers designated SL1 through to SL4.*

Figure 75 shows the full stepwise process of the new method of fabricating a 3D ASI over the corner of an aperture using galvo scan mode. The 3D ASI constitutes a complete unit cell of the diamond bond geometry and is comprised of four layers of wires. The lowest wire layer (SL4) and the uppermost layer (SL1) feature alternating coordination 4 and coordination 2

vertices, whereas the innermost layers (SL2, SL3) are exclusively comprised of coordination four vertices, this is clearly shown by labelling on **Figure 75f**.

As before, samples consisted of an aperture of approximate dimensions $50\ \mu m \times 50\ \mu m$ with four 3D ASI lattices, each $12\ \mu m \times 30\ \mu m \times 2.3\ \mu m$ suspended over each corner. Reference lattices, used to test the z-positioning of the write, were positioned on the substrate, located behind corners to act as identifying markers for labelling of lattices.

5.6.2 Deposition of Permalloy

The samples underwent a coating process involving an $Al/Py/Al$ tri-layer, with an increased thickness in the aluminum capping layer, measuring approximately $4\ nm/43\ nm/3\ nm$. Optical microscopy revealed that five samples exhibited minimal lattice deformation or damage post-deposition, with four fully formed lattices visible around each aperture. These selected samples underwent extended oxygen plasma exposure subsequently.

5.6.3 Oxygen Plasma Exposure

This sample set of five underwent varying exposure times to oxygen plasma as part of the fabrication process. Utilizing the results of the diamond experiment, and greater protection from a thicker capping layer, greater exposure times of 0 hours, 0.5 hours, 1 hour, 2 hours, and 4 hours were selected. Throughout this exposure, the samples, including the aperture substrate, remained affixed to the same glass slides they were used on during the evaporation stage, as described in Section 5.3.3. This approach was adopted to ensure that sheet film for each sample that had been subjected to the same oxygen plasma exposure, facilitating subsequent MOKE measurements. The samples remained securely in place on the glass substrate and were not lifted from it.

During this process, the samples were exposed to the same radio frequency power $(60\ W)$ as in previous experiments and an oxygen flow rate of $30\ SCCM$.

To prepare the samples for transportation to the ALBA synchrotron facility, it was necessary to remove the silicon apertures from the glass slides. This was accomplished in a manner consistent with previous procedures, using a scalpel to carefully cut through the GE Varnish

glue. Special attention was paid to avoid any chipping of the glue or glass that could potentially impact the integrity of the samples.

Table 4: *Sample labels with associated oxygen plasma exposure, expected deposited tri-layer thickness (based on QCM monitors) and measured average wire thickness, standard deviation shown as error values. Wire thickness measurements carried out using SEMs shown in Section 5.7.2.*

Sample Label	Oxygen Plasma Exposure Time (Minutes)	Deposited Al/Py/Al expected thickness (nm)	Estimated average wire thickness (µm)
210412E/C	0	4/43/3	0.81 ± 0.02
210412E/E	30	4/43/3	0.79 ± 0.02
210415E/A	60	4/43/3	0.73 ± 0.04
210415E/B	120	4/43/3	0.71 ± 0.07
210415E/H	240	4/43/3	0.72 ± 0.09

5.7 Characterisation of a suspended 3D ASI (Galvo Scan Mode)

Before the ALBA experiment, the samples underwent a characterization process like that shown previously in Section 5.4. This step was essential for identifying the best samples and determining the order of priority for experiments to be conducted during the ALBA experiment.

5.7.1 Optical Imaging

As in the previous experiment, optical images were captured after each successive stage of the fabrication process. The aim was to ascertain whether the samples had experienced any deformation during development, thermal evaporation, or following the oxygen plasma exposure process. To aid in the identification of individual lattices, labels that were generated during the two-photon lithography write were used, as depicted in **Figure 76**.

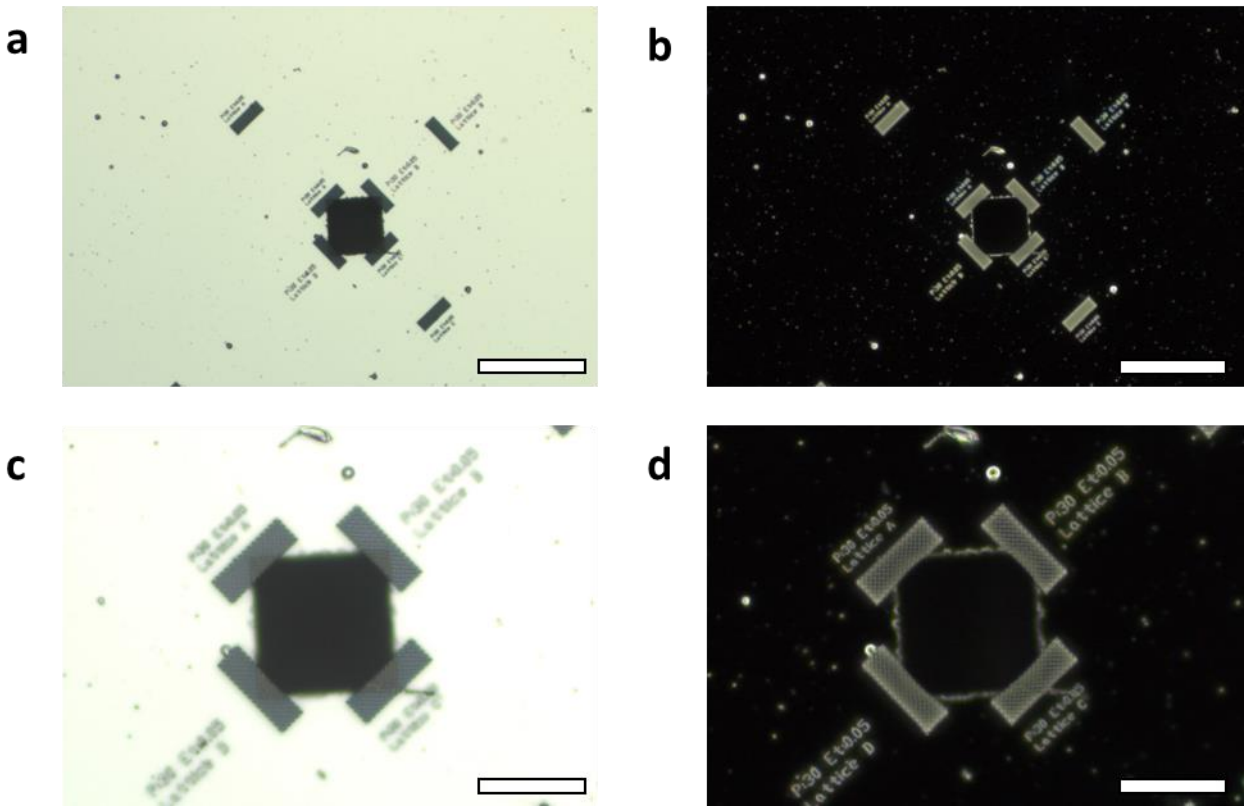

Figure 76: *Optical images of samples post thermal evaporation, prior to oxygen plasma exposure. Samples are labelled during the write process for ease of identification during the ALBA experiment. Bright-field images shown in* ***(a)*** *and* ***(c)****. Dark field images shown in* ***(b)*** *and* ***(d)****. Scale bars shown* ***(a-b)*** $100\ \mu m$*,* ***(c-d)*** $40\ \mu m$*.*

In the images provided here as an example, taken post thermal evaporation, it is evident that all samples have successfully retained all lattices. When magnified under 100x, shown in **Figure 76c** and **Figure 76d**, it becomes apparent that the lattices have remained fully formed, exhibiting minimal deformation and the absence of any significant dirt or contaminants.

5.7.2 Scanning Electron Microscopy

Scanning electron microscopy images taken after deposition of the tri-layer are shown in **Figure 77**. As displayed in **Figure 77a**, the SL4 layer exhibits significant deformation, which is attributed to both the movement of the photoresist and sagging of the lattice during the fabrication process. However, further layers SL3 through SL1 appear to be fully formed and in good condition. Notably, **Figure 77a** clearly illustrates sagging of the lattice into the aperture, with the edge of the lattice tilting the most into the aperture. A top-down image of the lattice

is shown in **Figure 77b**, with the sublattices appropriately labelled. **Figure 77c** provides a 45°-tilt SEM image of the control sample that did not undergo oxygen plasma exposure. The thickness of the unexposed lattice was measured using previously established methods and is presented in **Table 4**. A comparison of the measured thickness of the unexposed lattice generated using the GSM method of fabrication with that generated by PSM, demonstrates a notable 20% reduction in polymer scaffold thickness attributed to this methodological change alone. This can be attributed to the decrease in dose provided in GSM mode compared to PSM.

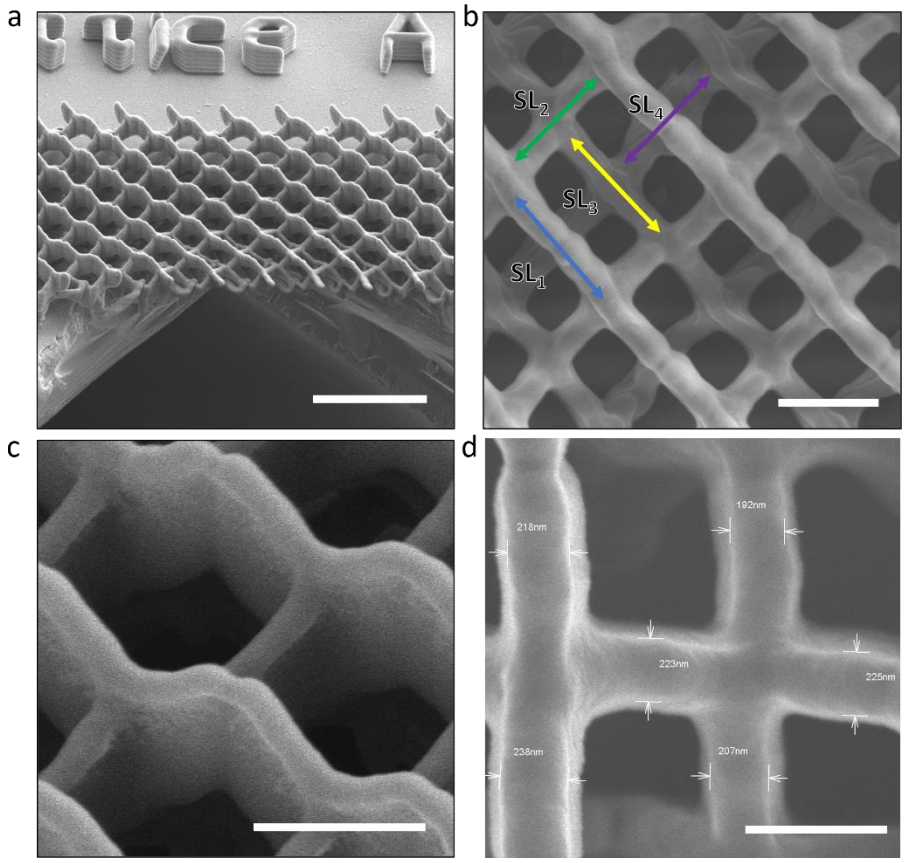

Figure 77: *A suspended 3D ASI lattice.* ***(a)*** *Scanning electron microscopy image (SEM) of 3D ASI lattice suspended over an aperture corner.* ***(b)*** *Top-view SEM of the suspended lattice. Sub-lattices of different depth are labelled SL1 (Highest), SL2, SL3 and SL4 (Lowest).* ***(c)*** *Zoomed SEM image of the upper surface of 210412EE.* ***(d)*** *A top-down image of 210412EC showing measured widths of each of the sub-lattices. Scale bar indicates* ***(a)*** 5 μm, ***(b-d)*** 1 μm.

In **Figure 78**, images **a-d** depict tilt SEM images of samples subjected to the range of plasma exposure times, as detailed in **Table 4**, in ascending order of plasma exposure duration. These

SEM images, which are part of a comprehensive SEM image set, were captured at a $45°$ tilt angle facilitating measurement of the average thickness of the polymer scaffold following plasma exposure. Measurements were taken from the uppermost party of the wire to the lowest viewable section of the polymer scaffold across various wires within each SEM image. The measured tilt thickness was then converted into an actual thickness value using Equation (128). An average polymer scaffold thickness was calculated for each oxygen plasma exposure, with the standard deviation of measurements serving as the error.

After the plasma ashing process, the wires maintain their stability and exhibit no visible deformation despite the heat and plasma exposure. Visually, there's a visually noticeable variance in the thickness of the reduced polymer, particularly emphasized in **Figure 78b**. Among the regions observed, those closer to the structural support near the aperture edge reveal fully formed wires and appear to be the most suitable for measurements of ASI properties. Specifically, the upper surface layers (SL1 – SL3) appear intact and fully formed, while severe deformation is evident in SL1 wires situated furthest from the aperture. This consistency in wire stability after plasma exposure hints at the potential for reliable ASI property measurements, especially closer to the structural support of the aperture edge where wires maintain their integrity.

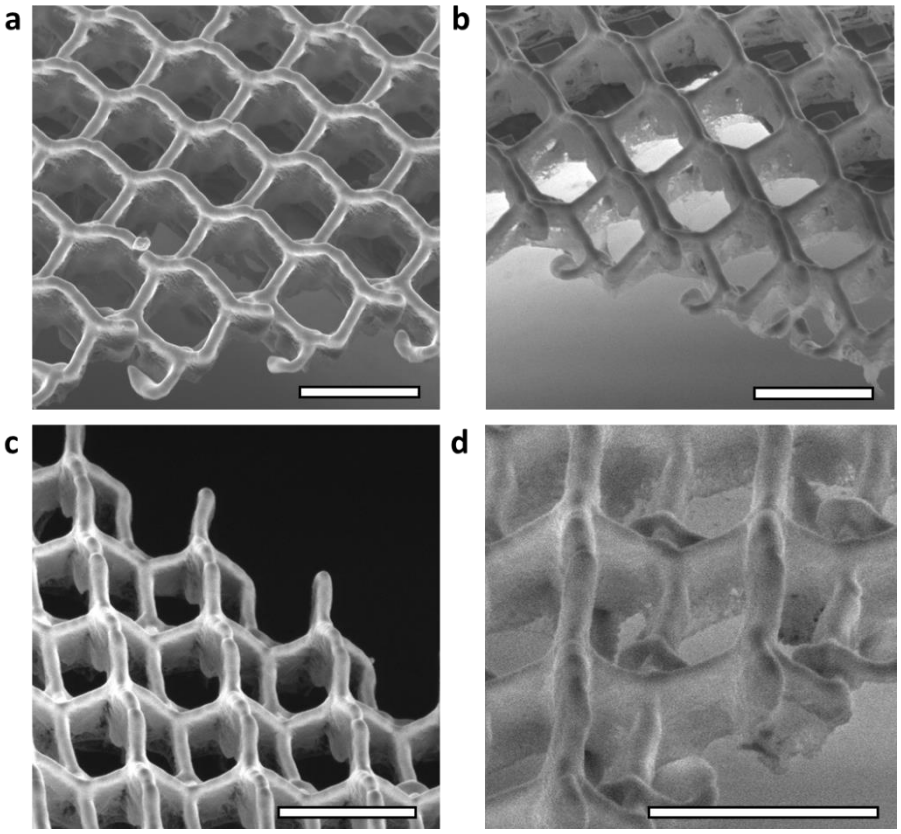

Figure 78: *Tilted SEM images showing the thickness of the polymer scaffold after oxygen plasma exposure of* ***(a)*** *30-minutes (210412EE),* ***(b)*** *1-hour (210415EA),* ***(c)*** *2-hours (210415EB),* ***(d)*** *4-hours (210415EH). Scale bars shown are* $2\ \mu m$.

The observed exponential-like decrease in measured polymer thickness, as depicted in **Figure 79**, introduces a novel pattern distinct from prior observations within the Diamond Light Source sample set. Analogous patterns of self-limiting reduction in polymer thickness have been documented in previous studies [90]. These studies observed a trend where the initial etch rate exhibited considerable rapidity, notably high within the initial two minutes, followed by a diminishing etch rate.

Notably, a point was reached around the 6-minute mark where almost negligible etching was observable. This behaviour aligns with findings from other studies, suggesting that at this stage, the etching process may have predominantly removed the organic components of the polymer, leaving behind an inorganic network [90].

The average measured thickness concerning the oxygen plasma exposure is graphically represented in **Figure 79**.

As the oxygen plasma exposure time increases, a greater variability in the measured polymer thickness is evident, as indicated by the increase in the standard deviation of these measurements. This variability is attributed to the differences in the thickness of the polymer scaffold removed beneath the tri-layer coating. Regions of the lattice that extend further over the aperture exhibit a more substantial reduction in polymer thickness, and across each wire forming the lattice, variations in the thickness reduction occur, this is seen most clearly in comparison of the exposed edge wires and those closest to the aperture edge in **Figure 78b**. While the overall thickness reduction enhances x-ray transmission through the polymer scaffold, this variability introduces a non-uniform absorption background to any measured signal.

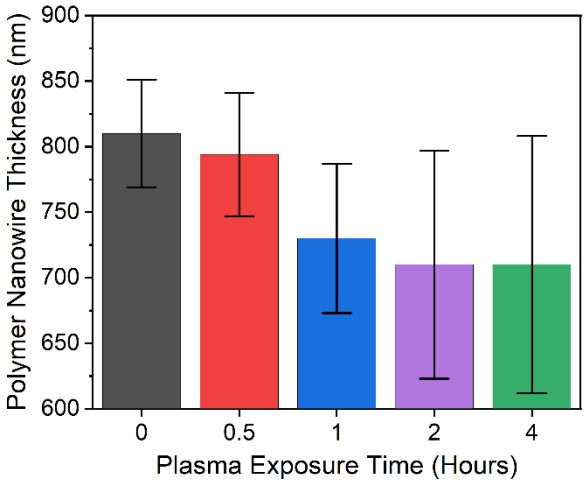

Figure 79: *Average polymer scaffold thickness measured via tilted SEM micrographs plotted against the exposure time to the oxygen plasma with standard deviation shown as error bars. A* $\sim 10\%$ *drop in scaffold thickness was measured after 1 hour of plasma exposure, with diminishing returns observed for further exposure. The standard deviation of wire thickness increases with greater plasma exposure time due to uneven exposure across wires.*

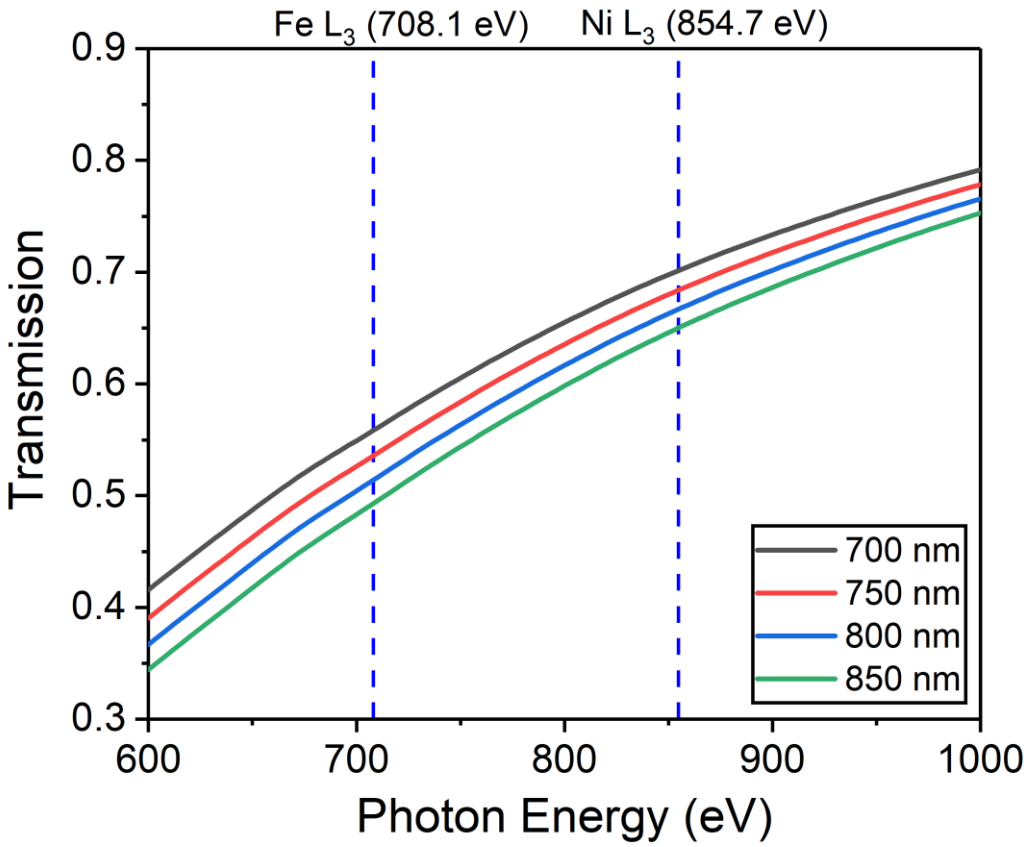

Figure 80: *Calculated transmission of x-rays through PMMA* $(C_5H_8O_2)$*.* Fe *and* Ni L_3 *edge shown. Transmission calculations carried out by CXRO Centre of Xray Optics online tool utilising Henke tables [63] using PMMA as approximate resist material.*

Figure 80 shows the calculated transmission of x-rays through PMMA for a range of different thicknesses, with both the Fe and Ni L_3 edge shown. Transmission values were calculated, as before, using Equation (129) and show a transmission for the average sample set thickness of $730 \pm 40\ nm$ of 69% at the Ni L_3 edge photon energy and 54% at the Fe L_3 edge photon energy. This shows an increase in the Ni and Fe transmission of approximately 10% and 20% respectively compared to average transmission measured of the Diamond Light Source sample set.

5.7.1 Magneto Optical Kerr Effect measurements

Magneto Optical Kerr Effect (MOKE) measurements were conducted on sheet film samples that had undergone the same plasma exposure as the samples intended for the ALBA synchrotron experiment. This was done to assess the influence of plasma exposure on the magnetic material and to anticipate any potential oxidisation effects. **Figure 81** presents a

comparison of MOKE loops for a thin film sample taken from: an unexposed sample (210412EC), a sample exposed for 0.5 hours (210412EE) and from a sample exposed for 1 hour (210415EA). Notably, the coercivity of these samples, which all fall within the expected range measured previously, decrease with increased oxygen plasma exposure time.

The reduction in coercivity can similarly be attributed to the influence of oxidization on the magnetic characteristics of the material. Oxidation will produce convert a surface layer of $NiFe$ into antiferromagnetic NiO, and antiferromagnetic $NiFe_2O_4$ and Fe_3O_4. This will reduce the materials overall magnetic moment per volume, lowering coercivity with increased exposure to oxygen plasma [81].

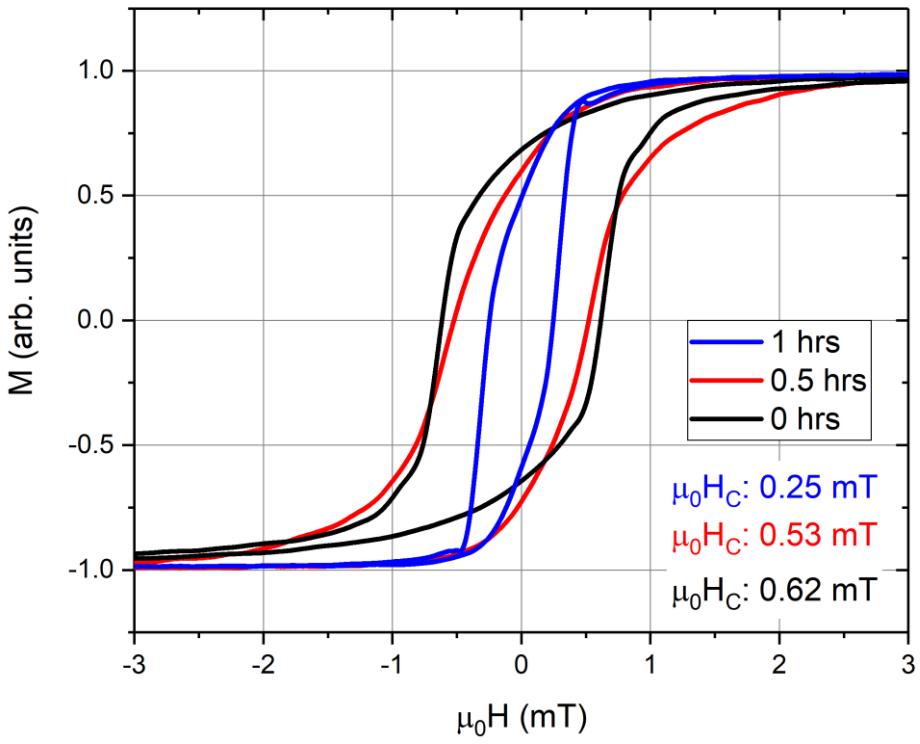

Figure 81: *Longitudinal magneto-optical Kerr effect loops depicted for thin-film samples: 210412EC (black line) unexposed to oxygen plasma, 210412EE (red line) exposed for 0.5 hours, and 210415EA (blue line) exposed for 1 hour. Coercivity values shown in respective colours.*

Figure 81 demonstrates that the permalloy retains magnetic properties despite exposure and some variation in coercive field. This informed the decision to proceed with the experiment while acknowledging that samples with greater plasma exposure would exhibit a reduced magnetic signal due to oxidation. This posed a dilemma in selecting priority samples, weighing the benefits of reduced polymer scaffold thickness (resulting from increased plasma

exposure) and the potential for increased transmission and visible magnetic signal against the desire to minimise plasma exposure to retain the strength of the magnetic signal to be measured.

5.8 ALBA Experiment (Galvo Scan Mode)

The TXM experiment at ALBA took place over three days, with oversight from Peter Fischer (Berkeley), David Raftrey (Berkeley), Sam Ladak and myself. Initially, the measurements were conducted in person at the synchrotron with the assistance of Beamline Scientist Lucia Abelle. Following these initial measurements and training, both David Raftrey and I conducted experiments remotely.

The experimental setup at the ALBA beamline was such that the convenient measuring protocol was fixing the x-ray beam polarisation to circular left and acquiring images at absorption edges with opposite dichroic contribution in order to extract the magnetic contrast [91], see Section 3.2.7.

The initial focus of this experiment was to determine whether the lattices exhibited the same deformation and movement observed during the Diamond experiment. Data collection proceeded as follows:

- **Wide View Image:** The first step involved capturing a wide-view image of the sample. This image served as a map for identifying each lattice through the labels written into the substrate, this is shown in **Figure 82**.
- **Region of Interest:** Using the wide-view image as a reference, a specific region of an exposed lattice was selected, and x-ray absorption spectroscopy (XAS) spectra were obtained across the desired energy range. Example wide-view image is shown in **Figure 82**
- **Peak Identification:** The acquired spectra were analysed to identify the $L_{2,3}$ edge peaks for the sample, which are relevant for the investigation. These are shown in **Figure 83**.
- **Images stacks:** Image stacks, typically consisting of around 300 images, were taken of the lattice. This process was repeated twice: once at the L_3 edge and

again at the L_2 edge. Stacks of images were aligned with one another and then averaged to produce a singular image at the $L_{2,3}$ photon edge.

- **Flat-Field Images:** For each edge, flat-field images were collected from a region away from the sample within the aperture. These flat-field images were crucial for normalising the image taken at the peak energy.

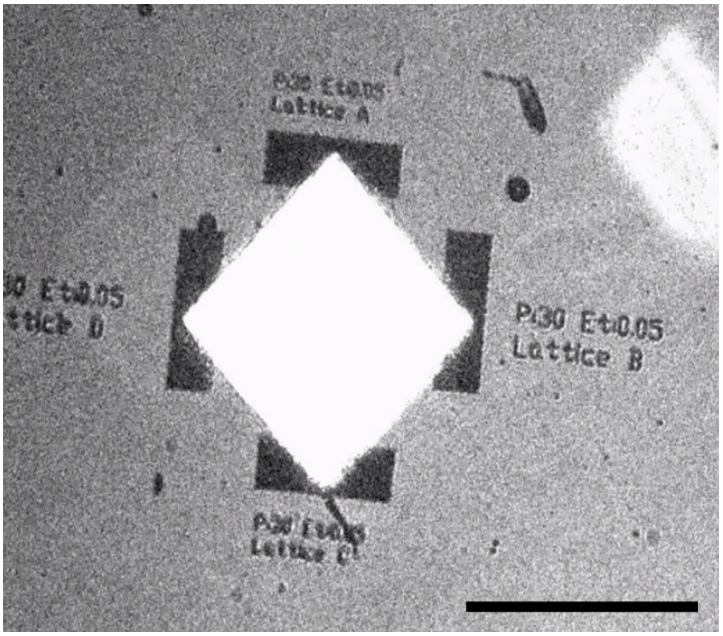

Figure 82: *An example wide-view image taken of a sample (210415EA) prior to use as a map for selection of regions of interest.*

The initial collection of images in this manner revealed that, after a brief period of deformation of the sample under the full beam exposure, the sample stabilised and remained motionless during repeated stack collection.

5.8.1 X-ray Absorption Spectra

As previously mentioned, before collecting of stacks of images of the lattices, the peak $L_{2,3}$ photon energy edge for each sample was identified. This was achieved by undertaking a spectroscopic scan across the energy range $(695 - 745\ eV)$, this process is explained in Section 3.2.7. Based upon literature values [87], the $Fe\ L_3$ peak is expected to be $706.8\ eV$ and $Fe\ L_2$ to be at $719.8\ eV$, however an offset in the spectrometer and varying sample oxidation can yield subtle differences. Therefore, for each sample measured, a scan was undertaken to ensure images were taken at resonance. By plotting average intensity of transmission against energy, a clear visualisation enabled precise identification of the $Fe\ L_3$

and $Fe\ L_2$ peak positions specific for each sample, depicted in **Figure 83**. This XAS spectra also provides insight into the level of oxidation in the samples, which increased with exposure to oxygen plasma despite the aluminium capping layers.

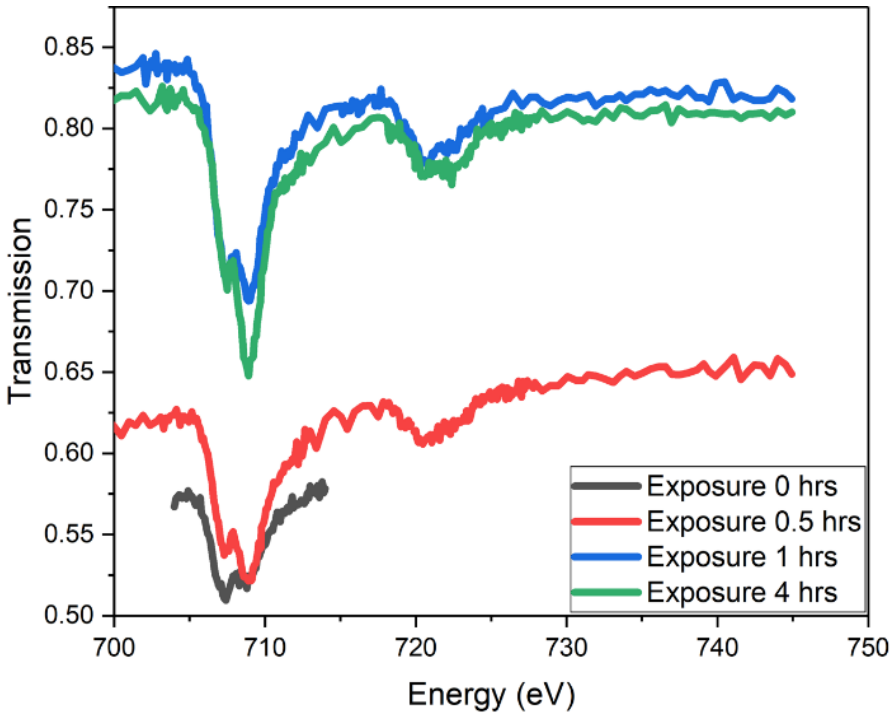

Figure 83: *Experimental $Fe\ L_{2,3}$ x-ray absorption spectra taken at ALBA synchrotron. Samples show an increase in shoulder peak clearly seen at the L_3 edge with increased exposure to oxygen plasma. The pre-edge absorption can be attributed to the underlying polymer.*

In the XAS spectra, the sample (210412EC) with no oxygen plasma exposure displays a peak at $707.5\ eV$ indicating the presence of metallic $Ni_{81}Fe_{19}$, this is made clearer in **Figure 84** which focuses on the $Fe\ L_3$ absorption edge.

The discernible shoulder around $709\ eV$ indicates a level of oxidation of the permalloy. This corresponds to the presence of Fe_3O_4, a compound formed in the presence of higher oxygen quantities, typically characterised in XAS spectra by a distinct shoulder at approximately $709\ eV$ [87]. Throughout the examination of samples subjected to escalating oxygen plasma exposure, evidence of a growing multiplet structure intensifying around $709\ eV$ is observed. Consequently, the oxidation of the samples is attributed to exposure to the oxygen plasma, a process that was not prevented by the inadequate aluminium capping layer.

The disparity in signal-to-noise observed between the spectra obtained in this dataset and the STXM Diamond data can be attributed to differences in the acquisition methodologies. During the STXM Diamond data collection, images were captured across a spectrum of energies, followed by the extraction of spectra from a precise location directly on the target of interest. Conversely, in this dataset, an average transmission response was derived over the lattice area, encompassing numerous wires along with surrounding features, potential debris, and oxidised regions of the wires. This broader sampling approach inadvertently led to a higher inclusion of background signals and variations in the surrounding environment, resulting in a lower signal-to-noise ratio in the obtained spectra. The STXM Diamond data, with its more localized and focused extraction method, inherently captured spectra with reduced background noise due to its narrower field of view and targeted measurement approach.

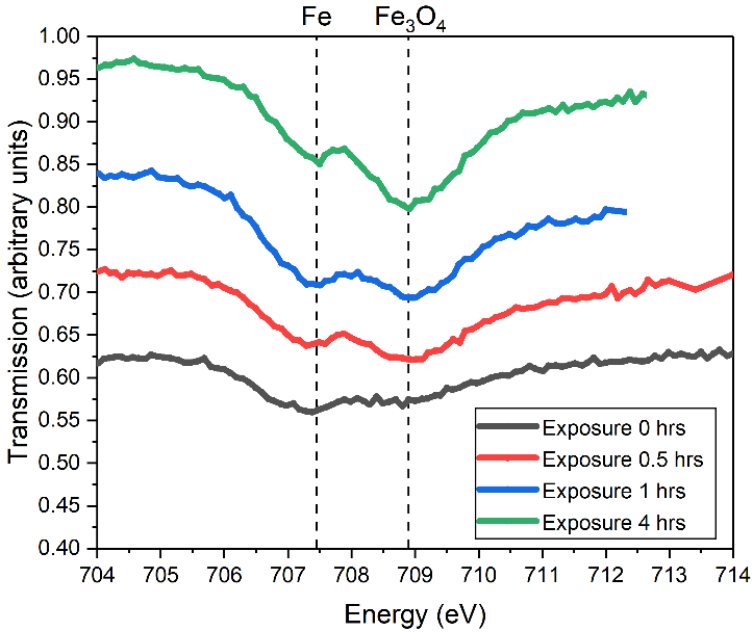

Figure 84: *$Fe\ L_3$ spectra for samples of increasing oxygen exposure time. The spectra have been artificially offset in the vertical axis for clarity. The $Fe\ L_3$ absorption edge present an oxidised component that appears as a shoulder peak at $709\ eV$ with intensity dependent on the oxygen plasma exposure time.*

This trend is particularly clear in **Figure 85**, where the ratio of the Fe peak to Fe_3O_4 peak decreases as the oxygen plasma exposure time increases. Overall, these results suggest that samples subjected to intermediate oxygen plasma exposure times strike a balance between

reduced polymer thickness and a significant volume fraction of metallic $Ni_{81}Fe_{19}$. For instance, the 60-minute oxygen plasma exposure resulted in a 10% reduction in polymer thickness, which should improve transmission while maintaining an Fe / Fe_3O_4 L_3 peak ratio of 0.95. Due to these considerations, this sample (210415EA) was identified as the best opportunity for detecting the magnetic signal of the wires and was particularly focused on for data collection.

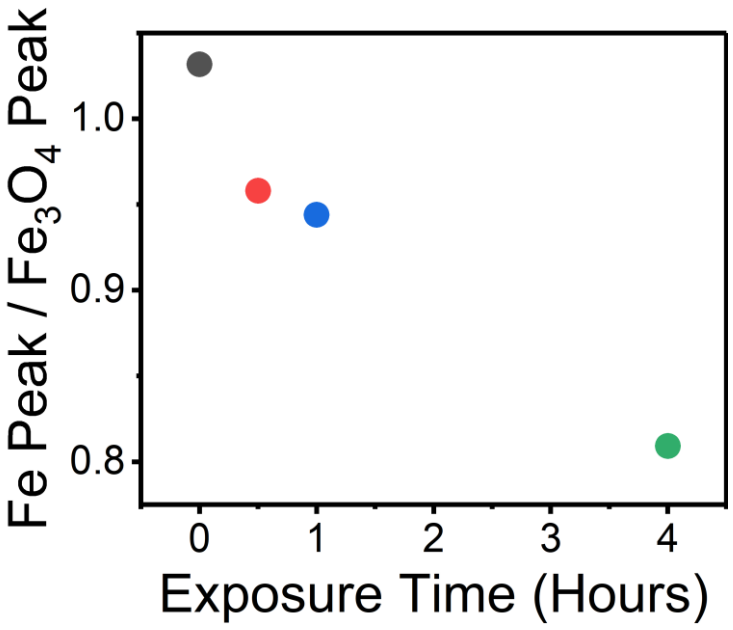

Figure 85: *Ratio of metallic* (Fe) *peak to oxide* (Fe_3O_4) *peak, as a function of plasma exposure time.*

5.8.2 XMCD: Initial Measurements

Initially, a comprehensive data collection effort was undertaken, involving various samples, with concurrent data processing during the acquisition process. The focus was adjusted based on the experiment's results. One of the key advantages provided by working at the ALBA synchrotron was the capability to manipulate the sample's tilt concerning the direction of the x-ray beam's propagation. This capability enabled compensation for the sample's natural tilt into the aperture, ultimately restoring it to a nearly perpendicular orientation concerning the plane of the 3D ASI structure. This adjustment enabled theoretical recovery of a portion of the magnetic signal that was oriented into the x-ray beam. Moreover, it reduced wire overlap within images, making wire identification more manageable.

To illustrate the quality of images produced by this data collection, one of the initial images collected is presented in **Figure 86**, featuring a lattice from the sample exposed to one hour of oxygen plasma (210415EA). The methodology of collecting images during this experiment is explained in Section 3.2.7.

The state of the lattice after exposure to the x-ray beam can be observed in **Figure 86a**. Notably, the SL4 sublattice appears deformed and disjointed throughout the lattice, as expected from SEM's, with some regions overlapping beneath the SL3 sublattice. These overlapping areas are clearly visible in the XAS image due to their darker contrast, indicating a significant reduction in transmission.

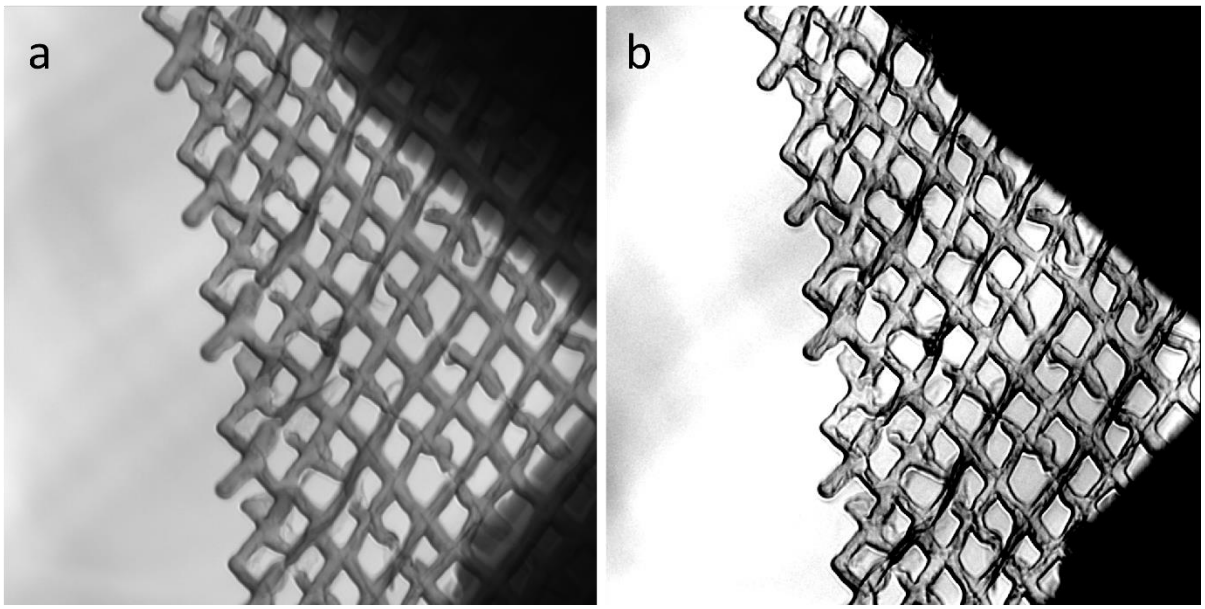

Figure 86: *Initial results of ALBA synchrotron experiment. Sample shown is 210415EA (1-hour oxygen plasma exposure).* ***(a)*** *An XAS image taken at the* $Fe\ L_3$ *photon energy edge and* ***(b)*** *an XMCD image calculated using image* ***(a)*** *and the* $Fe\ L_2$ *XAS image.*

Figure 86b presents an XMCD image calculated by subtracting the $Fe\ L_2$ XAS image from the $Fe\ L_3$ XAS image shown in **Figure 86a**, after appropriate alignment and normalisation. When compared to other XMCD experiments conducted at ALBA, the results appear both promising and complex. Throughout the lattice, regions with varying levels of bright and dark contrast are observed, suggesting potential patterns of magnetic signal. An area of particular interest within this image is the edges of each wire, displaying thick black contrast, indicating minimal transmission in these regions. As confirmed in Section 5.5.2, the wires possess a curved cross-

section, and these black-bordered areas likely correspond to regions where the thickness of the deposited magnetic material and the aluminium capping layer reaches its theoretical minimum. It is hypothesized that these segments of magnetic material have undergone extensive oxidation. The darker lines may be the result from the non-magnetic nature of the oxide, changes in the chemical state affecting absorption, increased overall X-ray absorption, and interference or scattering effects.

5.8.3 Statistical Analysis of XMCD images

The contrast within the delineated, black-bordered regions of the wires, excluding overlapping sections, was analysed, revealing no distinct separation into consistently bright or dark wires in the XMCD images. While certain regions exhibited predominantly bright or dark characteristics, other areas showed less definitive contrast. To determine the presence of magnetic signals, a statistical analysis across all four sub-layers, was conducted to quantify the contrast within the wire borders. In an ideal scenario, the presence of two distinct subsets, clearly segregating into bright and dark wires, would be revealed by measurements across all wires. This clear differentiation between subsets would allow for the straightforward categorization of wires based on their distinct contrast.

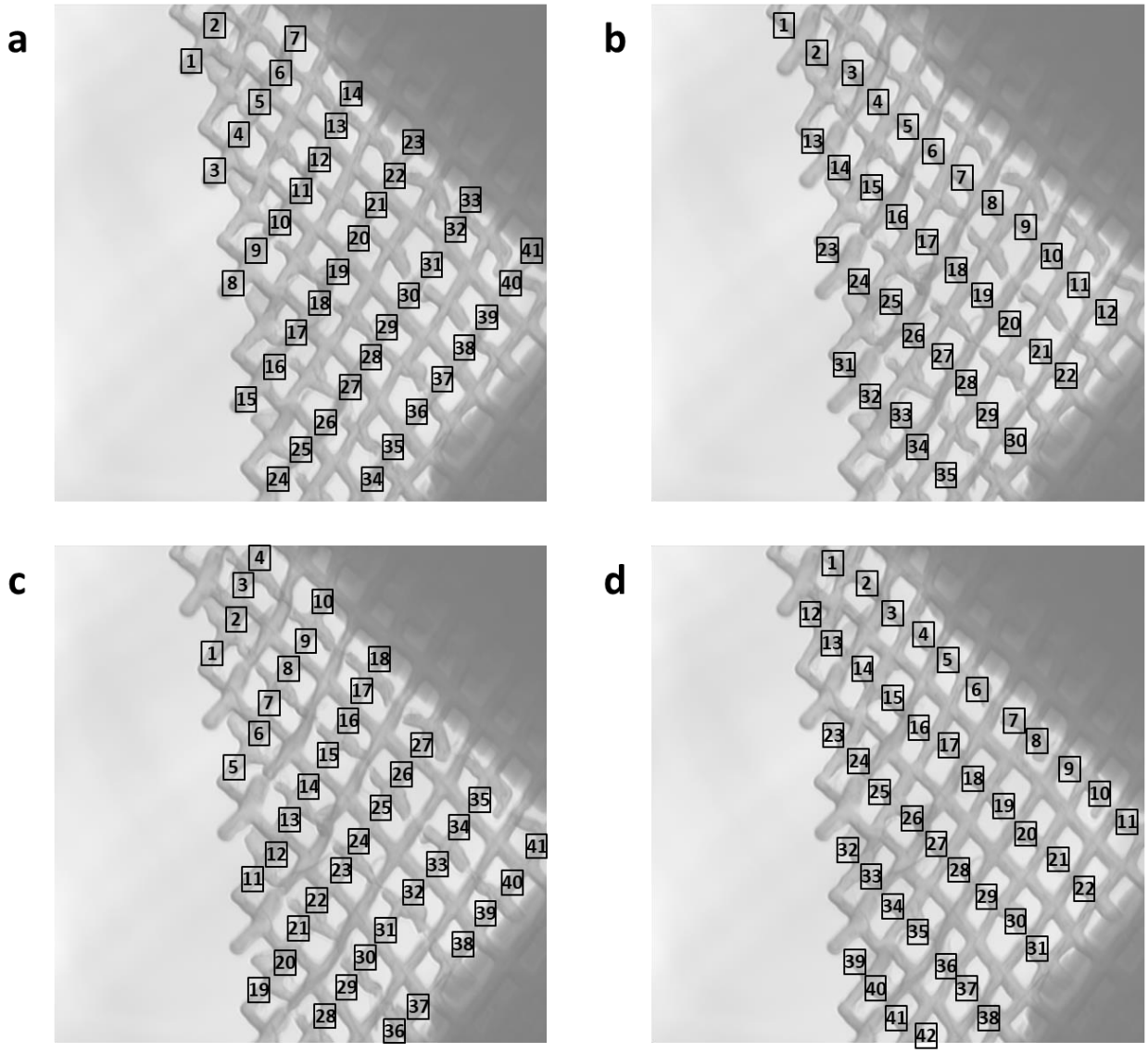

Figure 87: *Labelling of sub lattice wires upon the $Fe\ L_3$ XAS image shown in Figure 86a, for statistical analysis of the XMCD image shown in* ***Figure 86****.* ***(a)*** *SL1* ***(b)*** *SL2* ***(c)*** *SL3* ***(d)*** *SL4.*

To achieve this, wires were first labelled in every sub-lattice, as depicted in **Figure 87**. The ImageJ software package was used for normalising the XMCD image, such that a value of 1 corresponds to bright and 0 to dark. This normalisation process was executed using:

$$I_N = \frac{I - I_{Min}}{I_{Max} - I_{Min}} \qquad (133)$$

Where I_N represents the normalised image, I_{min} represents the minimum measured value of the image, and I_{max} the maximum measured value.

Next, the central region of each wire segment between connecting vertices was individually selected and its average intensity value was recorded. Subsequently, these values were plotted for all wires. For a structure composed of magnetic material imaged in this manner, the presence of two distinct bands separated by several standard deviations of measurements, signifying groups of "Bright" wires and groups of "Dark" wires, was anticipated. This plot is displayed in **Figure 88**.

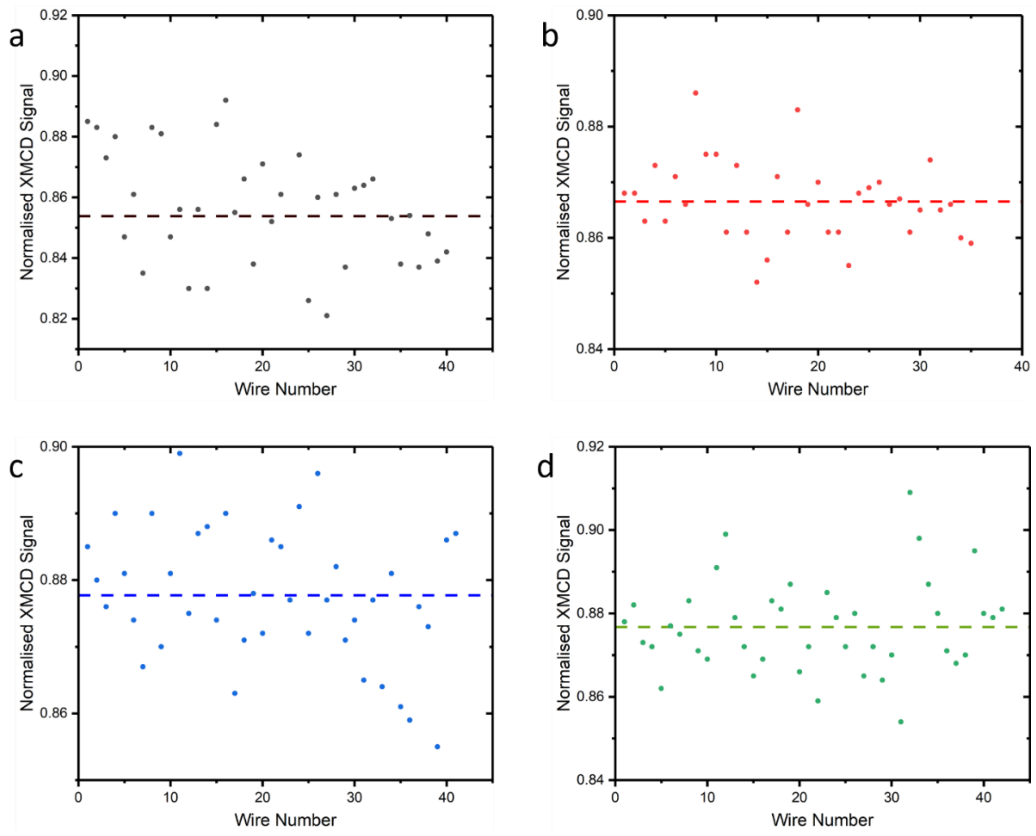

Figure 88: *Statistical analysis of the XMCD image shown in Figure 86. Each wire, labelled in Figure 87, is measured and the average normalised XMCD signal is plotted against its label for each sub-lattice within the image:* ***(a)*** *SL1,* ***(b)*** *SL2,* ***(c)*** *SL3,* ***(d)*** *SL4. The mean average value for each sublattice is shown by the dashed line in each plot.*

Figure 88 clearly indicates that any potential magnetic signal within the lattice is weak and possesses a low signal-to-noise ratio (SNR), requiring comprehensive statistical analysis to recover. Furthermore, considering this image was captured in an as-deposited state with minimal measured exposure to externally applied magnetic fields, uncertainties persist regarding the anticipated magnetic configuration of the lattice. To uncover definitive evidence of magnetic signal, an experiment was devised and conducted.

5.8.4 XMCD: Selective Analysis & Applied Field

For a comprehensive analysis of the magnetic signal in the measurements, wire regions without overlaps in both XMCD images, pre- and post-application of a $100\ mT$ magnetic field, were deliberately chosen, rather than solely relying on previously selected regions. Subsequently, chains of wires within each wire sublattice (SL1, SL2, SL3) were identified where no overlap was observed in XAS images or SEMs, and the average XMCD signal across the central region of each wire within these chains was measured. The resulting measurements were then plotted for each of the three wire sublattices, both in their as-deposited state and after the magnetic field

Measurements were conducted on the sample (210415EA) exposed to 1 hour of oxygen plasma exposure, chosen due to the substantial reduction in polymer scaffold and minimal oxidization of the magnetic material. To apply the magnetic field, a permanent magnet with a strength of approximately $100\ mT$ was employed, positioned at a proximity of $< 2\ mm$ behind a lattice to be measured on the sample, as depicted in **Figure 89**. Measurements were performed on both the lattice nearest to this magnet (Lattice B) and the lattice positioned opposite the aperture from the magnet (Lattice D). This oppositely positioned lattice is expected to exhibit a similar saturated magnetic configuration.

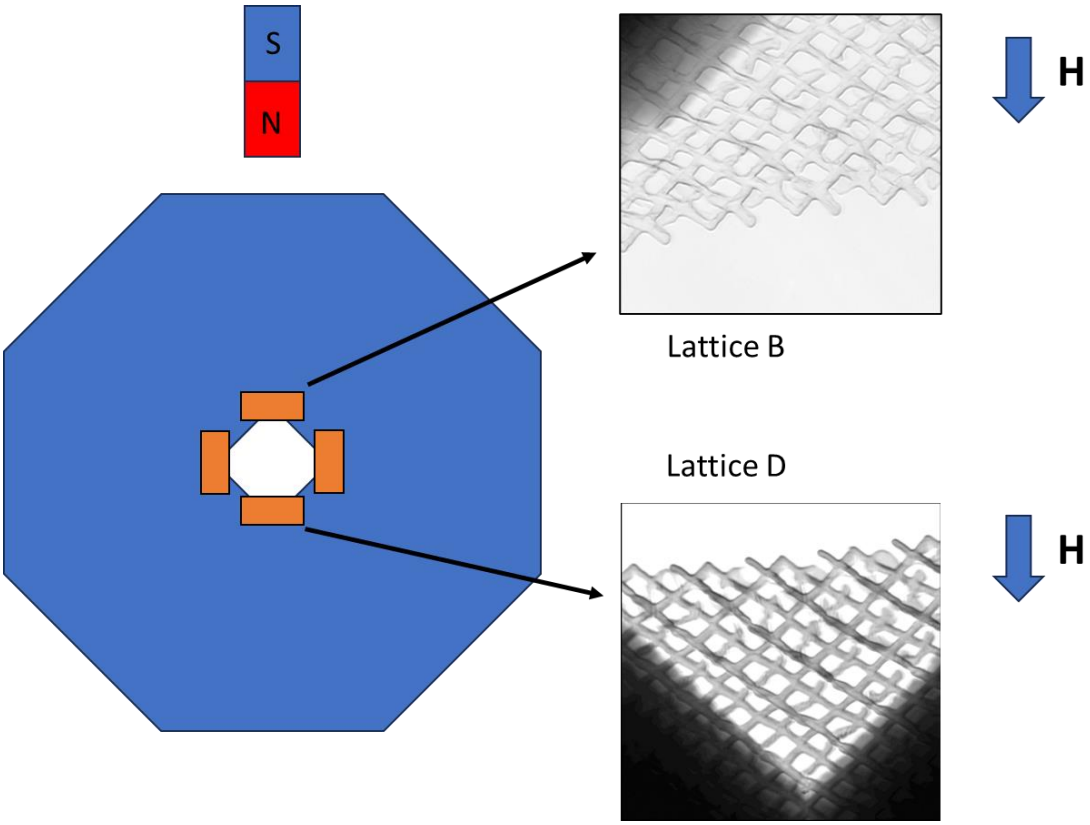

Figure 89: *The setup for application of the external magnetic field, locations of lattices measured are shown and labelled accordingly. Direction of applied field shown.*

Prior research has established the magnetic configuration expected following the application of a saturating magnetic field [43]. For a saturated sample the anticipation is to observe a single in-plane component in all wires but alternating out-of-plane contrast across chains of wires, as depicted in **Figure 90**.

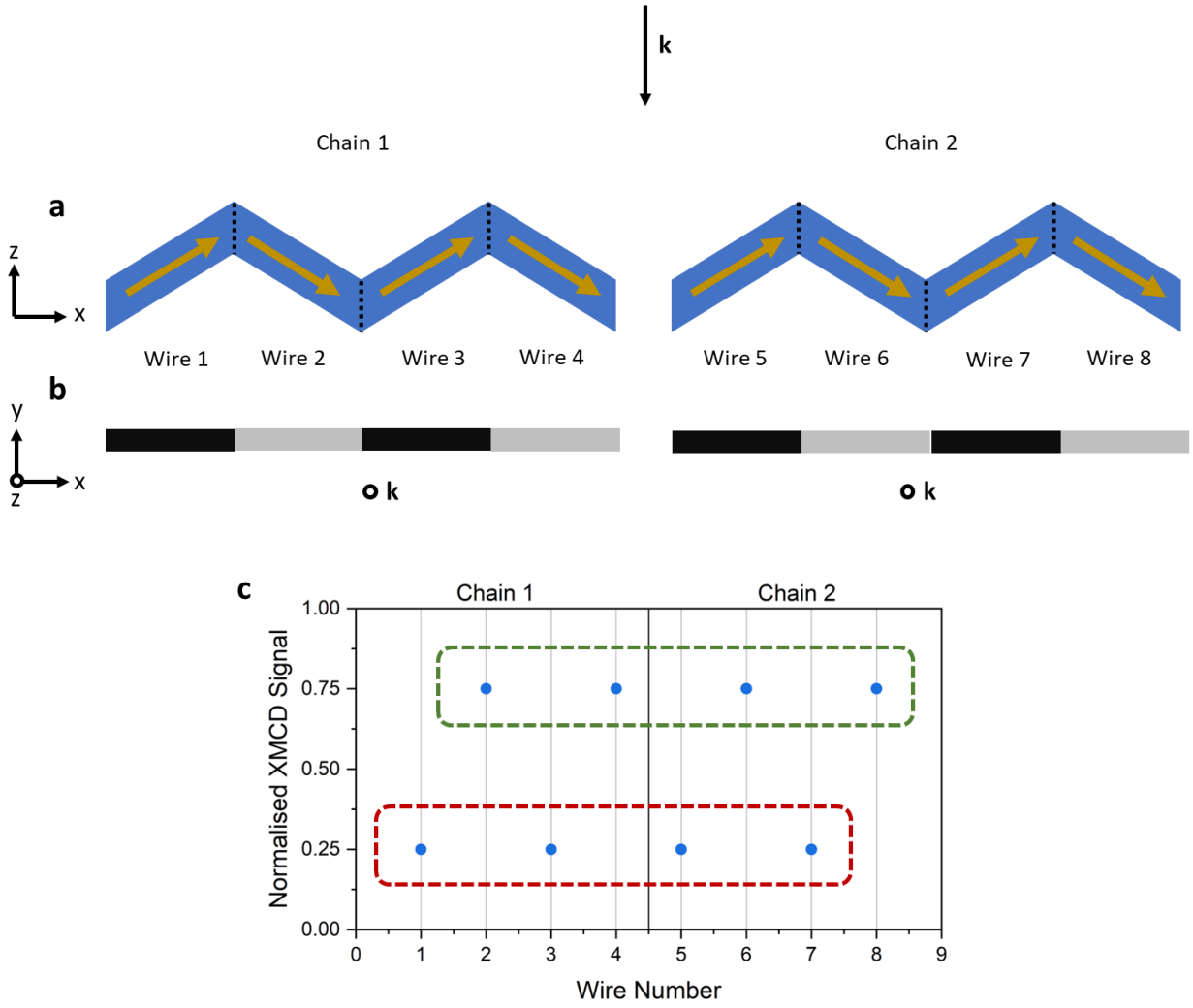

Figure 90: (a) *Diagram showing magnetisation arrangement within two chains of wires, Chain 1 and Chain 2, after in-plane saturation.* ***(b)*** *Schematic of x-ray magnetic circular dichroism (XMCD) signal shown for the magnetisation arrangement shown in* ***(a). (c)*** *Graph showing the expected XMCD trend for wire chains post-saturation. The highlighted segments on the graph indicate wires within the two example Chains 1 and 2 expected to exhibit similar contrast values based on the magnetisation arrangement, as demonstrated in* ***(a)*** *and* ***(b)****.*

In **Figure 90a** the expected magnetisation arrangement within chains of wires after in-plane saturation is shown. This would result in XMCD contrast for each chain of wires appearing in a bright-dark-bright pattern, as depicted in **Figure 90b**. Consequently, the XMCD measurement of wires post-saturation would produce alternating contrast, as shown in **Figure 90c**.

Additionally, comparability is anticipated among the wires observed on adjacent chains of the same sub-lattice. In other words, all wires expected to be bright after magnetic saturation should exhibit such brightness when comparing measured intensities, and the same principle applies to dark wires, this effect is illustrated by the highlighted regions of interest on **Figure 90c**.

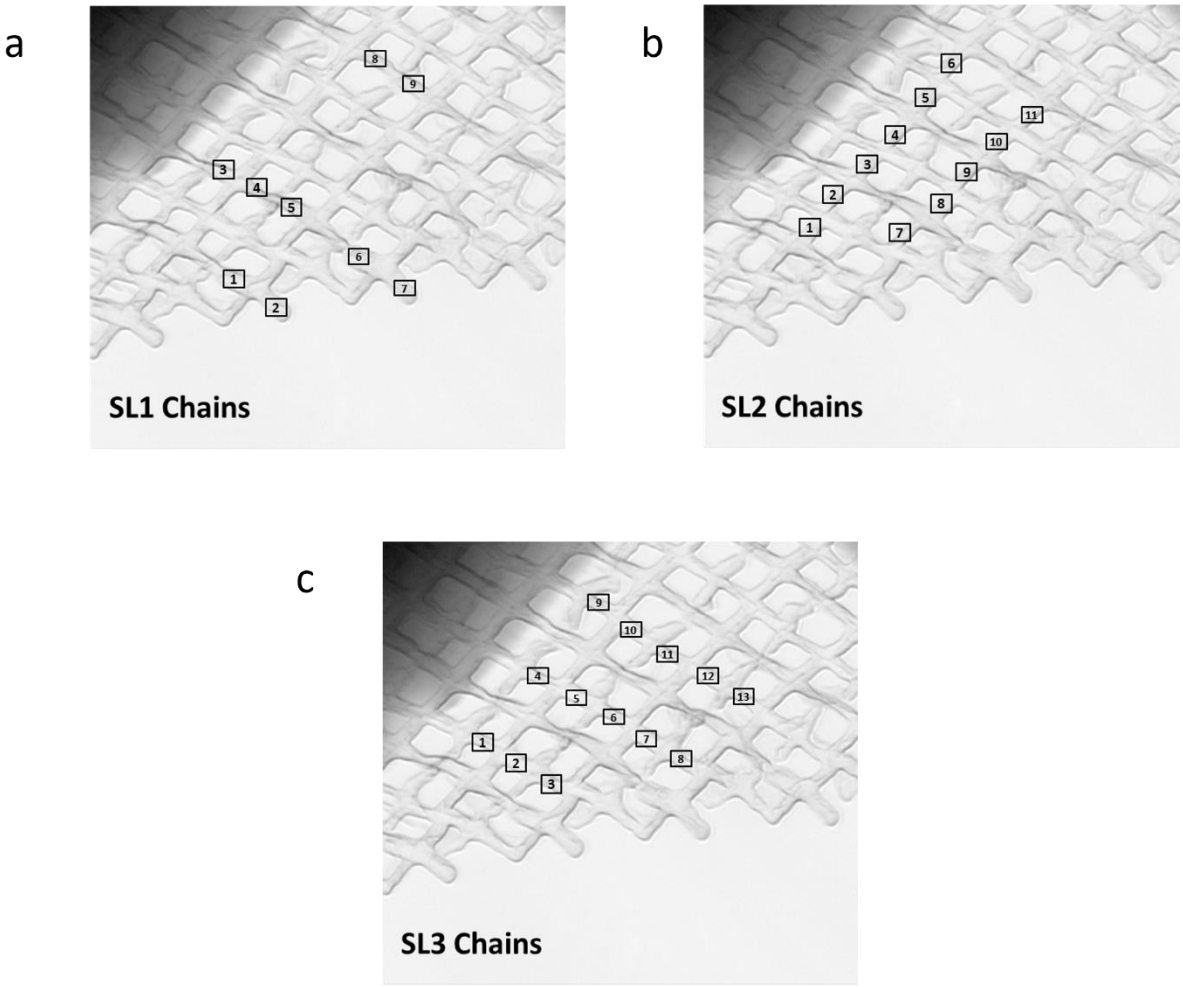

Figure 91: *$Fe\ L_3$ X-ray absorption images of Lattice B. Chains of individual wires with no overlap have been identified and labelled for* ***(a)*** *SL1 layer,* ***(b)*** *SL2 layer.* ***(c)*** *SL3 layer.*

Chains of wires, comprised of connected wires on a specific sub-lattice, were chosen from both Lattice B and Lattice D by carefully examining wires in each sublattice where the absence of overlapping wires underneath them could be confidently confirmed in both the pre- and post-application of the field images. This necessitated a detailed comparison between tilted XAS images of these lattices and SEM images to identify regions where wire overlap occurred. To ensure that only wires that were in complete chains with one another were selected,

individual wires surrounded by overlapping wires were excluded from this data collection. This process allowed selection of multiple wire chains across both lattices, upon each sublattice within each lattice, and these wires were then labelled for reference. This is visually illustrated in **Figure 91** and **Figure 92**.

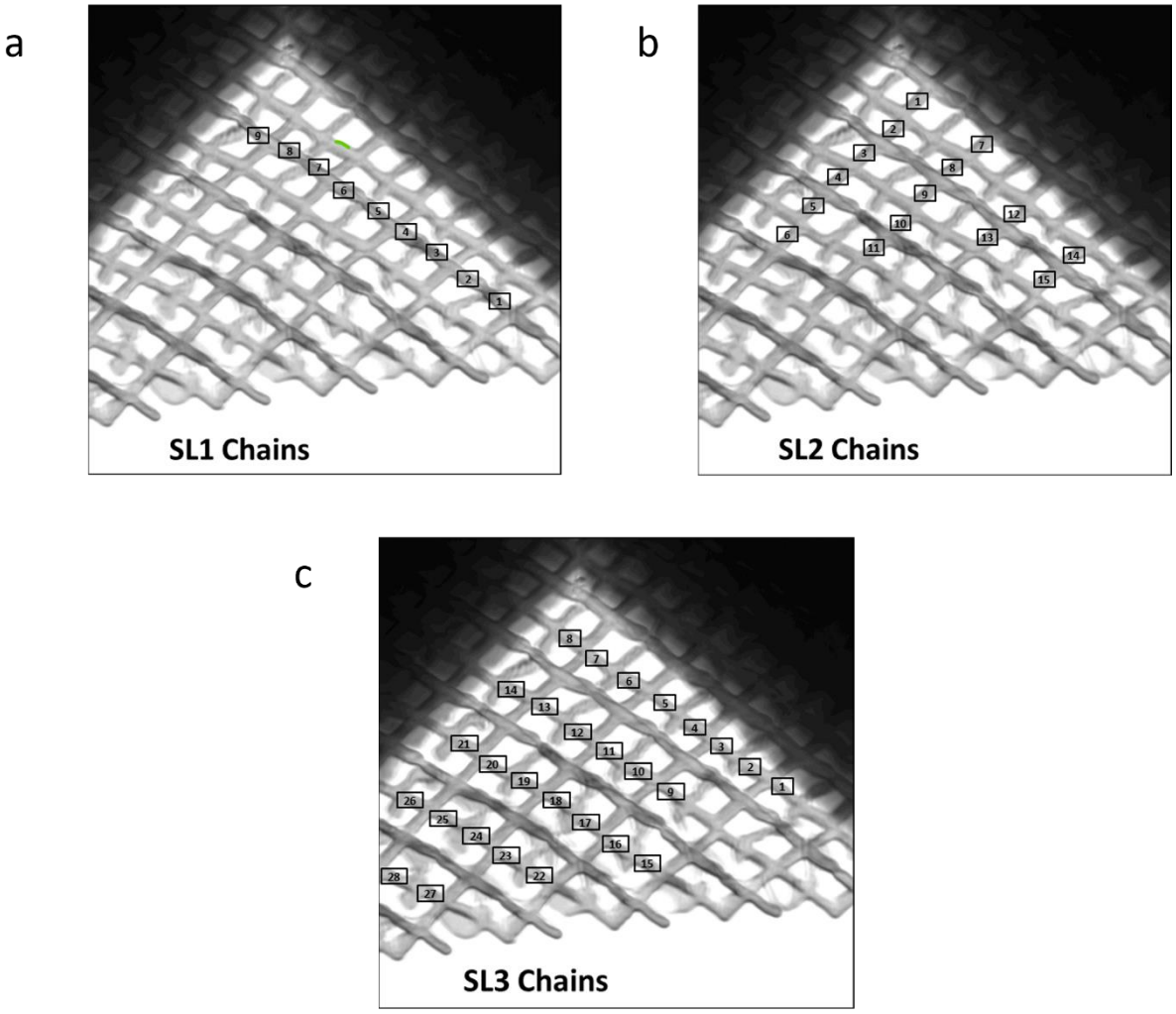

Figure 92: *$Fe\ L_3$ X-ray absorption images of Lattice D. Chains of individual wires with no overlap have been identified and labelled for* ***(a)*** *SL1 layer,* ***(b)*** *SL2 layer.* ***(c)*** *SL3 layer.*

The wires were measured multiple times, with a specific focus on the central area of each wire. Utilizing normalized images of both Lattice B and Lattice D, like Section 5.8.3, wire segments within their central regions were identified and measured. This methodology was derived from the consistent observation that the extreme edges consistently exhibited pure black regions (appearing as black outlines around wires), indicating minimal transmission, likely due to severe oxidation. These regions were anticipated to possess reduced aluminium

capping and thinner permalloy layers as evidenced by cross-sectional thickness measurements. In contrast, the central sections of each wire displayed contrast variation, implying partial transmission and detectable XMCD response. Throughout this measurement process, meticulous attention was paid to systematically selecting wires and ensuring alignment with the previously described labelling methods.

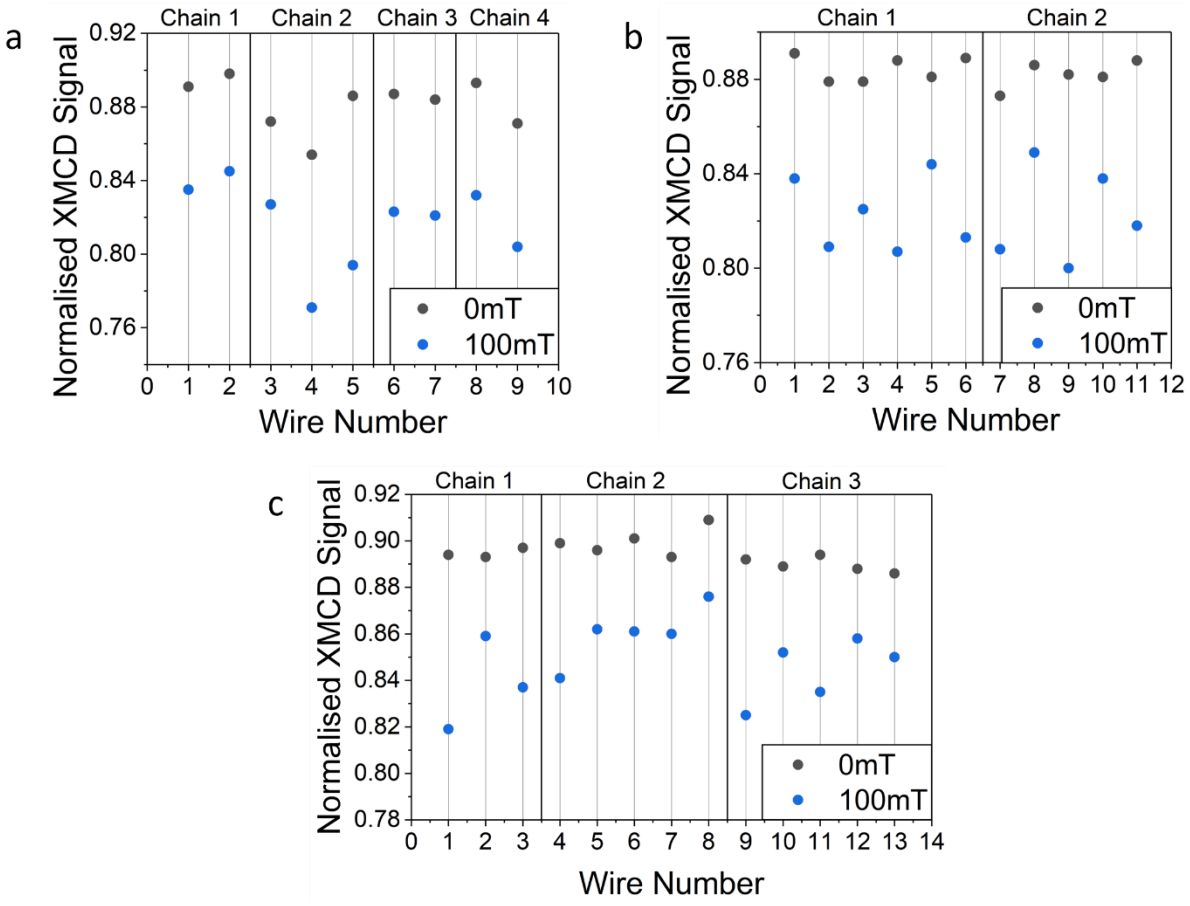

Figure 93: *Normalised XMCD signal upon Lattice B for wire chains in as-deposited state (Grey circles) and after application of* $100\ mT$ *field (Blue circles), for the SL1 sub-lattice* ***(a)****, the SL2 sub-lattice* ***(b)*** *and the SL3 sub-lattice* ***(c)****.*

The analysis of the SL1 chain contrast upon Lattice B, as depicted in **Figure 93a**, presents inconclusive results. Since the uppermost layer is particularly prone to artifacts due to overlapping wires, only short chains could be confidently identified. Moreover, these short chains do not exhibit a discernible change in trend when comparing their configurations before and after the application of a magnetic field. This suggests that any XMCD signal

originating from the SL1 sub-lattice falls below the measurement's noise floor, rendering it undetectable.

Conversely, the analysis of SL2 data, as shown in **Figure 93b**, offers more intriguing insights. The relative contrast between wires, when assessed before and after the magnetic field's application, shows noticeable differences. Notably, the data for chains collected after the magnetic field was applied conform to the anticipated pattern with alternating contrast, aligning with the depiction in **Figure 90c**.

The analysis of SL3 data in **Figure 93c** remains inconclusive. While there are some relative contrast changes observed after the application of the magnetic field, particularly noticeable in Chain 1 and Chain 2, these findings are complicated by the observations in Chain 2. In this chain, wires 6 and 8 exhibit a brightness orientation opposite to the expected magnetic configuration. This discrepancy arises from the observed contrast measurements. Wire 4 shows a possible dark contrast, while wire 5 exhibits a relative increase, indicating a bright arrangement. Wire 6's measured signal deviates from the expected sequence, displaying a brightness akin to wire 5 instead of a lower signal closer to wire 4. Similarly, wire 7's measured contrast aligns with wires 5 and 6, although it should resemble wire 5 only. Wire 8's signal, anticipated to resemble wire 4, exhibits a brighter measured value than any other data point. These observations collectively deviate from the expected pattern, resulting in a brightness arrangement within this wire chain of dark, bright, bright, bright, bright, contradicting the anticipated dark, bright, dark, bright, dark sequence as depicted in **Figure 90c**.

It's crucial to note that throughout the dataset, the XMCD signal remains small, approximately 4%. This modest signal can largely be attributed to the reduced magnetic moment resulting from oxidation.

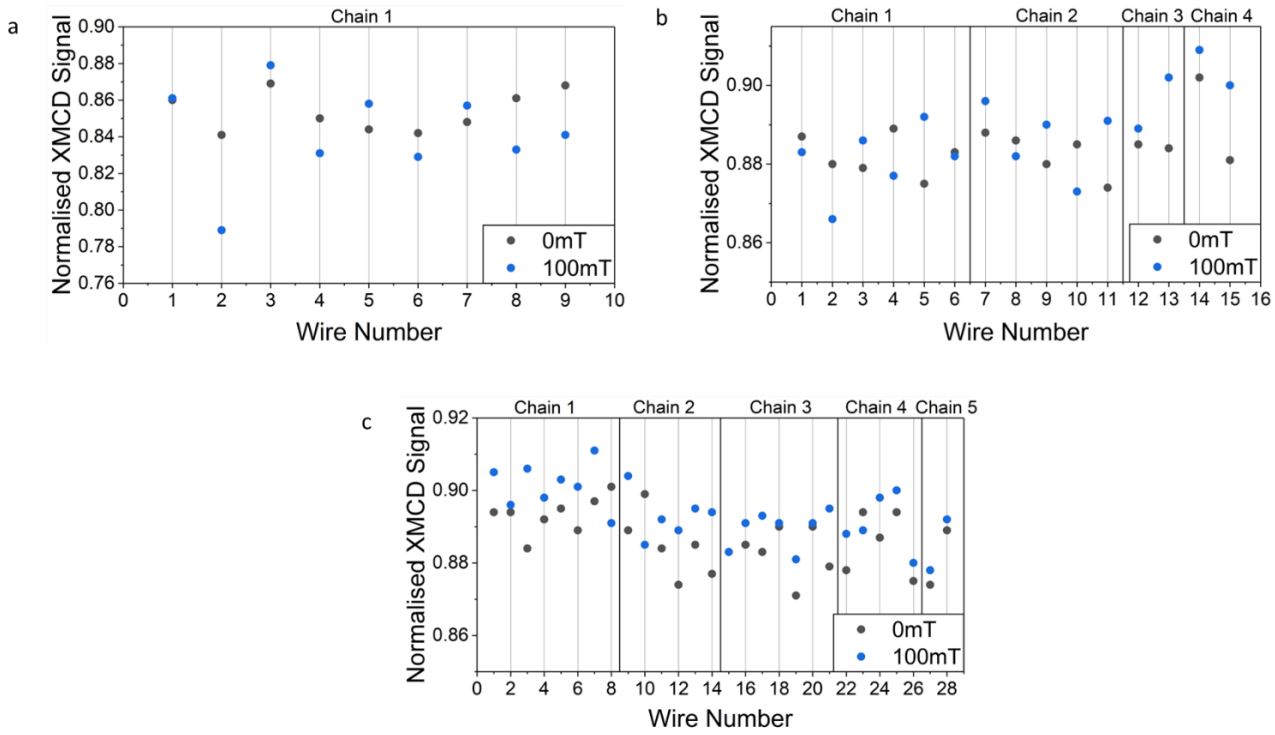

Figure 94: *Normalised XMCD signal upon Lattice D for wire chains in as-deposited state (Grey circles) and after application of 100mT field (Blue circles), for the SL1 sub-lattice* ***(a)****, the SL2 sub-lattice* ***(b)*** *and the SL3 sub-lattice* ***(c)****.*

The contrast analysis of the SL1 chain on Lattice D, as displayed in **Figure 94a**, suggests discernible trends. Within this lattice, a single chain comprising nine non-overlapping wires is identified on the SL1 sub-lattice. Before the application of the magnetic field, a noticeable pattern in the relative contrast is observed among the initial wires in the chain, especially wires 1 through 4. However, this pattern becomes less discernible in the subsequent wires. Following the field's application, notable differences emerge in the later wires, aligning somewhat with the expected alternating contrast pattern. However, the observed changes in relative signal between wires with opposing orientations appear relatively modest, measuring approximately below 4%.

Conversely, the analysis of SL2 data on Lattice D yields a mixed set of results across the measured chains, as depicted in **Figure 94b**. An evaluation of Chain 1 before the magnetic field's application shows a seemingly random orientation of wires. However, an argument can be made for the expected configuration after the magnetic field is applied. Notably, after the field's application, the relative contrast changes between wires align with the anticipated

arrangement. Nevertheless, when comparing the contrast between wires that should exhibit opposing magnetic orientations, specifically Wires 1 and Wire 6, it becomes evident that they produce nearly identical signals. Chains 2, 3, and 4, in contrast, exhibit the expected configuration without such issues, displaying minimal overlap between the observed signals for opposing orientations.

Figure 94c presents the SL3 data on Lattice D, with inconclusive findings. The expected configuration is partially observed in Chains 1 and 5. However, some wires in Chain 1 do not conform to the expected configuration. Moreover, the maximum change in contrast between the brightest and darkest wires measured within this dataset results in a percentage change of only 2%, suggesting an exceedingly weak signal, if present at all.

In summary, the chain analysis suggests that the optimal location to detect magnetic contrast may be on the SL2 sub-layer of the lattice. However, before drawing conclusions, an alternative analytical approach was considered to ensure confidence in these results. In this analysis, the magnitude of the contrast for wires in adjacent chains was examined. Distinct values for wires with positive and negative magnetisation projections onto k were anticipated. This analysis was conducted both before and after the field's application.

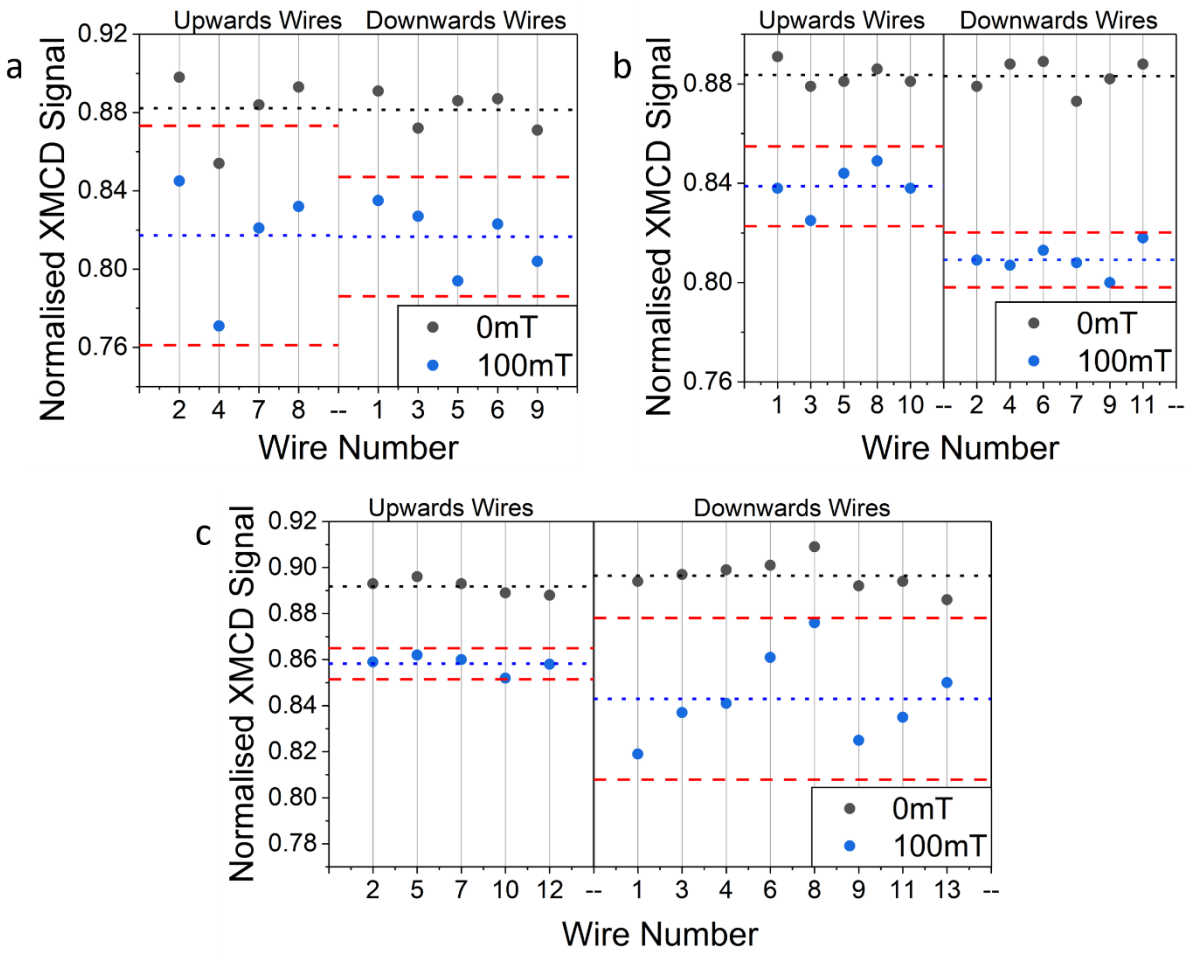

Figure 95: *Extracted XMCD contrast for nanowires upon the* ***(a)*** *SL1,* ***(b)*** *SL2 and* ***(c)*** *SL3 sub-lattices on Lattice B, for wires of different magnetic orientation after application of a saturating externally applied magnetic field. Grey symbols indicate XMCD signal for nanowires before application of a field, and blue symbols represent XMCD signal after application of field. In each case, blue dotted lines represent the mean of the populations, whilst dashed lines represent the 2σ boundary.*

Figure 95 presents the XMCD signal for two sets of wires, referred to as "Upwards" and "Downwards," both before and after the application of a magnetic field. This labelling refers to the magnetic wires with positive and negative magnetisation projections onto k and does not refer the geometric orientation, this is shown for clarity in **Figure 96**.

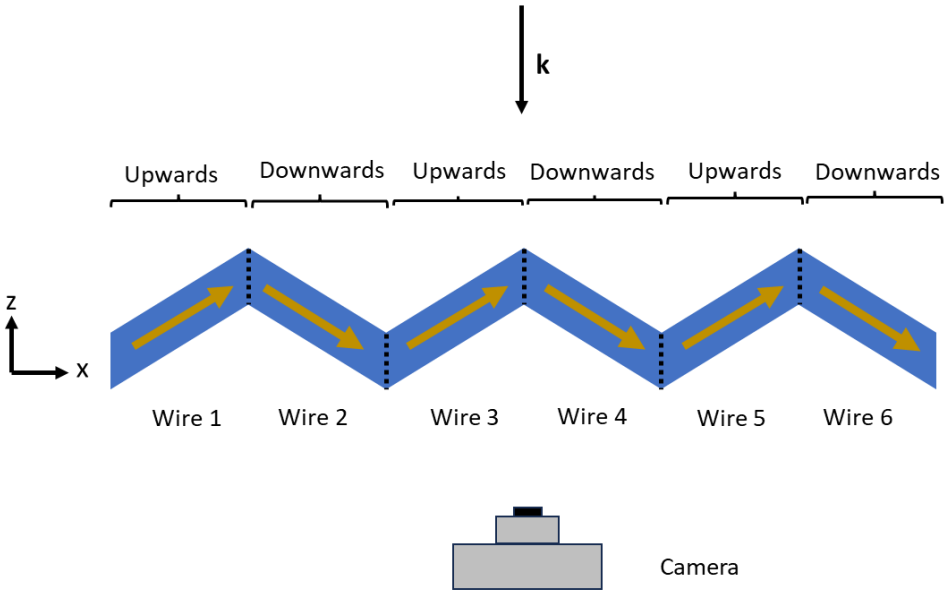

Figure 96: *Diagram showing the labelling arrangement for magnetic configuration within a chain of wire.*

The analysis shown in **Figure 95** is for Lattice B and covers all three sublayers: SL1, SL2, and SL3. Prior to the application of the magnetic field, the average XMCD values for both sets of wires in all three sublayers demonstrate are close, showing a difference of approximately 0.5%. This implies the potential for a random alignment of magnetic moments across these wires. Post-application of the magnetic field, SL2 and SL3 displayed an average difference of around 4% in their XMCD values between the "Upwards" and "Downwards" sets. While this consistency echoes the prior analysis, it might suggest the presence of a weak magnetic signal.

However, upon examination of the data, it was found that only SL2 has distinct populations of XMCD signal, for which there is no overlap within 2σ, suggesting high confidence of magnetic contrast. No overlap within 2σ between the "Upwards" and "Downwards" wire datasets signifies a substantial variance between these two sets of measurements. In the context of identifying magnetic signals, this separation is crucial as it suggests a notable difference in the XMCD values between wires oriented oppositely. The 2σ threshold provides a statistical confidence interval beyond the variation inherent in the data. When this threshold is met, it implies a consistent distinction between the two wire orientations, indicating a probable presence of a magnetic signal.

Analysing the SL1 chain, **Figure 95a**, it was observed that the average values for both "Upwards" and "Downwards" wires were nearly identical, lacking distinct separation, as all data points for both sets fell within 2 standard deviations of the opposite set.

Moving to the SL2 dataset, the analysis shown on **Figure 95b** revealed distinct average values with modest 2 standard deviations, suggesting potential significance in the differentiation between the "Upwards" and "Downwards" sets.

Finally, in the SL3 dataset, **Figure 95c**, some discrepancy in the average values was noticed. The "Upwards" wires displayed a narrower range of standard deviation, resulting in a tighter grouping. However, the "Downwards" set exhibited greater variance, with broader 2 standard deviation values overlapping with the entire "Upwards" wire dataset, indicating a lack of clear differentiation between the sets.

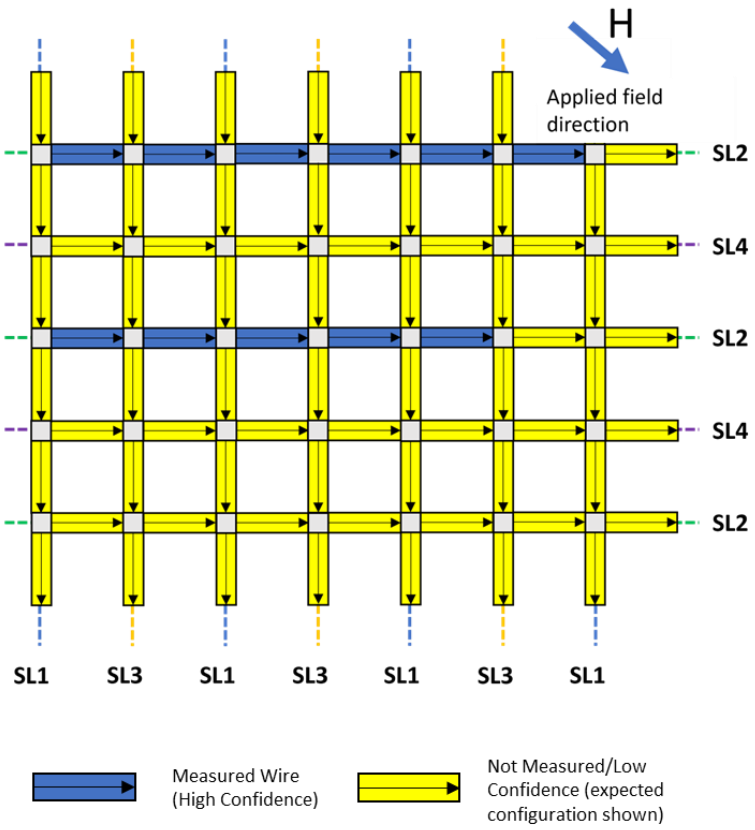

Figure 97: *Schematic of extracted magnetisation contrast from XMCD measurements. Blue dashed line labels the SL1 sub-lattice, green dashed line labels the SL2 sub-lattice, yellow dashed line indicates the SL3 sub-lattice, and purple labels the SL4 sub-lattice. Measured magnetic nanowires are coloured blue whilst the yellow wires show the expected configuration given the applied field direction.*

Plotting the magnetisation of SL2, shown in **Figure 97**, also shows that the measured configuration is consistent with the direction of external field, providing additional confidence. However, it's important to note that only SL2 demonstrates distinct populations of XMCD signal. These populations do not overlap within their 2σ range, suggest magnetic contrast may be present within the SL2 sublayer.

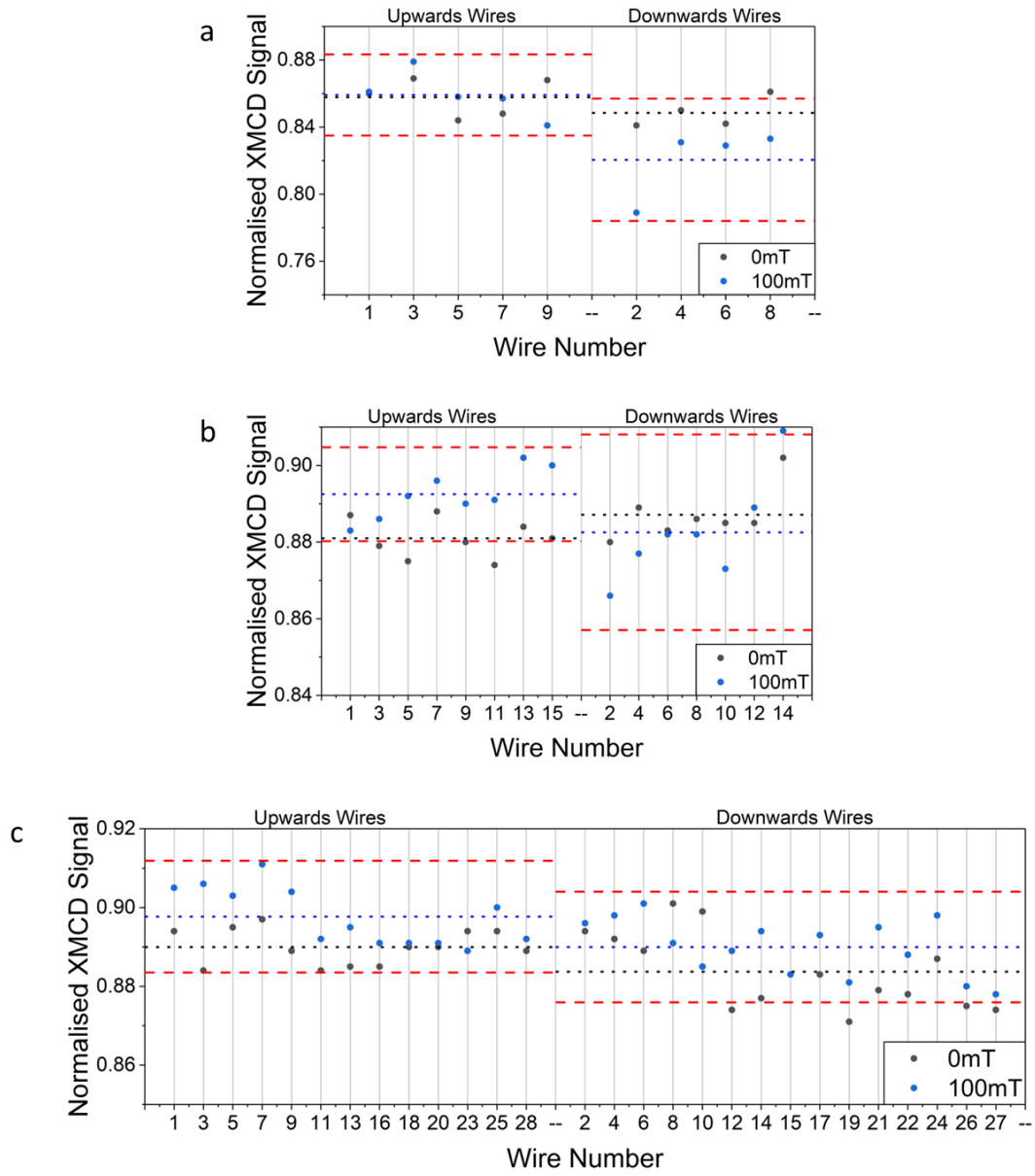

Figure 98: *Extracted XMCD contrast for nanowires upon the* ***(a)*** *SL1,* ***(b)*** *SL2 and* ***(c)*** *SL3 sub-lattices on Lattice D, for wires of different magnetic orientation after application of a saturating externally applied magnetic field. Grey symbols indicate XMCD signal for nanowires before application of a field, and blue symbols represent XMCD signal after application of field. In each case, blue dotted lines represent the mean of the populations, whilst dashed lines represent the 2σ boundary.*

The same analysis was replicated for Lattice D, covering all three sublayers: SL1, SL2, and SL3. This data is illustrated in **Figure 98**. Before application of the magnetic field, the average XMCD signal across all three sublayers is found to be quite similar, displaying only a marginal difference of 0.5% between the mean average populations. After the application of the

magnetic field, the anticipated changes in the measured contrast across all three sublattices were observed, although this effect was not as pronounced as that seen in Lattice B. The most significant change in the average contrast between populations was observed in SL1, with a difference of less than 2.5%. However, it is essential to note that distinct populations separated by 2σ or even 1σ were not observed on the SL2 sublattice on this lattice.

Overall, a significant question revolves around the apparent magnetic contrast observed in specific sub-lattices within the 3D ASI structure while others lack this contrast. Although the oxygen plasma exposure is expected to be uniformly administered to the sample within the described chamber (Section 3.1.3, see **Figure 33**) analysing the reduction in polymer scaffold thickness in the Diamond Light Source dataset (**Figure 64**) reveals that increased plasma exposure occurs when the sample is lifted by the edge. This implies uncertainty regarding the plasma's penetration into the $50\ \mu m\ \times\ 50\ \mu m$ aperture when samples remain flat within the chamber.

Moreover, the magnetic $NiFe$ coating on the polymer scaffold generates stray magnetic field lines that might partially shield the lattice, particularly affecting the lower layers. This shielding effect could vary the degree of oxidation in different $NiFe$ sub-lattices and result in a gradient of polymer thicknesses from SL1 to SL4.

Consequently, a discernible pattern is anticipated: SL1 experiences the most significant polymer removal yet undergoes the most pronounced reduction in magnetisation due to oxidation. Conversely, SL3 and SL4 are likely to retain higher magnetisation while experiencing less polymer removal, potentially leading to a lower signal-to-noise ratio in XMCD measurements. Therefore, the SL2 sub-lattice seems to strike an optimal balance in terms of magnetisation and polymer removal.

5.8.5 Focus Change Analysis

During the XMCD measurements conducted on Lattice B and Lattice D, the sample (210415EA) was taken out of the synchrotron to apply an external magnetic field before capturing subsequent images. This process might have introduced alterations in focus or tilt, potentially contributing to the observed changes in magnetic contrast. A modification in focus

could impact the alignment and clarity of the X-rays on the sample, altering the X-ray absorption and, subsequently, the recorded XMCD signal. Such variations might explain the discrepancies in contrast between wires, which would affect the interpretation of the lattice's magnetic configuration. Therefore, it's imperative to thoroughly investigate any potential alterations in focus to ensure the accuracy and reliability of the XMCD measurements and their subsequent interpretation.

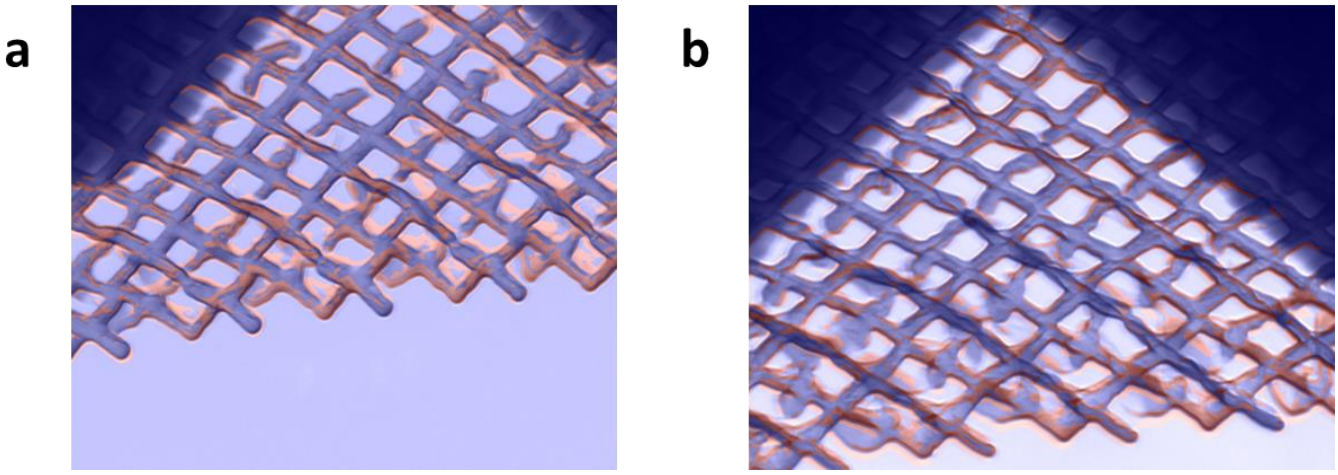

Figure 99: *A difference image between the pre- and post-application of a magnetic field to* ***(a)*** *Lattice B and* ***(b)*** *Lattice D. The initial state is denoted by the blue image, whilst the areas of change post-field application are highlighted in orange. Chains of wires measured for XMCD analysis, shown in* ***Figure 91****, confirm that wires measured are located away from the area of lattice which exhibits greatest tilt into aperture.*

Notably, visible changes in the lattices structure were observed between these two images, these can be seen in **Figure 99**. These alterations were attributed to an increased tilt of the lattice into the aperture, stemming from drift of the lattice during the unloading and loading procedures involved. To thoroughly investigate the potential impact of a focus drift between these images, an analysis of the raw x-ray absorption images was carried out. A focus drift would manifest as a consistent difference in the measured width of the wires between the pre- and post-application images.

To ensure a comprehensive assessment, the $Fe\ L_3$ XAS images for each dataset (Lattice B and Lattice D) underwent a specific processing methodology. Initially, the pre- and post-application images were loaded into ImageJ image processing software and consolidated into an image stack. Subsequently, a plugin called "Linear Stack Alignment with SIFT" (previously employed for aligning stacks of 300 images at the ALBA synchrotron) was utilized to align the two $Fe\ L_3$ images. To standardize measurements, a scale was established using a known distance between two vertices, extracted from top-down SEMs. After this calibration, a minimum of 20 wire width measurements were taken for both images across each sub-lattice layer (SL1, SL2, and SL3). The alignment procedure ensured consistency, ensuring measurements were made across the same section of each wire. An average wire width was calculated and plotted alongside error bars representing the standard error of measurements. This comparative analysis was performed for both Lattice B and Lattice D.

In this instance, the choice to use the standard error as error bars instead of the standard deviation is rooted in the need for a more stringent evaluation of the measured wire width. The standard deviation for error bars has typically been employed in analysis, offering a measure of data variability around the mean. However, the standard deviation tends to present a larger range, encompassing a broader spectrum of potential measurement fluctuations.

Given the specific context of this analysis where precision in measuring wire width is critical and where even subtle changes in wire width might be significant, the standard error was used instead. The standard error, being in this case on average a factor of 10 smaller than the standard deviation, provides a more conservative estimation of the error associated with the average measurement. In this scenario, it offers a stricter representation of the variability in wire width measurements, allowing for a more discerning evaluation of any differences between datasets.

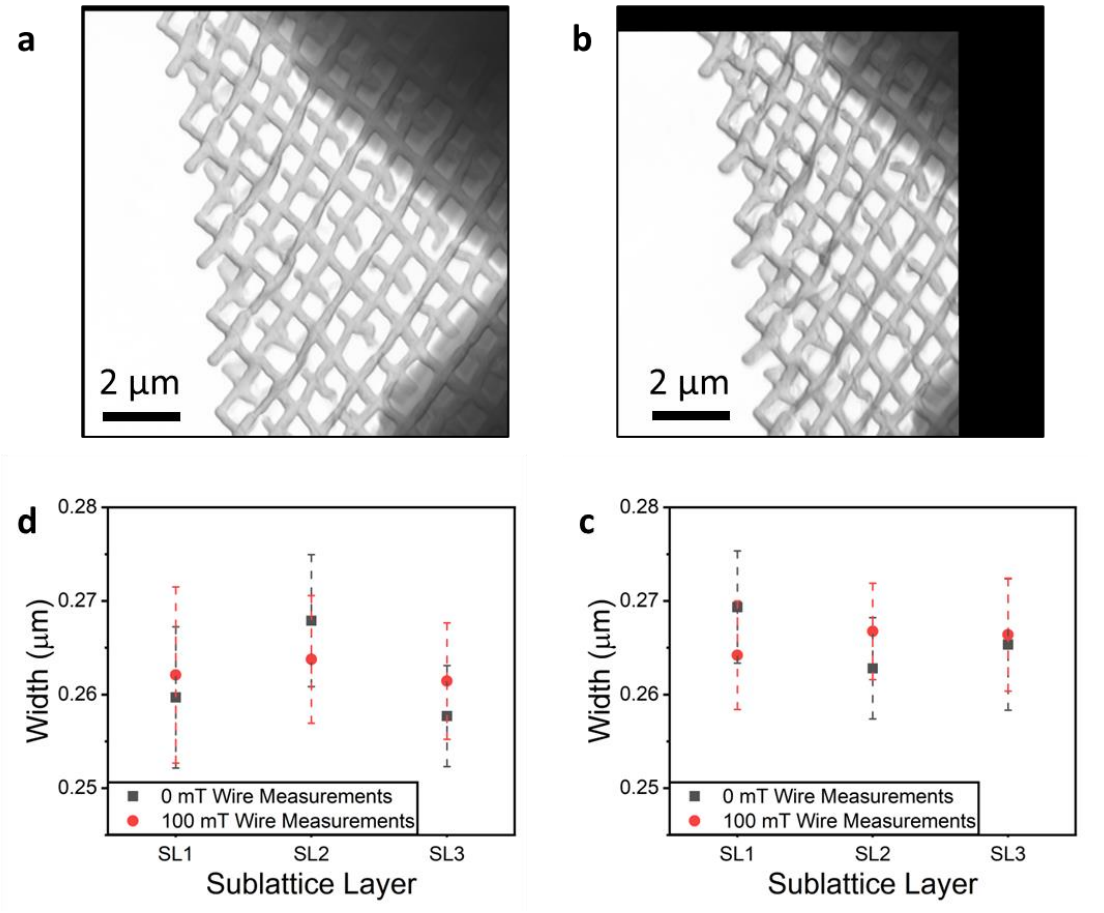

Figure 100: ***(a)*** *Aligned XAS $Fe\ L_3$ image of measured lattice, pre application of field.* ***(b)*** *Aligned XAS $Fe\ L_3$ image of measured lattice, post field application. Scale bar shown is $2\ \mu m$. A total of 50 wire width measurements were taken across both images at same locations for each sublattice layer.* ***(c)*** *Lattice B graph of mean wire width of each sublattice layer for pre- and post- magnetic field images with standard error shown as error bar.* ***(d)*** *Lattice D graph of mean wire width of each sublattice layer for pre- and post- magnetic field images with standard error shown as error bar.*

Comparison of the measured wire width across both datasets show that there is no difference within the error of the measurements. This is shown for both Lattice B and Lattice D in **Figure 100**.

5.8.6 Tilt Effects Analysis

Potential shifts in lattice tilt within the structure were explored as a potential contributor to the observed changes in XMCD signal across both datasets. An adjustment in the tilt along

the wire's long axis could systematically vary transmission across wires. This effect, influenced by Equation (129) and subsequent thickness changes due to tilt, results in varied X-ray transmission due to fluctuations in wire thickness. Moreover, it's important to note that tilt-induced changes could also impact the magnetisation component aligned with the k direction, which combined with a change in transmission may drastically change the measured XMCD signal.

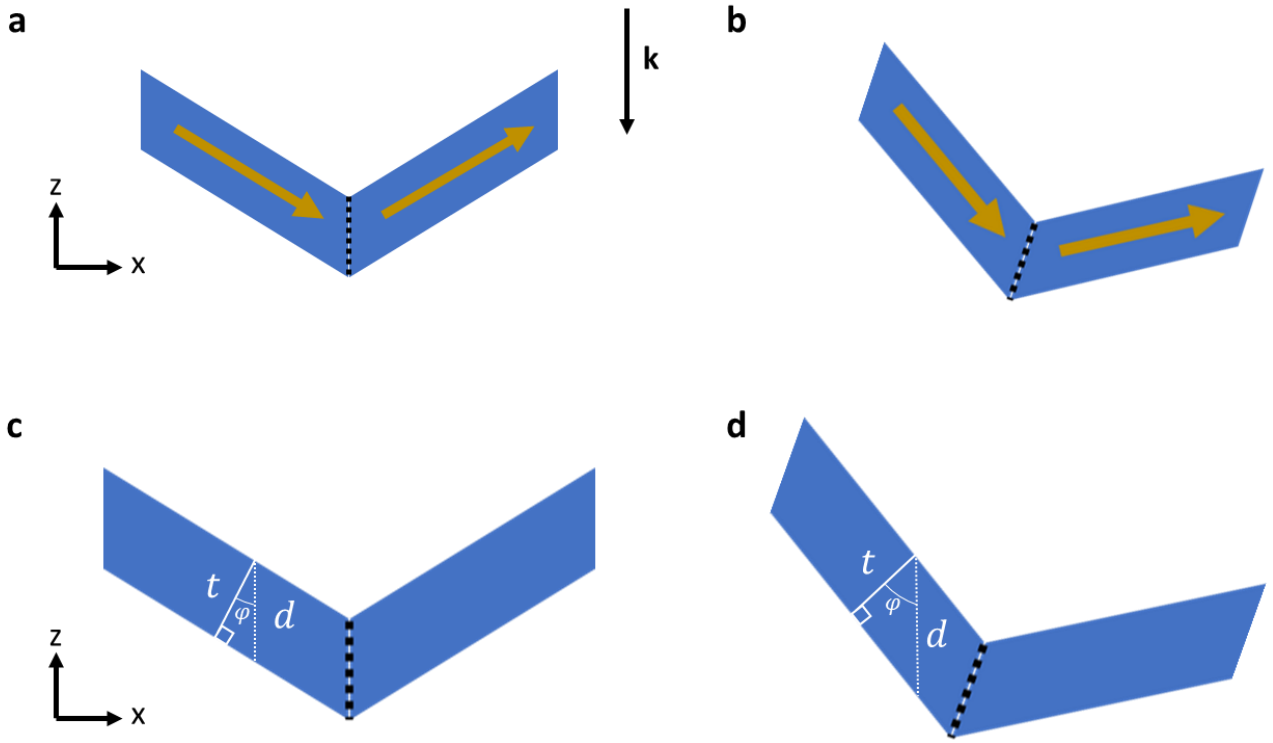

Figure 101: (a-b) *An exaggerated representative diagram highlighting the change a tilt would incur on the orientation of the magnetisation relative to the k-direction.* ***(c-d)*** *a diagram showing the change in thickness incurred by a change in tilt.*

Figure 101 illustrates these effects, albeit exaggerated, showcasing rotation around the unit vector $(0, 1, 0)$. However, in the measured lattices, the tilt experienced aligns along the $(1, 1, 0)$ axis, resulting in a reduced impact on both XMCD and transmission compared to the illustrated scenario.

Analysis of XAS images before and after saturating field application indicated minimal differences in measured wire widths, see **Figure 100**, suggesting limited structural changes

across most dataset wires. While some tilt was noticeable, it predominantly occurred at the extreme edge of the lattice, an area deliberately avoided during wire selection for measurement, this is clearly seen in difference images presented in **Figure 99**.

Moreover, the ALBA synchrotron enabled image capturing at various tilt angles. For both datasets, a series of images were obtained at tilt angles of -10, -5, 0, 5, 10 degrees. Subsequent XMCD analysis, shown in Section 5.8.4, utilised images taken at angles selected to negate any tilt within the lattice section measured. Between the $0\ mT$ and $100\ mT$ images, a tilt occurred in the lattice, predominantly noticeable at the edge of the lattice furthest from the aperture edge. The $0\ mT$ XMCD images used in XMCD analysis were captured at a 0-degree tilt angle at ALBA. In contrast, the $100\ mT$ XMCD image was taken at a -5-degree tilt angle, effectively minimizing lattice tilt except in regions where it was more pronounced furthest from the aperture edge.

In addition, if tilt were the sole cause of the observed changes in transmission, it would likely affect all measured layers uniformly in both datasets. However, the observed signal patterns do not exhibit this consistent uniformity across all sub-lattices. Instead, certain sub-lattices (SL2) display this distinct change more prominently and this sub-lattice is theoretically the most structurally sound as it is supported by sub-lattices above and below.

An examination was conducted on XMCD signals across both lattices, specifically targeting chains that extend farthest from the aperture's structural support. An anticipation was held for an increase in measured XMCD signal for wires aligning with the k-component. It was expected that wires aligned in this manner would exhibit an enhanced signal compared to those becoming orthogonal to the k-component. Consequently, a greater difference in signal was expected between these two types of wires within the data.

However, this anticipated relationship is not observed. An illustrative instance from the SL1 data of Lattice B, as depicted in **Figure 93a**, reveals that both Chain 1 and Chain 3 wires—comprising wires situated at the extreme lattice edge, farthest from the aperture, and experiencing the most significant tilt shown in **Figure 99**—should theoretically undergo the anticipated effect due to tilt. Notably these two wire chains displayed XMCD signals that were

< 2% apart from each other. This observation indicates a minimal effect of the anticipated change due to tilt on these wires.

The discrepancies observed in XMCD signal changes, contrary to the expected alterations due to a tilt change, indicate that while tilt could contribute to transmission variations and signal changes in specific wires, its impact appears minimal. This suggests that tilt alone may not be the primary factor driving the observed selective XMCD signal changes across different sub-lattices, hinting at the measurement of a weak magnetic signal. Other nuanced factors, uneven reduction in polymer scaffold, specific to individual wires within sub-lattices might contribute to the observed patterns, warranting further investigation into the distinct behaviours observed within these sub-lattices.

5.8.7 Polymer Thickness Influence on XMCD Signal

The measured XMCD signal changes within the lattice might be linked to the impact of uneven reduction on the polymer scaffold beneath the permalloy nanowires. If this were the case, one would expect that wires displaying an increased measured XMCD signal would also showcase a higher degree of polymer removal, as a result of an augmented transmission and an increased magnitude of the received XMCD signal.

As previously mentioned, the degree of polymer reduction varies across both the lattices and the measured wires. Specifically, wire thicknesses measured farthest from the aperture edge exhibit a heightened reduction in polymer thickness compared to the majority of the lattice within 2-3 vertex distances from the aperture edge. However, this predicted selective reduction of alternating wires within the lattice is not observed.

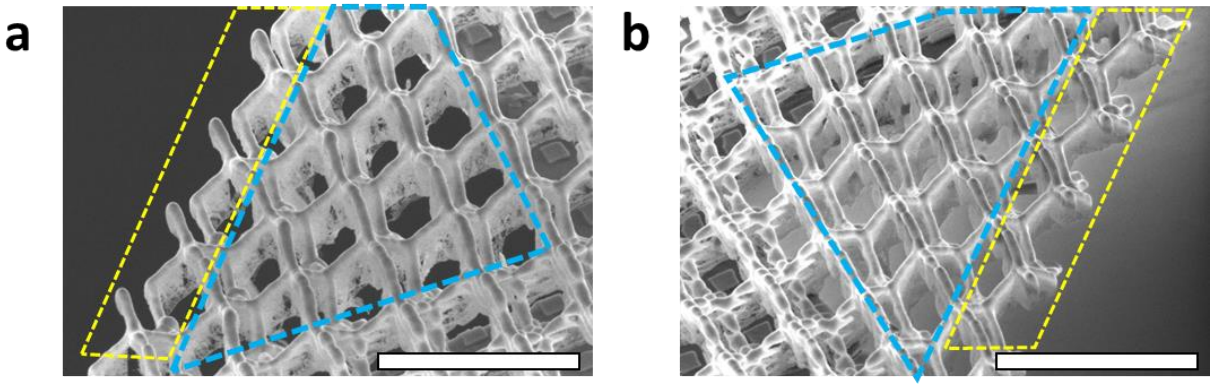

Figure 102: *SEM image of* ***(a)*** *LatticeB and* ***(b)*** *LatticeD, subjected to 1-hour oxygen plasma exposure, suspended over the aperture viewed from a* 45^0 *tilt. Blue ROI shows region within which XMCD measurements were conducted; yellow ROI shows region exhibiting significant increase in polymer thickness reduction. Scale Bar shown is* $4\ \mu m$.

SEM images taken at a 45-degree tilt angle to reveal the polymer nanowire beneath the upper surface layer of permalloy, are displayed in **Figure 102** for both LatticeB and LatticeD. Owing to the orientation of the lattice concerning the SEM camera, certain sections of the wire are obscured. However, the images do indicate that while thickness variation is evident, especially near the lattice's farthest edge from the aperture (indicated by the yellow ROI), this effect is not seen within the bulk regions of the lattice where XMCD wire measurements were predominantly conducted. These specific areas are highlighted using the blue ROI on the SEMs.

Furthermore, whilst there is some variance in the polymer removed across each individual wire, causing a porous effect, this effect is visually identifiable as being applied across all wires within the measured region, systematically altering the transmission and therefore XMCD signal obtained. Therefore, the uneven removal of polymer beneath the permalloy nanowires is discounted as being the cause of the alternating XMCD signals seen, suggesting presence of a weak magnetic signal within the 3D ASI.

5.9 Summary, Conclusions and Future Work

The research journey detailed in these sections has been driven by the desire to enable precise measurements of complex thermal systems using 3D ASI structures and Synchrotron-

based STXM and TXM. The main objective was to establish the feasibility of measuring these intricate systems and to refine the necessary techniques for their characterization.

The journey commenced with a focus on scaffold fabrication techniques, with a particular emphasis on minimizing scaffold dimensions effectively. Various methods were explored, including the utilization of Galvo Scan Mode and the strategic layering of wires to prevent sagging into the aperture. Oxygen plasma exposure was incorporated to further refine scaffold thickness while preserving the critical magnetic properties of the Permalloy material. A fundamental aspect of this research journey was the reduction in scaffold dimensions, aimed at increasing signal clarity and transmission while retaining the unique magnetic characteristics of ASI.

Throughout this exploration, the central motivation remained to advance the capability to measure thermal systems. As previously discussed in Section 5.1, the ability to conduct non-invasive measurements of thermal systems is crucial for understanding their behaviour without perturbing them. This is especially significant in the context of rapidly changing thermal states where the timing of measurements is critical to capture meaningful data. A significant step toward achieving this goal and ultimately contributing to a better understanding of complex thermal systems is taken by improving the techniques for characterizing 3D ASI structures.

5.9.1 Conclusions

The culmination of this extensive research journey reveals several significant findings.

The preliminary investigations conducted at Diamond Light Source demonstrated the resilience of the polymer nanowire structures, coated with metal, against high-intensity x-ray exposure. Minimal deformation was observed once the lattice settled within the measurement chamber, a positive outcome that bolstered confidence in utilizing synchrotron radiation for measurements of TPL fabricated nanostructures. However, further analysis of the structure and examination of the XMCD images uncovered issues in the 3D ASI fabrication methodology.

A lack of clear magnetic contrast across the measured area was notably encountered. This absence of signal is primarily attributed to a significant loss of transmission due to the thickness of the polymer scaffold layer. This thickness was exacerbated by extended dwell times inherent in Piezo scan mode during TPL fabrication. Additionally, scrutiny of the XAS spectra indicated an oxidation of the magnetic material, resulting in a weakened magnetic signal. The combined effect of these factors accounts for the absence of visible contrast in the XMCD images.

The cross-sectional profile of the permalloy deposited atop the polymer nanowires was successfully confirmed by leveraging the collected experimental data. This revealed a crescent-shaped cross-section, long hypothesized through SEM analysis but previously unconfirmed. Moreover, this initial experiment offered valuable insights into synchrotron techniques and informed improvements to the fabrication process, crucial for subsequent experiments at the ALBA synchrotron.

Transitioning to Galvo Scan Mode and strategic layering during scaffold fabrication has yielded an impressive reduction in scaffold dimensions, resulting in a refined 3D ASI structure. The addition of layers and oxygen plasma exposure has played a pivotal role in this refinement. However, the influence of oxidation on the magnetic properties cannot be ignored, as evident in the reduction of coercivity observed in MOKE measurements and by the increasing oxidised Fe peak seen in XAS spectra. Nonetheless, the Permalloy retains its magnetic characteristics, indicating a promising foundation for future studies.

The ALBA synchrotron experiment offered invaluable insights into the magnetic properties of the 3D ASI structures. Although challenges related to lattice deformation and movement were initially encountered, stability was eventually achieved, enabling data collection. X-ray Absorption Spectroscopy (XAS) spectra provided a clear representation of the progressive increase in oxidation in samples exposed to oxygen plasma. This underscores the importance of minimizing exposure of the magnetic material to maintain clear magnetic signal detection.

The XMCD measurements, the crux of this study, have a hint of magnetic behaviour within the ASI structure. While the SL1 sublayer exhibited no detectable XMCD signal, the SL2 sublayer displayed noticeable contrast changes following the application of a magnetic field.

However, the SL3 sublayer yielded inconclusive findings, emphasizing the complexity of the system. An alternative analytical approach further suggested the presence of a weak magnetic signal, particularly within the SL2 sublayer, where distinct populations of XMCD signal were identified.

An analysis was conducted to pinpoint potential causes behind the observed alternating XMCD signal. Three factors were considered: focus changes between images, tilt variations between images, and the impact of uneven polymer removal across alternating wires within the lattice.

The influence of focus changes was ruled out. Discrepancies observed between images were attributed to increased tilt of the lattice into the aperture. Notably, greater tilt was observed at the lattice's edge farthest from the aperture edges. However, upon closer examination of the tilt and considering the positions of the measured wires within the lattice, the impact of tilt of the lattice was mitigated by selectively using images taken at a tilt angle of -5 degrees at ABLA. Consequently, this tilt factor was deemed irrelevant in causing the alternating XMCD contrast.

Additionally, post-oxygen plasma exposure procedure SEMs were scrutinized, revealing no alternating reduction in polymer thickness across chains of measured wires. Instead, a systematic reduction in overall polymer thickness within the measured wires dataset was observed. Hence, this factor was also discounted as the cause of the observed contrast changes.

In summary, the collective findings suggest that a weak magnetic signal likely underlies the contrast changes observed, discounting both tilt variations and uneven polymer removal as primary causes.

In essence, this research journey advances the understanding of the 3D ASI structures, their fabrication, and their magnetic properties. Despite the challenges of low signal-to-noise ratios and the impact of oxidation, this work stands as a significant step towards the in-depth exploration of magnetic behaviours within intricate nanostructures. The delicate equilibrium

between scaffold refinement and magnetic property preservation has yielded improved fabrication designs that hold great promise for future investigations in this field.

5.9.2 Future Directions:

The research conducted provides a strong foundation for several potential avenues of progression and exploration in the field of 3D Artificial Spin Ice (ASI) structures. Building upon the insights gained through this work, the following directions can be pursued:

The reduction of scaffold dimensions played a pivotal role in the research's success, and further refinement of the fabrication process is an attractive prospect. One approach could involve fabricating over a smaller aperture with anchor points on all sides of the aperture. By polymerizing from the anchor points towards the central region, a fully formed 3D ASI structure with reduced sagging may be achievable.

To mitigate the impact of oxidation on magnetic properties, an innovative approach could be adopted. This involves initially depositing an aluminium layer and then subjecting it to aggressive oxygen plasma exposure to completely remove the underlying polymer scaffolding. The result would be a robust aluminium-only framework that can be overlaid with Permalloy, significantly less oxidized due to its absence during the plasma exposure. This approach has the potential to produce a fully magnetic 3D ASI, clearly visible under synchrotron measurements, revealing the internal magnetic configuration with greater clarity.

By fine-tuning scaffold fabrication and deposition techniques, it may be possible to create 3D ASI structures with tailored magnetic properties. These structures could be designed for specific applications, such as data storage or magnetic logic devices. Understanding and controlling the magnetic configurations within these ASI structures opens exciting possibilities for custom magnetic materials.

In conclusion, the research presented here marks the beginning of a new phase in the exploration of 3D Artificial Spin Ice structures, with promising avenues for future investigation. Continuous refinement of fabrication techniques, the utilization of advanced

synchrotron capabilities, and the exploration of innovative approaches to manage oxidation all hold the potential to uncover deeper insights into magnetic behaviour at the nanoscale. The exciting potential for groundbreaking discoveries that could reshape the understanding of magnetism and pave the way for transformative applications in technology and beyond is offered by this interdisciplinary fusion of materials science, nanotechnology, and condensed matter physics.

6 Conclusion and Future Directions

The exploration of 3D ASI systems has unveiled a complex landscape where theoretical predictions often diverge from experimental observations. Discrepancies between predicted and observed states in these intricate systems stem from multiple factors, notably the distinct behaviour exhibited by different sub-lattices. Studies have highlighted the unfavourable nature of magnetic charges at coordination-two vertices within 3D ASI systems, necessitating monopole/anti-monopole pair nucleation over two lattice spacings due to elevated energy requirements. This phenomenon is largely influenced by the effective chemical potentials, notably $\mu^* = 1.22$ for SL1 and $\mu^* = 1.03$ for SL2, impacting the stability of monopole pairs and influencing charge ordering.

The interplay between SL1 and SL2 sub-lattices significantly influences the observed charge configurations, wherein the higher effective chemical potential on SL1 restrains anti-ferromagnetic ordering, favouring a single charge crystal. Conversely, the lower effective chemical potential on SL2 promotes the formation of charge crystallites owing to increased monopole pair stability, leading to observed charge-ordered patches.

Furthermore, insights garnered from the absence of charge ordering in 2D Square ASIs due to prevailing energy landscapes, particularly dictated by vertex types, offer crucial implications. The predominance of Type 1 vertices, with an associated effective chemical potential of $\mu^* \approx 2.5$, diminishes the probability of charge ordering, contrasting with higher energy Type 2 vertices ($\mu^* \approx 0.44$). Simulations hint at the potential for charge crystallization in 2D systems through modified geometries favouring decreased energy in Type 2 vertices, yet the dominance of Type 1 vertices hampers this observation.

The attempt to modify the 3D ASI design to enable the realization of a double-charged monopole crystal by introducing defects on bipods reveals initial challenges. Though these modifications led to increased observations of coordination-two monopoles, inconsistencies in achieving the targeted state underscore the need for refined fabrication processes before effectively exploring this system.

The study not only deepens comprehension of the phase space within 3D ASI systems but also expands the efficacy of measurement tools, unearthing previously unidentified vertex types and shedding light on their energy landscapes. The alignment between simulations and experimental findings aids interpretation, emphasizing the need for comprehensive approaches in understanding vertex types. Rigorous methodologies in signal analysis enable overcoming signal-to-noise challenges in deeper measurements, offering a broader understanding of the demagnetized ground state compared to Monte Carlo simulations.

Moreover, the complexities in effective potentials across sub-lattices provide avenues for potential refinements in topography and geometry, expanded demagnetisation protocols, and advancements in measurement techniques like x-ray magnetic circular dichroism through synchrotron methodologies. These avenues hold promise in realizing the predicted double-charged crystal and advancing our comprehension of these intricate systems beyond the limitations of single-unit cell thickness measurements.

The comprehensive research journey embarked upon to refine measurement techniques for 3D ASI structures using STXM and TXM has been a quest to enable precise future observations of complex thermal systems and measure beyond single unit cell thickness. It commenced with a primary focus on scaffold fabrication techniques, where fabrication methods were explored, aiming to minimize scaffold dimensions effectively while retaining the unique magnetic properties of the ASI.

Throughout this exploration, the central objective remained to enhance measurement capabilities in thermal systems without perturbation. The research unveiled crucial findings, commencing with investigations at the Diamond Light Source, which showcased the resilience of polymer nanowire structures against high-intensity x-ray exposure. Despite promising outcomes, issues arose in the 3D ASI fabrication methodology, particularly related to inadequate magnetic contrast in the measured area due to a thick polymer scaffold layer and oxidation of magnetic material.

However, advancements in applied fabrication techniques, such as transitioning to Galvo Scan Mode and strategic layering during scaffold fabrication, led to reductions in scaffold dimensions, refining the 3D ASI structure. Yet, challenges persisted, primarily related to

oxidation impacting magnetic properties, as observed in the reduction of coercivity and increased oxidation in XAS spectra.

Experiments at the ALBA synchrotron provided invaluable insights into the magnetic properties of 3D ASI structures, despite challenges in lattice stability and deformation. XAS spectra highlighted the progressive increase in oxidation, emphasizing the need to minimize exposure of the magnetic material for clear signal detection. The XMCD measurements, pivotal in this study, revealed nuanced magnetic behaviours within the ASI structure, notably observed in the SL2 sublayer, though the SL3 sublayer presented inconclusive findings, indicating the system's complexity.

Analysing potential causes behind observed contrast changes discounted tilt variations and uneven polymer removal, suggesting a weak magnetic signal underlies these alterations.

This research, despite signal-to-noise challenges and oxidation impacts, significantly advances understanding of 3D ASI structures, fabrication techniques, and magnetic properties. The refined equilibrium between scaffold optimization and magnetic property preservation marks substantial progress for future explorations into these intricate nanostructures, offering a promising foundation for further investigations in the field.

The thesis uncovers compelling avenues for future exploration. Achieving ground states resembling Monte Carlo simulations might be feasible by altering the surface topography of the 3D ASI structure. This modification could lower the effective chemical potential for coordination-two vertices, promoting increased monopole formation on these surface termination bipods. Such adjustments hold the potential to realize the predicted double-charge monopole crystal state. Moreover, improving the existing demagnetisation protocol, currently limited to single-plane rotation, could better emulate a genuinely thermal system's ground state.

For deeper insights into the 3D ASI structure, initial inquiries in this thesis propose XMCD as a promising avenue. Unlike surface-level methods like MFM, XMCD offers non-interfering measurements, potentially allowing scrutiny of genuinely thermal systems. Challenges faced in the proof-of-concept XMCD study have actionable solutions. To mitigate oxidation during

the reduction of the polymer nanowire scaffold, a delayed deposition of the magnetic material could be applied. Employing an initial layer of aluminium on the polymer scaffold followed by aggressive removal through extended oxygen plasma exposure would yield a thinner purely metallic scaffold with minimized oxidation. Subsequent steps involving the deposition of magnetic material and a capping layer could produce a purely metallic structure with reduced dimensions, enhancing signal transmission. Additionally, constructing this structure over a smaller aperture size would bolster its structural integrity, reducing lattice sagging and ensuring a well-formed 3D ASI.

7 Bibliography

1. Krishnan, K.M., *Fundamentals and Applications of Magnetic Materials*. 2016: Oxford University Press.

2. O'Handley, R.C., *Modern Magnetic Materials: Principles and Applications*. 1999: Wiley.

3. Getzlaff, M., *Fundamentals of Magnetism*. 2007: Springer Berlin Heidelberg.

4. Blundell, S., *Magnetism in Condensed Matter*. 2001: OUP Oxford.

5. Streubel, R., et al., *Magnetism in curved geometries.* Journal of Physics D-Applied Physics, 2016. **49**(36).

6. Rohart, S.T., A. , *Skyrmion confinement in ultrathin film nanostructures in the presence of Dzyaloshinkskii-Moriya interaction.* Phys. Rev. B, 2013. **88**(18): p. 184422.

7. DeJong, M.D. and K.L. Livesey, *Analytic theory for the switch from Bloch to Neel domain wall in nanowires with perpendicular anisotropy.* Phys. Rev. B, 2015. **92**(21).

8. Nakatani, Y., A. Thiaville, and J. Miltat, *Head-to-head domain walls in soft nano-strips: a refined phase diagram.* Journal of Magnetism and Magnetic Materials, 2005. **290**: p. 750-753.

9. Jamet, S., et al., *Head-to-head domain walls in one-dimensional nanostructures: An extended phase diagram ranging from strips to cylindrical wires.*, in *Magnetic Nano- and Microwires*, M. Vazquez, Editor. 2015, Woodhead Publishing. p. 783-811.

10. Pauling, L., *The structure and entropy of ice and of other crystals with some randomness of atomic arrangement.* Journal of the American Chemical Society, 1935. **57**: p. 2680-2684.

11. Nisoli, C., R. Moessner, and P. Schiffer, *Artificial Spin Ice: Designing and imaging magnetic frustration.* Rev. Mod. Phys., 2013. **85**(4): p. 1473-1490.

12. Bramwell, S.T. and M.J.P. Gingras, *Spin Ice State in Frustrated Magnetic Pyrochlore Materials.* Science, 2001. **294**(5546): p. 1495-1501.

13. Wang, R., et al., *Artificial `Spin Ice' in a Geometrically Frustrated Lattice of Nanoscale Ferromagnetic Islands.* Nature, 2006. **439**: p. 303-306.

14. Tanaka, M., E. Saitoh, and H. Miyajima, *Asymmetric field variation of magnetoresistance in Permalloy honeycomb nanonetwork.* Journal of Applied Physics, 2006. **99**(8).

15. Marrows., C., *Experimental Studies of Artificial Spin Ice*, in *Spin Ice*, M. Udagawa and L. Jaubert., Editors. 2016.

16. Wang, R.F., et al., *Demagnetization protocols for frustrated interacting nanomagnet arrays.* Journal of Applied Physics, 2007. **101**(9): p. 09J104.

17. Nisoli, C., et al., *Ground State Lost but Degeneracy Found: The Effective Thermodynamics of Artificial Spin Ice.* Phys. Rev. Lett., 2007. **98**(21): p. 217203.

18. Budrikis, Z.M., J. P.; Akerman, J; Stein, A.; Politi, Paolo; Langridge, S;. Marrows, C. H.; Stamps, R. L., *Disorder Strength and Field-Driven Ground State Domain Formation in Artificial Spin Ice: Experiment, Simulation, and Theory.* Phys. Rev. Lett., 2012. **109**(3): p. 037203.

19. Marrows, C., *Experimental Studies of Artificial Spin Ice*. 2021. p. 455-478.

20. Nisoli, C., et al., *Effective Temperature in an Interacting Vertex System: Theory and Experiment on Artificial Spin Ice.* Physical review letters, 2010. **105**: p. 047205.

21. Morgan, J., et al., *Thermal ground-state ordering and elementary excitations in artificial magnetic square ice.* Nature Physics, 2011. **7**(1): p. 75-79.

22. Skjærvø, S.H., C.H. Marrows, and R.L. Stamps, *Advances in artificial spin ice.* Nature Reviews Physics, 2020. **2**(1): p. 13-28.

23. Castelnovo, C., R. Moessner, and S.L. Sondhi, *Magnetic monopoles in spin ice.* Nature, 2008. **451**(7174): p. 42-45.

24. Ladak, S., et al., *Direct observation of magnetic monopole defects in an artificial spin-ice system.* Nature Physics, 2010. **6**(5): p. 359-363.

25. Mellado., P., et al., *Dynamics of magnetic charges in artificial spin ice.* Physical Review Letters, 2010. **105**(18).

26. Pimpin, A. and W. Srituravanich, *Review on Micro- and Nanolithography Techniques and their Applications.* Engineering Journal, 2012. **16**: p. 37.

27. Sharma, E., et al., *Evolution in Lithography Techniques: Microlithography to Nanolithography.* Nanomaterials (Basel), 2022. **12**(16).

28. De Teresa, J., et al., *Review of magnetic nanostructures grown by focused electron beam induced deposition (FEBID).* Journal of Physics D: Applied Physics, 2016. **49**(24): p. 243003.

29. Huth, M., et al., *Focused electron beam induced deposition: A perspective.* Beilstein Journal of Nanotechnology, 2012. **3**: p. 597-619.

30. Fourkas., J.T., *Chapter 1.3 - Fundamentals of Two-Photon Fabrication*, in *Three-Dimensional Microfabrication Using Two-Photon Polymerization*, T. Baldacchini, Editor. 2016, William Andrew Publishing. p. 45-61.

31. Andrzejewska, E., *Chapter 2 - Free Radical Photopolymerization of Multifunctional Monomers*, in *Three-Dimensional Microfabrication Using Two-photon Polymerization*, T. Baldacchini, Editor. 2016, William Andrew Publishing: Oxford. p. 62-81.

32. Mueller., J.B., J. Fischer., and M. Wegener., *Chapter 3 - Reaction Mechanisms and In Situ Process Diagnostics*, in *Three-Dimensional Microfabrication Using Two-photon Polymerization*, T. Baldacchini, Editor. 2016, William Andrew Publishing. p. 82-101.

33. Zhou, X., Y. Hou, and J. Lin, *A review on the processing accuracy of two-photon polymerization.* Aip Advances, 2015. **5**(3).

34. Hunt, M., et al., *Harnessing multi-photon absorption to produce three-dimensional magnetic structures at the nanoscale.* Materials, 2020. **13**(3): p. 761.

35. Chern, G., C. Reichhardt, and C. Nisoli, *Realizing three-dimensional artificial spin ice by stacking planar nano-arrays.* Applied Physics Letters, 2014. **104**(1): p. 4861118.

36. Mol, L.A.S., W.A. Moura-Melo, and A.R. Pereira, *Conditions for free magnetic monopoles in nanoscale square arrays of dipolar spin ice.* Physical Review B, 2010. **82**(5).

37. Perrin, Y., B. Canals, and N. Rougemaille, *Extensive degeneracy, Coulomb phase and magnetic monopoles in artificial square ice.* Nature, 2016. **540**(7633): p. 410-+.

38. Ribeiro, I.R.B., et al., *Realization of Rectangular Artificial Spin Ice and Direct Observation of High Energy Topology.* Scientific Reports, 2017. **7**(1): p. 13982.

39. Fernández-Pacheco, A., et al., *Three dimensional magnetic nanowires grown by focused electron-beam induced deposition.* Scientific Reports, 2013. **3**(1): p. 1492.

40. Pip, P., et al., *X-ray imaging of the magnetic configuration of a three-dimensional artificial spin ice building block.* APL Materials, 2022. **10**(10).

41. Mistonov, A.A.G., N. A.; Chumakova, A. V.; Eckerlebe, H.; Sapoletova, N. A.; Napolskii, K. S.; Eliseev, A. A.; Menzel, D.; Grigoriev, S. V., *Three-dimensional artificial spin ice in nanostructured Co on an inverse opal-like lattice.* Phys. Rev. B, 2013. **87**(22): p. 220408.

42. May, A., et al., *Realisation of a frustrated 3D magnetic nanowire lattice.* Communications Physics, 2019. **2**(1): p. 13.

43. May, A., et al., *Magnetic charge propagation upon a 3D artificial spin-ice.* Nature Communications, 2021. **12**(1): p. 3217.

44. Sharma, E., et al., *Evolution in Lithography Techniques: Microlithography to Nanolithography. .* (2079-4991 (Print)).

45. Hosaka, S., *Updates in Advanced Lithography*. InTech. 2013. 262.

46. van den Berg, A., et al., *Combining two-photon lithography with laser ablation of sacrificial layers: A route to isolated 3D magnetic nanostructures.* Nano Research, 2023. **16**(1): p. 1441-1447.

47. Askey, J., et al., *Use of Two-Photon Lithography with a Negative Resist and Processing to Realise Cylindrical Magnetic Nanowires.* Nanomaterials, 2020. **10**(3): p. 429.

48. Nanoscribe. *Nanoscribe GmbH*. 2015 [cited 2023 25th December]; Available from: http://www.nanoscribe.de.

49. Purtov, J., et al., *Improved development procedure to enhance the stability of microstructures created by two-photon polymerization.* Microelectronic Engineering, 2018. **194**: p. 45-50.

50. Puliyalil, H. and U. Cvelbar, *Selective Plasma Etching of Polymeric Substrates for Advanced Applications.* Nanomaterials (Basel), 2016. **6**(6).

51. Nanosensors. *SuperSharpSilicon - MagneticForceMicroscopy Reflex Coating AFM Tip*. 2023 [cited 2023 25th December]; Available from: https://www.nanosensors.com/supersharpsilicon-magnetic-force-microscopy-reflex-coating-afm-tip-SSS-MFMR.

52. Kazakova, O., et al., *Frontiers of magnetic force microscopy.* Journal of Applied Physics, 2019. **125**(6): p. 060901.

53. Bruker. *Dimension Icon User Guide*. 2010 [cited 2023 27th December]; Available from: https://www.nanophys.kth.se/nanolab/afm/icon/bruker-help/Content/Cover%20page.htm.

54. Sutton, M.A., et al., *Scanning Electron Microscopy for Quantitative Small and Large Deformation Measurements Part I: SEM Imaging at Magnifications from 200 to 10,000.* Experimental Mechanics, 2007. **47**(6): p. 775-787.

55. Allwood, D.A., et al., *Magneto-optical Kerr effect analysis of magnetic nanostructures.* Journal of Physics D: Applied Physics, 2003. **36**(18): p. 2175.

56. Hunt, M., *Optical magnetometry and micromagnetic simulations of three-dimensional magnetic nanostructures*. 2017, Cardiff University.

57. Guo, J., *Soft-X-ray spectroscopy study of nanoscale materials*. Vol. 5929. 2005. 59290K-59290K.

58. Guo, J.H., et al., *Resonant and nonresonant x-ray scattering spectra of some poly(phenylenevinylene)s.* The Journal of Chemical Physics, 1998. **108**(14): p. 5990-5996.

59. Yano, J. and V.K. Yachandra, *X-ray absorption spectroscopy.* Photosynth Res, 2009. **102**(2-3): p. 241-54.

60. van der Laan, G. and A.I. Figueroa, *X-ray magnetic circular dichroism—A versatile tool to study magnetism.* Coordination Chemistry Reviews, 2014. **277-278**: p. 95-129.

61. Nichols, C.I.O.B., *Tiny Space Magnets: X-ray Microscopy and Nanopaleomagnetism of Meteoritic Metal*. 2017: Apollo - University of Cambridge Repository.

62. Laan, G.v.d., *Applications of soft x-ray magnetic dichroism.* Journal of Physics: Conference Series, 2013. **430**(1): p. 012127.

63. B.L. Henke, E.M.G., J.C. Davis, , *X-Ray Interactions: Photoabsorption, Scattering, Transmission, and Reflection at E = 50-30,000 eV, Z = 1-92,.* Atomic Data and Nuclear Data Tables, , 1993. **54**(2): p. 181-342.

64. Attwood, D., *Soft X-Rays and Extreme Ultraviolet Radiation: Principles and Applications*. 1999, Cambridge: Cambridge University Press.

65. Fernandez-Roldan, J., et al., *A Comparative Study of Magnetic Properties of Large Diameter Co Nanowires and Nanotubes.* Nanomaterials, 2018. **8**(9): p. 692.

66. Hermosa-Muñoz, J., et al., *3D magnetic configuration of ferrimagnetic multilayers with competing interactions visualized by soft X-ray vector tomography.* Communications Physics, 2022. **5**(1): p. 26.

67. Fischbacher, T., et al., *A systematic approach to multiphysics extensions of finite-element-based micromagnetic simulations: Nmag.* Ieee Transactions on Magnetics, 2007. **43**(6): p. 2896-2898.

68. Wang, R.F., et al., *Demagnetization protocols for frustrated interacting nanomagnet arrays.* Journal of Applied Physics, 2007. **101**(9).

69. Ryzhkin, I., *Magnetic relaxation in rare-earth oxide pyrochlores.* Journal of Experimental and Theoretical Physics, 2005. **101**(3): p. 481-486.

70. Giblin, S.R., et al., *Creation and measurement of long-lived magnetic monopole currents in spin ice.* Nature Physics, 2011. **7**(3): p. 252-258.

71. Fennell, T., et al., *Magnetic Coulomb phase in the spin ice Ho2Ti2O7.* Science, 2009. **326**(5951): p. 415-417.

72. Brooks-Bartlett, M., et al., *Magnetic-Moment Fragmentation and Monopole Crystallization.* Physical Review X, 2014. **4**(1).

73. Jaubert, L.D.C., et al., *Spin ice Thin Film: Surface Ordering, Emergent Square ice, and Strain Effects.* Physical Review Letters, 2017. **118**(20).

74. Perrin, Y., B. Canals, and N. Rougemaille, *Quasidegenerate ice manifold in a purely two-dimensional square array of nanomagnets.* Physical Review B, 2019. **99**.

75. Wang, R.F., et al., *Artificial 'spin ice' in a geometrically frustrated lattice of nanoscale ferromagnetic islands (vol 439, pg 303, 2006).* Nature, 2007. **446**(7131): p. 102-102.

76. Saccone, M., et al., *Exploring the phase diagram of 3D artificial spin-ice.* Communications Physics, 2023. **6**(1): p. 217.

77. Koraltan, S., et al., *Tension-free Dirac strings and steered magnetic charges in 3D artificial spin ice.* npj Computational Materials, 2021. **7**(1): p. 125.

78. Parkin, S.S.P., M. Hayashi, and L. Thomas, *Magnetic domain-wall racetrack memory.* Science, 2008. **320**(5873): p. 190-194.

79. Parkin, S. and S.H. Yang, *Memory on the racetrack.* Nature Nanotechnology, 2015. **10**(3): p. 195-198.

80. Thomas, L., et al., *Racetrack Memory: a high-performance, low-cost, non-volatile memory based on magnetic domain walls.* 2011 Ieee International Electron Devices Meeting (Iedm), 2011.

81. Lyng-Jørgensen, J., *Investigating the Magnetic Characteristics of Oxidized Ni80Fe20 Structures and the Integrity of Al Capping Layers Used as an Oxidation Barrier*, in *Department of Electronic Systems*. Norwegian University of Science and Technology.

82. Irfan, M., et al., *Synthesis and characterization of NiFe2O4 magnetic nanoparticles with different coating materials for magnetic particle imaging (MPI).* Journal of Magnetism and Magnetic Materials, 2021. **537**: p. 168150.

83. Moriyama, T., et al., *Spin torque control of antiferromagnetic moments in NiO.* Scientific Reports, 2018. **8**(1): p. 14167.

84. Akhter, M.A., et al., *Thickness and grain-size dependence of the coercivity in permalloy thin films.* Journal of Applied Physics, 1997. **81**(8): p. 4122-4124.

85. Bearden, J.A.B., A. F.;, *Reevaluation of X-ray Atomic Energy Levels.* Reviews of Modern Physics, 1967. **39**(1): p. 125-142.

86. van der Laan, G., et al., *Orbital polarization in NiFeO4 measured by Ni - 2p x-ray magnetic circular dichroism.* Physical Review B, 1999. **59**(6): p. 4314-4321.

87. Regan, T.J., et al., *Chemical effects at metal/oxide interfaces studied by x-ray-absorption spectroscopy.* Physical Review B, 2001. **64**(21): p. 214422.

88. Hitchcock A., *aXis2000 is written in Interactive Data Language (IDL). It is available free for noncommercial use from* http://unicorn.mcdmaster.ca/axis2000.html. 01/02/2023.

89. Gaididei, Y., V.P. Kravchuk, and D.D. Sheka, *Curvature Effects in Thin Magnetic Shells.* Physical Review Letters, 2014. **112**(25): p. 257203.

90. Seniutinas, G., et al., *Beyond 100 nm resolution in 3D laser lithography - Post processing solutions.* Microelectronic Engineering, 2018. **191**: p. 25-31.

91. Fernandez-Roldan, J.A., et al., *Spatial magnetic imaging of non-axially symmetric vortex domains in cylindrical nanowire by transmission X-ray microscopy.* Nanoscale, 2022. **14**(37): p. 13661-13666.

8 Appendices

8.1 MFM Processing Code

The commented code used to process the AFM/MFM data and enhance the contrast is shown below. AFM and MFM files processed using Gwyddion are saved in an ASCII text file format.

```
# Load MFM and AFM data
MFM = np.loadtxt(fname+"_MFM.txt", skiprows=4)
AFM = np.loadtxt(fname+"_AFM.txt", skiprows=4)

# Rough contrast parameter for MFM
# Value represents number of standard deviations from the mean
contrast = 3

# Calculate mean and standard deviation of MFM data
m = np.mean(MFM)
s = np.std(MFM)

# Clip MFM data based on contrast parameter
MFM = np.clip(MFM, m - contrast * s, m + contrast * s) - (m - contrast * s)

# Blank array for subtracted MFM
subMFM = np.zeros_like(AFM)

# Subtract AFM from MFM line-by-line
for i in range(NumberOfLines):
    afmslice = AFM[i, :]
    popt, pcov = curve_fit(afmfit, x, MFM[i, :])
    subMFM[i, :] = MFM[i, :] - afmslice * popt[0] + popt[1]

    # Parabolic flatten
    popt, pcov = curve_fit(parab_fit, x, subMFM[i, :])
    subMFM[i, :] = subMFM[i, :] - parab_fit(x, *popt)

# Calculate mean and standard deviation of processed MFM data
subm = np.mean(subMFM)
subs = np.std(subMFM)

# Clip processed MFM data
subMFM = np.clip(subMFM, subm - contrast * subs, subm + contrast * subs) -
(subm - contrast * subs)
```

8.2 Vertex Type Examples and Simulated Spin Textures

The following set of figures presents a comprehensive examination of coordination-four vertex types. First examples on the SL1/SL2 layers will be shown and then examples found on the deeper SL2/SL3 layers. These examples were carefully gathered and assessed both visually and using a line profile methodology to determine the magnetisation arrangement. The following figures showcase vertex types which have previously been measured in literature, and where comparisons can be made these are presented. Additionally, these measurements are juxtaposed with simulated results presenting the simulated MFM contrast, M_z component and the representative spin texture of the vertex type which has been identified.

Understanding these figures and interpreting the presented data is crucial before delving into an analysis of the discovered vertex types. The figures aim to provide a comparative analysis between documented vertex types and their manifestation within demagnetized MFM images before proceeding to uncover and identify novel vertex types not previously observed.

Figure 103a displays a masked MFM image highlighting specific contrast observations on a Type 2 vertex situated on the SL1/SL2 junction, utilising coloured arrows to indicate the magnetisation direction of each wire. An x- and y- axis have been clearly shown with SL1 being aligned along the x-direction and SL2 along the y-direction. This is maintained for consistency throughout all subsequent figures. The dashed line shown on the figure encloses all four wires which constitute the vertex, these are called “connecting wires”. Those wires situated outside of this dashed line are hereafter called “neighbouring” wires. Within analysis, reference will be made to the vertex centre. This is located at the meeting point of all four wires connected to the vertex (centre of dotted square), and the visual contrast within this centre is interpreted to aid with vertex determination.

In **Figure 103b**, a direct comparison is presented with a previously imaged Type 2 vertex [43] and this shows good agreement with **Figure 103a**. In **Figure 103c**, a side profile view of SL1 and SL2 wires visible in **Figure 103a** is depicted, featuring similarly coloured arrows illustrating the magnetisation arrangement within the measured vertex and allowing comparison with **Figure 103a**. Contrast indicators have been placed on wires, showing the contrast visible in

Figure 103a and later measured by line profiles. The dashed line denotes the centre of the vertex being analysed, while dotted lines indicate separations between individual wires.

The contrast across the SL1 wire layer, as illustrated in **Figure 45a** and observed in earlier works [42, 43], is discernible by observing contrast changes across two SL1 wires, and this is therefore depicted in **Figure 103c** with singular positioning of contrast on this wire layer (one contrast indicator per wire). This contrast pattern, where one wire is bright and another dark, signifies the magnetisation orientation based on the bright-to-dark pattern across the two wires.

Contrast interpretation across SL2 and subsequent wire layers is focused on individual wires, evident from the presence of two contrast indicators per individual wire in **Figure 103c**. Here, contrast is primarily analysed along each individual wire in a similar bright-to-dark manner. Interpreting these layers (SL2 and SL3) requires observing both the wire connected to the considered vertex and its neighbouring wire. This approach is essential for two primary reasons. Firstly, there is a reduced signal strength attributed to increased depth, particularly noticeable on SL2 and subsequently the SL3 layer. By factoring in the orientation of neighbouring wires, this method provides more data for an informed decision and compensates somewhat for reduced signal strength providing supplementary information crucial for determining magnetisation orientation. Secondly, when applying orientation across a broader MFM image consisting of many vertices, overlooking neighbouring wires leads to assumed vertex orientations inconsistent with observed contrast. Neglecting neighbouring wires while applying orientations around a specific vertex result in neighbouring vertices being assigned vertex types that contradict their MFM contrast.

Figure 103d-e present line profiles taken across the SL1 surface layer, covering the entire length of SL1 wires but excluding measurement of contrast at the vertex centre itself. These line profiles traverse SL1 wires from left to right, employing the previously defined x-axis from **Figure 103a** and **Figure 103c**. Coloured arrows situated beneath each line profile show the magnetisation orientation, enabling identification of the line profile's relevance by comparison with **Figure 103a** and **Figure 103c.**

In **Figure 103f-g**, line profiles are depicted across the SL2 wire layers as observed in **Figure 103a**. These profiles, measured left to right, exclusively capture visible contrast on SL2 wires, without including the contrast on the vertex centre. These measurements utilize the previously defined y-axis for positioning. Similarly, coloured arrows are situated beneath each line profile showing the magnetisation orientation and for identification of line profiles relevance by comparison with **Figure 103a** and **Figure 103c.**

Figure 104 illustrates simulated MFM contrast and spin texture of the Type 2 vertex depicted in **Figure 103**. Notably, neighbouring wires on SL1 or SL2 are not factored into this simulation. Coloured arrows, positioned nearest to wires, depict the identical magnetisation arrangement observed in **Figure 103** for the purpose of comparison.

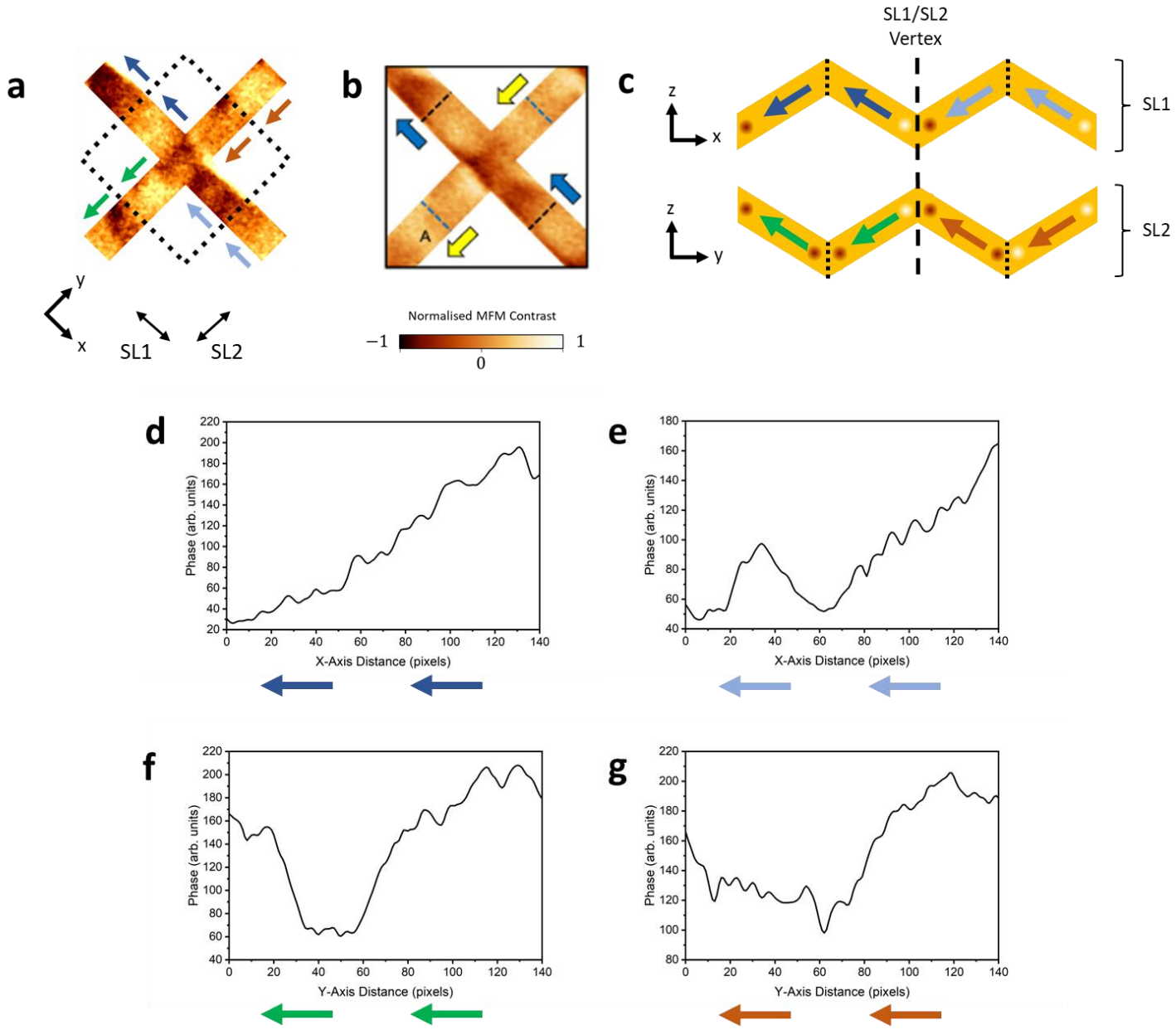

Figure 103: *Masked MFM contrast for* ***(a)*** *Type 2* $(Q = 0)$ *identified on SL1/SL2 coordination-four vertices with defined x- and y-axis reflecting the SL1 and SL2 directions. The dotted line encompasses the vertex's four wires.* ***(b)*** *Exhibits a comparison with previously measured Type 2 vertex for comparison which illustrates magnetisation orientation with arrows. Taken from [43].* ***(c)*** *Side profile view of considered wires, highlighting the axis, vertex location (dashed line), and individual wires separated by dotted lines with contrast visible shown. Legend for* ***(a-c)*** *denotes normalised MFM contrast.* ***(d-e)*** *Line profiles across defined x-axis along the SL1 wires with representative arrows showing wire magnetisation orientation.* ***(f-g)*** *Line profiles across defined y-axis along SL2 wires with representative arrows showing wire magnetisation orientation.*

Examining **Figure 103a** the orientation of the SL1 wires is visually identifiable, and is comparable to the previously discovered Type 2 vertex which is shown in **Figure 103b**. The orientation of this magnetisation is shown by the coloured arrows on **Figure 103a** and **Figure 103c**. This has been determined visually and is supported by analysis of the subsequent line scans, see **Figure 103d-e,** indicating a consistent head-to-tail arrangement across this junction.

Upon analysing the bottom-left SL2 wire (green arrows), visual inspection and overall phase changes shown in **Figure 103f** suggest a head-to-tail configuration oriented away from the vertex. A distinct bright lobe, seen in previously measured data [3], on the connecting SL2 wire and a subsequent dark phase on the neighbouring SL2 wire further clarify this orientation. The increase in brightness on the furthest wire is identified by a reverse tip image to be an artifact from the topography, which did not invert contrast with tip reversal [76].

Comparisons with vertices measured on the SL2/SL3 junction in later figures contribute to the analysis of the upper-right SL2 wire, for which the line profile is presented in **Figure 103g**. Although a lower peak is visible in the line scan for the connecting SL2 wire, indicating a potential head-to-head arrangement toward the SL2/SL3 vertex across this wire, it deviates from expectations. Such an arrangement typically produces significantly brighter lobes upon the junction of the connecting SL2 wire with the SL1/SL2 vertex, as is seen on the bottom-left connecting SL2 wire, and a notably darker phase is anticipated at the SL2/SL3 junction, located at the intersection of the upper-right vertex connected SL2 wire with its neighbouring SL2 wire. This is not observed here. If this connecting SL2 wire were directed away from the SL1/SL2 junction, it would denote this SL1/SL2 vertex as a Type 3. However, comparing the overall phase of the vertex centre with examples of an SL1/SL2 Type 3 ($Q = -2q$) depicted later, an anticipated bright centre is not observed in this instance. This discrepancy reinforces the configuration depicted in the figure, suggesting this vertex as a Type 2.

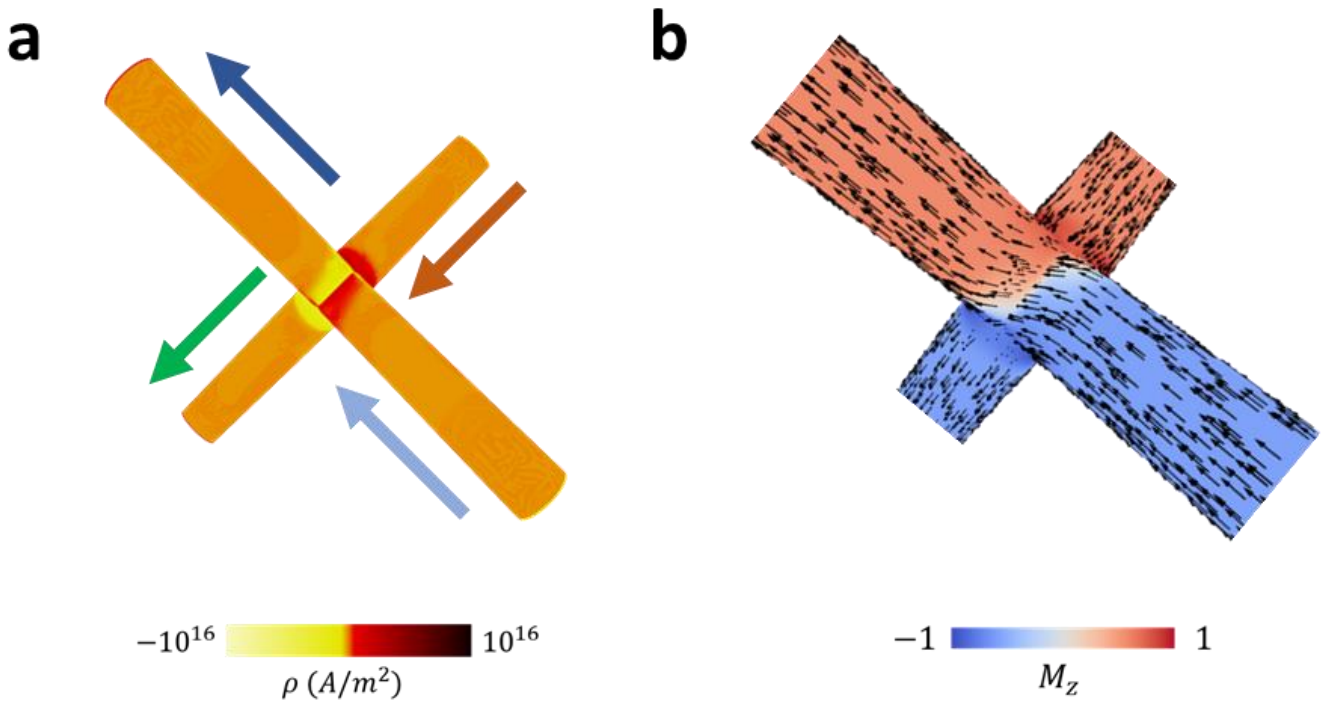

Figure 104: (a) *Simulated Type 2 vertex with magnetic charge density depicted on surface, legend shown.* ***(b)*** *Type 2 vertex with colouration determined by magnitude of M_z component, legend shown. Representative spin texture arrows are illustrated on surface and coloured vertex arrows are shown alongside for clarity with previous figures.*

In **Figure 104a**, the simulated magnetic charge density, representing the MFM contrast, exhibits notable consistency with the experimentally measured Type 2 vertex shown in **Figure 103**. A clear correspondence is evident between the bright and dark lobes observed on connecting SL2 wires in the experimental Type 2 example. Bright lobes distinctly manifest in both simulated and experimental data on wires where the magnetisation orientation is directed outward from the vertex. Conversely, dark lobes are observed on wires where the magnetisation is directed inward, accompanied by a bleed effect where the contrast extends onto the vertex itself. These characteristics are observed across both simulated and experimental data.

However, the sharp, clean-cut approximation of the vertex centre within simulated contrast, see **Figure 104a**, which display a distinct transition does not agree with experimental MFM data. This discrepancy can be attributed to the limited resolution of experimental measurements, resulting in the detection of stray fields emanating across the vertex during

measurement. Specifically, it should be noted that MFM resolution is approximately equal to the lift height used ($90\ nm$). Consequently, a smeared effect is encountered within the vertex centre region during experimental observations. Examining the collective phase of the vertex centre in simulated MFM contrast provides a potential better comparison with experimental data. In **Figure 104a**, the collective phase of the bright and dark sections negate one another resulting in a predicted vertex centre which is neither bright nor dark. This shows good agreement with the experimental data, when compared to later clear examples of bright/dark vertex centres seen in Type 3 vertices.

In **Figure 104b** the spin texture of the Type 2 vertex identified in **Figure 103** is shown. Close to the vertex there's a distinct 90-degree reorientation at the intersections between the SL1 and SL2 wires. Across the SL1 wires, whilst the in-plane component remains conserved there's a nuanced canting phenomenon near the vertex, deviating from a traditional domain wall. For the SL2 wires, the 90-degree reorientation at the wire intersections contributes to the formation of a domain wall at the junction of the SL2 wires with the SL1 wires. Overall, the spin texture reveals a homogeneous magnetisation directed in this case along the $(-1, -1)$ unit direction.

Overall, visual and analytical methods have been applied to this vertex and show good comparison with a Type 2 vertex previously discovered. Further comparison with simulated MFM contrast and observations of the spin-texture of a Type 2 vertex show good agreement, overall determining successful identification of a Type 2 vertex within the experimental data.

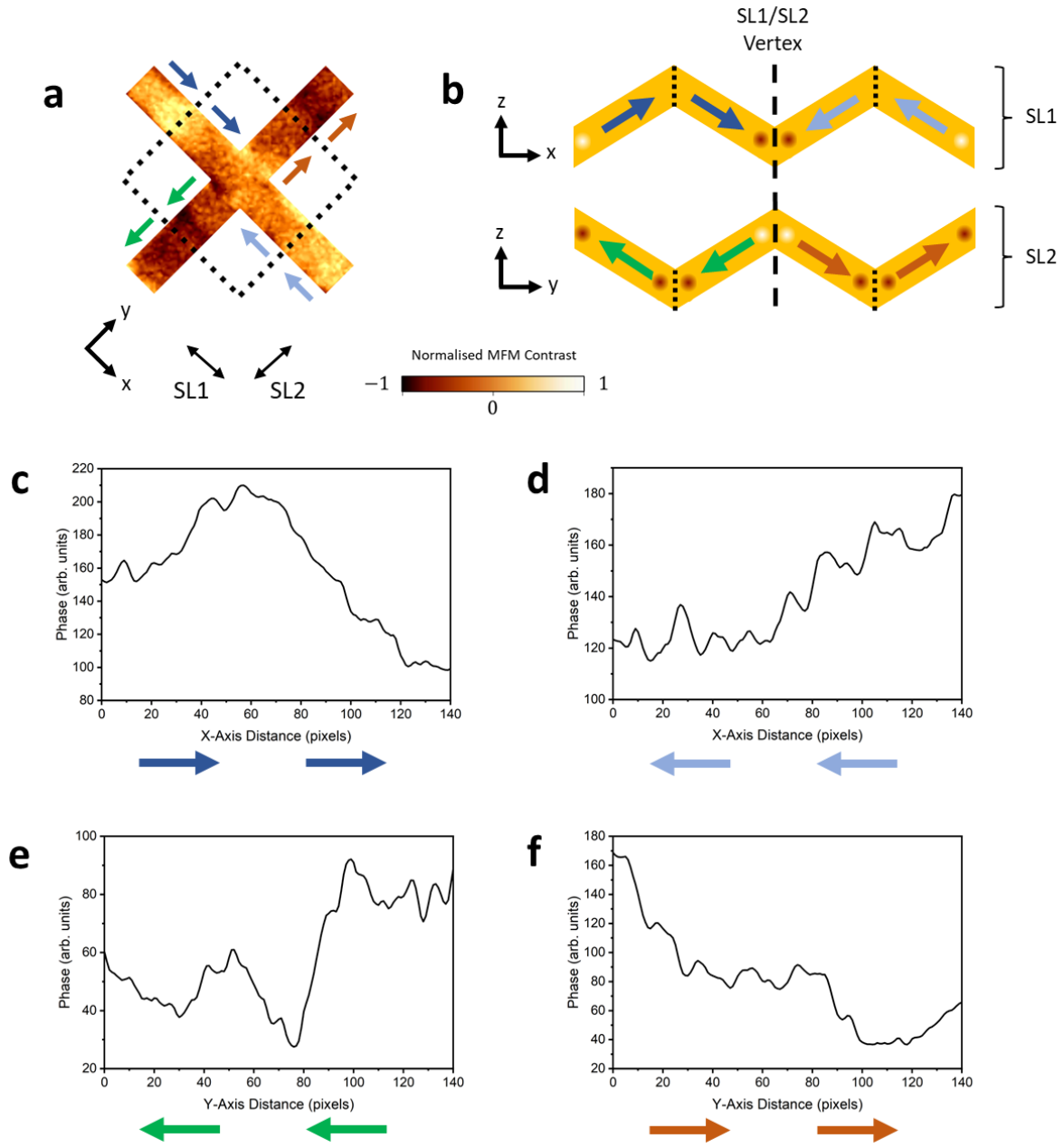

Figure 105: *Masked MFM contrast for* ***(a)*** *Type 1* $(Q = 0)$ *identified on SL1/SL2 coordination-four vertices with defined x- and y-axis reflecting the SL1 and SL2 directions. The dotted line encompasses the vertex's four wires.* ***(b)*** *Side profile view of considered wires, highlighting the axis, vertex location (dashed line), and individual wires separated by dotted lines with contrast visible shown. Legend for* ***(a-b)*** *denotes normalised MFM contrast.* ***(c-d)*** *Line profiles across defined x-axis along the SL1 wires with representative arrows showing wire magnetisation orientation.* ***(e-f)*** *Line profiles across defined y-axis along SL2 wires with representative arrows showing wire magnetisation orientation.*

In **Figure 105a**, a masked MFM image showcases the visible contrast specific to a Type 1 vertex situated on the SL1/SL2 junction. A side-profile visual representation of the constituent SL1 and SL2 wires of this vertex is shown in **Figure 105b**. The contrast observed on the SL1 wires is notably clear and well-defined, aligning closely with previous SL1 measurements. This alignment strongly suggests that both SL1 wire magnetisations are inwardly oriented toward the vertex. Line profiles of the contrast measured across both SL1 wires are shown in **Figure 105c-d**, and they depict a consistent transition from high to low phase across each wire as it approaches the vertex.

The clarity of visual identification is notably diminished for the bottom left SL2 wires (green arrows). This is evident from the reduced overall phase change observed in the line profile across these wires, as depicted in **Figure 105e**. Analysis of the line profile suggests a head-to-tail arrangement across these two SL2 wires, directed away from the SL1/SL2 vertex. Another significant observation which aids in the identification of the bottom left SL2 wire pertains to the overall phase located at the vertex centre of this SL1/SL2 vertex when compared to subsequent vertex types. Type 3 and Type 4 vertices consistently exhibit either a bright or dark vertex centre whereas Type 1 and Type 2 vertices display a notably reduced phase magnitude. As a result, the orientation of the magnetic configuration for this SL2 wire is set to that suggested by the line scans.

Upon visual inspection, the upper right SL2 wires (brown arrow) exhibits a marked phase change, evidenced by a distinct bright lobe at the junction between the vertex and the connecting SL2 wire. This phase change spans the entire length of the connecting SL2 wire and spreads onto its neighbour indicating a head-to-tail arrangement in the wire's magnetic configuration, as indicated by the arrows adjacent to the image. This is supported by the line profile measurement shown in **Figure 105f**. Upon evaluating the line scans and visual cues, the masked MFM configuration suggests a Type 1 vertex.

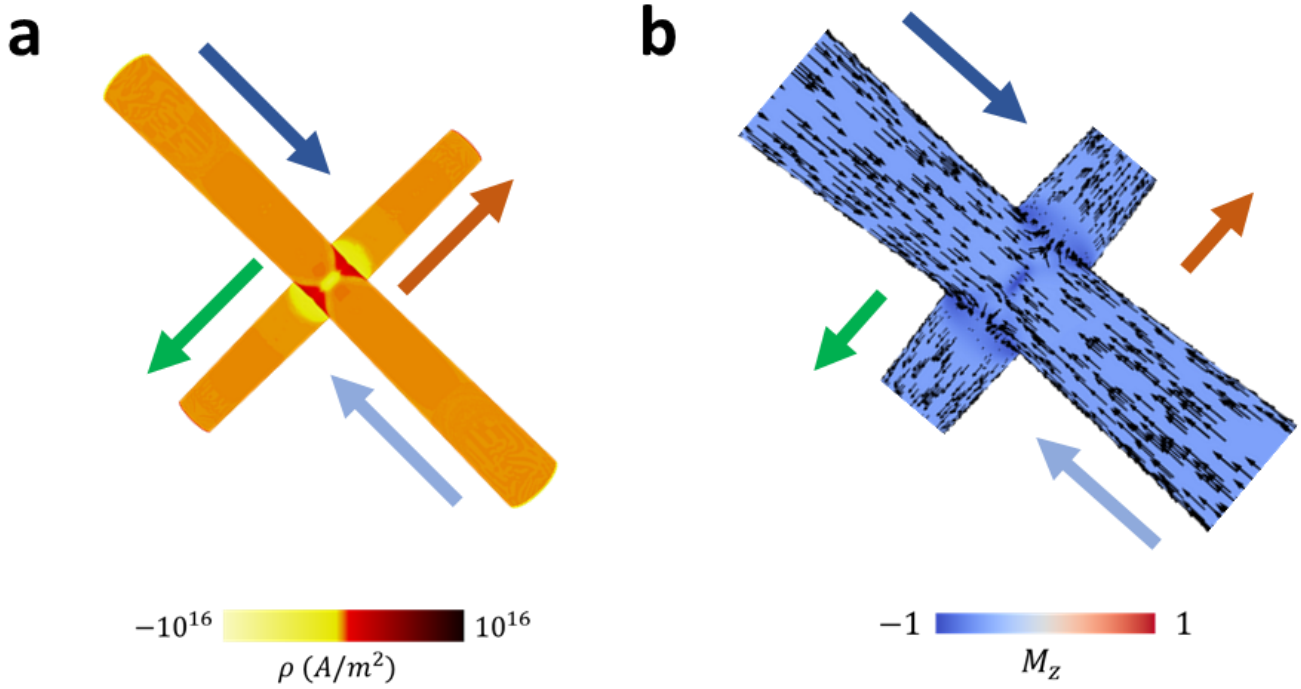

Figure 106: (a) *Simulated Type 1 vertex with magnetic charge density depicted on surface, legend shown.* ***(b)*** *Type 1 vertex with colouration determined by magnitude of M_z component, legend shown. Representative spin texture arrows are illustrated on surface and coloured vertex arrows are shown alongside for clarity with previous figures.*

In **Figure 106a** a simulated Type 1 vertex with the same magnetisation orientation of the vertex analysed in **Figure 105** is shown. Significant agreement is again found with the location of a bright lobe located on the upper-right SL2 wire (brown arrow). The corresponding bright lobe found on the bottom-left SL2 wire (green arrow) is not as visually distinct yet identifiable through line profile measurement. The collective phase of the vertex centre, suggested by MFM appears to show a similar neither bright nor dark as was observed in the Type 2 example. This also agrees with the experimental example.

In **Figure 106b**, a simulation of a Type 1 vertex is shown corresponding with the magnetisation orientation suggested by analysis in **Figure 105**. Spins directed into the vertex along the SL1 wires undergo a 90-degree rotation onto the SL2 wires and result in the formation of an anti-vortex spin texture with spins oriented out of the plane (-z) at the vertex centre. The MFM's sensitivity to the second derivative of H_z anticipates strong negative contrast within the

vertex centre, identifiable within **Figure 106a**, owing to the anti-vortex domain wall. However, this anticipated negative contrast is absent in the measured MFM data due to the constraints imposed by the limited resolution of experimental techniques. The spin texture shown by a Type 1 vertex with an inverted magnetisation orientation as to that shown in **Figure 106b** results in an anti-vortex domain wall with spins oriented out of the plane at the vertex centre. This suggests a distinct polarity between Type 1 vertices, with their configuration either directed out of or into the plane. However further simulations are required to determine if each Type 1 state can exist with either polarity – i.e. a degeneracy in the polarity.

The spin texture in Type 1 vertices signifies a more abrupt change in magnetic orientation over a shorter spatial distance. This rapid transition of spin orientation within a confined region demands a higher exchange energy cost. In contrast, the wider asymmetric domain walls in Type 2 vertices, shown in **Figure 104b,** allow for a rotation that utilizes the entire vertex area for the full spin reorientation. This understanding of the spin texture elucidates the observed difference in the energy landscape between Type 1 and Type 2 vertices previously observed by simulation [43] and suggests Type 1 vertices should be the lowest energy ice-rule in this 3D systems.

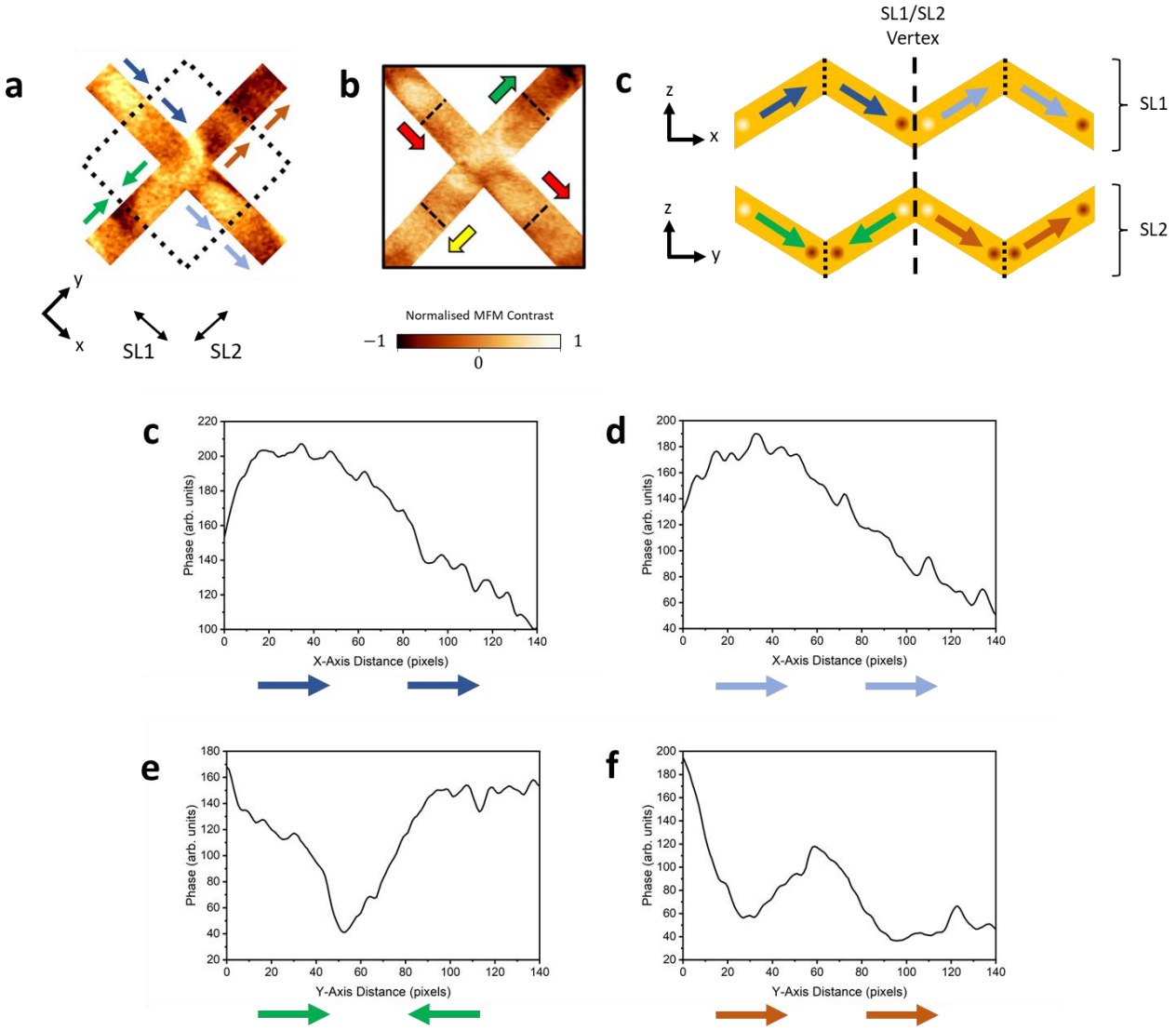

Figure 107: *Masked MFM contrast for* ***(a)*** *Type 3* $(Q = -2q)$ *identified on SL1/SL2 coordination-four vertices with defined x- and y-axis reflecting the SL1 and SL2 directions. The dotted line encompasses the vertex's four wires.* ***(b)*** *Exhibits a comparison with previously measured Type 3* $(Q = -2q)$ *vertex for comparison which illustrates magnetisation orientation with arrows. Taken from [43].* ***(c)*** *Side profile view of considered wires, highlighting the axis, vertex location (dashed line), and individual wires separated by dotted lines with contrast visible shown. Legend for* ***(a-c)*** *denotes normalised MFM contrast.* ***(d-e)*** *Line profiles across defined x-axis along the SL1 wires with representative arrows showing wire magnetisation orientation.* ***(f-g)*** *Line profiles across defined y-axis along SL2 wires with representative arrows showing wire magnetisation orientation.*

In **Figure 107a**, a Type 3 $(Q = -2q)$ vertex on an SL1/SL2 junction is examined and compared with a literature example in **Figure 107b**. A side-profile view of the measured vertex is shown in **Figure 107c** with the designated magnetisation orientation determined from visual identification and line profiles.

Analysis of the SL1 wire shows good agreement with previous examples in this thesis, literature and the specific example shown in **Figure 107b**. One pair of SL1 wires (dark blue arrows) are directed into the vertex, and the subsequent pair (light blue) are directed out.

The analysis of the bottom left SL2 wire (green arrows) exhibits a clear visual and measurable vertex configuration, see **Figure 107e**. A bright lobe is seen on the connecting SL2 wire, and a subsequent dark lobe is seen at its junction with the neighbouring SL2 wire. This neighbouring SL2 wire then shows a distinct bright lobe at its own connection with the neighbouring SL1/SL2 vertex. Overall, this reveals a head-to-head arrangement of these two wires, directed onto the SL2/SL3 vertex they are part of.

On the upper-right SL3 wire, there is distinct visual and measurable contrast, see **Figure 107f**, revealing a head-to-tail arrangement away from the wire, characterized by a bright lobe connecting the SL2 wire with the vertex and an overall bright-to-dark transition across the connecting SL2 wire and its neighbour. A reduced peak is discernible on the connecting SL2 wire however this was observed not to change contrast with tip inversion and is identified as a topological feature for this wire. Both SL2 wires show good agreement with the previous literature example shown in **Figure 107b**.

The overall phase of the vertex centre of this vertex being examined is significantly brighter compared to Type 1 and Type 2 examples on SL1/SL2. This brighter phase is seen in this measured example, and the previous literature example. Overall, after identification of each individual wires' magnetisation orientation, analysis suggests this to be a Type 3 $(Q = -2q)$ vertex.

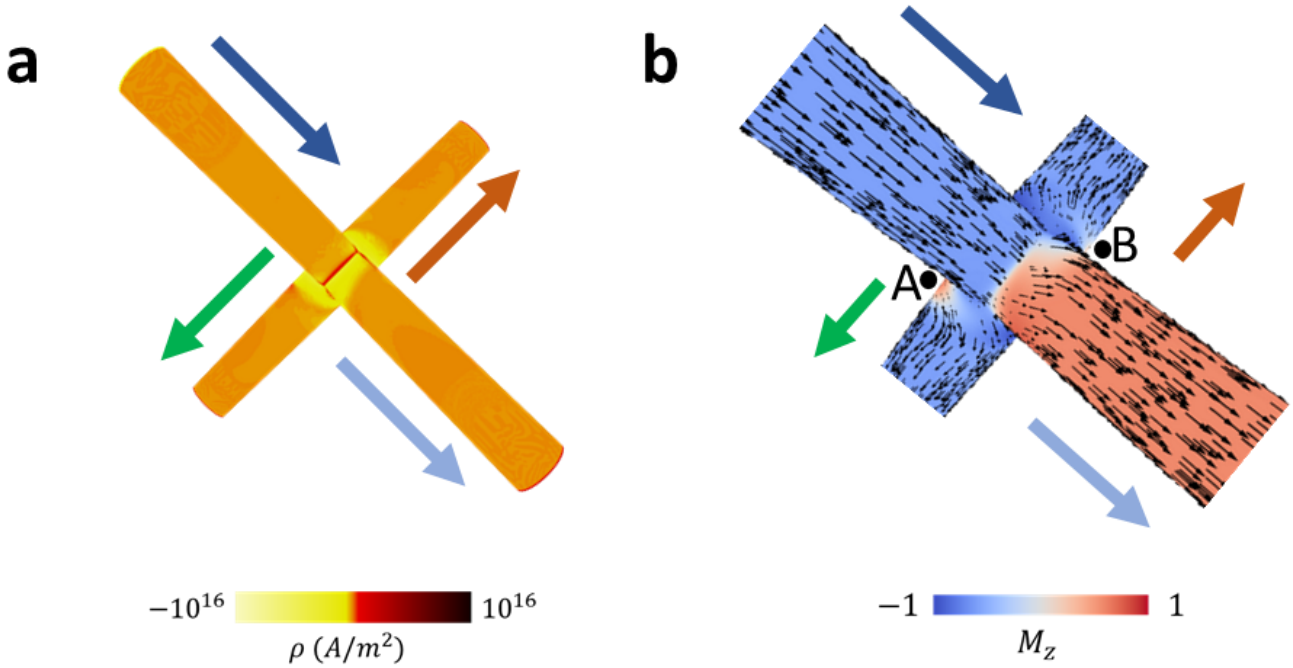

Figure 108: (a) *Simulated Type 3 $(Q = -2q)$ vertex with magnetic charge density depicted on surface, legend shown.* ***(b)*** *Type 3 $(Q = -2q)$ vertex with colouration determined by magnitude of M_z component, legend shown. Representative spin texture arrows are illustrated on surface and coloured vertex arrows are shown alongside for clarity with previous figures. Points A and B on the lower SL2 wires indicate location of point source of magnetic field oriented in positive M_z direction.*

In **Figure 108a**, the expected magnetic contrast for a Type 3 $(Q = -2q)$ vertex, mirroring the magnetisation configuration depicted in **Figure 107**, is displayed. The discernible bright and dark lobes observed along the SL2 wire chain in the experimental data align closely with the patterns observed in the simulation results. This consistent correspondence reinforces the agreement between experimental findings and simulated outcomes.

Similar to earlier observations, the overall phase profile of the vertex in the experimental data appears as a composite representation, amalgamating characteristics observed across different phases in the simulations. While the distinct and sharp transitions seen in simulations are absent in the experimental data, the overall brightness of the experimental Type 3 $(Q = -2q)$ vertex, depicted in **Figure 107a** and **Figure 107b**, surpasses that observed in the experimental Type 1, Type 2, and Type 3 $(Q = +2q)$ examples. This suggests that the

observed vertex phase in the experimental findings is influenced collectively by various phases witnessed in the simulation results. Notably the bright vertex contrast will also facilitate identification, later in vertex maps.

The spin texture depicted in **Figure 108b** aids in interpreting both the experimental (**Figure 107**) and simulated (**Figure 108a**) MFM contrasts for the Type 3 ($Q = -2q$) vertex. The spin texture analysis across this vertex reveals the presence of a symmetric domain wall, encompassing the entire vertex area and leading to the expected overall change in the M_z component's orientation. Specifically, the M_z orientation transitions from being directed into the vertex along the SL1 wire to being directed outwards along the opposing SL1 wire. This transition occurs across the centre of the vertex.

This flow pattern of spins can be observed as originating from the SL1 wire directed into the vertex, then extending outward and upward along the opposite SL1 wire. Additionally, there's a downward flow and a subsequent 90-degree rotation onto the connecting SL2 wires at the junction. The transition in M_z orientation across the SL1 wires occurs uniformly across the entire junction.

In both experimental and simulated data, the presence of bright lobes appears to arise from a disruption in symmetry within the vertex structure. Specifically, at the junction where upper SL1 wires meet the lower SL2 wires, both SL2 wires encounter difficulty (on opposing sides of the wire) in aligning its magnetic moments with the overall configuration. This can be observed as the brighter red spot located on left-hand side of the bottom-left SL2 wire (point “A" on **Figure 108b**) and the right-hand side of the upper-right SL2 wire (point “B” on **Figure 108b**). To achieve alignment with the surrounding wire sections, a localized segment of magnetic moments within the lower wire needs to orient in the positive M_z direction. This localized alignment serves as a point source of magnetic field, perhaps contributing to the observed bright lobes, which broaden in this vicinity. This phenomenon occurs to ensure consistency in magnetic alignment across both connecting lower wires, creating a localized region of distinct magnetic orientation to reconcile the overall magnetic configuration.

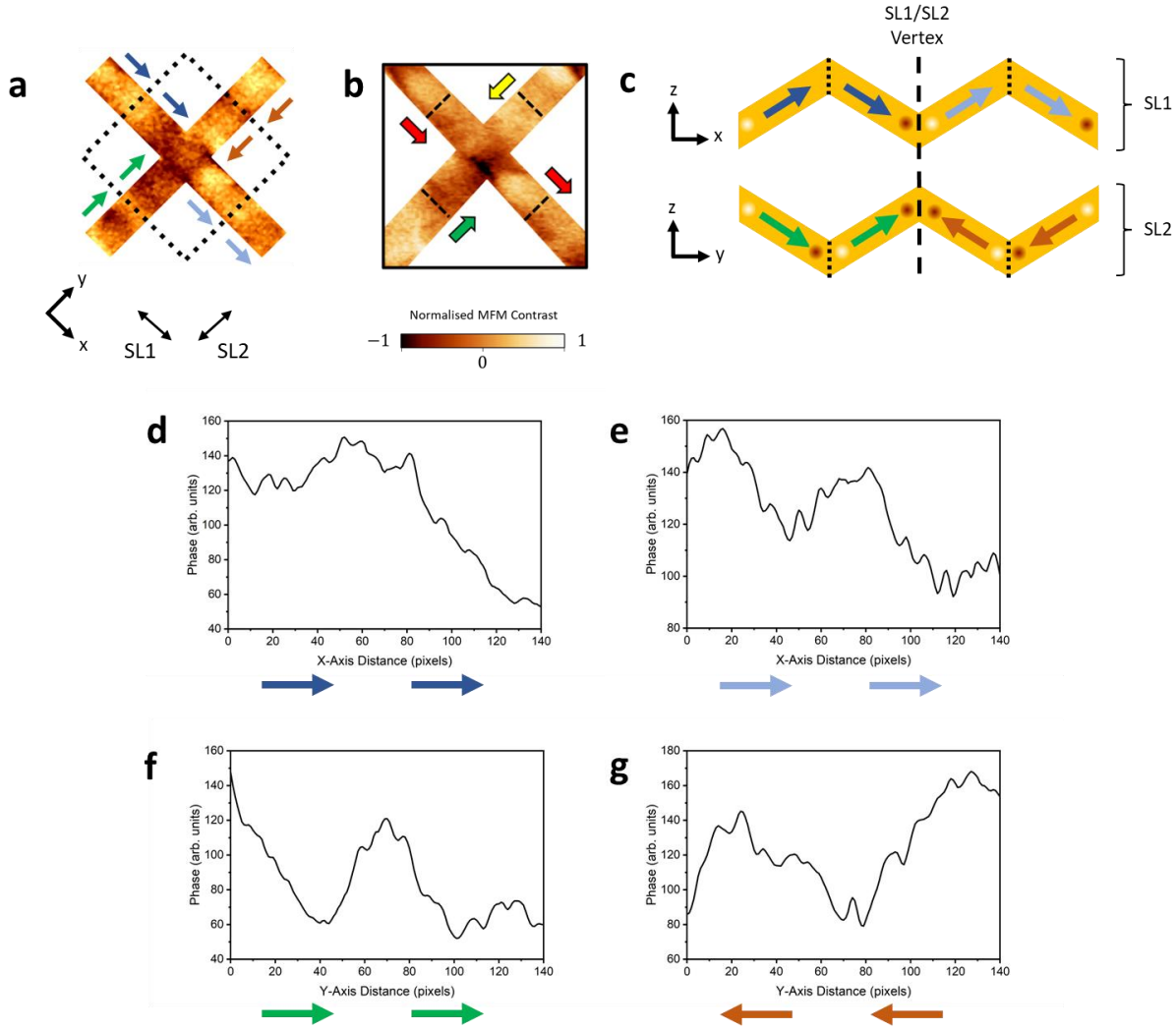

Figure 109: ***(a)*** *Masked MFM contrast for a Type 3* $(Q = 2q)$ *identified on SL1/SL2 coordination-four vertices with defined x- and y-axis reflecting the SL1 and SL2 directions. The dotted line encompasses the vertex's four wires.* ***(b)*** *Exhibits a comparison with previously measured Type 3* $(Q = 2q)$ *vertex for comparison which illustrates magnetisation orientation with arrows. Taken from [43].* ***(c)*** *Side profile view of considered wires, highlighting the axis, vertex location (dashed line), and individual wires separated by dotted lines with contrast visible shown. Legend for* ***(a-c)*** *denotes normalised MFM contrast.* ***(d-e)*** *Line profiles across defined x-axis along the SL1 wires with representative arrows showing wire magnetisation orientation.* ***(f-g)*** *Line profiles across defined y-axis along SL2 wires with representative arrows showing wire magnetisation orientation.*

In **Figure 109a**, a Type 3 $(Q = +2q)$ SL1/SL2 vertex is presented, alongside a previous literature example shown in **Figure 109b**, showcasing significant alignment. The finalized magnetic configuration on the constituent SL1 and SL2 wires is depicted in side-profile in **Figure 109c**. Notably, the SL1 wires exhibit a consistent head-to-tail arrangement, consistent with prior observations and established literature, corroborated by line profiles showcased in **Figure 109d** and **Figure 109e**.

The lower-left SL2 wire (green arrows) prominently displays a clear head-to-tail alignment directed into the vertex. This alignment is evident as a robust phase transition from bright-dark along its neighbouring SL2 wire, followed by bright-dark transition along the connecting wire directed into the vertex. This discernible pattern is visually observed and supported by the corresponding line profile in **Figure 109f**.

Analysis of the upper-right SL2 wires (brown arrows) necessitates an evaluation of phase changes via line profile, the overall phase at the SL1/SL2 vertex centre, and examination of the SL2/SL3 vertex centre which the two SL2 wires are a part of. Visual inspection and line profile measurements shown in **Figure 109g** indicate a bright-to-dark transition directed into the vertex. However, a diminished peak is noted on the connecting SL2 wire, which is to be examined, but overall line profile measurements indicate a head-to-tail configuration directed into the vertex.

Examination of the diminished bright peak on the connecting SL2 wire shows that it does not exhibit proximity to the junction itself, appearing as a bright lobe. This is unlike the clear pattern observed in **Figure 107a**, where a clear and distinct bright lobe is visually discerned and measured. This reduced peak was remeasured with inverted tip magnetisation and did not invert contrast, indicating that it is a possible topographical artifact occurring due to the abrupt upwards change in topography onto the vertex at this location [42, 43, 76].

Considering an alternate scenario where this SL2 wire points away from the SL1/SL2 vertex, this would entail a bright lobe formed at the junction of the connecting SL2 wire with the SL1/SL2 vertex followed by a darker phase at the associated SL2/SL3 vertex that this SL2 wire would point into. This contradicts the observed pattern here. Exploring this scenario further, this alternate configuration would result in a potential Type 2 configuration, as depicted in

Figure 103a. However, a comparative analysis between the central section of the Type 2 SL1/SL2 vertex in **Figure 103a** and the corresponding region in this instance reveals a distinct disparity in the overall vertex phase, supporting the suggestion that this is a Type 3 $(Q = +2q)$ configuration, as is depicted in the figure.

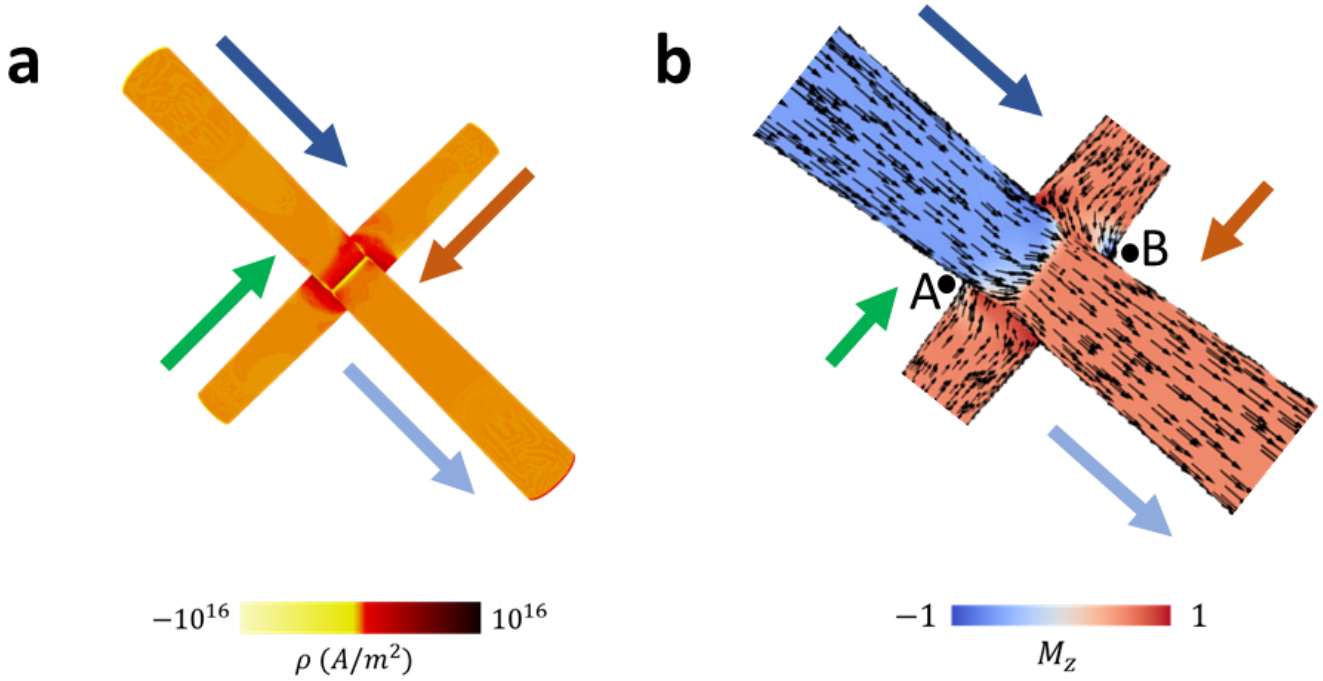

Figure 110: (a) *Simulated Type 3* $(Q = +2q)$ *vertex with magnetic charge density depicted on surface, legend shown.* ***(b)*** *Type 3* $(Q = +2q)$ *vertex with colouration determined by magnitude of* M_z *component, legend shown. Representative spin texture arrows are illustrated on surface and coloured vertex arrows are shown alongside for clarity with previous figures. Points A and B on the lower SL2 wires indicate location of point sink of magnetic field oriented in negative* M_z *direction.*

Figure 110a depicts the anticipated magnetic contrast for a Type 3 vertex, characterized by a net magnetic charge $(Q = +2q)$, and with the same configuration as is determined in **Figure 109**. Consistent with prior observations, the alignment between the dark and bright lobes evident on the SL2 wires in experimental findings showcases strong concordance with simulation outcomes. Furthermore, the collective phase profile of the vertex centre observed in experimental data harmonizes well with the collective phases observed in simulations.

Figure 110b depicts the spin texture and magnetisation magnitude for the same vertex configuration depicted previously. Type 3 $(Q = +2q)$ vertices, being oppositely charged counterparts to the previously examined Type 3 vertices $(Q = -2q)$, exhibit a symmetrical spin texture inversion. Notably, bright lobes observed in the $Q = -2q$ configuration transform into dark lobes in the $Q = +2q$ configuration. Additionally, point sinks, indicative of moments within the wires unable to align with the vertex flow, appear at precisely the same locations as point sources observed previously - specifically, on the lower SL2 wires directly linked to the junction itself, these are marked here with points “A” and “B” as before.

In subsequent figures featuring the analysis of SL2/SL3 vertex examples, the orientation of the SL2 layer consistently remains along the defined y-axis. Meanwhile, the SL3 layer, running parallel to the SL1 layer, is depicted along the x-axis. To enhance clarity, the arrows representing the SL2 layer will maintain consistent colouring, while the colouration of SL3 arrows will differentiate them from the SL1 layer.

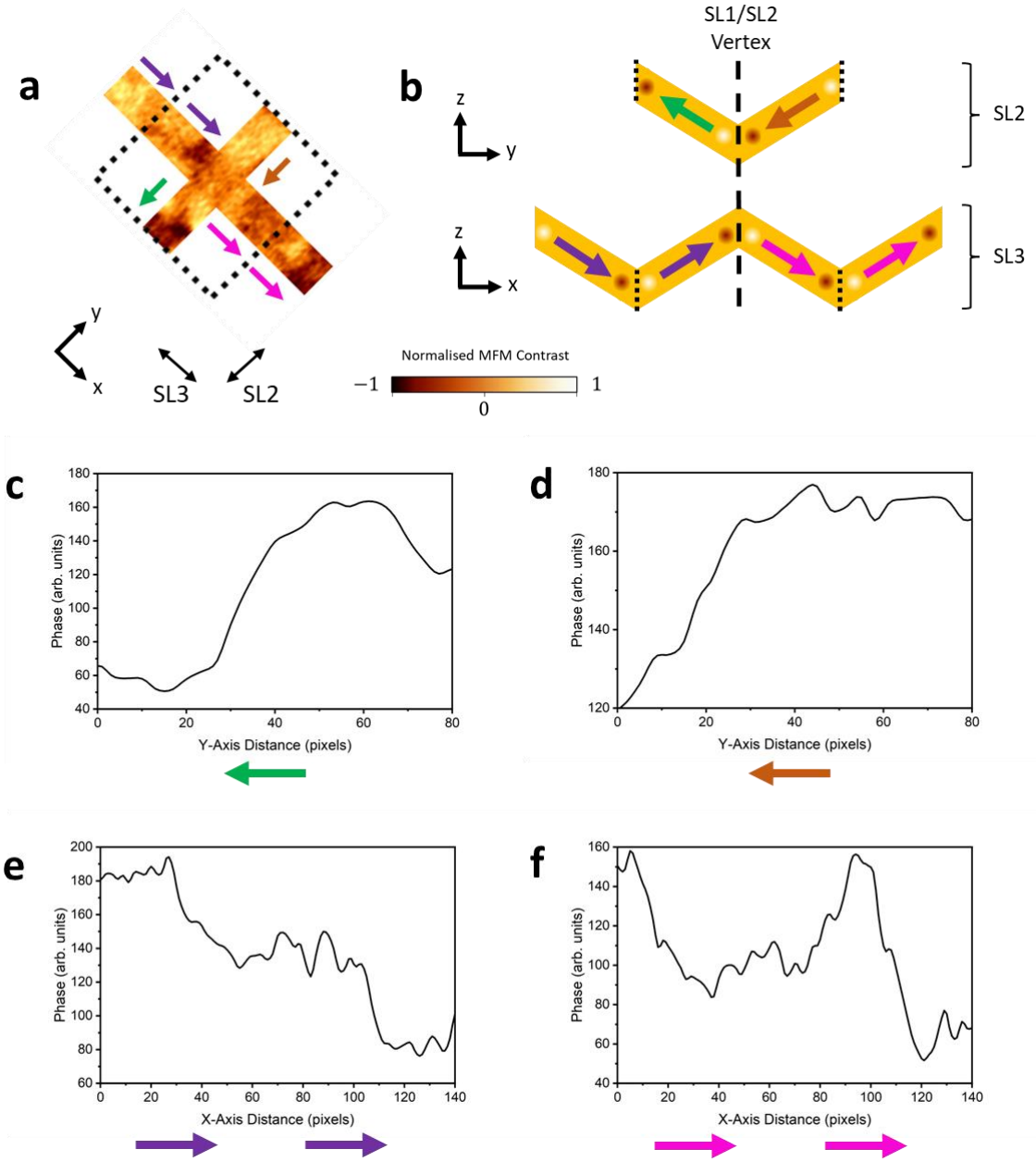

Figure 111: ***(a)*** *Masked MFM contrast for a Type 2* $(Q = 0)$ *identified on SL2/SL3 coordination-four vertices with defined y- and x-axis reflecting the SL2 and SL3 directions respectively. The dotted line encompasses the vertex's four constituent wires.* ***(b)*** *Side profile view of considered wires, highlighting the axis, vertex centre location (dashed line), and individual wires separated by dotted lines with contrast visible shown. Legend for* ***(a-b)*** *denotes normalised MFM contrast.* ***(c-d)*** *Line profiles across defined y-axis along the SL2 wires with representative arrows showing wire magnetisation orientation.* ***(e-f)*** *Line profiles across defined x-axis along SL3 wires with representative arrows showing wire magnetisation orientation.*

With all vertex types identified on the SL1/SL2 layers, the analysis now shifts to examining the vertex types found on the SL2/SL3 junctions. The signal-to-noise measuring the constituent SL2/SL3 wires is significantly worsened due to the increased depth of these wires in the 3D structure. The axis orientation remains consistent with the previous configuration, where SL2 aligns along the y-axis, while SL3 (parallel in orientation to SL1) aligns along the x-axis. As only the two SL2 wires connected to this junction are considered, this is reflected in the side-profile representation of the magnetisation.

A Type 2 vertex situated on an SL2/SL3 junction is examined in **Figure 111a**. A side-profile view showing overall magnetisation orientation of constituent wires is shown in **Figure 111b**. Analysis of the SL2 wires that constitute this vertex show an overall head-to-head configuration showing that the bottom-left SL2 wire (green arrow) is pointed away from the vertex, see **Figure 111c**, and the top-right SL2 wire (brown arrow) is pointed into the vertex, **Figure 111d**. Visual inspection of the phase of vertex centre shows no clear bright or dark phase.

Analysing the upper-left SL3 wire (purple arrows) reveals a visually discernible head-to-tail phase change directed toward the vertex, a pattern corroborated by the line profile, see **Figure 111e**.

Conversely, the bottom-right connecting SL3 wire (pink arrows) exhibits a bright lobe at its junction with the vertex, followed by a dark phase towards its junction with its neighbouring SL3 wire. The neighbouring SL3 wire continues this pattern with a transition from bright to dark along its length. This collective observation signifies a head-to-tail arrangement across this wire segment, directed away from the vertex, consequently suggesting this vertex is a Type 2 configuration.

In **Figure 104a**, the simulated magnetic contrast of the vertex type identified in **Figure 111** is shown. The presence of bright and dark lobes is seen again in the examined vertex and

approximated well in the simulated contrast. The collected phase of the vertex centre in simulated contrast results agree well with the observed contrast in experimental results.

In **Figure 104b** the spin texture of the Type 2 vertex identified in **Figure 111** is shown. As seen in previous Type 2 vertices there's a distinct 90-degree reorientation at the intersections between the SL2 and SL3 wires. Across the SL2 wires, whilst the in-plane component remains conserved there's a slight canting effect near the vertex, deviating from a traditional domain wall. For the SL3 wires, the 90-degree reorientation at the wire intersections contributes to the formation of a domain wall at the junction of the SL3 wires with the SL2 wires resulting in the formation of the bright and dark lobes seen experimentally and in simulations.

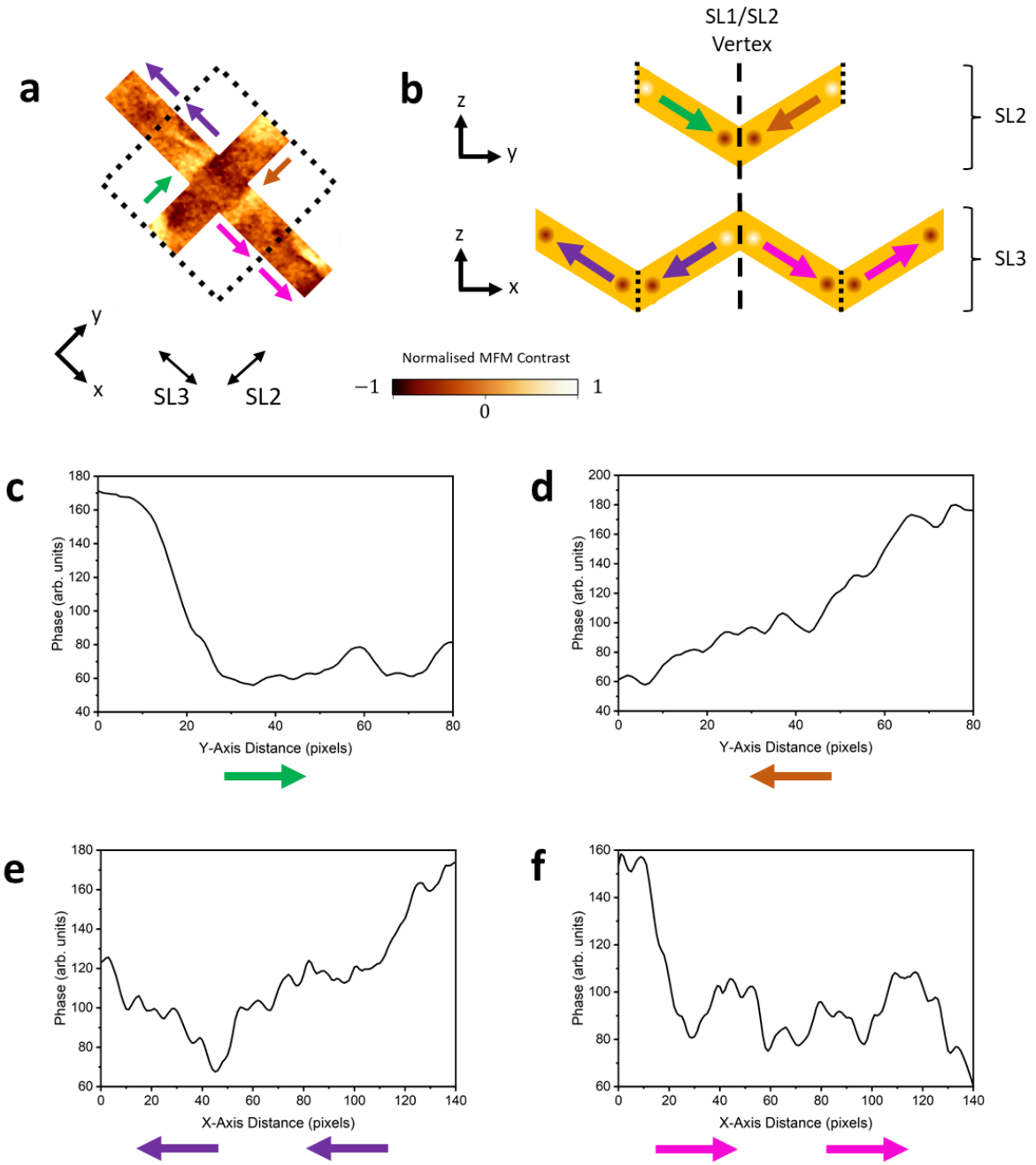

Figure 112: ***(a)*** *Masked MFM contrast for a Type 1* $(Q = 0)$ *identified on SL2/SL3 coordination-four vertices with defined y- and x-axis reflecting the SL2 and SL3 directions respectively. The dotted line encompasses the vertex's four constituent wires.* ***(b)*** *Side profile view of considered wires, highlighting the axis, vertex centre location (dashed line), and individual wires separated by dotted lines with contrast visible shown. Legend for* ***(a-b)*** *denotes normalised MFM contrast.* ***(c-d)*** *Line profiles across defined y-axis along the SL2 wires with representative arrows showing wire magnetisation orientation.* ***(e-f)*** *Line profiles across defined x-axis along SL3 wires with representative arrows showing wire magnetisation orientation.*

Figure 112a shows an identified Type 1 $(Q = 0)$ vertex situated at the junction of the SL2 and SL3 wires. A side-profile view showing the identified magnetisation orientation of the constituent SL2 and SL3 wires is shown in **Figure 112b**.

The visual examination of the SL2 wires shows distinct bright contrast lobes at both ends, juxtaposed with a clear dark contrast in the central vertex area, signifying an overarching head-to-head configuration, as depicted in the figure. Line profile analysis, shown in **Figure 112c** and **Figure 112d**, further elucidates this transition along the entire expanse of the SL2 wire, revealing bright phases at either end and a trough at the central portion within the SL2/SL3 vertex centre.

Similarly, examination of the two constituent SL3 wires, via visual inspection and line profiles, shown in **Figure 112c** and **Figure 112d,** reveals a discernible shift from bright to dark starting from the vertex junction and extending outward, indicating unequivocal head-to-tail arrangements along the entirety of both SL3 wires directed out of the vertex. This arrangement suggests that this vertex is a Type 1.

The relevant simulated MFM contrast, **Figure 106a**, and representative spin texture, **Figure 106b**, for the vertex example shown in **Figure 112** show good agreement with previously discussed features of a Type 1 vertex. A significantly darker phase is visually seen in the measured SL2/SL3 Type 1 vertex centre compared with the measured SL2/SL3 Type 2 vertex centre; however, this dark phase is not comparable to later Type 3 $(Q = +2q)$ examples. Overall, the simulated results agree well with experimental analysis, suggesting that this is a Type 1 vertex.

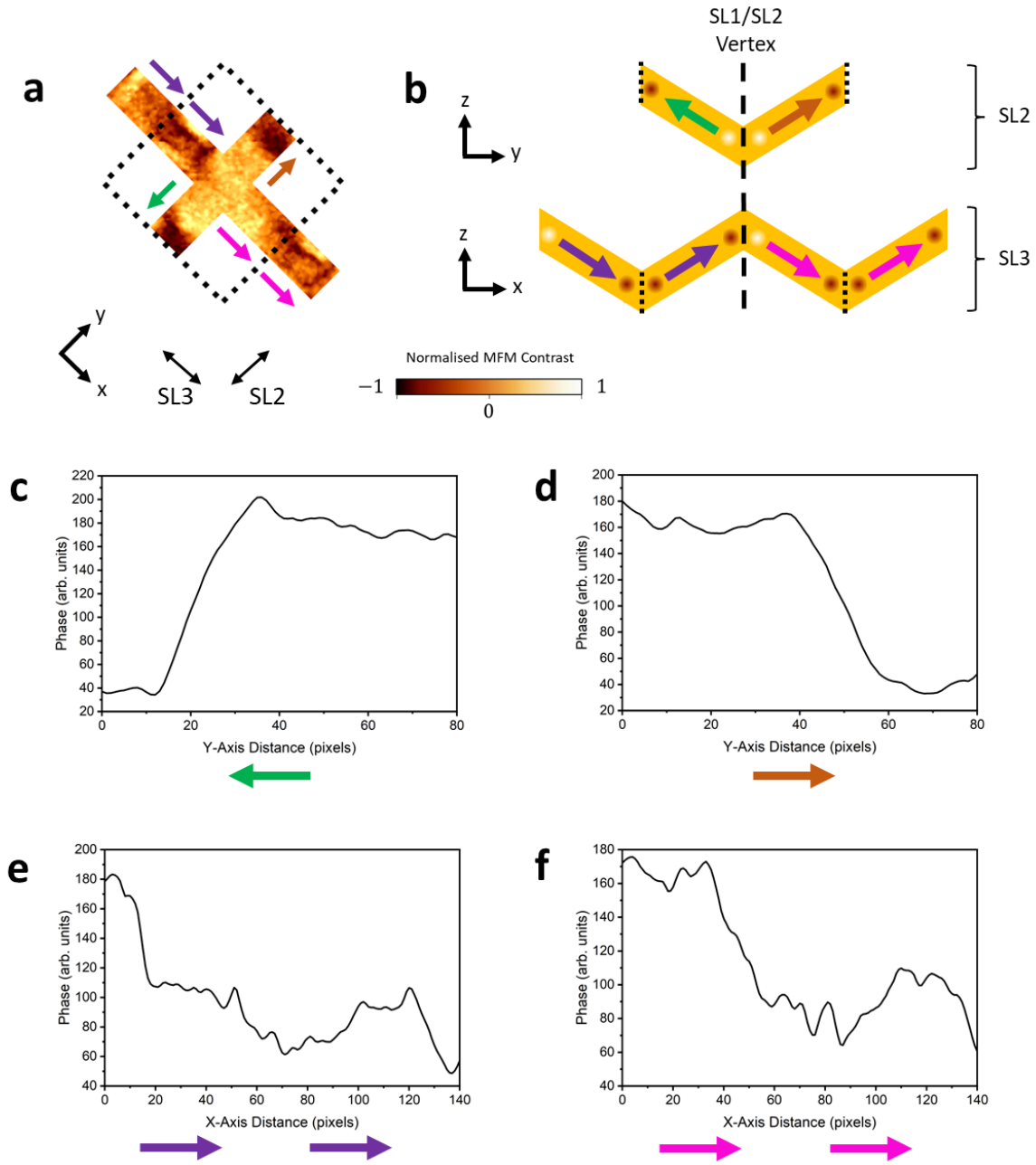

Figure 113: (a) *Masked MFM contrast for a Type 3* $(Q = -2q)$ *identified on SL2/SL3 coordination-four vertices with defined y- and x-axis reflecting the SL2 and SL3 directions respectively. The dotted line encompasses the vertex's four constituent wires.* ***(b)*** *Side profile view of considered wires, highlighting the axis, vertex centre location (dashed line), and individual wires separated by dotted lines with contrast visible shown. Legend for* ***(a-b)*** *denotes normalised MFM contrast.* ***(c-d)*** *Line profiles across defined y-axis along the SL2 wires with representative arrows showing wire magnetisation orientation.* ***(e-f)*** *Line profiles across defined x-axis along SL3 wires with representative arrows showing wire magnetisation orientation.*

In **Figure 113a**, a Type 3 $(Q = -2q)$ vertex on an SL2/SL3 junction is examined, with a side-profile view of the final determined magnetisation configuration shown in **Figure 113b**. The analysis of the SL2 wire exhibits a clear visual and measurable vertex configuration. The wire's central portion appears bright, with dark lobes at both ends, indicating a tail-to-tail arrangement directed away from the vertex. This arrangement is supported by the line profile measurements shown in **Figure 113c-d**.

On the upper-left SL3 wire (purple arrows), there is distinct visual and measurable contrast, revealing a head-to-tail arrangement directed into the vertex, characterized by a dark lobe on the connecting SL3 wire with the vertex. This again is supported by the line profile measurement of these two wires. Conversely, the bottom-right SL3 wire exhibits an overall head-to-tail arrangement directed away from the vertex. A visually noticeable bright lobe near the vertex transitions into a dark lobe at the opposite end of the two SL3 wires. This arrangement is supported by the line profile measurements shown in **Figure 113e-f**.

Visual examination of the overall phase within the vertex centre, see **Figure 113a**, shows a distinct bright contrast, visually identifiable from surrounding vertices within a broader MFM image. This is like the overall phase seen on the Type 3 $(Q = -2q)$ vertex on the SL1/SL2 junction, though a direct comparison is not possible between the two. The vertex situated on the SL2/SL3 junction is deeper into the 3D structure, and therefore signal to noise is decreased by the decrease in interaction between the MFM tip and these wires. A vertex situated on the SL1/SL2 junctions will have significant increase in measured signal in comparison.

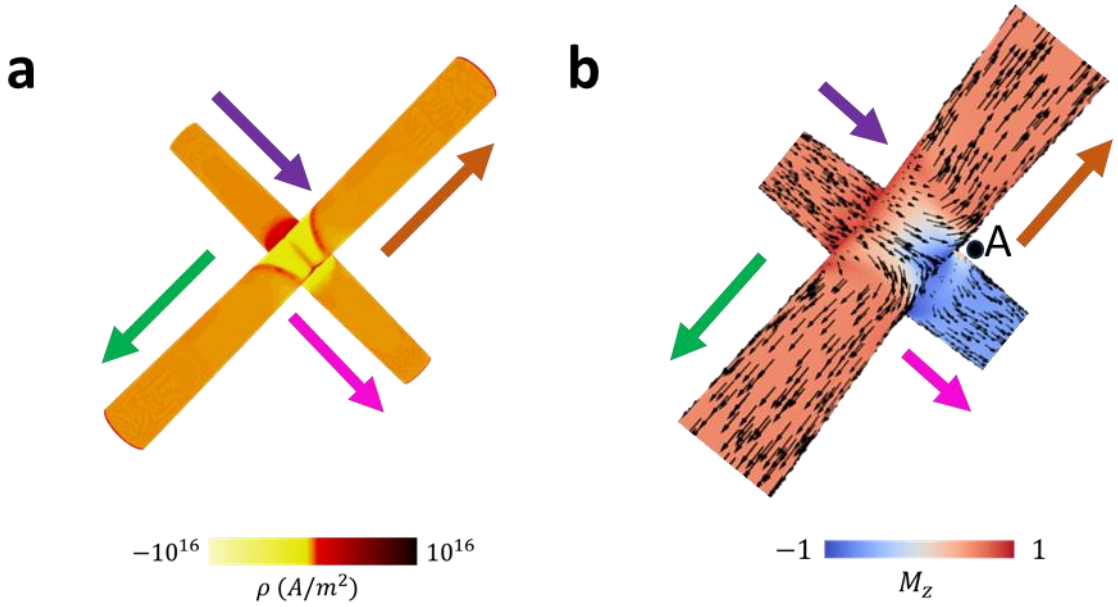

Figure 114: (a) *Simulated Type 3 $(Q = -2q)$ vertex with magnetic charge density depicted on surface, legend shown.* ***(b)*** *Type 3 vertex with colouration determined by magnitude of M_z component, legend shown. Representative spin texture arrows are illustrated on surface and coloured vertex arrows are shown alongside for clarity with previous figures.*

The simulated MFM contrast, **Figure 114a,** and spin texture, **Figure 114b,** for the vertex analysed in **Figure 113** show good agreement with the features identified. The collective simulated MFM contrast at the vertex centre predicts an overall bright phase and this is reflected in the experimental data, showcasing good agreement between the two. The presence of bright and dark lobes on SL3 wires is again noted between experimental and simulated data.

In **Figure 114b**, the simulated spin textures reveal an asymmetric domain wall configuration distinct to the Type 3 $(Q = -2q)$ vertex type discovered on the SL1/SL2 surface layer previously, see **Figure 108**. Notably, one of the lower SL3 wires (purple arrow) is directed into the vertex, while all other wires extend outwards. This configuration results in an off-centre asymmetric domain wall formation across the vertex. This asymmetry leads to the manifestation of a conspicuous bright lobe, visible on the right-hand side of the bottom wire in **Figure 114b**. This feature has been marked by the location of point "A". Unlike the previously simulated Type 3 example where the domain wall was centrally located, in this

instance, the domain wall is positioned off-centre, closer to the lower SL2 wire directed out of the vertex.

This off-centre placement of the domain wall induces a sharp transition in orientation on the vertex, but close to the lower wire directed out of the vertex. This transition contributes significantly to the increased energy cost associated with this specific vertex type. Previous micromagnetic simulations research has quantified this increase, showing a 13% greater energy cost for this type of vertex compared to the previously examined Type 3 ($Q = -2q$) [43].

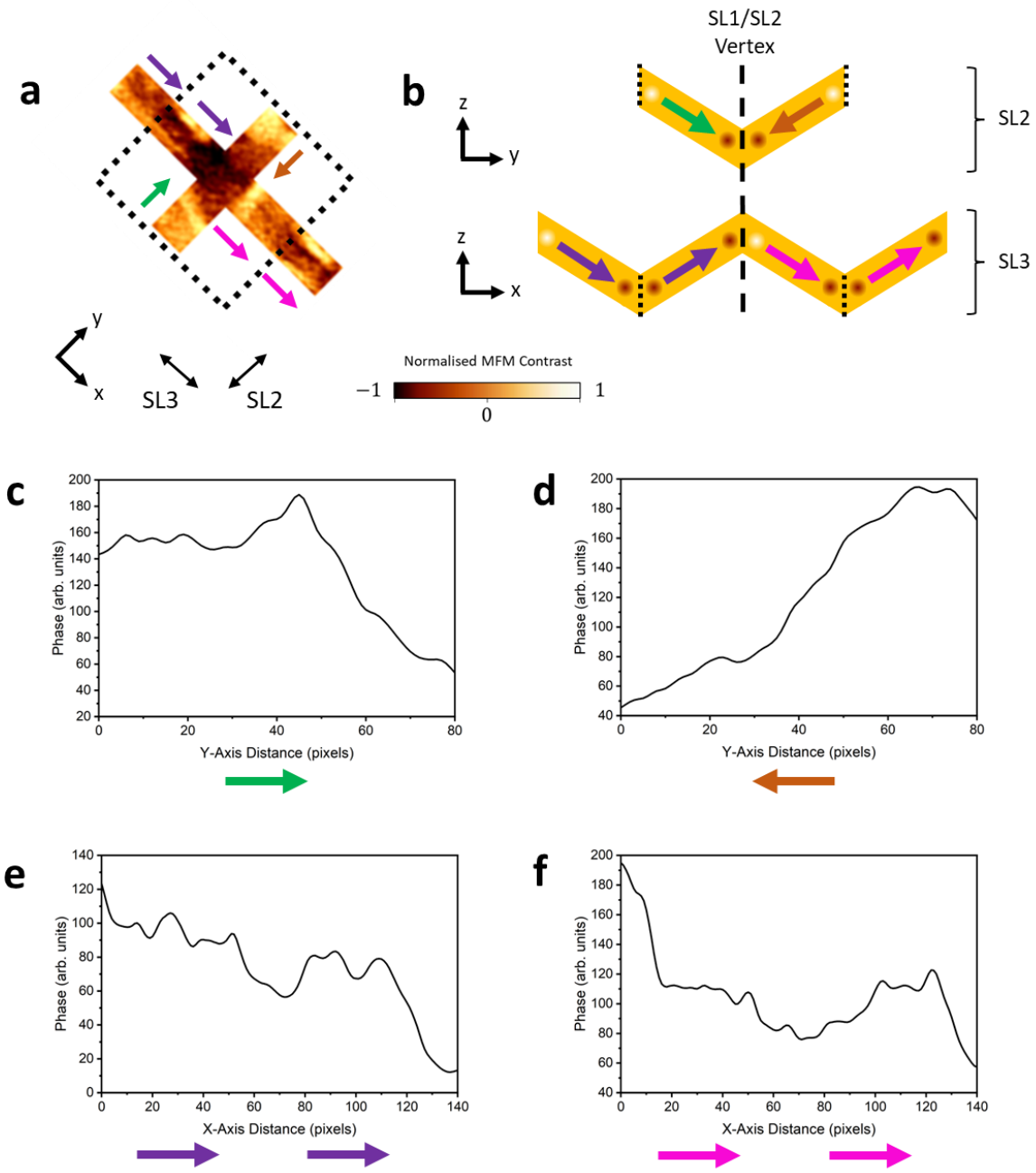

Figure 115: (a) *Masked MFM contrast for a Type 3* $(Q = +2q)$ *identified on SL2/SL3 coordination-four vertices with defined y- and x-axis reflecting the SL2 and SL3 directions respectively. The dotted line encompasses the vertex's four constituent wires.* ***(b)*** *Side profile view of considered wires, highlighting the axis, vertex centre location (dashed line), and individual wires separated by dotted lines with contrast visible shown. Legend for* ***(a-b)*** *denotes normalised MFM contrast.* ***(c-d)*** *Line profiles across defined y-axis along the SL2 wires with representative arrows showing wire magnetisation orientation.* ***(e-f)*** *Line profiles across defined x-axis along SL3 wires with representative arrows showing wire magnetisation orientation.*

In **Figure 115a**, an oppositely charged Type 3 ($Q = +2q$) vertex is presented with a side-profile diagram showing the magnetisation arrangement of the constituent wires shown in **Figure 115b**. The central portion of the wire displays clear and distinct dark contrast, reminiscent of Type 3 SL1/SL2 junctions measured previously and identified Type 3 ($Q = +2q$) vertices in literature, see **Figure 109**. Both SL2 wires visually show bright lobes situated at either end, signifying a head-to-head arrangement directed into the vertex. Line profile measurements for both SL2 wires agree with this assessment with an overall bright-to-dark oriented into the vertex shown by both **Figure 115c**-**d**.

The upper-left SL3 wires demonstrates a clear head-to-tail configuration directed into the vertex, with bright-to-dark contrast extending over the neighbouring and then connected SL3 wire and into the vertex. This is visually identifiable and confirmed with the line profile measurement, **Figure 115e**.

On the other hand, the bottom-right SL3 wire exhibits a head-to-tail configuration directed away from the vertex. A bright lobe is observed at the junction of this connecting SL3 wire with the vertex, visually and within the respective line profile (**Figure 115f**), portraying a bright-to-dark transition over these SL3 wires.

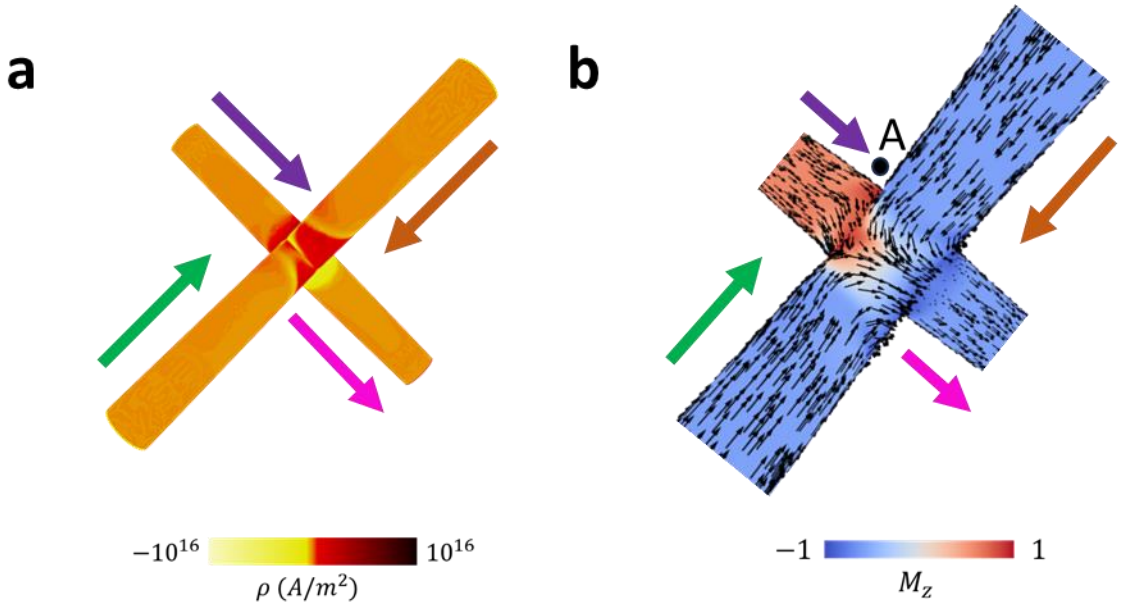

Figure 116: (a) *Simulated Type 3 $(Q = +2q)$ vertex with magnetic charge density depicted on surface, legend shown.* ***(b)*** *Type 3 vertex with colouration determined by magnitude of M_z component, legend shown. Representative spin texture arrows are illustrated on surface and coloured vertex arrows are shown alongside for clarity with previous figures.*

Similarly, **Figure 116a-b** offers a direct comparison to the vertex example showcased in **Figure 115**. Once more, a robust agreement is evident in simulated MFM contrast with the identification of lobes and the overall phase characteristics between experimental findings and simulation results.

Figure 116b showcasing the spin texture for this vertex, being oppositely charged counterparts to the previously examined Type 3 vertices $(Q = -2q)$ in **Figure 113** and **Figure 114**, exhibit a symmetrical spin texture inversion. Notably, bright lobes observed in the $Q = -2q$ configuration transform into dark lobes in the $Q = +2q$ configuration. Additionally, point sinks, indicative of moments within the wires unable to align with the vertex flow, appear at precisely the same locations as point sources observed previously - specifically, on the lower SL3 wire directly linked to the junction itself (see point A).

An approximate 12% increase in energy cost has also been observed between the two Type 3 $(Q = +2q)$ vertex types that have now been observed, mirroring previous findings for Type 3 $(Q = -2q)$. This increase is associated with the presence of a sharp domain wall in the spin

texture, occurring at the convergence point of spins directed into the vertex. This domain wall's formation is attributed to the altered spin configuration, contributing to the elevated energy requirement similarly observed in the $Q = -2q$ configuration.

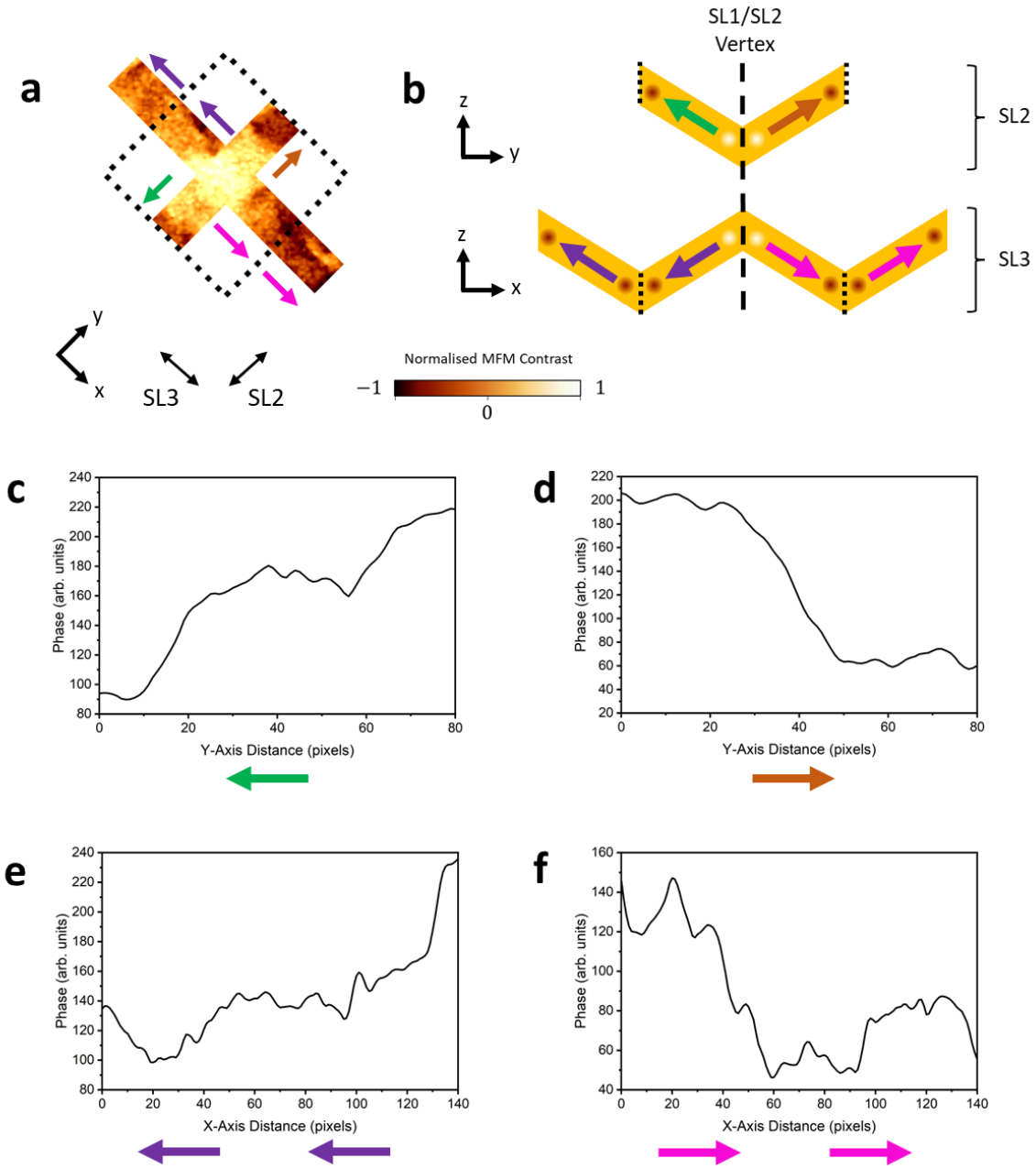

Figure 117: (a) *Masked MFM contrast for a novel Type 4* $(Q = -4q)$ *identified on SL2/SL3 coordination-four vertices with defined y- and x-axis reflecting the SL2 and SL3 directions respectively. The dotted line encompasses the vertex's four constituent wires.* ***(b)*** *Side profile view of considered wires, highlighting the axis, vertex centre location (dashed line), and individual wires separated by dotted lines with contrast visible shown. Legend for* ***(a-b)*** *denotes normalised MFM contrast.* ***(c-d)*** *Line profiles across defined y-axis along the SL2 wires with representative arrows showing wire magnetisation orientation.* ***(e-f)*** *Line profiles across defined x-axis along SL3 wires with representative arrows showing wire magnetisation orientation.*

Figure 117a displays a masked MFM example revealing a previously unidentified Type 4 $(Q = -4q)$ vertex situated on a SL2/SL3 coordination-four junction. A side-profile illustrating the determined magnetisation orientation for SL2 and SL3 wires is presented in **Figure 117b**.

Visually this Type 4 vertex and its oppositely charged version shown later, distinctly stand out in MFM scans due to their intense magnitude of their vertex centres amidst a broader MFM image. The central portion of this example exhibits a notably brighter contrast, surpassing the magnitude of the Type 3 $(Q = -2q)$ example. All wires visually display a bright-to-dark pattern directed out of the vertex, suggesting this is a Type 4 $(Q = -4q)$ vertex.

Line profiles taken across wires connected to this vertex confirm an overall outward-directed configuration. The line profiles of the SL2 wire resemble those of previously observed Type 3 $(Q = -2q)$, see **Figure 107** and **Figure 113**, suggesting a tail-to-tail arrangement across this wire. Line profiles of the SL3 wires also agree with visual identification, with bright lobes seen to connect the SL3 wires with the vertex, while darker phases on the neighbouring SL3 wires suggest an overall head-to-tail arrangement.

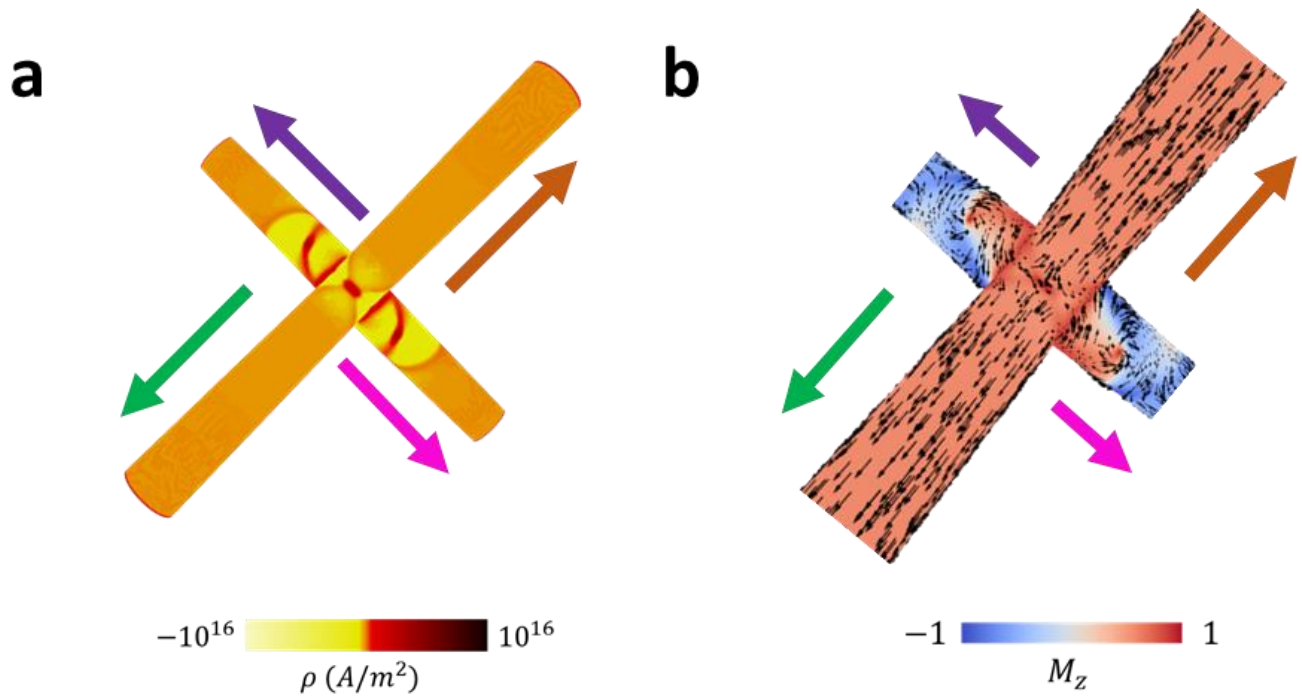

Figure 118: (a) *Simulated Type 4 $(Q = -4q)$ vertex with magnetic charge density depicted on surface, legend shown.* ***(b)*** *Type 4 vertex with colouration determined by magnitude of M_z component, legend shown. Representative spin texture arrows are illustrated on surface and coloured vertex arrows are shown alongside for clarity with previous figures.*

Figure 118a and **Figure 118b** illustrate the simulated contrast and spin texture, respectively, for the Type 4 $(Q = -4q)$ vertex examined in **Figure 117**. The overall phase profile observed in the experimental data consistently aligns with the collective phases observed in simulations. The collective phase of the simulated contrast implies an overall bright phase extending across all constituent wires in the experimental data, which corresponds to the experimental observations.

Examining the spin texture reveals that the Type 4 vertex consists of an anti-vortex domain wall forming at the vertex centre, with the spin orientation directed out of the plane. This configuration resembles the spin texture previously observed in Type 1 vertex centres. For the lower SL3 wires to be directed into the junction to form this anti-vortex wall and simultaneously be directed away from the junction, so that the vertex is a Type 4, is achieved by the presence of two visually identifiable vortex domain walls situated on the lower SL3

wires. These domain walls both exhibit clockwise chirality and upwards polarity, resulting in a brighter contrast observed across the entire vertex and constituent wires.

Overall, analysis of the experimental and simulated data agree that this example is a Type 4 $(Q = -4q)$ vertex.

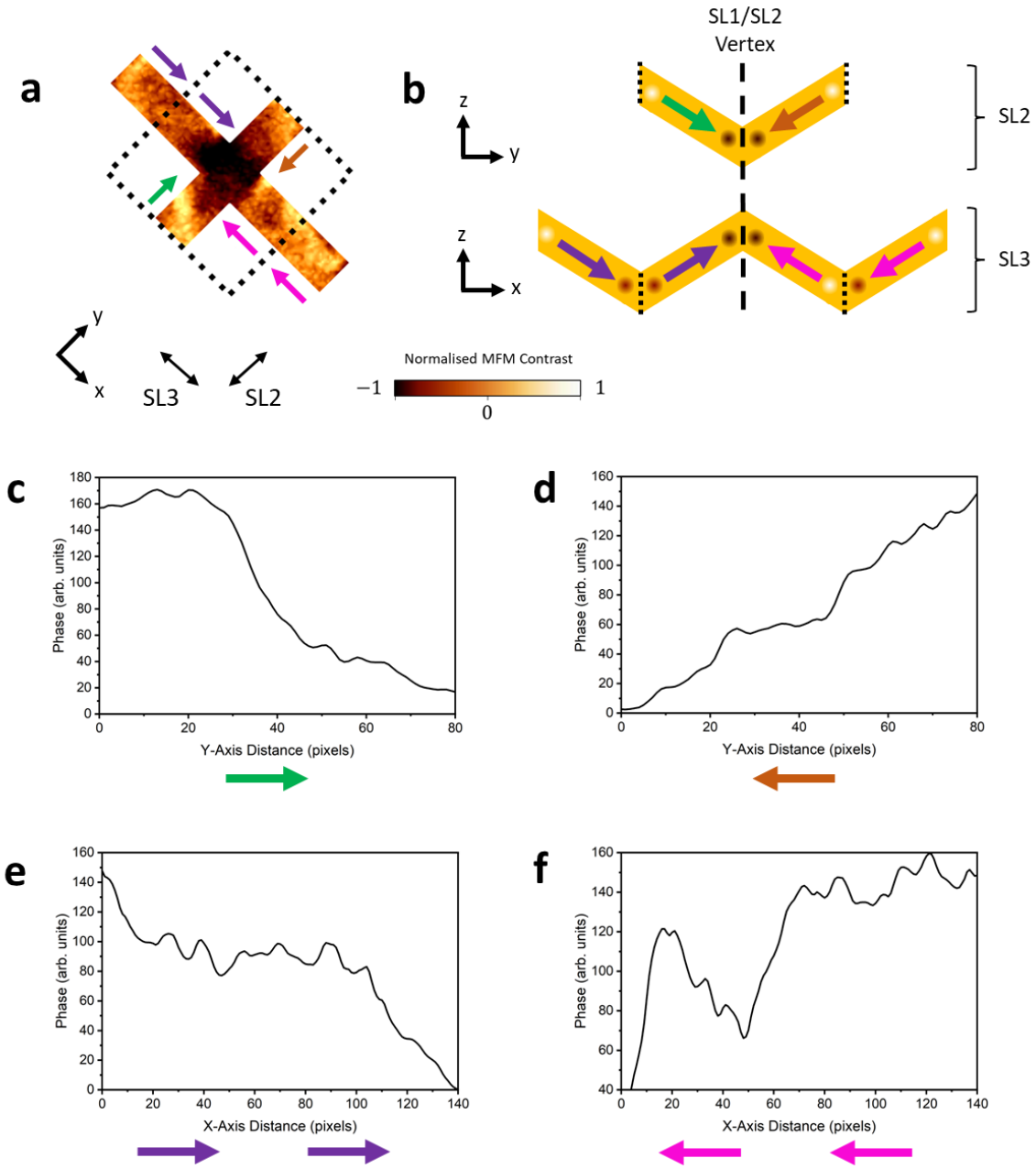

Figure 119: (a) *Masked MFM contrast for a novel Type 4* $(Q = +4q)$ *identified on SL2/SL3 coordination-four vertices with defined y- and x-axis reflecting the SL2 and SL3 directions respectively. The dotted line encompasses the vertex's four constituent wires.* ***(b)*** *Side profile view of considered wires, highlighting the axis, vertex centre location (dashed line), and individual wires separated by dotted lines with contrast visible shown. Legend for* ***(a-b)*** *denotes normalised MFM contrast.* ***(c-d)*** *Line profiles across defined y-axis along the SL2 wires with representative arrows showing wire magnetisation orientation.* ***(e-f)*** *Line profiles across defined x-axis along SL3 wires with representative arrows showing wire magnetisation orientation.*

Figure 119a showcases an example of a Type 4 $(Q = +4q)$ vertex situated on an SL2/SL3 junction. The magnetisation configuration for this vertex, derived from analysis of experimental and simulated data is depicted in **Figure 119b**. A visual examination of the vertex centre reveals distinct dark contrast, surpassing the magnitude observed in Type 3 $(Q = +2q)$ vertex examples.

Upon visual examination of the SL2 wire, a characteristic peak-trough-peak pattern consistent with observations in SL1/SL2 and SL2/SL3 Type 3 $(Q = +2q)$ vertices is apparent. This visual observation is supported by subsequent line profile measurements taken across the two SL2 wires, shown in **Figure 119c-d**.

The upper-left SL3 wire (indicated by purple arrows) distinctly exhibits a head-to-tail arrangement directed into the vertex, corroborated by the line profile. Similarly, the bottom-right SL3 wire (marked by pink arrows) visually displays an orientation directed into the vertex with an overall phase change from bright-to-dark. However, line profile measurements across these SL3 wires reveal a reduced peak on the line profile for this bottom right connecting SL3 wire prompting further examination.

Considering the possibility of this connecting SL3 wire being directed out of the vertex would result in a head-to-head arrangement within the SL3 wires, similar to the observed pattern across the SL2 wire in this vertex example. However, this scenario contradicts the line profile observed across the two bottom-right SL3 wires. The line profile clearly exhibits a strong bright-to-dark phase pattern across the neighbouring bottom-right SL3 wire, continuing up the connecting SL3 wire directed into the SL2/SL3 vertex under consideration.

Additionally, the reduced peak observed does not align with all previously examined bottom-right connecting SL3 wires. In all other SL2/SL3 vertex examples, an orientation directed out of the vertex is consistently characterized by a bright lobe with an overall phase change from bright-to-dark away from the vertex. However, this characteristic is not evident in this connecting wire. Hence, it is concluded that the magnetisation of this wire is directed into the vertex, suggesting this vertex as a Type 4 $(Q = +4q)$.

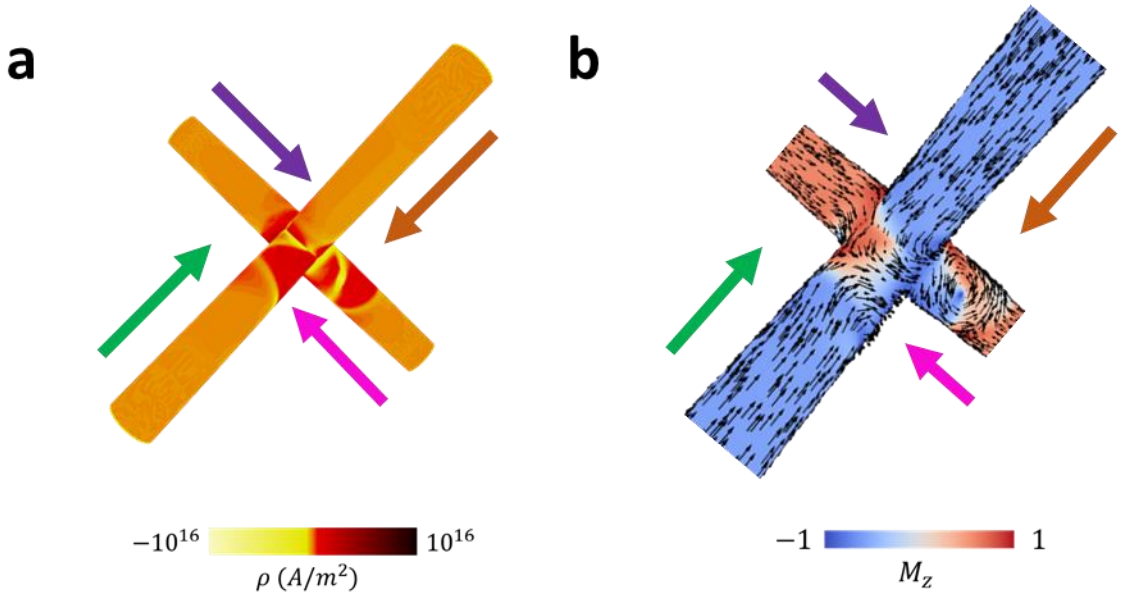

Figure 120: (a) *Simulated Type 4* $(Q = +4q)$ *vertex with magnetic charge density depicted on surface, legend shown.* ***(b)*** *Type 4 vertex with colouration determined by magnitude of* M_z *component, legend shown. Representative spin texture arrows are illustrated on surface and coloured vertex arrows are shown alongside for clarity with previous figures.*

Figure 120a-b show the simulated contrast and spin texture respectively for the Type 4 $(Q = +4q)$ vertex examined in **Figure 119**. The observed overall phase profile in the vertex centre of experimental data aligns consistently with the collective phases seen in simulations. The simulated contrast collective phase implies an overall dark phase in experimental data extending out across all constituent wires. This aligns with what is seen experimentally. Moreover, the simulated contrast presents an asymmetry not evident in the oppositely charged Type 4 simulation. However, there's evidence of at least one vortex domain wall present on the bottom-right SL3 wire in the simulated contrast, potentially causing the reduced bright peak observed on this wire in the experimental data.

The simulated spin texture for this Type 4 reveals a complex arrangement of domain walls present within this vertex. An asymmetric domain wall is noted at the convergence of three of the vertex wires, resembling a Type 3 configuration. Additionally, a single vortex domain wall is situated exclusively on one of the lower SL3 wires, displaying an anti-clockwise chirality and negative polarity directed into the plane.

In both the Type 3 $(Q = +2q)$ spin texture, as seen in **Figure 116**, and this Type 4 example, the contrast observable in both experiment and simulation notably extends across three constituent wires, with the fourth wire exhibiting lesser darkness. This characteristic stems from asymmetric spin texture of the Type 4 vertex. The previously anticipated high energy cost [43] of this vertex type can now be attributed to the presence of vortex domain walls and the asymmetric domain walls observed in prior high energy cost Type 3 examples.